STRUCTURAL BEHAVIOR OF PASSIVELY REINFORCED ULTRA-HIGH PERFORMANCE CONCRETE (UHPC) BEAMS

BY

SAHEED KOLAWOLE ADEKUNLE

A Dissertation Presented to the
DEANSHIP OF GRADUATE STUDIES

KING FAHD UNIVERSITY OF PETROLEUM & MINERALS

DHAHRAN, SAUDI ARABIA

In Partial Fulfillment of the
Requirements for the Degree of

DOCTOR OF PHILOSOPHY

In

CIVIL ENGINEERING

JUNE 2017

KING FAHD UNIVERSITY OF PETROLEUM & MINERALS

DHAHRAN- 31261, SAUDI ARABIA

DEANSHIP OF GRADUATE STUDIES

This thesis, written by **Saheed Kolawole Adekunle** under the direction his thesis advisor and approved by his thesis committee, has been presented and accepted by the Dean of Graduate Studies, in partial fulfillment of the requirements for the degree of **DOCTOR OF PHILOSOPHY IN CIVIL ENGINEERING.**

Dr. Shamsad Ahmad
(Advisor)

Salah U. Al-Dulaijan
Department Chairman

Dr. Husain Jubran Al-Gahtani
(Co-Advisor)

Dr. Salam A. Zummo
Dean of Graduate Studies

Dr. Mohammed Maslehuddin
(Member)

7/6/17
Date

Kalimur Rahman
Dr. Muhammad K. Rahman
(Member)

Dr. Salah U. Al-Dulaijan
(Member)

This Dissertation is dedicated to my dear loving parents, my lovely wife, my blessed children and my adorable brothers

ACKNOWLEDGMENTS

Firstly, all praise is due to Allah, Who guided me, and granted me knowledge, courage, and health, to complete this study successfully. Next, I appreciate the moral and spiritual support of my dear parents. I am highly indebted for the huge support of my blessed wife, in all forms thinkable, and my children (Ibraheem, AbdulRahman, and Maryam), all of whom maintained their love, support and care with patience throughout my Graduate studies, even though they had to endure less than two hours a day of my company. May Allah reward them all with Jannat Al-Firdaws, the highest, Aameen.

I am very grateful to the custodian of the two holy Mosques, through whom Allah had given me the chance to achieve this PhD degree at KFUPM, and the Civil Engineering department, for giving me the necessary resources, human and materials, to complete the study. I must to acknowledge the kind support of BASF Construction Chemicals, Dammam, for their generous supply of the superplasticizer used in this research.

My special gratitude goes to my committee Chairman, Dr. Shamsad Ahmad Sahab, and my co-advisor, Dr Husain Jubran Al-Gahtani, as well as my committee members, Dr. Mohammad Maslehuddin Sahab, Dr. Salah Al-Dulaijan, and Dr. Muhammad Kalimur Rahman, including a non-official member – Dr. Muhammad Al-Osta, for the positive inspirations which I benefitted from them all. I invoke Allah, the Lord of the majestic throne to continue to grant their desires in this world, and increase your Darajaat in Al-Firdaws, the great abode, Aameen.

Finally, I thank the entire Nigerian/African community in and around KFUPM, and my friends from the Indo-Pakistan subcontinent, as well as colleagues of other nationalities, for your company all along. May Allah continue to help all of them, Aameen.

TABLE OF CONTENTS

LIST OF TABLES

LIST OF FIGURES

LIST OF ABBREVIATIONS

ANOVA: Analysis of variance

LVDT : Linear variable displacement transducer

UHPC : Ultra-high performance concrete

NZ : Natural zeolite

LSP : Limestone powder

MS : Microsilica

UMS : UHPC Mixture containing MS

UMN : UHPC Mixture containing NZ, partially replacing MS in UMS

UML : UHPC Mixture containing MS and LSP

UMSN: UHPC Mixture containing NZ, partially replacing cement in UMS

Avg : Average

SD : Standard deviation

COV : Coefficient of variation

ULS : Ultimate limit state

SLS : Serviceability limit state

ABSTRACT

Full Name : [Saheed Kolawole Adekunle]

Thesis Title : [Structural Behavior of Passively Reinforced Ultra-High Performance Concrete (UHPC) Beams]

Major Field : [Civil Engineering]

Date of Degree : [June 2017]

Ultra-high performance concretes (UHPC), having a much denser microstructure than the conventional normal strength and high strength concretes, with compressive strength above 150 MPa, tensile strength exceeding 15 MPa, modulus of elasticity above 45 GPa, and high ductility. This study aimed first to conduct mechanical characterization of selected UHPC mixtures made with local materials and secondly to study the structural response of passively reinforced UHPC beams leading towards formulation of guidelines for the design of safe, economical and sustainable civil infrastructure.

In the present study, an experimental program was carefully planned and executed to generate data required for detailed mechanical characterization of selected UHPC mixtures and to study the structural behavior of passively reinforced UHPC beams of various sizes. The study of the flexural response of passively reinforced UHPC beams was carried out utilizing twelve UHPC beams incorporating high strength steel bars (with f_y = 1400 MPa) as passive reinforcements and fabricated with two different UHPC mixtures, namely, UMS and UMSN. The UHPC mixture UMS had cement content of 900 kg/m^3, while UMSN had 30 % of cement in UMS replaced by natural zeolite, resulting in cement content of 630 kg/m^3. The experimental matrix included SB-Series beams having cross-section size of 150 × 225 mm, a/d = 3.25, and ρ levels of 1.2, 1.8, 2.4, and 3.1 %; and four DB-Series beams having cross-section size of 150 × 300 mm, a/d = 2.43, and ρ levels of 0.9, 1.3, 1.8, and 2.2 %.

It was found in this study that high strength steel bars ($f_y \geq$ 1000 MPa) are the appropriate choice of passive reinforcement for efficient flexural action of UHPC beams, rather than conventional high yield bars. As ρ increased, the failure modes of SB-Series beams changed from flexural tension-controlled to compression-controlled modes accompanied by shear and bearing damages, while the failure modes of DB-Series beams changed from flexural tension-controlled to shear failures which were preceded by extensive network of inclined shear cracks. The UHPC beams studied exhibited highly ductile responses, offering sufficient visible warnings of impending failure, even at high passive reinforcement ratios in which their failures were compression-controlled. Based on the experimental data, a semi-mechanistic model is proposed to predict the flexural capacity of passively reinforced UHPC beams, with a fair degree of accuracy.

ملخص الرسالة

الاسم كاملا: بسعيد كولالي كيوني

عنوان الرسالة: السلوك الإنشائي للجسور المصنوعة من الخرسانة فائقة الأداء مع الحديد الخامل

التخصص: هندسة مدنية

تاريخ الدرجة العلمية: مايو 7102

الخرسانة فائقة الأداء (UHPC) تمتلك بنية مجهرية أكثر كثافة من الخرسانة العادية وهي خرسانة عالية المقاومة حيث أن مقاومة تلك الخرسانة للضغط في حدود (150 – 200 MPa) ومقاومتها للشد تتجاوز 15 MPa . هذه الدراسة تهدف إلى فهم كيفية سلوك الخرسانة فائقة الأداء مع وجود حديد تسليح خامل تحت تأثير قوى الإنحناء وطرق التصميم للمنشآت الخرسانية بأكثر أمان وبتكلفة أقل مع إعتبار الديمومة لتلك المنشآت. أيضاً هذه الدراسة تتضمن الخصائص الميكانيكية والإنشائية للجسور ذات الأحجام المختلفة المصنوعة من الخرسانة فائقة الأداء.

نتائج الإختبارات العملية تمت تحليلها ونمذجتها بإستخدام الأدوات الهندسية والإحصائية المتوفرة، حيث وجد أن الحديد عالي المقاومة ($f_y \geq 1000$ MPa) أكثر ملائمة للجسور المصنوعة من الخرسانة فائقة الأداء والمعرضة لقوى الإنحناء مقارنة بالحديد العادي.

بالإضافة إلى ذلك سلوك الجسور المصنوعة من الخرسانة فائقة الأداء مع الحديد الخامل تمت دراستها ووجد أنها أكثر ليونة حتى لو تم استخدام نسب حديد كبيرة. أيضا وجد أن مقاومة العزوم لتلك الجسور الخرسانية كبيرة مقارنة بتلك الجسور المصنوعة من الخرسانة العادية إلى المتوسطة. كما وجد أن تلك الجسور تحتاج مقاطع أصغر بأربع مرات من تلك المطلوبة للخرسانة العادية في نفس مقاومة العزم.

CHAPTER 1

INTRODUCTION

1.1 Background

Recent decades have witnessed significant advances in concrete technology in various forms, one of which is the development of an exceptional concrete material, named: “ultra-high performance concrete (UHPC).” UHPC usually exhibits compressive strengths in the range of 150 to 200 MPa, which is almost the same as the yield strength of mild steel. Unlike the traditional normal- or high-strength concrete, the tensile strength of UHPC exceeds 15 MPa and its flexural strength (modulus of rupture) can be as high as 50 MPa, while exhibiting a ductile failure behavior, both in tension and compression – thanks to presence of high tensile strength fine steel fibers [1, 2].

Apart from its high strength, UHPC exhibits a much denser microstructure than the conventional normal- and high-strength concretes. It has negligible capillary porosity and therefore it is impervious to liquids and gases. Consequently, the corrosion risk of its reinforcing fibers is practically negligible, while that of active or passive reinforcement embedded in it is exceptionally low. With these attributes, UHPC, since its emergence around two decades ago, has enjoyed numerous applications in circumstances critical to durability. For example, in case of bridges and other civil infrastructures exposed to aggressive conditions in various parts of the world, from France, its birthplace, to North

America, Australia, Netherlands, Japan, Korea, Austria, Australia, Italy, and many other countries. As compared to conventional concrete, UHPC itself is more expensive. However, very high strength of UHPC enables material saving, and its excellent durability helps to minimize maintenance costs and conserves the resources due to long life cycle. As such, properly designed structures built using UHPC are considerably more cost-effective than those made from conventional concrete if the overall cost, including life cycle cost, is considered [3, 4].

Up till now, the UHPC has been used mainly in construction of bridges [5], partially (such as casting of girders and wearing course) or completely for the entire bridge. The main reason behind this may be attributed to the fact that the material saving advantage of UHPC (as a result of its high stiffness and ultra-high strength) is better harnessed by prestressing, which in turn gives structural elements made from UHPC very high strength-to-weight ratio, besides „maintenance-free‟‟ quality.‟ As mentioned earlier, all these benefits are at a relatively higher cost in the short-term, but much more cost-effective in the long-term. This makes UHPC an attractive choice in the bridge engineering community. Furthermore, many researchers have claimed that the design of infrastructure in the future will be governed primarily by the service life and, even to a greater extent, by sustainability considerations [6-8]. This means that in the near future, this new material may be required in virtually all civil infrastructures, particularly in harsh environmental conditions.

For nearly last two decades of emergence and development of UHPC, major emphasis had been placed on the determination of relevant properties and structural behavior of prototype and full-scale UHPC elements. While these research works are still going on, the available data on UHPC have been utilized to create some initial systematic guides for structural design of UHPC members, starting from France in 2002 [9], then some guides from MIT, USA in 2003 and 2007 [10, 11], and Japan in 2004 (English version in 2006) [12, 13] (both building on the French interim code of 2002 [9]). In addition, an international standard for the structural design of UHPC by the International Federation for Structural Concrete (fib - Fédération internationale du béton) is awaited. Currently, all of these guidelines are still in their draft or preliminary forms. Perfecting them into full design codes will rely on continuous generation of large amount of data from research studies worldwide.

Most of the studies conducted so far have focused more on structural testing and design of prestressed UHPC flexural members than passively reinforced ones. Since preparation of prestressed concrete members essentially requires a factory environment, application of UHPC will be very limited. Therefore, to have wider applications of UHPC in in-situ construction of structural concrete members, research on exploring possibility of using passively reinforced UHPC members should also be conducted. This is where the present study fits into the whole picture: contributing to better understanding of the structural response of passively reinforced UHPC beams, towards the design of safe, economical and sustainable civil infrastructure. Besides the contribution to the global knowledge base on the structural response of UHPC members, the current study aimed at developing guidelines on the use of UHPC made with locally available ingredients (dune sand and indigenous by-products as micro-fillers).

This study started from extensive mechanical and structural characterization of three locally developed UHPC mixtures, and then proceeded to the evaluation of the structural behaviors of passively reinforced beams of various sizes and passive reinforcement ratios. The study of the flexural response of passively reinforced UHPC beams was carried out utilizing twelve UHPC beams incorporating high strength steel bars (PSB1080 with f_y = 1400 MPa) as passive reinforcements and fabricated with two different UHPC mixtures, namely, UMS and UMSN. The UHPC mixture UMS had cement content of 900 kg/m^3, while UMSN had 30 % of cement in UMS replaced by natural zeolite, resulting in cement content of 630 kg/m^3. The experimental matrix included SB-Series beams having cross-section size of 150 × 225 mm, a/d = 3.25, and ρ levels of 1.2, 1.8, 2.4, and 3.1 %; and four DB-Series beams having cross-section size of 150 × 300 mm, a/d = 2.43, and ρ levels of 0.9, 1.3, 1.8, and 2.2 %. The experimental data was analyzed and modeled using various statistical and engineering tools.

1.2 Significance of this Study

Since the structural behavior of UHPC mixtures are quite different as compared to those of the normal concrete mixtures, the use of existing design formulation, suitable for normal concrete, would not be appropriate for design of the beams using UHPC mixtures. As emphasized earlier, UHPC as a structural material is still relatively new, and so all of existing design guidelines are still in their draft or preliminary forms. Primarily, it is important to have a better understanding of the structural response of UHPC members in flexure, which would enable formulating the design of safe, economical and sustainable civil infrastructure, locally and globally. Secondarily, as elaborated earlier, there is a lack of enough information on the structural response of UHPC beams incorporating passive reinforcements. Therefore, as a mark of novelty on a global scientific platform, the current research work sought to furnish a comprehensive structural behavior of non-prestressed UHPC beams with a wide variety of passive reinforcement ratios.

Furthermore, some UHPCs have been developed using locally available ingredients – and they have proven very suitable for the local service conditions, based on preliminary material characterization [68] – but have not been assessed so far to evaluate their structural performance as flexural members. Therefore, the another benefit of the current research lies in its initiation of the development of guidelines on the utilization of local ingredients-based UHPC for economical and sustainable infrastructure for local service conditions in the Arabian Gulf environment. The outcome of this research is highly beneficial for the Kingdom, the entire Gulf region and the world in general.

1.3 Research Objectives and Scope

The main objective of the proposed research work is to study the structural behavior of passively reinforced UHPC beams, contributing to the development of structural design guidelines for UHPC flexural members.

The specific objectives are the following:

1. Assess the fundamental mechanical behavior (in compression and tension) of selected locally developed UHPCs,
2. Study the flexural behavior of passively reinforced UHPC beams prepared with the selected locally developed UHPCs,

3. Develop models related to the design of passively reinforced UHPC beams, and
4. Initiate proposing guidelines for design of passively reinforced UHPC beams.

1.4 Research Approach

The approach employed to achieve the stated objectives of this research work consisted of three major phases. The first phase of this work was the initiation phase, which involved the conduct of literature review. A comprehensive up-to-date literature survey was conducted, as presented in Chapter 2. Existing research findings that are relevant to the proposed research were gathered as background information needed for the planning and execution of the experimental work.

The second phase was the preparatory phase, in which the experimental work was designed, and the required materials and consumables were estimated and ordered.

The third phase is the execution phase in which all experimental activities were completed, while the last phase was the ending phase, in which the findings of the work were analyzed, presented and discussed.

1.5 Organization of the Dissertation

This dissertation was presented in seven different chapters. The coverage of these chapters is itemized as follows.

- Chapter 1 contains the research objectives, scope, novelty and organization of the dissertation.
- Chapter 2 presents the literature review.
- Chapter 3 contains the experimental program.
- Chapter 4 presents the discussions of the experimental results for the mechanical characterization of the UHPC mixtures considered in the present study.
- Chapter 5 presents the experimental results and discussion of the flexural behavior of UHPC beams reinforced with passive high-strength steel bars.
- Chapter 6 presents the analysis of passively reinforced UHPC beam sections, leading to the development of a mechanistic equation for estimating the flexural capacity of the studied reinforced UHPC beams
- Chapter 7 presents the conclusions derived from the results of the study and recommendations.

CHAPTER 2

LITERATURE REVIEW

The literature review presented here covers the background information on materials and mix proportioning of UHPC, relevant information on mechanical properties of UHPC, structural behavior of full-scale flexural members, and state-of-the-art information on the design of UHPC flexural members. Having linked the background ideas in a logical manner with a view to exposing the theme of this research, the comprehensive review presented herein would enable to understand the need and importance of the present research work.

2.1 UHPC material concepts

Recent decades have witnessed significant advances in concrete technology in various forms. One of such major advances is the development of ultra-high performance concretes (UHPC) that have compressive strengths in the range of 150 to 200 MPa, which is almost the same as that of mild steel. The incorporation of high tensile strength steel fibers helps UHPC to be ductile, reaching tensile strength exceeding 15 MPa and flexural tensile strength of up to 50 MPa [1]. High compressive and tensile strengths of UHPC are due to much denser microstructure than the conventional normal strength and high strength concretes. It has negligible capillary porosity, which makes it impervious to liquids and gases. The high penetration resistance provides the protection of metallic fibers and steel bars embedded in UHPC against corrosion. With these attributes, UHPC can be used as the wearing course on a bridge deck without any additional protection against chlorides, alkalis or de-icing salts [2]. As compared to conventional concrete, the UHPC itself is more expensive, but its ultra-high strength and durability enable material saving and reduction in the maintenance costs during intended service life of the structures. As such, properly designed structures made from UHPC are considerably more cost-effective than those made from conventional concrete if the overall cost including life cycle cost is considered [3, 4].

2.2 Principles, Development and Production of UHPC

The basic idea behind a concrete with a very high strength and very high durability due to dense microstructure was presented in the 1980s by a Danish researcher, Hans Hendrik Bache [14], who developed a material with high fiber content, and called it Compact Reinforced Concrete (CRC). His idea is based on the principles that need to be followed to achieve the outstanding properties of an UHPC. The basic principles of producing UHPC include the following [8]:

- limiting the aggregate grain size (to as low as 0.3 mm) to prevent decrease in strength due to stress concentrations caused by large grains,
- optimizing the matrix packing density with the help of fine materials, making the microstructure very dense that ensures increasing the stress level at which micro-cracks begin to form by reducing contact surface stresses,

- ensuring that the amount of cement used is such that the water is fully bound through hydration of cement and the remaining un-hydrated cement particles act as fillers, and
- incorporating steel fibers in order to ensure a ductile behavior

Bache‟s ideas were adopted in 1994 by Richard and Cheyrezy of Bouygues (company) in developing a new concrete mix formulation, named „Reactive Powder Concrete‟ (RPC) in conjunction with Lafarge Company [8]. Currently, this mix exists in the form of a commercial product named Ductal®. The emergence of high efficiency superplasticizer led to the practical breakthrough that enabled the production of a concrete containing a high proportion of tightly packed ultrafine particles and very low water/binder ratio of about 0.20 or less with a self-compacting consistency. This is the source of UHPC‟s exceptional properties [8, 15, 16].

The popular idea is the production of UHPC as a fine-grained concrete with a maximum particle size of 1 mm and a highly-flowable consistency. However, it was reported [17] that replacing fine ground quartz sand with an equal volume of optimally graded natural aggregate with a maximum size of 8 mm did not affect the compressive strength at the same water-cement ratio. Also, UHPC class materials have been developed with up to 60 % by volume of well-graded 8 mm or 16 mm coarse aggregate (though to varying workability levels) without affecting the hardened concrete properties [15, 16, 18].

Since its development in the modern form, UHPC has been used in several applications in various countries, including France, Japan, Austria, Australia, Italy, Croatia, Malaysia, the Netherlands, New Zealand, and South Korea. However, majority of its use worldwide, up till the moment has been in bridges [5, 19], partially for some components or completely for the entire bridge.

2.3 Mechanical properties of the UHPC

As mentioned earlier, UHPC exhibits higher strength and stiffness (modulus of elasticity) as compared to normal- and high-strength conventional concretes – owing to its very dense microstructure. The high brittleness of UHPC is countered effectively by the inclusion of high-strength fibers in an appropriate manner. On the onset of cracking of the brittle matrix of UHPC, the fibers get activated. This enhances the post-peak behavior in compression and tension, which brings the desired ductility for favorable structural response in which an impending failure is accompanied by visible warnings. In addition, the enhanced ductility ensures the possibility of using the relatively higher UHPC flexural tensile strength, with a good level of reliability, for load bearing (as compared to conventional concrete in which the tensile strength is usually neglected). Various relevant mechanical properties of the hardened concrete are discussed in the following sub-sections.

2.3.1 UHPC Behavior in Compression

Compressive strength is the most frequently measured property of any concrete, simply because it is an important material property that comes first in the design of any concrete structure, and many other properties of concrete are correlated with it. Compressive strengths of UHPC mixtures have been reported as cube (50 and 100 mm size) and cylinder (various sizes and aspect ratios) strengths. Graybeal [20] reported the compressive strength of almost 1,000 UHPC specimens subjected to different curing conditions [20]. Most tests were conducted on 76 by 152 mm cylindrical specimens with ground ends, while some cube specimens were also tested. He obtained the average 28-day compressive strength for steam cured specimens in the range of 171 to 190 MPa (depending on the treatment procedure), while specimens cured in the ambient condition in the laboratory, the corresponding value was 126 MPa. From the same research program, it was reported that loading rates between 0.24 and 1.7 MPa/s gave almost the same compressive strength, modulus of elasticity, and Poisson's ratio. Also, Perry and Zakariasen [21] reported compressive strength of thermally treated UHPC in the range of 158 to 228 MPa. Generally, similar to the conventional concrete, the compressive strength and behavior will depend on constituent materials and their relative quantities and curing procedure. The UHPC compressive strength results reported in the literature for example in [22-24] have shown a general trend of compressive strength increase with increasing heat treatment temperature. Richard [25] reported that with curing at 90 °C in the conventional production mode, a compressive strength of 280 MPa can be achieved. Also, he claimed that achieving compressive strengths as high as 550 MPa is possible if the curing temperature is increased to 250 °C. In an extreme case, curing in combined high pressure with 250 °C temperature can produce a concrete with a compressive strength of 810 MPa [25].

As regards to the effect of including high strength fibers in UHPC, both the pre-cracking compressive strength and elastic modulus are not significantly enhanced by the incorporation of these fibers. However, there is a significant enhancement of the post cracking behavior and failure mechanism [26]. These claims can be seen convincingly in Figure 2.1 that shows a typical behavior of both plain UHPC mixtures (in their nomenclature) and fiber-reinforced concrete (UHPFRC, in their nomenclature) in uniaxial compression, as obtained by Hassan et al. [26]. From their results, as indicated in Figure 2.1, the duration of air curing after the initial heat treatment seems to have no significant effect on the compressive behavior of UHPC. This observation is more pronounced in the plain UHPC without fiber reinforcement.

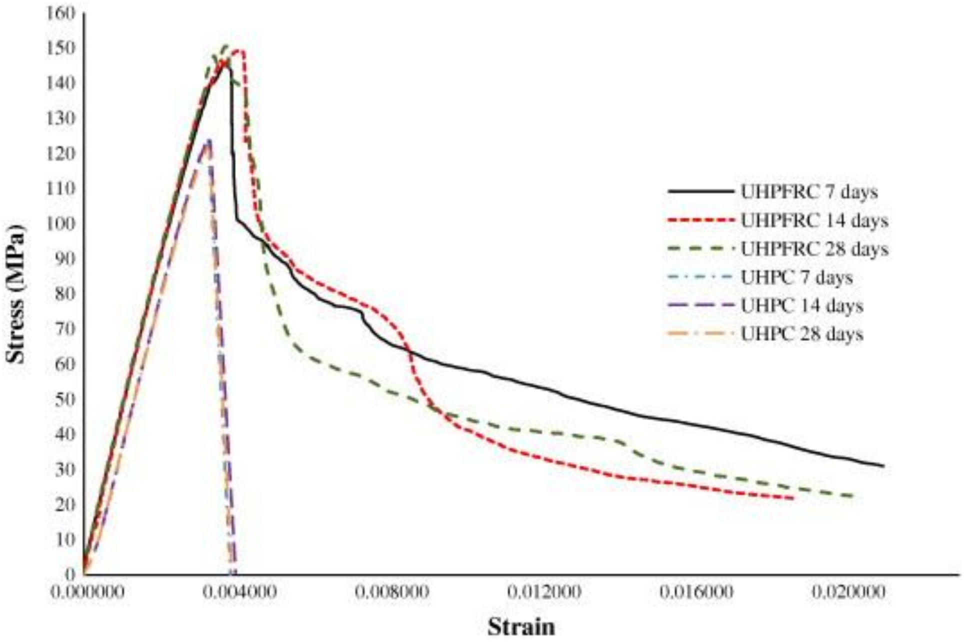

Figure 2.1 Stress‑strain curves of UHPC in compression [26]

2.3.2 Behavior in Direct Tension

Besides having a higher tensile strength much more than that of conventional concrete, UHPC exhibits sustained post-cracking (after first cracking) tensile strength, and so, both the first cracking strength peak and post-cracking strength are often reported in order to have a more complete tensile property for design considerations [5]. The large post-cracking tensile strength of UHPC can be illustrated in Figure 2.2, which shows the stress-strain curves obtained by Hassan et al. [26] for UHPC (fiber-reinforced and unreinforced) on dog-bone specimens.

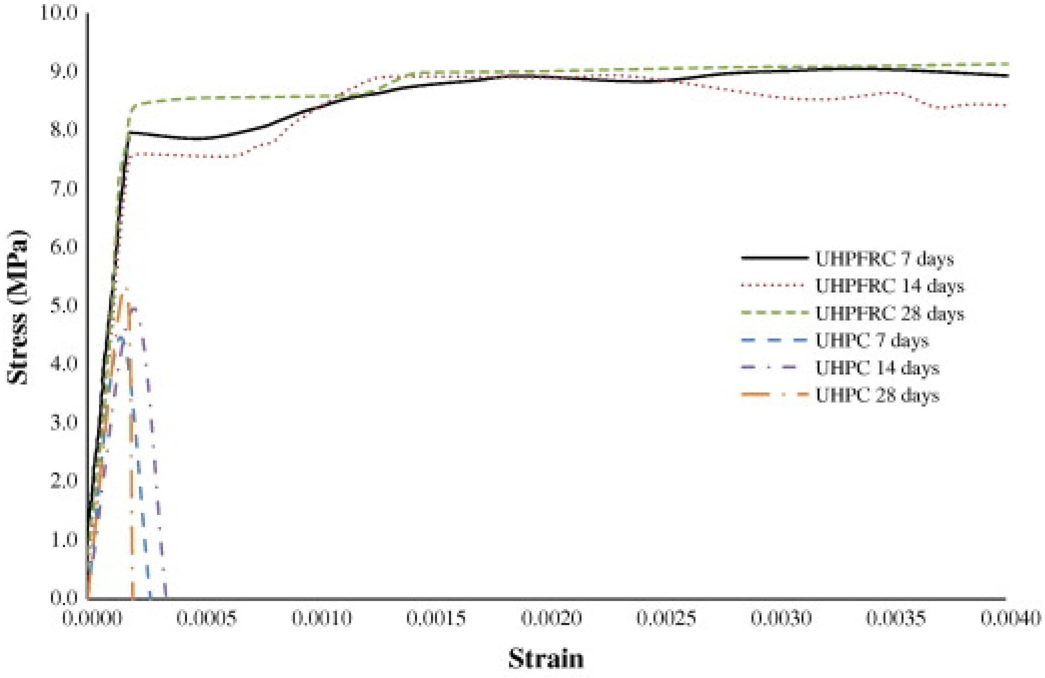

Figure 2.2 Stress‑strain curves of UHPC in uniaxial tension [26]

Another example of uniaxial stress-strain response, obtained by Graybeal [27] is shown in Figure 2.3, similar to the set of curves as shown in in Figure 2.2. Based on direct tension tests of two types of UHPC with varying fiber contents, Graybeal [27] proposed an idealized tensile stress-strain response, which is a conceptual illustration of the pre- and post-cracking tensile stress-strain response of UHPC. This is shown in Figure 2.4. He recognized four distinct phases in stress-strain behavior of UHPC. Followed by the elastic Phase I, Phase II is characterized by the formation of multiple tightly spaced cracks in the UHPC matrix, while the hardening Phase III begins at the strain level at which further cracking between existing cracks is unlikely, but each crack continues to widen until its strain limit is reached. Following this, the last Phase IV starts with the fibers bridging action, and subsequent pullouts from the matrix.

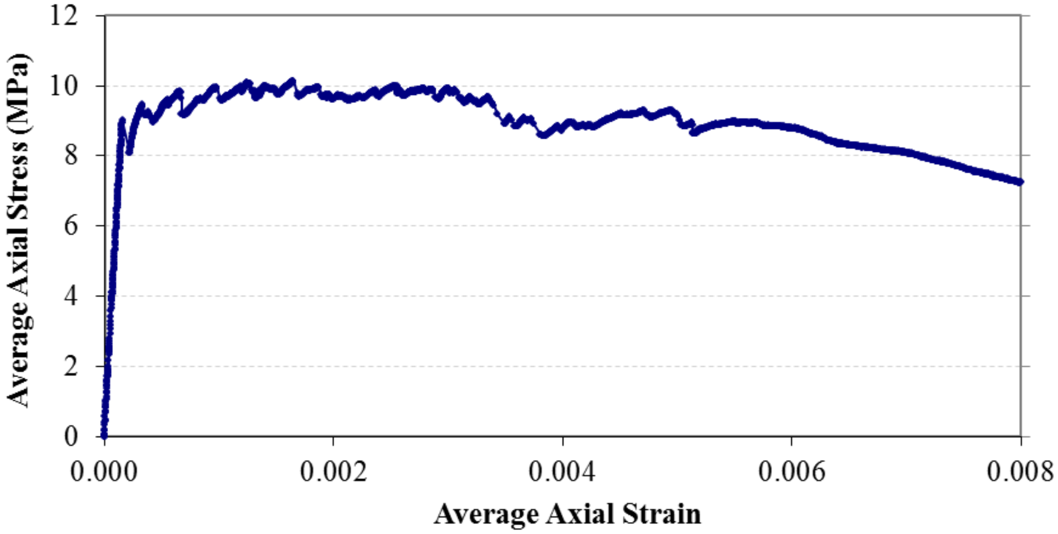

Figure 2.3 Stress‑strain curves of UHPC in uniaxial tension [27].

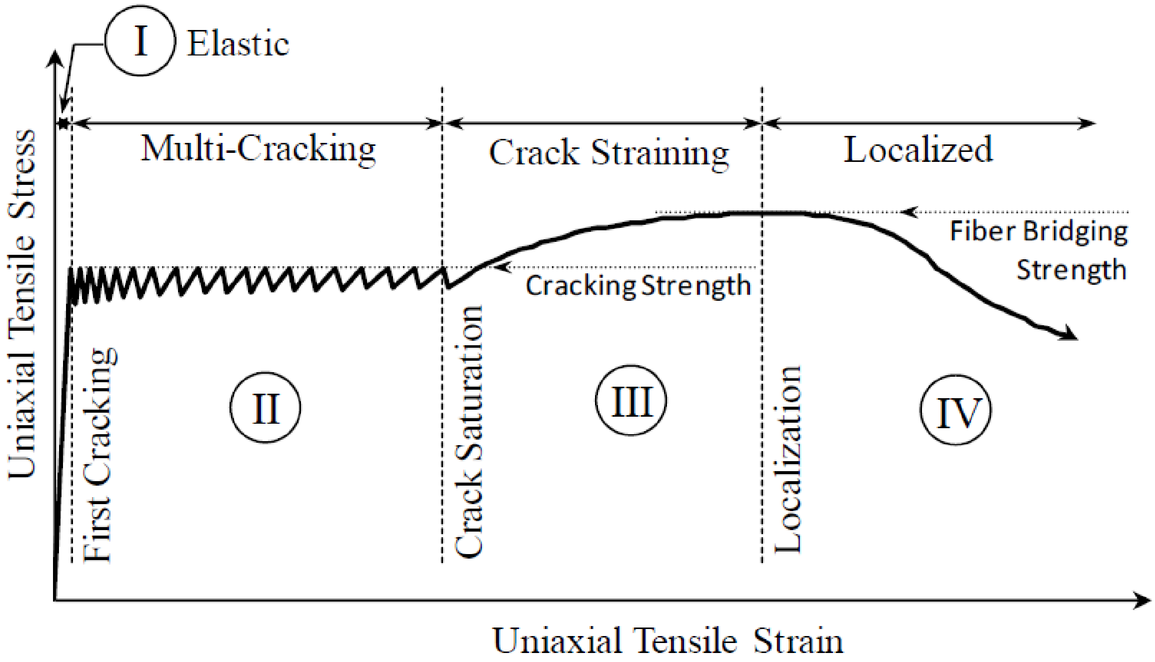

Figure 2.4 **Idealized uniaxial tensile mechanical response of a UHPC [27].**

Hakeem [28] reported values of uniaxial tension tests on six non-heat treated UHPC prismatic specimens (25 × 25 × 285 mm) in the range of 8.8 to 11.6 MPa. Using 102 × 203 mm cylindrical specimens, Graybeal [20] reported direct tensile strength (first tensile cracking) ranging between 7.6 and 11.0 MPa for steam-cured specimens, and between 5.5 and 6.9 MPa for untreated specimens.

A very important property of UHPC class materials is the stress–crack width relationship. This is an important item of information required in the design of UHPC members for serviceability state and ultimate load carrying capacity [9-11]. Unlike in the determination of the tensile strength of UHPC where tests on un-notched prismatic specimens are suitable, tests for obtaining the stress–crack width relationship are more appropriately carried out on notched specimens [29]. Leutbecher [30] studied the post-crack load-carrying mechanism in UHPC containing 0.5 and 1.5% of 20 mm high strength steel fibers. Figure 2.5 shows the results of the stress–crack width measurements on notched prisms.

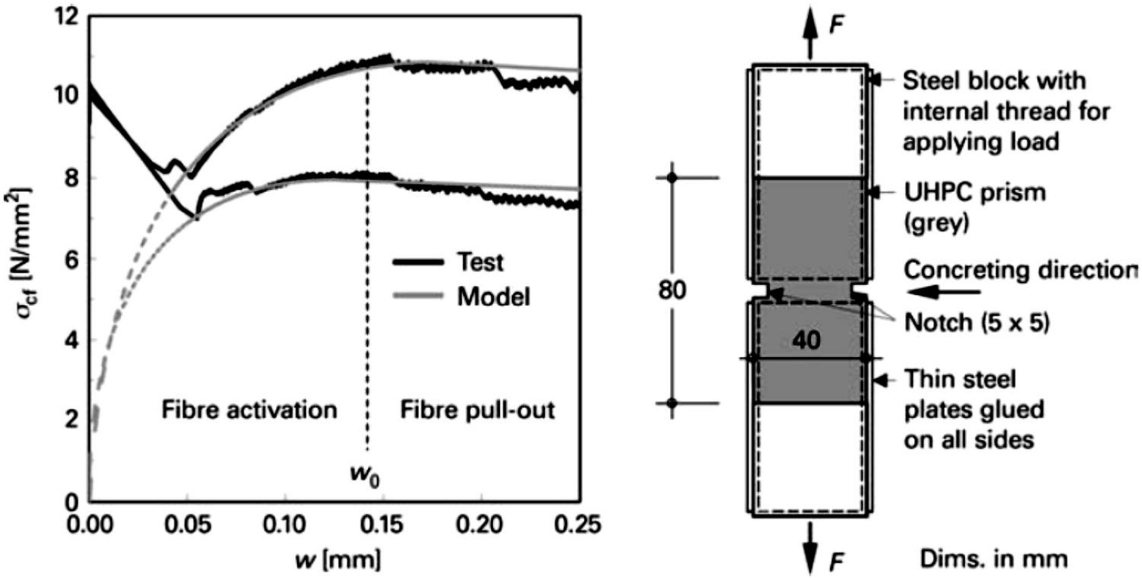

Figure 2.5 **A stress–crack width curve of UHPC in uniaxial tension [30].**

Following the post-crack softening of the matrix, Figure 2.5 shows the fiber activation occurring around 50-μm crack width (resulting in composite hardening), while the fibres pullout from the matrix begins when the crack width increases to around 150 μm, accompanied by softening towards the final failure. Based on various tests, generalized stress–crack width relationships have been proposed [9-11, 30-34].

2.3.3 Flexural Behavior

Apart from the behavior in direct tension, several studies have reported the flexural strength of UHPC using two- or tree-point flexural prisms. Flexural tensile tests are often preferred for determining the tensile strength properties due to their advantage of being easy to carry out with a compression-testing machine in simple loading arrangements. Also, using the technique referred to as inverse analyses [35, 36], the flexural tensile test results for UHPC can be used to derive the uniaxial tensile response. Graybeal [20] reported the first cracking flexural strength values (determined according to ASTM C1018 prism flexure test [37]) between 9.0 and 10.3 MPa for steam-cured specimen, and an average value of 9.0 MPa for untreated specimens.

It has been claimed [20, 21, 38-40] that the flexural strength of heat-treated UHPC ranges from 27–50 MPa, while exhibiting exceptional levels of post-cracking strength and ductility owing to the addition of high strength fibers, in addition to the inherently tightly packed matrix microstructure – which in itself enhances the fiber-matrix bond.

Figure 2.6 shows equivalent stress–deflection curves for Ductal®, the popular commercial UHPC, two other FRCs and a normal strength conventional concrete [39]. Figure 2.6 shows not only the good post-cracking ductility of UHPC but also the overall tensile response in flexure for various grades of FRC. The implication of the tensile resilience of UHPC is that concrete design philosophy has to change from the traditional ideas of neglecting tensile contribution of conventional concrete to a new approach in which due attention has to be paid to the contribution of UHPC in the tensile part of internal resistance of concrete elements.

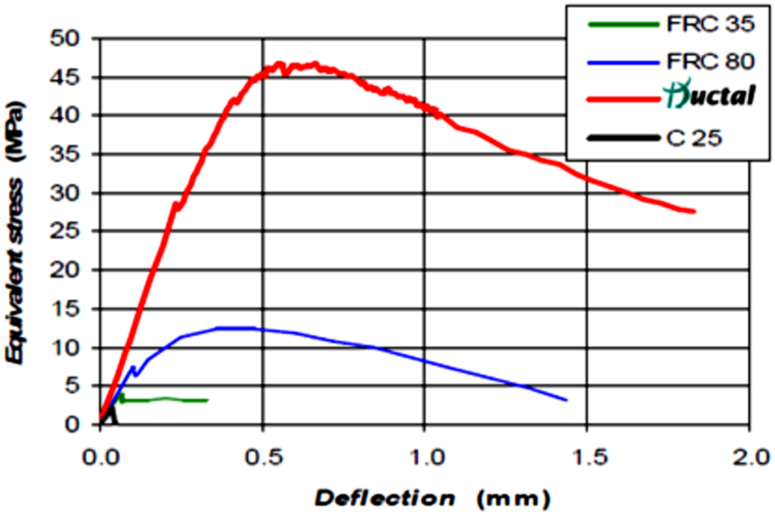

Figure 2.6 Equivalent stress–deflection curves for four types of concrete [39].

2.3.4 Modulus of elasticity and Poisson's ratio

The modulus of elasticity of UHPC generally lies in the range 45–55 GPa, depending on curing treatment. For example, Graybeal [20] reported average value of compressive modulus of elasticity of about 50 GPa for heat-treated cylinder UHPC specimens, and about 42.7 GPa for specimens cured under standard laboratory conditions at 28 days. In direct tension, he obtained the average values of about 51.9 GPa for steam-cured specimens and 47.6 GPa for the air-cured specimens [20]. Comparing these values with those obtained in compression, UHPC appears to be stiffer in tension than in compression.

The elastic Poisson‟s ratio was obtained in the range of 0.18 – 0.19 for fine-grained UHPC [41] and about 0.21 for coarse-grained (containing basalt chippings of 5–8mm max. aggregate size) UHPC [29]. These values show that the typically assumed value of elastic Poisson‟s ratio of 0.2 for normal-strength concrete will also be good for UHPC in the absence of reliable experimental data.

2.3.5 Fatigue behavior

Graybeal and Hartmann [42] reported the results of flexural fatigue tests conducted on prisms of 51 mm square cross-section [42]. A set of un-cracked beam specimens were loaded to various stress ranges. Most of these specimens failed after more than 6 million cycles of loading. A second set of pre-cracked specimens were also tested in fatigue loading cycles. Most of these set of specimens failed after 129,700 cycles. An important observation made in these tests was that the failure of the specimens was accompanied by fracturing of some of the steel fiber reinforcement, rather than pulling out of the UHPC matrix. Another set of flexural fatigue tests were conducted by Behloul et al. [43] on beams of 100 mm square cross-section. The specimens were first loaded to produce a crack width 0.3 mm, and then tested in 1 million fatigue loading cycles between 10 and 90 percent of the first cracking strength. After the fatigue cycling, the specimens were loaded monotonically to failure. It was observed that the fatigue loading appeared to have no significant effect on the overall mechanical behavior. In another report on flexural fatigue test, at a peak load of 75 percent of the static strength, it took between about 29,000 to 170,000 cycles to achieve fatigue fracture [44].

Schmidt et al. [45] investigated the fatigue behavior of UHPC cylinders in axial compression loaded to various stress levels. They reported that specimens loaded to a stress range of 45 percent of static compressive strength sustained 2 million loading cycles without failure, while suffering only a slight reduction in compressive strength when tested in monotonic compression after the fatigue load cycles. Under varying peak stress levels in Uniaxial compression tests, some other researchers have reported about 2.5 to 7.1 million cycles to achieve fatigue failure [46, 47].

2.3.6 Creep and Shrinkage

Fehling and coworkers [48] reported UHPC specific creep of between 47 and 22 millionths/MPa and creep coefficients between 2.27 and 1.08 for ages at the time of loading between 1 and 28 days. Francisco and coworkers [49, 50] reported the results of creep tests conducted on UHPC using 70 mm diameter cylinders, cured at 50 °C before loading at an age of 2 days. They reported creep strain of around 17 millionths/MPa after 30 days, while drying creep was found to be negligible. Similarly, Ichinomiya et al. [51] reported specific creep values ranging from 28 to 40 millionths/MPa after 150 days of loading for specimens loaded at 2 and 4 days. However, for specimens loaded at 28 days, the specific creep reduced drastically to about 11 millionths/MPa after about 120 days. Following the same trend, Graybeal [20] reported specific creep values after 1 year of loading, ranging from 21.2 to 5.7 millionths/MPa for 102 mm diameter cylinders loaded at ages of 4, 21, and 28 days, and cured under various conditions. These reports indicate severe effect of age at loading on creep response of UHPC. Further, these studies on creep of UHPC indicate that the creep of UHPC is significantly lower than that of the creep of conventional concrete that ranges from 36 to 145 millionths/MPa.

Graybeal [20] reported the shrinkage results of UHPC prisms (76 mm square cross-section), measured in accordance with the requirements of ASTM C157 [52]. He obtained a steady-state drying shrinkage ranging from 620 to 766 millionths for steam-cured specimens, and 555 millionths for untreated specimens. Autogenous shrinkage is not only present in UHPC but can also be very pronounced. A peak shrinkage of 64 millionths/hour was reported in the initial shrinkage rate of UHPC during the early hydration period, resulting in as much as 400 millionths of shrinkage in the first 24 hours for the specimens not treated by heat. After steam curing, further shrinkage was found to be insignificant [20, 48, 53]. The information available in the literature show that the autogenous shrinkage is the most significant source of the measured total shrinkage. This fact can be seen clearly in a report by Francisco et al. [49] in which an autogenous shrinkage of about 270 millionths was reported, while just a drying shrinkage of about 100 millionths was measured at 350 days on 70 mm diameter cylinders cured at 50 °C. Also, Burkhart and Müller [54] showed that the total shrinkage measured (about 300 millionths after 200 days of exposure) on sealed and unsealed cylinders specimens were nearly the same, showing that most of the measured shortening was caused by autogenous shrinkage, with very little contribution by drying shrinkage. In an extreme case, autogenous shrinkage values of 600 to 900 millionths were reported by Eppers and Müller [55] at 28 days of exposure.

In countering the very high autogenous shrinkage of UHPC, the incorporation of a basalt coarse aggregate (2 to 5 mm) [56], the replacement of silica fume by metakaolin [57, 58], and the use of an expansive or a shrinkage reducing admixture [59, 60] are proven solutions as shown by experimental results.

2.4 Flexural Design of UHPC Members

2.4.1 General

Traditionally, the flexural resistance of concrete components is generally calculated based on the conditions of equilibrium of forces and strain compatibility in the cross-section. The usable compressive strain in unconfined concrete is limited to a maximum value of 0.003 using the usually assumed simplified rectangular stress block for the compression zone, while the tensile strength of the concrete is neglected in the tensile zone. However, for the UHPC, the case may not be same due to the behavior of UHPC different from normal concrete, as discussed earlier. It should be noted that the design of UHPC members for flexure is usually governed by tension action in both UHPC and steel placed in the tensile zone of the member's cross-section. As such, full utilization of the potential mechanical benefits of UHPC is realized via prestressing, so that the activation of full tension action is delayed to ultimate state, rather than near service loading conditions. This in turn raises the load carrying capacity of the member that enables to use a much lighter section. This is why most of the marketing and promotion activities for UHPC, since its recent emergence, have centered mostly around application in bridge girders, where such very high capacity-to-weight ratios and the inherent outstanding durability of UHPC are most rewarding. Uses in buildings are more of architectural than structural, due to economic reasons – where the owner of the building is forced to pay a very high cost for a very high load carrying capacity that is far beyond the building's structural needs.

However, in some cases – such as large span beams – steel beams are usually employed, even in buildings and factories. If the environmental condition around the building is aggressive, then such steel beams are bound to be unsafe after a short period of service. In such a case, a material such as UHPC is the best choice. An example of this scenario is a case that happened to be one of the earliest applications of UHPC in which steel beams had to be replaced by UHPC beams in the cooling towers of a power station at Cattenom in France. The steel beams were rapidly corroding in the extremely harsh environment inside the cooling towers [8]. In this case, the controlling factor for the decision was the durability of the UHPC, which made it a better fit for the anticipated very long service life without maintenance or repairs, rather than the very high load bearing capacity of the UHPC beams. Another point that is worthy of consideration is the sustainability aspect of civil infrastructures, including buildings. Sustainability and long service-life of structures is not required only for bridges, but also buildings. Therefore, due attention is needed for the development and optimization of the UHPC technology for structural use in buildings as well. This fact was only recently considered in reports, such as those by Stürwald and Fehling [61] who tested passively reinforced (rather than prestressed) beams in flexure.

Subsequently they developed a simplified approach for the flexural design of reinforced UHPC beams based on their experimental results. However, Stürwald and Fehling [61] did not publish the full details of their research outcome.

2.4.2 Structural Testing and Design Principles

Graybeal [62] reported a four-point flexure testing of a prestressed concrete AASHTO Type II girder made of UHPC with a depth of 910 mm and a test span of 23.9 m. The girder failed by a combination of tensile fracture of the prestressing strands and pullout of the fibers, accompanied by a deflection of about 480 mm prior to the peak load. A flexural analysis in line with the traditional approach for normal strength concrete, assuming a rectangular stress block and neglecting the post-cracking tensile forces in UHPC yielded an estimated moment capacity of 3150 kN.m, far less than the experimentally measured strength of 4370 kN.m. Consequently, based on the analysis of the measured data, Graybeal proposed that the flexural capacity could be more accurately calculated by making the following amendments to the traditional concrete analysis.

1. In compression, a linear stress-strain relationship up to a stress of 0.85 times the compressive strength. With this, he recommended a triangular compression stress block, instead of the rectangular stress block employed to approximate the parabolic stress-strain curve of normal strength concrete [63]. This is illustrated in Figure 2.7.

2. In tension, a linear elastic-perfectly-plastic stress-strain relationship was recommended with a conservative value of post-cracking tensile strength and a limiting tensile strain (0.006 – 0.007). This would mean, there is the need for a rectangular tensile stress block. This is illustrated in Figure 2.8.

These ideas can be combined to arrive at a simplified UHPC stress-strain response, as shown in Figure 2.9.

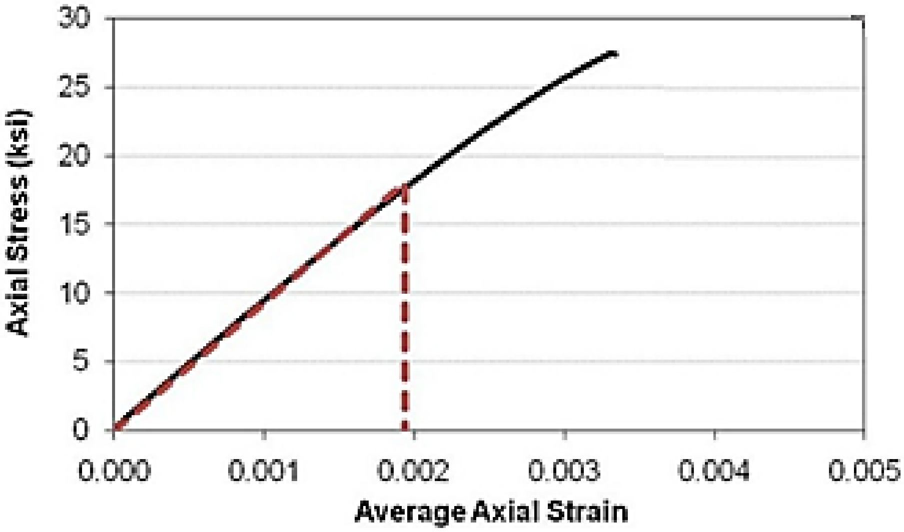

Figure 2.7 Assumed compression behavior for design [63].

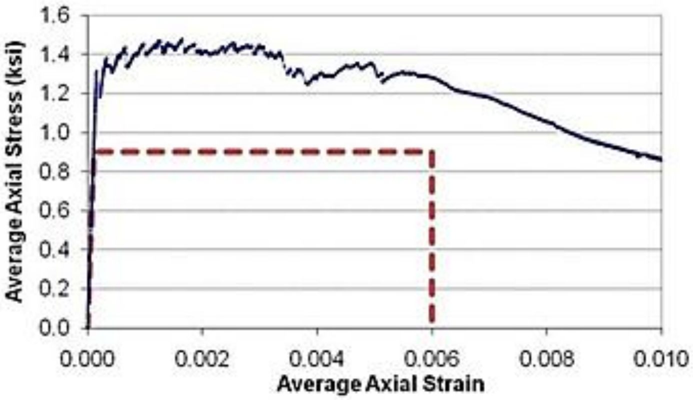

Figure 2.8 Assumed tensile behavior for design [63]

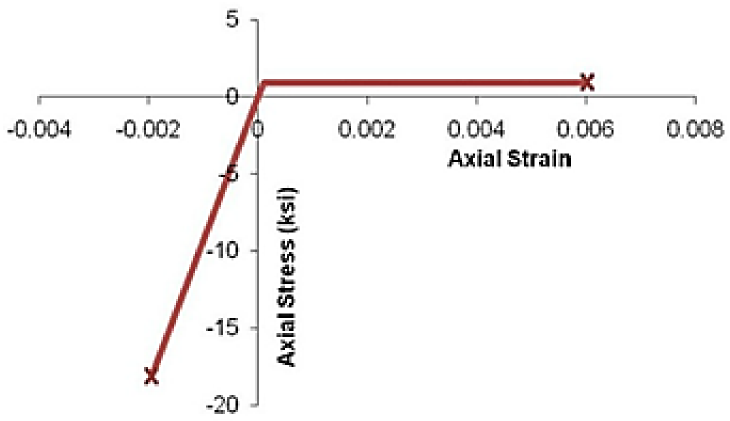

Figure 2.9 **Simplified UHPC stress-strain response [63].**

Meade and Graybeal [64] reported the results of four-point bending tests on sixteen 152 mm by 381 mm rectangular UHPC beams containing passive reinforcement (0 to 1.0 percent by area) on a test span of 4.88 m. The beams were made with UHPC containing varying fiber contents (0, 1, and 2 percent by volume) and having varying compressive strengths (170 to 203 MPa). They observed that the beams containing fiber reinforcement generally had higher first cracking strengths, better post-cracking flexural response, and higher peak loads compared to those without fibers. Failure of the plain UHPC beams (without fibers) occurred when flexure-shear cracks extended into the compression region under the load points, resulting into a shear failure of the flexural compression block within the shear-span. The beams with 2 percent fiber content had stiffer post-cracking response and higher peak loads than those with 1 percent fiber content. The failures of the fiber-reinforced UHPC beams were accompanied with fibers pullout across a critical crack, leading to rupturing of the passive reinforcing bars without crushing of the flexural compressive concrete block. This is expected for beams with such a low reinforcement ratios (to be shown later in this study).

Stürwald and Fehling [61] reported the results of 10 rectangular passively reinforced UHPC beams tested in four-point bending over a test span of 1.70 m. The beams had cross-sectional areas of either 150 mm by 350 mm or 150 mm by 150 mm, and were made with UHPC containing varying fiber contents (0, 0.5, and 1.5 % by volume) corresponding to compressive strengths in the range of 180 to 200 MPa. The reported failure behavior and flexural response of the plain and fiber-reinforced UHPC beams (passively reinforced) were in close agreement with those reported by Meade and Graybeal [64]. On the basis of their experimental results, Stürwald and Fehling [61] developed a simplified approach for design of UHPC beams in flexure. This involves the use of a triangular compressive stress block and a rectangular tensile stress block. This approach enabled to calculate flexural strength within 5 percent of the measured values for three of the tested beams. This approach is very similar to the methodology of strength design proposed by Graybeal [62], as discussed earlier.

It should be noted and emphasized that nearly all reported studies on the structural behavior of UHPC beams considered prestressed concrete beams. The research work reported by Meade and Graybeal [64] and Stürwald and Fehling [61] are the only two studies known to the proponent of the current study, which considered the use of passive reinforcements in UHPC beams, rather than prestressing. Incidentally, both of these studies limited their coverage to low reinforcement ratios, thus limiting the full understanding of the structural response of such types of structural members from the outcomes of those works. Therefore, the use of low to high passive reinforcement ratios in non-prestressed UHPC beams was made a core aspect of the current study.

The last nearly two decades of emergence and development of UHPC have witnessed major emphasis on the material development and determination of relevant properties and structural behavior of prototype and full-scale UHPC elements, including optimization at both material and structural levels. While these research works are still going on, the available "preliminary" information on UHPC needs to be put together to create systematic guidelines for structural design of UHPC members. Of course, all the several dozens of UHPC infrastructures built to date were designed in one way or the other. There is the need for the establishment of systematic and comprehensive design guidelines. In 2002, the Association Française de Génie Civil (AFGC) published the first an "interim" design guidelines for UHPC in France [9]. This pre-standard for design of prestressed UHPC beams has been used since then, within and outside France. The French code was built mainly on empirical information obtained from several experimental tests. The first Japanese design guideline also appeared in 2004. Building on the French interim code and a UHPC mechanical model developed by Chuang [65], MIT has published a model-based design guidelines [11] (a little different from the empirical-based French interim guidelines [9]), which was later refined further [10]. An effort to compile an international standard for the structural design of UHPC is underway by the fib Task Group TG 8.6 [66].

In the foregoing discussion, examples of some attempts to establish some guidelines for structural design of UHPC, among many others available in the literature, have been explored. At this stage of the literature review, it is pertinent to highlight the theme of this dissertation. Since UHPC as a sustainable and reliable material is still relatively „new,‟ no design code can emerge now from anywhere that will cater for all types and grades of

UHPC once-and-for-all. Perfection of a standard of practice relies on continuous review as new and more comprehensive material behavior data are generated. An example to illustrate this fact is the case of the 2002 French interim design code [9] in which many papers presented at UHPFRC 2009 conference called for review of the code, based on the new ideas that emerged after the release of the interim code. Consequently, an updated version of the code was released in 2013 [67]. Therefore, all efforts towards generating more understanding of material behavior at all levels – with a view to expanding the knowledge base for structural design of safe, economical, and sustainable UHPC structures – constitute important contributions to beneficial engineering knowledge.

The current research work was intended to address the following aspects:

- to initiate the effort of developing specific guidelines for UHPC grades of concrete developed with local materials for local service conditions in the Arabian Gulf environments
- to consider passively reinforced UHPC beams consisting of reinforcement area ratio in a wider range

CHAPTER 3

EXPERIMENTAL PROGRAM

The experimental work involved the tasks of characterization and testing of UHPC specimens with a view to extracting information relevant to design within the framework of the research objectives. The experimental work had three major tasks. The first task was the characterization of the constituent materials utilized to prepare the UHPC mixtures. These materials included fine sand (dune sand) and powders–cement, microsilica, limestone powder, and natural zeolite. The second task was the preparation, curing and comprehensive mechanical characterization of specimens made of the UHPC mixtures. Apart from the UHPC specimens, the ultra-high strength steel rebar utilized to reinforce the UHPC beams was also characterized mechanically. The last task was the preparation, curing and mechanical testing of reinforced UHPC beam specimens in four-point flexure.

3.1 Materials Utilized for the Fabrication of UHPC Specimens

UHPC is a composite system of matrix and fibers. The matrix is the main material, responsible for UHPC's high strength and microstructural density. However, since high strength materials are usually brittle (which leads to the sudden failure), high strength fibers are incorporated to the UHPC mixture as micro-reinforcements to produce a ductile composite. The incorporation of these fibers does not significantly enhance pre-cracking compressive strength and elastic modulus of UHPC composite. However, they do produce significant enhancements of the post cracking behavior and failure mechanism, both in tension and compression [26, 27]. A number of high-strength fiber materials have been reportedly used for producing UHPC. These include, but not limited to, steel fibers (straight, bent, plain and deformed), glass fibers, carbon fibers and aramid fibers. A typical fine-grained UHPC matrix is a blend of fine aggregate, cement, micro-fillers (commonly microsilica and/or others), and water. As a result of the characteristic ultra-low water content in UHPC matrix, use of high dosages of hyperplasticizer is inevitable. The following subsections enumerate the materials utilized in this study.

3.1.1 Materials utilized in the preparation of UHPC mixtures

A total three different matrix compositions were utilized in this study. They were selected from previous and ongoing studies pertaining to the development of alternative UHPC mixtures. The component materials used for these UHPC matrices are as follows.

(i) Cement

Ordinary Portland cement (Type I, ASTM C 150) with a specific gravity of 3.15 was used for all three UHPC mixtures. The cement was sourced from a local supplier in Saudi Arabia.

(ii) Microsilica

Microsilica (MS) is a highly siliceous material (85–95% SiO_2) generated as a byproduct of the carbothermic reduction of quartz and quartzite in electric arc furnaces during the production of silicon and ferrosilicon alloys. Microsilica is a popular choice of micro-filler in many UHPC formulations, commercial and proprietary, due to its extremely fine nature. However, it is generally known to cause reduction in workability of concrete [68, 69]. Interestingly, the extent to which MS affects workability of concrete depends on the type of MS used. Based on the previous studies, a single brand of MS, among dozens of MS brands available in KSA, had been identified to cause the least reduction in the workability of UHPC mixture. That brand is Elkem Microsilica, which was obtained from a local supplier in Saudi Arabia. This excellent material was imported to Saudi Arabia, by the local supplier, from the Norwegian manufacturing company, Elkem.

(iii) Limestone Powder

Limestone powder (LSP) is a non-pozzolanic by-product of the quarrying process of carbonate rocks, composing mainly of calcium carbonate, $CaCO_3$. The LSP used in the present research was sourced from an asphalt company in the Eastern Province of Saudi Arabia. Limestone is the major rock type used for concrete aggregate in the whole of the Eastern Province of Saudi Arabia. Hence, it is a highly abundant industrial waste.

(iv) Natural Zeolite (NZ)

Volcanic natural zeolite is an aluminosilicate, usually composed mainly of silica and alumina with low contents of calcium and iron oxides. It generally possesses a low pozzolanic activity, but was found in an ongoing study to perform well in UHPC. The volcanic sites of the Western Province of Saudi Arabia host several millions of tons of NZ [70, 71], just like several regions of the world where volcanic activities have taken place.

The chemical compositions of these four powder materials are shown in Table 3.1. These properties have been previously obtained at the material characterization laboratory (MCL) of the Center for Engineering research (CER) in the Research Institute at KFUPM.

Table 3.1 Chemical Composition (m/m %) of the powder materials

Component	Cement	MS	LSP	NZ
CaO	64.35	0.48	45.7	8.06
SiO_2	22.00	92.5	11.79	42.13
Al_2O_3	5.64	0.72	2.17	15.33
Fe_2O_3	3.80	0.96	0.68	12.21
K_2O	0.36	0.84	0.84	0.84
MgO	2.11	1.78	1.80	8.50
Na_2O	0.19	0.5	1.72	2.99
Equivalent alkalis ($Na_2O + 0.658K_2O$)	0.33	-	2.27	3.54
SO_3	2.10	-	-	-
Loss on ignition	0.70	1.55	-	-
C_3S	55.00	-	-	-
C_2S	19.00	-	-	-
C_3A	10.00	-	-	-
C_4AF	7.00	-	-	-

(v) Fine Sand

Dune sand, the most abundant single material in Saudi Arabia – covering the extensive Arabian deserts, was used as the aggregate phase for the UHPC mixtures considered in this study.

Figure 3.1 shows the particle size distributions for all the four granular components used in the UHPC mixtures.

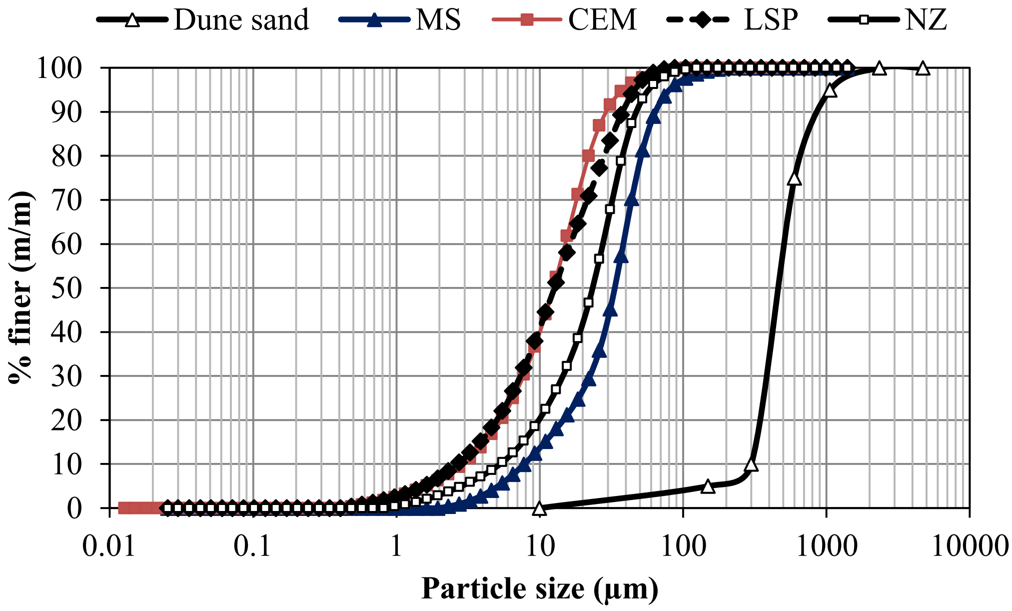

Figure 3.1 **Grading curves for all the four solid components used in the UHPC mixtures.**

(v) Superplasticizer

Glenium 51® produced by BASF was used as superplasticizer was used in all the mixtures of UHPC. It is a new generation polycarboxylic-based ether hyperplasticiser. The technical data of Glenium 51® is shown in Table 3.2, as per the product data sheet.

Table 3.2 Technical data of Glenium 51®

Appearance	Brown liquid
Specific gravity @ 20°C	1.08±0.02 g/cm^3
pH-value @ 20°C	7.0±1.0
Alkali content	≤5.0
Chloride content	≤0.1%

(v) Steel Fibers

High strength steel fibers were incorporated to the UHPC mixtures as micro-reinforcements for the required ductility of the UHPC composite. The steel fiber dosage was 2 % by volume of concrete. The fibers were plain smooth copper coated micro-steel fibers, having a nominal diameter of 0.22 mm and length of 13 mm, resulting to an aspect ratio of 59. As per the manufacturer‟s data, the minimum tensile strength of the micro-steel fibers was 2500 MPa.

3.1.2 Reinforcement bars

Although the UHPC mixtures contain micro-steel fibers, a beam made with these mixtures will definitely require longitudinal reinforcement bars to take care of high-intensity normal stresses when the beam is heavily loaded as a structural member. The original idea of Compact Reinforced Concrete (CRC) of Hans Hendrik Bache [14], which metamorphosed into the modern day UHPC, did not require reinforcement bars to make a structurally functional beam. The basic reason is that the CRC had continuous steel wires as reinforcement, thus ensuring full efficiency of micro-steel reinforcements. However, the current form of UHPC makes use of chopped discontinuous fibers, which are expected to be dispersed and oriented randomly in the matrix, thus helping to ensure multidirectional ductility. Consequently, the reinforcing efficiency in a chosen direction, e.g., parallel to the beam axis, will definitely be very low.

Therefore, the actions of the discontinuous randomly oriented fibers will only be useful for localized crack bridging anywhere within the stressed region of structural members, but inefficient in the global direction parallel to the beam axis. Based on these ideas, a structurally functional UHPC beam requires continuous reinforcement bars on the tensile side of the beam‟s cross-section aligned in the direction parallel to the beam axis, in order to ensure a „pick-up‟ of the tension forces as soon as the fiber bridging action gets exhausted.

In this study, all beam specimens were passively reinforced with 15 mm diameter high strength steel bars (PSB 1080), conforming to ASTM A722/A722M specifications, which were utilized as main reinforcement bars, while stirrups were made from the conventional grade 60 (high yield) steel bars of 10 mm diameter, conforming to ASTM A615 specifications. Figure 3.2 shows the uniaxial tensile response of the steel bars used in this study.

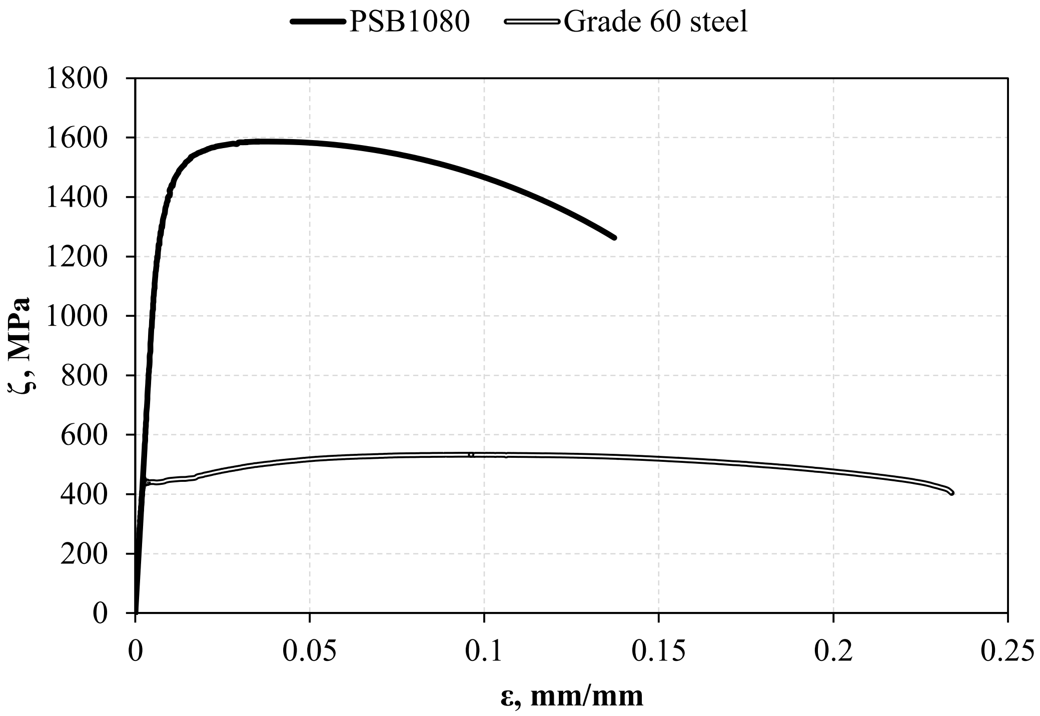

Figure 3.2 **Uniaxial tensile response of the steel bars used in UHPC beams.**

3.2 Composition of UHPC Mixtures

In this study, a total of four UHPC mixtures were considered. Table 3.3 shows the proportions of the mixture constituents for 1 m^3 of UHPC. These mixtures are essentially different from one another only by the respective compositions of their component granular materials – sand and powders. Apart from the granular constituents the other mixture parameters were constant for the four UHPC mixtures considered in this study. The water/powder and superpasticizer/powder mass ratios were 14.5 % and 3.6 %, respectively, while the fiber volume fraction was 2 % by volume of each UHPC mixture, resulting in 157 kg of fibers per cubic meter of the concrete – considering the specific gravity of the steel fibers as 7.85.

Table 3.3 Mixture constituents (kg) of 1 m^3 of UHPCs utilized in the study

Constituent (kg)	UMS	UMN	UML	UMSN
Cement	900.0	900.0	900.0	630.0
MS	220.0	132.0	176.0	220.0
NZ	0.0	88.0	0.0	270.0
LSP	0.0	0.0	44.0	0.0
TMA	220.0	220.0	220.0	490.0
Powders	1120	1120	1120	1120
Water	162.4	162.4	162.4	162.4
SP	40.3	40.3	40.3	40.3
Steel fibers	157.0	157.0	157.0	157.0
Sand	1005.1	1029.9	985.0	994.3

MS = Microsilica; NZ= natural zeolite; LSP = limestone powder; SP = superplasticizer; TMA = total mineral admixture

The first mixture (UMS) is a reference mixture containing 900 kg/m^3 of cement and 220 kg/m^3 of MS. In the second and third mixtures, UMN and UML, the MS in the reference mixture was partially replaced in mass by 40 % NZ and 20 % LSP, respectively. These mixtures were studied in a previous funded research at KFUPM, and some properties of the three mixtures have been reported elsewhere [72]. These three mixtures were utilized for the material mechanical characterization study conducted in this research.

The fourth mixture shown in Table 3.3, UMSN, has the cement in the reference mixture partially replaced by 30 % NZ, resulting in a cement content of only 630 kg/m^3, as compared to the cement content of 900 kg/m^3 in the reference. This UHPC mixture was selected from an ongoing UHPC material development study, involving high volume replacement of cement by NZ. The chosen mixture has similar mechanical properties with the reference mixture, based on the findings of that study. Therefore, a set of beams made with the fourth mixture can serve as replicate for those made with the control mixture on structural ground, even though the material composition of the two mixtures are remarkably different.

The reason for this choice of the fourth UHPC mixture (UMSN) was to seek possible answers to the question of whether the expected high heat generation of a high cement content (900 kg/m^3) material, like the reference mixture, can be lowered by taking out some cement without compromising the resultant mechanical properties in reference to the control material. This mixture (with 30% cement replacement) was expected to show a lower heat generation in the course of hydration. The heat evolution study, conducted on 300 mm deep beams, will be presented later in this dissertation for both the reference mixture (UMS) and this „low‟ cement‟ mixture (UMSN). As will be seen later in this dissertation, only UMS and UMSN were utilized for the casting of the reinforced beam specimens.

3.3 Mechanical Characterization of UHPC mixtures

As stated earlier, the mechanical characterization of the UHPC mixtures was the second major task in this experimental program. The UHPC mixtures were prepared in the laboratory. The preparation procedures are described in the following paragraphs.

3.3.1 Mixing and casting procedures of UHPC mixtures

As a result of the characteristic ultra-low water content used in UHPC matrix, high dosages of hyperplasticizers are necessary. This implies that the evolution of the required self-consolidating consistency of a fresh UHPC mixture is highly dependent on the complete plasticization reaction between superplasticizer molecules and powder particles. Obviously, the efficiency of this reaction depends, in turn, on the effectiveness of mixing energy dissipation to the plasticizing mixture, which can only be guaranteed by high shear rate. Therefore, unlike the traditional normal strength concrete mixtures, mixing of UHPCs requires high shear capacity mixer.

Graybel [73] opined that most conventional concrete mixers, including ready-mix trucks, can handle the mixing of UHPC, though the resulting increased mixing time might cause overheating. Therefore, to solve the overheating problems a modification of the batching procedure would be required, such as pre-cooling the constituents. Mazanec *et al.* [74] have reported that the typical mixing times for UHPC range from 7 to 18 minutes, but the mixing time can be reduced to as low as two minutes, just like the traditional normal strength concrete mixtures, by manipulating the mixture composition and/or particle size distribution of the constituents.

The mixing of UHPC mixtures was done using a horizontal planetary mixer in the concrete laboratory at the Civil and Environmental Engineering Department at KFUPM, shown in Figure 3.3. The mixing water and superplasticizer were thoroughly pre-mixed, producing a slightly viscous liquid mixture, and allowed to rest for about one hour before use. For each UHPC mixture, the measured quantities of dune sand and powders – cement, microsilica and either of limestone powder or natural zeolite – are mixed for about three minutes in the planetary mixer. Then, about 80 to 85 % of the liquid mixture was slowly added to the dry mix in a course of 6 to 8 minutes, while the blending action was still in progress. The slow addition of the liquid mixture is necessary to avoid splashing off and subsequent loss of the mixing liquid to the wall and roof of the mixing chamber, and sometimes outside of the mixing pan via the open spaces on the roof of the chamber.

Figure 3.3 Planetary mixer used for mixing of UHPC mixtures.

A critical behavior change point in the mixture can be observed around 10 minutes of mixing, when the mixture would have turned from moist granular mixture into a thick deformable plastic mass in the pan of the mixer. The addition of the remaining liquid mixture, in a gradual fashion, to the plastic mass would cause it to break rapidly into highly flowable slurry. At this stage, the slurry is ready to receive a gradual addition of the micro-steel fibers, over a period of about three minutes, while the mixing process can be allowed to continue for about two more minutes afterwards. The slow addition of the micro-steel fibers is necessary to ensure uniform dispersion of the steel fibers and to prevent clumping of the fibers, a phenomenon that will culminate in defective regions in the hardened concrete. Altogether, the total mixing time of UHPC mixtures varied from about 18-25 minutes, depending on the mixture and batch size.

A batch volume of 30 liters was used for the preparation of mechanical characterization specimens. The planetary mixer used could comfortably accommodate up to a batch volume of 35 liters using the mixing procedure highlighted. However, for larger batch sizes used for casting of the passively reinforced beam specimens, the previously detailed mixing procedure was slightly modified. The modification involves excluding all, or a part of, the fine sand from the initial dry mixture. Once the plastic stage is attained by the powder mixture, the remaining dry sand can be gradually added to the nearly flowing mixture, adding some liquid mixture at intervals as deemed necessary. This modification was meant to prevent the mixer from being stuck in a stiff plastic mass in the mixing pan. Once all the remaining liquid mixture had been added, the mixture would have become the usual flowing slurry, and the addition of fibers can then follow. In spite of this slight modification of the mixing procedure for larger batch sizes, it was confirmed through a side study that both the fresh and hardened properties remained unaffected.

As soon as mixing was completed, a scoop of the fresh UHPC mixture was taken from the mixing pan for the measurement of the UHPC flow via a flow table test. In this test, the mini slump cone was filled and leveled, and then removed to allow the UHPC mixture to flow outward. The flowing concrete was allowed to reach a steady state, and then the average diameter across two orthogonal diametric lines was obtained. Subsequently, the flow table was dropped 20 times in about 20 seconds, and the concrete was again allowed to settle, and then its average diameter is taken.

The casting of the specimens commenced immediately after the completion of the mixing in parallel with the flow measurement. From the wheeled mixing pan, the fresh concrete was scooped into the molds, which were arranged on the vibrating table. Once filled, the molds were given a few seconds of vibration and then had extra concrete removed by screeding their top surfaces. Three important precautions should be noted, as learned in the course of previous and the current research work. Firstly, it is not allowed to compact plastic UHPC in molds by poker compactor or rodding, as this will destroy the uniformly random arrangement of the fibers, and thus create regions of weakness in the hardened specimen. Secondly, filling of concrete in molds must be done in one single lift before vibration, as a subsequent fill after a previous vibrated fill will form a poorly bonded layer with respect to fiber distribution. Thirdly, prism specimens should be cast by filling concrete from one end of the mold, and allowing the concrete to fill the rest of the mold by flowing under its self-weight, in order to ensure proper fiber distribution in prisms.

After casting, the surfaces of the specimens were covered with plastic sheets to avoid drying out of the surface, a phenomenon that could result in evolution of shrinkage cracks, and subsequently render the specimens useless. After about 24 hours following the casting, the specimens were demolded and moist-cured for 28 days by immersion in water tanks. After curing, the specimens were moved to the structural mechanics laboratory for mechanical testing.

3.3.2 Mechanical Characterization Test Program

As stated earlier, the first three UHPC mixtures shown in Table β3.3 were utilized for the mechanical characterization study conducted in this study. Table β3.4 shows the details of UHPC specimens utilized for the material mechanical characterization study.

Table 3.4 Test matrix for material characterization per UHPC mixture.

Test	Specimen size and shape	Number of specimens
Cube compressive strength	50 mm cubes	4×4 = 16
Characteristic stress-strain behavior in compression	75 × 150 mm cylinder with ground ends	4×4 = 16
Flexural tensile behavior (third-point loading)	70 × 70 × 280 mm, un-notched prism	3×4 = 12
Post-cracking constitutive (stress-crack width) law (mid-point loading)	70 × 70 × 280 mm, notched prism	3×4 = 12
Characteristic stress-strain behavior in direct tension	40 × 40 × 490 mm, un-notched dogbone	3×2 = 6
Stress-crack width behavior in direct tension	40 × 40 × 490 mm, notched dogbone	3×2 = 6

There were two main purposes for this phase of the research. The first purpose was to determine reliable characteristic values of the mechanical properties of locally developed UHPC mixtures relevant to structural design. Various properties of the UHPC mixtures have been obtained and reported in past studies under which these materials were developed. However, the mechanical properties among those reported ones may not be correctly taken for design purposes. The values of the mechanical properties relevant to the structural design are better obtained from a large number of specimens with statistical significance and from comprehensive stress-strain behaviors. Hence, sixteen specimens were utilized for each mechanical test in this study, apart from the direct tension tests, which were done with twelve specimens due to constraints in the number of available molds. In addition, stress-crack width relationship is a central property for any UHPC material, which has not been obtained previously for the UHPC mixtures selected for this study.

The second purpose of this phase of the research was to determine the level of reliability of the characteristic design-relevant mechanical properties of these locally developed UHPC mixtures. UHPC is a highly heterogeneous composite material which has been reported as highly sensitive to changes in compositional and operational parameters. There is hardly any guarantee that the compositional and operational parameters in batching and placing will remain perfectly constant from time to time. Hence, it was decided to divide the total number of specimens into four, so that the mixing and casting operation would be repeated at four different times. Hence, the results of these tests was planned to be statistically analyzed for variations across different times of casting. The next paragraphs cover the details of these mechanical characterization tests.

Cube compressive strength test

The compression tests of the UHPC mixtures were conducted using 50 mm cube specimens, using a 3000 kN capacity hydraulic type compression machine. The testing machine, shown in Figure 3.4, had a top platen supported on a spherical steel bearing. Compressive loading was applied to the cube specimen at a constant stress rate of 0.4 MPa/s, until the specimen failed by softening, and the maximum load recorded. As shown in Table 3.4, four cube specimens were tested for each of the three UHPC mixtures in each of the four casting repetitions. This made a total of sixteen specimens for each UHPC. It is widely known that cubes generally‟ overestimate‟ concrete‟‟s‟ compressive strengths, considering cylinder strengths as reference. However, a cube concrete specimen is much easier to test, as it hardly requires any surface preparation, such as sulfur capping or grinding, as compared to a cylindrical specimen.

Figure 3.4 Hydraulic type compressive strength testing machine.

Although there is no universally correct factor for every type of concrete for converting a cubical strength into a corresponding cylindrical strength, the report by Graybeal [75] gives a good idea of equivalent cylinder strength of UHPC cube strength. For UHPC with varying cylindrical compressive strengths in the range of 150 – 210 MPa, Graybeal obtained compressive strengths of 51 mm cube specimens as 5 – 6 % greater than that of 76 mm diameter cylinder specimens. Hence the cube strength results can be used for obtaining design strengths.

Test for characteristic stress-strain behavior in compression

Compression test on UHPC was conducted according to ASTM C39 using 76 mm diameter cylinder specimens. Normal strength concrete is usually sulfur-capped before testing. However, due to the low strength of hardened sulfur as compared to UHPC matrix, ends of test cylinder specimens are smoothened using grinding to achieve parallel plane contact surfaces with the compression machine platens, which should also be perpendicular to the cylinder axis. The cylinder specimens were cast in plastic molds of 152 mm height, but a thin layer of the top surface was carefully cut off from each specimen instead of using a grinder, using concrete cutting machine, in order to make their top surfaces plane for testing. This resulted into final cylinder heights of 145 mm. Figure 3.5 shows the UHPC cylinder specimens with prepared top surfaces before testing in uniaxial compression.

Figure 3.5 UHPC cylinder specimens before testing in uniaxial compression.

It is nearly impossible to make all the specimens have smooth and plane surfaces by end cutting, with the type of cutting tool used, as mentioned above. The proper way is to grind the ends by concrete grinder, which was not available in the concrete laboratory at the time this study was conducted. However, the planeness of the cut surfaces were tested, and it was observed that well above 50 % of the specimens could be used for testing. The real problem with specimens having imperfect ends is in the late pre-peak and post-peak behavior. Hence only those specimens with proper ends can be used to evaluate the stress-strain constitutive behavior correctly. However, the other „imperfect‟ specimens are still useful for the evaluation of tangent modulus of elasticity, since this is obtained from the linear pre-peak regime of the compressive behavior.

As shown in Table 3.4, 75 mm × 145 mm concrete cylinder specimens were used for the determination of the stress-strain response of the UHPC mixtures in compression. Three parameters can be extracted from this test: the moduli of elasticity (tangent and secant), the compressive strength, and the overall constitutive behavior in compression. The concrete cylinder specimens were tested using the same automatic hydraulic compression machine used in cube compressive strength tests. Figure 3.6 shows the test arrangement for the determination of the compression stress-strain response of the UHPC mixtures.

Figure 3.6 **Test arrangement for the stress-strain behavior in compression.**

The test setup included a compressometer designed for measuring the axial deformation of a 76 mm concrete cylinder. The two parallel rings of the compressometer were securely attached to the concrete cylinder specimen with an 87 mm gage length between the two rows of pin points. The lower ring holds two diametrically opposite linear variable displacement transducers (LVDTs) with the plunger of each LVDT bearing on the corresponding receiver plates attached to the upper ring of the compressometer. Compression load was applied to the UHPC cylinder specimen, held in the compressometer, via a 1000 kN capacity load cell, until it failed. The test was controlled by an average platen-to-platen displacement rate of 0.2 mm/min, corresponding to initial elastic compressive loading rate of 0.5 MPa/s. The applied load (in kN) from the load cell and the corresponding axial deformation (in mm) from the LVDTs were digitally recorded through a portable data logger for each 0.04 mm platen-to-platen displacement, resulting into 5 data points per minute.

Flexural tensile test

Traditionally, in concrete technology, the smallest dimension of a test specimen is dictated by the size of largest component of the composite mixture, for example maximum size of aggregate. Conventionally, three times the size of the largest ingredient of composite mixtures is considered the least dimension of a test specimen acceptable. However, a minimum dimension of a test specimen equal to five times the size of the largest particle in the concrete mixture is recommended for low spread of test results. In case of UHPC, five times the fiber length is therefore recommended as the least dimension of the specimen's cross-section. Thus for the fiber length of 13 mm, considered in this study, the recommended minimum cross-section dimension is 65 mm. Additionally, in line with this general idea, the French interim UHPC guideline annex [76] has specified 70 mm for the cross-section size of flexural prism specimens made from fibers with a length up to 15 mm. Therefore, in the present study, the flexural tensile test was conducted on UHPC specimens using un-notched 70 × 70 × 280 mm prism specimens. The casting procedure for prismatic specimens was similar to other types, except for the important precaution of casting from one side of the mold and allowing the entire mold filled by flowing action of the fresh concrete.

Figure 3.7 Test arrangement for the un-notched flexural tensile (4-point) behavior.

The UHPC prisms were loaded in a 4-point loading configuration, as shown in Figure 3.7, on a flexure span of 210 mm (three times the depth). The flexural tensile test was conducted on an INSTRON 200 kN-capacity twin-screw universal testing machine (UTM), as shown in Figure 3.7. The A crosshead displacement-controlled loading was applied at a constant rate of 0.25 mm/min throughout each test session. The resultant load (in kN) from the load cell and the corresponding center point deflection (in mm) of the UHPC prism from the LVDT were digitally recorded on a portable data logger for each 0.05 mm deflection interval, resulting into 50 data points per minute.

Flexural post-cracking constitutive (stress-crack width) test

The UHPC prisms utilized for the post-cracking stress-crack width test had same dimensions as those for flexural tensile (un-notched) test. However, 7 mm deep (10 % of depth, based on RILEM recommendation [77]) central notch was cut into the underside each prism. Furthermore, all testing conditions (displacement-controlled load rate, data capture rate, and test span) for the un-notched test were maintained for the notched test, except that the notched test was carried out using a center-point loading configuration, as shown in Figure 3.8. More importantly, the growth of crack width was tracked by a pi-type crack mouth opening displacement (CMOD) transducer/extensometer having a gauge length of 50 mm, which was installed across the notch, as shown in Figure 3.9

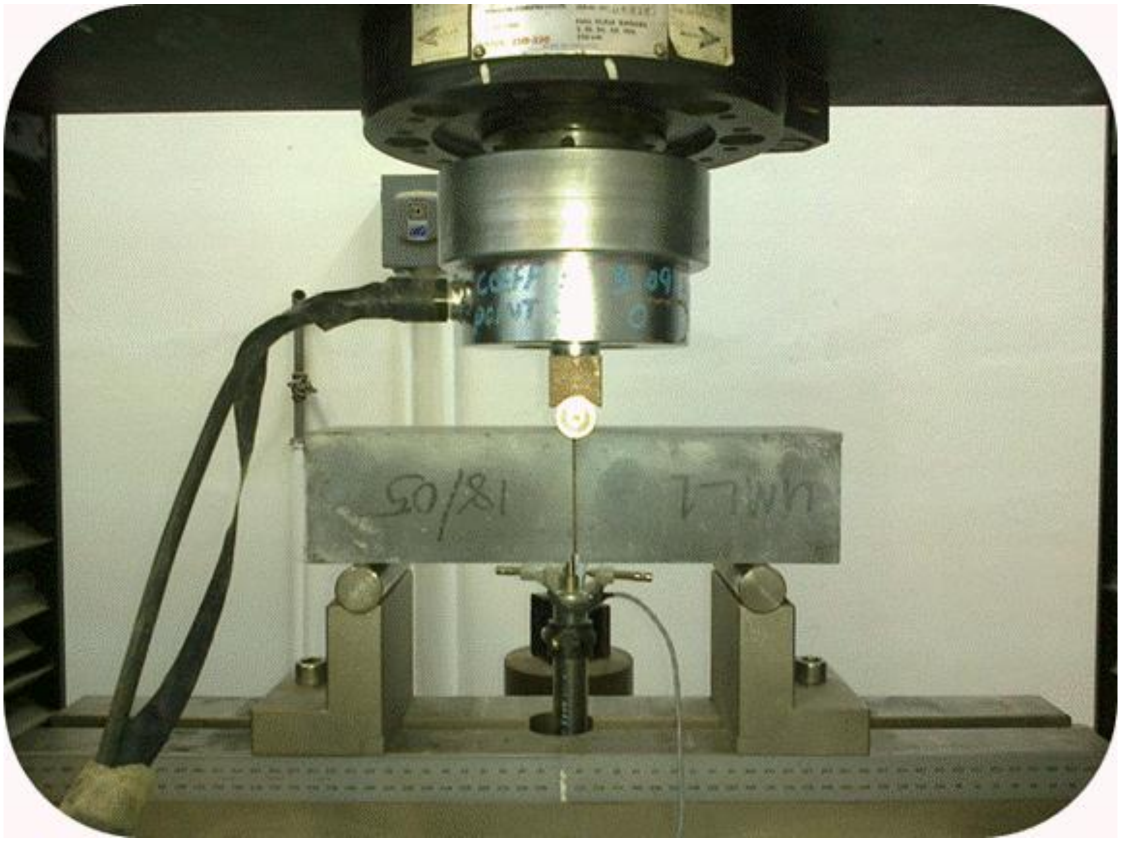

Figure 3.8 Test arrangement for the notched flexural tensile (3-point) behavior.

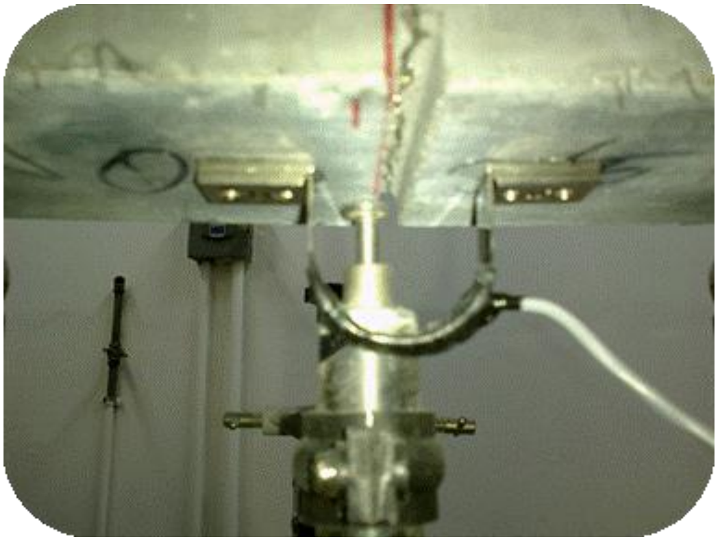

Figure 3.9 A closed up view of the CMOD installation across a notch on UHPC prism.

Test for characteristic stress-strain behavior in direct tension

The characteristic stress-strain behavior in direct tension was assessed for the UHPC mixtures using un-notched dogbone specimens with a length of 490 mm and cross-section dimensions of 40 × 40 mm. The small cross-section size was considered as a result of constraints in the available mold size. Since the length of chopped steel fiber utilized to prepare the UHPC mixtures was 13 mm, the cross-section size still satisfies the conventional acceptable least test specimen dimension of three times the size of the largest particle of composite mixtures.

Figure 3.10 Test arrangement for the stress-strain behavior in direct tension

The test setup for direct tension tests is shown in Figure 3.10. The test was conducted on an INSTRON 500 kN-capacity twin-screw UTM. Two steel gripping adapters were fixed to each head of the dogbones to facilitate their testing. The gripping adapters had protruding rods which were held securely in the hydraulic grips of the UTM. The stress-strain behavior in direct tension was tested by applying crosshead displacement-controlled loading at a constant rate of 0.5 mm/min throughout each test session. The resultant load (in kN) from UTM load cell and the corresponding axial deformation (in mm) of the UHPC prism from the installed extensometer (with a gauge length of 100 mm) were digitally recorded on the UTM as well as on a portable data logger for each 0.1 mm crosshead displacement interval, resulting into 5 data points per minute.

It is worth noting that the dogbone specimens were reinforced with fiber-reinforced polymer (FRP) in order to prevent failures at sections out of the instrumented middle region. The middle regions of the dogbones were excluded from the coverage of FRP strengthening, as indicated by the dark region of the dogbone as shown in Figure 3.10. The FRP used for strengthening was terminated at about 20 mm on both sides of the gauge length.

Test for stress-crack width behavior in direct tension

The characteristic stress-crack width behavior of the UHPCs in direct tension was assessed using notched dogbone specimens with the same test setup as shown in Figure 3.10. Notches with 4 mm depth were cut at the mid-length of the prisms on all sides, resulting in notched cross-section dimension of 32 × 32 mm. The crack width growth was tracked by a pi-type CMOD transducer/extensometer having a gauge length of 50 mm, which was installed across the notch on two opposite sides of the cross-section. Apart from the notch, all testing conditions for the un-notched test were maintained for the notched test.

3.4 Flexural behavior of Reinforced UHPC Beams

3.4.1 UHPC mixtures utilized in Reinforced UHPC Beam Specimens

As stated earlier in Section 3.2, two different UHPC mixtures were utilized for the fabrication of reinforced UHPC beam specimens in this study. It was decided to limit the number of mixtures to just two, since the preliminary material characterization study showed that all the mixtures were similar in their mechanical characteristics. The material constituents for the two mixtures adopted for the fabrication of the reinforced beam specimens are shown in Table 3.5 for a quick reference. The details of these mixtures are presented in Section 3.2. The mixture abbreviated as UMSN is essentially a „low cement‟ version of the mixture UMS.

Table 3.5 Constituents of UHPC mixtures (kg per m^3) utilized for reinforced beams in the study

Constituent	UMS(1*)	UMSN(2*)
Cement	900.0	630.0
MS	220.0	220.0
NZ	0.0	270.0
LSP	0.0	0.0
TMA	220.0	490.0
Powders	1120	1120
Water	162.4	162.4
SP	40.3	40.3
Steel fibers	157.0	157.0
Sand	1005.1	994.3

*Mixture ID number as used in beam numbering notation

MS = Microsilica; NZ= natural zeolite; LSP = limestone powder; SP = superplasticizer; TMA = total mineral admixture

3.4.2 Experimental Matrix for the Reinforced UHPC Beams

The test matrix adopted for the reinforced UHPC beams in this research involved the simultaneous variation of the longitudinal reinforcement ratio (ρ), cross section size (width, b × depth, h) and type of UHPC mixture (i.e., UMS and UMSN). Table 3.6 shows the details of the UHPC beam specimens utilized for the flexural testing in this study. As can be seen in Table 3.6, there were two SB-Series and one DB-Series beams. SB-Series beams have cross-section dimension 150 × 225 mm (i.e., b = 150 mm and h = 225 mm), while DB-Series beams have cross-section dimension 150 × 300 mm (i.e., b = 150 mm and h = 300 mm). Additionally, the beam specimen naming convention in Table 3.6 is **(Beam Series)-(ρ)-(UHPC mixture)**. For example, SB-1.2-UMS stands for a beam in SB-Series (having b = 150 mm and h = 225 mm), passively reinforced with ρ

= 1.2 % and made with UMS mixture. Altogether, twelve beams were fabricated and evaluated for their flexural responses in this study.

Table 3.6 Test matrix adopted for the reinforced UHPC beams.

SN	Specimen ID	L	b	h/b	h	$a/d>1$	# bars Prov.	$A_{s,\text{ prov.}}$, mm^2	$\rho_{\text{prov.}}$, %
1	SB-1.2-UMS	1750	150	1.5	225	3.25	2	353.4	1.2
2	SB-1.8-UMS						3	530.1	1.8
3	SB-2.4-UMS						4	706.9	2.4
4	SB-3.1-UMS						5	883.6	3.1
5	SB-1.2-UMSN	1750	150	1.5	225	3.25	2	353.4	1.2
6	SB-1.8-UMSN						3	530.1	1.8
7	SB-2.4-UMSN						4	706.9	2.4
8	SB-3.1-UMSN						5	883.6	3.1
9	DB-0.9-UMS	1750	150	2	300	2.34	2	353.4	0.9
10	DB-1.3-UMS						3	530.1	1.3
11	DB-1.8-UMS						4	706.9	1.8
12	DB-2.2-UMS						5	883.6	2.2

The larger depth beam DB-series (with depth, h = 300 mm) was included in order to achieve more variations in the longitudinal reinforcement ratios ($\rho = A_s/bd$). This is because there is a limit on the number of bars that can be accommodated by SB beam with h = 225 mm, given the requirement for geometrical symmetry of reinforcement bars. For example, the minimum number of bars in SB-series beams is two, meaning that obtaining lower value of ρ than that given by two bars can only be achieved with increased beam depth. Consequently, the depth of beam was part of the experimental parameters, such that the experimental setup offered the chance of studying the effect of simultaneous variations of the structural parameters ρ and h, in addition to the effect of the type of UHPC mixture. Consequently, there were eight values of ρ involved in the experimental matrix. However, there was one case of coincidental value of ρ (for beams SB-1.8 and DB-1.8), leaving only seven unique values of ρ, as can be seen in Table 3.6.

The shear span to effective depth ratio, *a*/*d,* for DB-series was below 2.5, making it a “short beam” ($1.0 \leq a/d \leq 2.5$) [78], in terms of their expected behaviors with regards to shear-flexure interaction. Hence their structural responses were expected to be controlled mainly by shear. This was not considered as a problem, but rather an advantage, as this beam series was expected to furnish information about the shear resistance of this type of UHPC beam.

3.4.3 Mixing, Placing, Curing and Storage of UHPC Beams

Prior to concrete batching process, the beam mold was oiled on the internal surfaces, while the steel cage, with strain gauges attached with it, was carefully placed in the mold and then held in place by side and bottom cover spacers.

As described in Section 3.3.1, the mixing procedure for UHPC batches for casting beam specimens was a modified version of that used for casting the specimens used for mechanical characterization of the UHPC mixtures, which required small batch volume. The modification was necessary due to the larger batch size of concrete required for the beam specimens (75 and 100 liters), as against the relatively small mixing pan size. After mixing, the fresh mixture was quickly scooped into plastic buckets and then covered closely with plastic sheets, avoiding air access to the fresh concrete surface. The plastic sheet covering was meant to prevent surface dehydration, a phenomenon that leads to the formation of damaging so-called „elephant skin‟, if allowed to take place.

The fresh concrete-filled plastic buckets were then carefully emptied in the beam mold in a way to simulate ejection of fresh concrete from a concrete pump, so that the flow of fresh self-compaction UHPC mixture could be aided. Like the small prism specimens, beam specimens were cast by filling from one end of the mold, and allowed the concrete to fill the rest of the mold by flowing under its self-weight. This is an essential process to ensure the proper fiber distribution in the beams.

Additionally, to ensure an even and random arrangement of the fibers, compaction of the filled beam mold was carried out by slight manual lateral mechanical agitation of the filled mold, since it behaved like a self-compacting concrete mixture. Alternatively, a low frequency mechanical vibration may also be used. However, at a high frequency, mechanical vibration may cause some air bubbles to form in the beam, causing pockets of local weak regions. After filling of the beam molds, extra concrete was removed by screeding the beam top surface. Figure 3.11 shows the beam mold, before and after placement of the fresh UHPC mixture. Following filling and finishing, the surface of the beam specimen was covered with plastic sheets to avoid drying out of the surface.

Figure 3.11 **Preparation and casting of beam specimens: (a) steel cage secured in the mold before placing of fresh concrete; (b) covering of concrete surface after concrete placement.**

After about 24 hours of the casting, the beam form was removed and transferred to a water-curing tank for moist-curing in outdoor conditions where curing temperature ranged from 28 to 35 °C for 28 days. After completion of curing, the beam specimens were moved from the curing tank to the structural mechanics laboratory for flexural testing. Figure 3.12 shows the process of placement for curing and retrieval of UHPC beam specimens from the curing tank.

Along with the casting of beam specimens, small quality control specimens were also cast in parallel with each beam from the same UHPC mixture. The quality control specimens cast were $40 \times 40 \times 160$ mm prisms, 75×150 mm cylinder, and 50 mm cube specimens. These specimens were also cured in the same condition as the corresponding beams. The beams were in storage for about two to four weeks before testing. The control specimens were tested at the same time with the corresponding beams.

Figure 3.12 **Curing and retrieval of beam reinforced UHPC beam specimens.**

3.4.4 Post-casting thermal characteristics

Heat evolution measurement was conducted on 300 mm deep beams made of both the UHPC mixtures (reference-UMS and low cement-UMSN), used for the fabrication of reinforced UHPC beam specimens. Figure 3.13 shows the thermal Instrumentation scheme to monitor the heat evolution of the UHPC mixtures as they go through hydration process after casting. Thermocouples were utilized to monitor the side, bottom and core temperature of the beams.

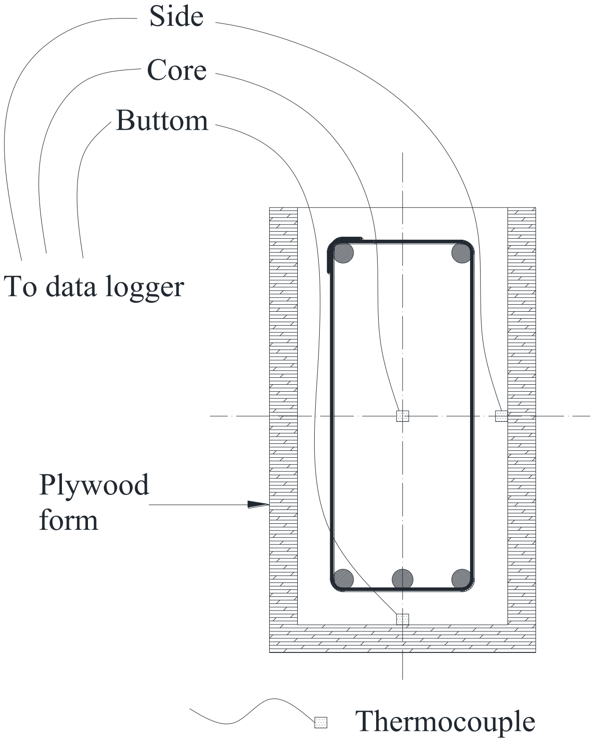

Figure 3.13 Thermal Instrumentation scheme.

3.4.5 Structural Configuration for the Reinforced UHPC Beams

As stated in Section 3.4.2, the beams tested in this study had various structural configurations. As mentioned earlier, for all reinforced UHPC beams studied, 15 mm diameter high strength steel bars (PSB 1080), conforming to ASTM A722/A722M specifications, were utilized as longitudinal reinforcement bars, while stirrups were made from the conventional high yield (grade 60) steel bars of 6 mm diameter, conforming to ASTM A615 specifications. Figure 3.14 shows the structural configurations for all the reinforced UHPC beam sections tested in this study. As shown in Figure 3.14, the number of longitudinal bottom (tension) bars for both SB- and DB-series beams ranged from two to five, while the longitudinal top bars were maintained at two for all the beams.

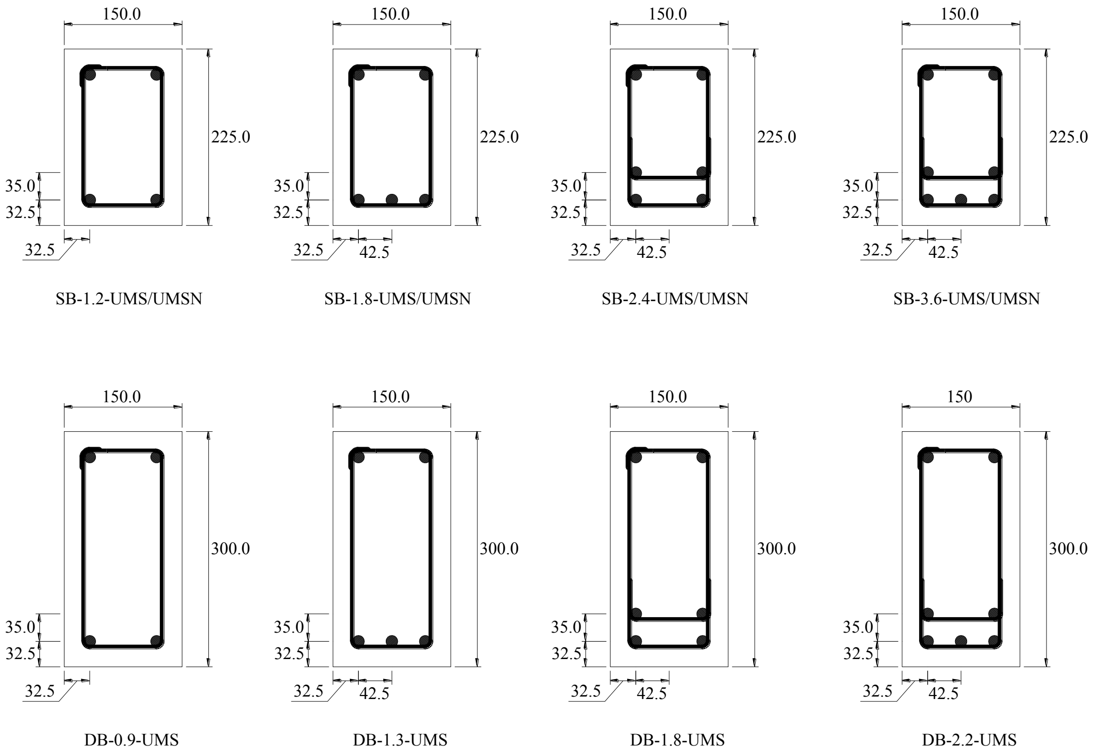

(Note: all dimensions are in *mm*)

Figure 3.14 Structural configurations of the reinforced UHPC beam sections.

The top bars were provided to hold the stirrups in place, which themselves maintain the general geometrical balance of the entire steel cage system. However, the top bars are expected to act as compression bars in some or all cases, hence their contributions were also studied. Stirrups spacing was 150 mm c/c and 180 mm c/c for SB- and DB-series beams, respectively. Obviously, based on the small diameter and large spacing of the stirrups, all the beams studied in this research are practically not reinforced against shear failure. This was done in order to evaluate the flexural capacity of the beams as well as some information about their shear resistance without shear reinforcements.

In order to monitor the progression of load-induced deformations of the longitudinal steel bars in the course of structural testing of the reinforced UHPC beams, the bars were instrumented with surface mounted strain gauges before casting concrete on them. The strain gauge instrumentation scheme is shown in Figure 3.15. The steel surface-mounted strain gauges with 7 mm gauge length were glued using the epoxy, recommended by the manufacturer (Tokyo Sokki Kenkyujo Company, Limited). After bonding, the strain gauges were protected against possible damage due to placement of fresh UHPC in the mold and due to capillary water, using plastic electrical tape. Figure 3.16 is a picture showing close-up details of strain gauge installation on the reinforcement bars.

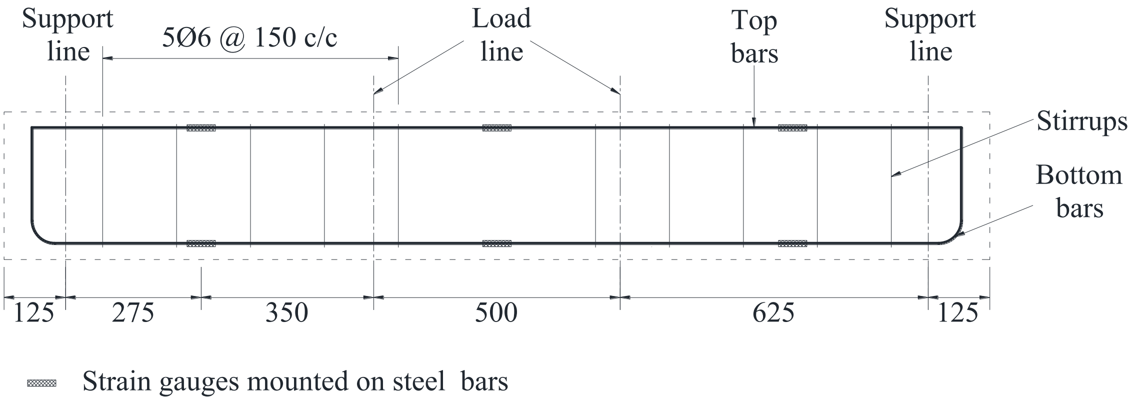

Figure 3.15 Instrumentation scheme for the reinforcement bars embedded in UHPC beams.

Figure 3.16 Details of strain gauge installation on the reinforcement bars.

3.4.6 Flexural Testing Setup for the Reinforced UHPC Beams

All reinforced UHPC beam specimens were tested in 4-point loading configuration. The same loading geometry and configuration was maintained for all the tested beams. Four-point loading is generally used for flexural testing of any structural element that are expected to impart linear or volumetric heterogeneity to the element in question. This is because the volumetric material elements within the area between the two vertical loading planes are expected to be under the same uniform stress at a given depth of the beam. Hence the weakest point within the constant stress region will experience failure first. Thus, the failure load will be associated with the strength of the weakest point in the beam material body. This is as opposed to mid-point (also called 3-point) loading in which the maximum stress is enforced at a single vertical plane for a given depth of the beam, in which case a weaker material point in the beam may „escape" failure if it is located far enough from the single point of maximum stress.

Figure 3.17 shows the schematics of the Four-point loading configuration adopted for the flexural testing of the reinforced UHPC beams. The setup consisted of the reinforced UHPC beam on rigid metallic supports over a flexure span of 1.75 m. A quasi-static jack displacement-controlled load was applied by a hydraulic actuated loading jack that bore on a rigid reaction frame. The load from the jack was applied to the beam via the rigid spreader beam bearing on two loading noses which were 500 mm apart. The applied loads were recorded by a 2000 kN-capacity load cell sandwiched between the loading jack and the spreader beam. The whole loading arrangement was carefully centralized and aligned on the beam span, in order to avoid eccentricity in the two orthogonal directions on the horizontal plane.

The central bottom LVDT was installed to track the beam deflections. In order to prevent local bearing damage at each of the points of contact with the spherical knife edge supports, 10 mm-thick rigid rubber strip was sandwiched between the beam underside and a steel 13 mm-thick plate. Consequently, the central LVDT tracks not only the beam deflection but also the support settlements resulting from the deformation of the rubber sheets. In other words, the recorded displacement through the central LVDT (d_{total}) includes the downward rigid body motion of the beam (as loading progressed) and the actual deflection of the beam due to the flexural bending produced by the same load. This phenomenon is illustrated in Figure 3.18. Therefore, the top LVDTs over the beam at the support line were installed to track the rigid body motion of the beam, d_{s1} and d_{s2}, so that the pure flexural deflection can be extracted from the central LVDT readings. A similar protection against bearing damage of the beam employed at the support points was installed at the interface of the loading noses and the beam top.

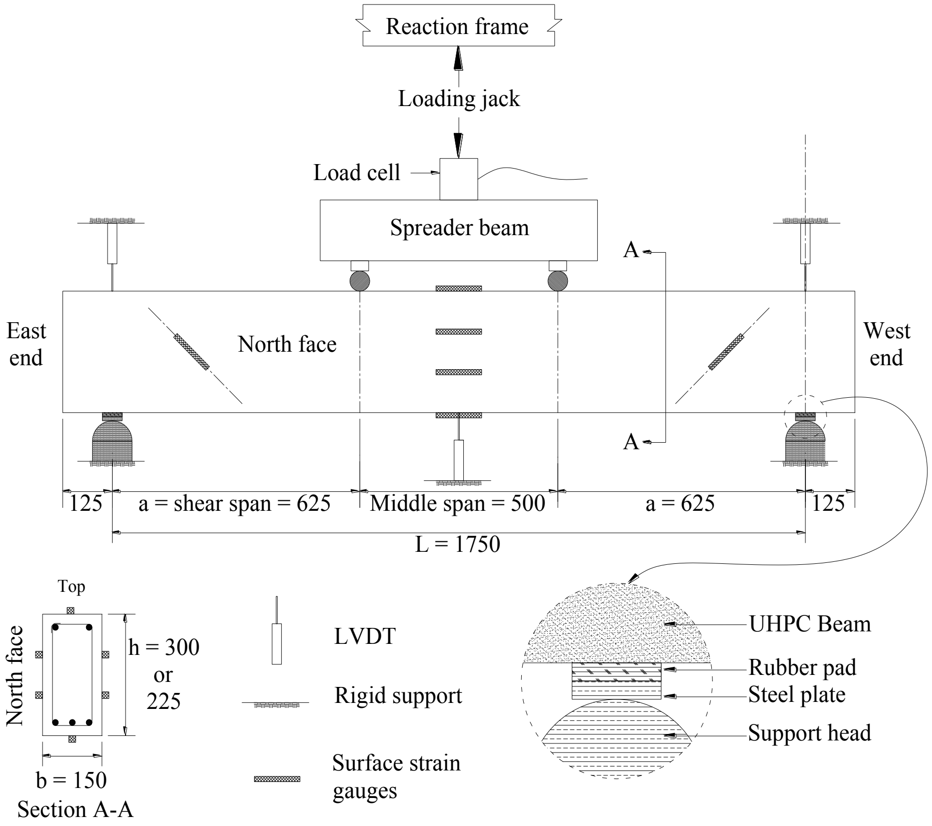

(Note: all dimensions are in *mm*)

Figure 3.17 **Flexural testing configurations adopted for reinforced UHPC beams.**

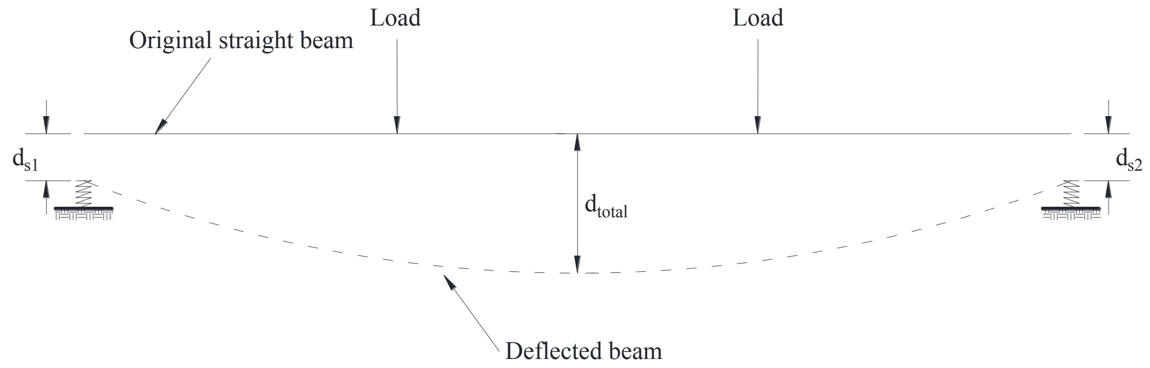

$$d_{bend} = d_{total} - \frac{1}{2}(d_{s1}+d_{s2})$$

Figure 3.18 Illustration of static deflection/rigid body motion system.

Also shown in Figure 3.17 was the instrumentation scheme for monitoring of the surface strains on the UHPC beams as loading progressed. The central array of strain gauges having 60 mm gauge length was installed to monitor the top, bottom and side face strains. This array is expected to furnish the neutral axis transition as a function of the load level before the beam would start to experience significant damages. The inclined gauges around the shear critical regions were installed to monitor the evolution of shear stresses and subsequent incidence of shear tension damages.

CHAPTER 4

RESULTS AND DISCUSSION-PART I

(MECHANICAL CHARACTERIZATION OF UHPC MIXTURES)

This chapter presents the results and discussion pertaining to the experimental work conducted for mechanical characterization of the UHPC mixtures used to fabricate the passively reinforced UHPC beam specimens. As stated earlier, the mechanical characterization program was meant to achieve two main aims. The first aim was to determine the characteristic values of the mechanical properties of the locally developed UHPC mixtures that would be utilized for structural design of the beams. The second aim of the mechanical characterization program to examine the level of reliability/repeatability of these mechanical properties, considering the highly heterogeneous nature of UHPC as a composite material, as well as its sensitivity to changes in compositional and operational parameters. Hence, the results of these tests were statistically analyzed for showing variations across different times of casting.

4.1 Cube compressive strength

The compression test on UHPC was conducted on Group-I UHPC mixtures (UMS, UMN, and UML). The compositions of theses mixtures are shown in Table 3.3. For each of the three UHPC mixtures, four batches were prepared and five number of 50 mm cube specimens were cast for each batch, making a total of 20 specimens for each UHPC mixture. Table 4.1 shows the cube compressive strength results for Group-I UHPC mixtures.

Table 4.1 Cube compressive strength results for Group-I UHPC mixtures.

Mix ID	Batch No.	Compressive strength, MPa					Avg.*	SD^{+}
UMS	1	176	157	168	180	167	170	9.0
	2	163	164	170	168	169	167	3.2
	3	164	165	167	166	166	166	1.0
	4	165	168	163	170	170	167	3.1
UMN	1	151	168	167	172	169	165	8.4
	2	162	170	171	169	170	169	3.5
	3	176	173	171	177	170	173	3.0
	4	169	172	167	170	164	168	2.8
UML	1	169	164	175	182	174	173	6.8
	2	172	169	168	178	170	171	3.9
	3	168	176	178	169	172	173	4.4
	4	170	162	168	177	176	170	6.0

*Average of 5 replicates for each batch

$^{+}$Standard deviation of 5 replicates for each batch

The data shown in Table 4.1 clearly shows that the inter-batch (i.e., among different batches) mean compressive strength ranges (differences between maximum and minimum) for all the UHPC mixtures varied from 2 MPa to 8 MPa. However, the intra-batch (i.e., within the same batch) strengths were more varied, from 2 to 23 MPa, as can be seen in Table 4.1. This intra-batch strength variability is better represented by the values of standard deviation as shown in the last column of Table 4.1. Given this fact, it is important to carry out inferential statistical analyses to test two classes of hypotheses. The first class of hypothesis relates to batch-to-batch consistency of the mean strength, which is one major objective for this phase of the research. The other class relates to variation of mean strengths within the three UHPC mixtures. Although there is a little difference in the material composition, the resulting strengths seemed close enough to demand statistical evidence to judge whether they are indeed different mechanically or not. Two-way analysis of variance (ANOVA) was carried out on the entire compressive strength dataset. The two independent factors considered were *mixture* and *batch*, while the response variable was the *cube compressive strength*. The tested hypotheses are stated as follows:

For the *mixture* factor,

H_{m0}: The *mean compressive strength* is the same for all the *mixtures*

H_{m1}: The *mean compressive strength* for at least one *mixture* differs from that of other *mixture*s

And for the *batch* factor,

H_{b0}: The *mean compressive strength* for a given mixture is the same for all the *batch*es

H_{b1}: The *mean compressive strength* for at least one *batch* differs from that of other *batch*es of the same mixture

It should be noted that H_{m0} and H_{m1} are null and alternate hypothesis for the *mixture* test, while H_{b0} and H_{b1} have same meanings for *batch*.

The ANOVA was carried out using the „Analysis ToolPak‟ add-in in MS Excel. For the testing of the two hypotheses, the upper threshold of the probability of committing a Type-I error, usually denoted by α, was set to α = 0.05. The usual inferential statistics treatment is to reject the null hypothesis for a factor with *P-value* ≤ α. Table 4.2 shows the ANOVA output for the Group-I UHPC mixtures. It can be concluded from Table 4.2 that there is no variation in mean strength from one *batch* to another for the same UHPC mixture, as the *P-value* for *batch* is much larger than α. However (since the *P-value* for *mixture* is less than α) there is no justification for concluding, at 95% confidence level, that all the three UHPC mixtures have the same mean compressive strength, even though they may appear so from manual judgment. Consequently, it becomes necessary to single out the mixture with different mean compressive strength from the rest. For this purpose, *t*-test was carried out with the mixtures paired.

Table 4.2 ANOVA output for Group-I UHPC mixtures.

Source of Variation	SS	df	MS	F	P-value	F crit
mixture	201.621	2	100.811	3.8155	0.02899	3.19073
batch	30.3867	3	10.1289	0.38336	0.76545	2.79806
Interaction	193.941	6	32.3236	1.22339	0.31099	2.2946
Within	1268.22	48	26.4213			
Total	1694.17	59				

For the paired tests, all the batch results for each UHPC mixture were merged, since it has been previously concluded that there were no significant variations of the compressive strengths from one batch to another. Table 4.3 shows the *t*-test results. The

F-test result shown in the second column of Table 4.3 indicates that all the pairs had equal variances at 95 % confidence level, so the two-tailed t-test results presented in the last column of Table 4.3 were obtained using the MS Excel built-in *TTEST* function, specifying equal variance in each case. As can be seen in Table 4.3, UMS mixture was indicated as having a significantly different mean compressive strength from UML, at 95 % confidence level.

Table 4.3 ‘t-test’ results for Group-I UHPC mixtures.

Pair	*F*-Test *P-value*	*t*-Test *P-value*
UMS, UMN	0.60898	0.32031
UMS, UML	0.85157	0.00721
UMN, UML	0.74532	0.10003

Table 4.4 shows the overall mean cube compressive strengths along with standard deviation (SD) and coefficient of variation (COV) for the Group-I UHPC mixtures, considering 20 replicates for each mixture. Table 4.4 also indicates that all the mixtures have almost equal degree of variability in their compressive strengths, pointing to a high degree of repeatability in the compressive strengths of these mixtures that may be attributed to consistency in composition of the mixtures and the workmanship in preparation and testing used in the present study. Consequently, the locally developed UHPC mixtures can be said to possess consistent mean compressive strengths.

Table 4.4 **Overall mean cube compressive strengths for the Group-I UHPC mixtures.**

Mixture	$f_{cu,\mathrm{avg}}$* (MPa)	SD (MPa)	COV^{+}
UMS	167	4.8	2.9
UMN	169	5.4	3.2
UML	172	5.1	2.9

*Average cube compressive strength considering 20 replicates

$^{+}$Coefficient of variation (SD/ $f_{cu,\mathrm{avg}}$)

The „significant‟ difference in the strength of UMS and UML mixtures indicated by ANOVA and t-test, as shown in Table 4.3 and Table 4.4, respectively, is due to the fact that the UML had a higher mean cube compressive strength of 172 MPa than the UMS with 167 MPa. Though this strength difference is only 3 % (which may be insignificant on practical ground), the result is useful for reaching to a conclusion that the partial replacement of microsilica (MS) by limestone powder (LSP) does not affect the resulting compressive strength of UHPC, but may rather increase it. The use of LSP in normal strength concrete has been reported to impart excellent densification to the concrete microstructure [79-82], even though, it is non-pozzolanic [81, 83]. Therefore, it can now be concluded that the LSP can be effectively used in both conventional concrete as well as in UHPC mixtures.

4.2 Characteristic stress-strain behavior in compression

Since the previously detailed analysis of the results of compressive strength of cube specimens has shown substantial evidences of technical repeatability of compressive strengths from one batch to another of the same mixture, 10 randomly selected cylindrical specimens were tested for stress-strain behavior in compression across four batches for each of the three mixtures of Group-I. The stress-strain test in compression on UHPC was conducted using cylinder specimens having finished dimensions as 76 × 145 mm, as mentioned earlier.

4.2.1 General uniaxial compression behavior

Figure 4.1 shows Type-I uniaxial compression response of UHPC cylinders, including the individual LVDT strain records. The strains have been obtained by dividing the recorded LVDT displacements by the gauge length of 87 mm, which was fixed throughout the study. As can be seen in Figure 4.1, individual LVDT strain records were not sufficient to correctly describe the stress-strain response for the specimen. However, the average curve gave a good behavior throughout the entire loading regime.

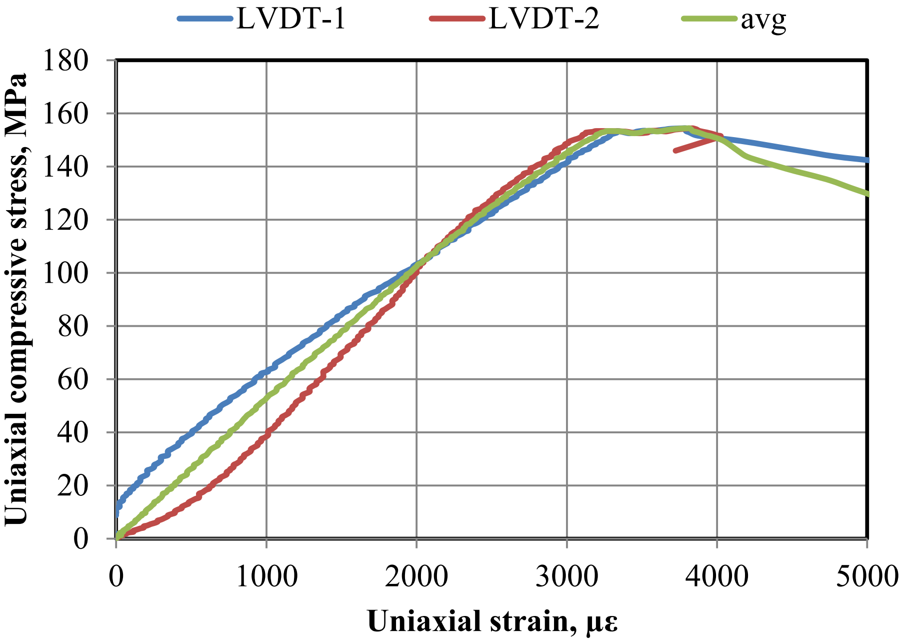

Figure 4.1 **'Type-I' response of UHPC (UML1) cylinder in uniaxial compression.**

In addition, it can be observed from Figure 4.1 that the average response is nearly linear up to the peak load, while the post peak regime shows some ductile softening until the complete loss of compression resistance. Subsequently, this particular specimen exhibited a relatively large ultimate strain in the neighborhood of 5000 με. However, the actual physical post-peak behavior was usually characterized by rapid loss of stability by the extensively damaged specimens, even though the final damage stages were non-violent in all cases, due to highly efficient activation of fiber actions.

Figure 4.2 shows the various documented types and degrees of damage exhibited by the UHPC cylinders after complete loss of resistance in uniaxial compression. The implication of these varying degrees of extensive damage is that the seemingly large ultimate strain cannot be relied upon. This post-peak response type, characterized by large apparent ultimate strain was referred to as a „Type-I‟ response‟‟. The reason behind unreliability of a large apparent ultimate strain can be illustrated by another type of response (Type-II) as shown in Figure 4.3. In this case, the ultimate strain was not as large as in Type-I. This was because a part of a failed specimen suffers a slight rotation relative to the other part, leading to the type of behavior captured in Figure 4.3, referred to as „Type-II‟‟ post-peak response. For this case, the documented ultimate strain was about 3500 με.

Figure 4.2 **Types and degrees of damaged exhibited by UHPC cylinders after compression failure.**

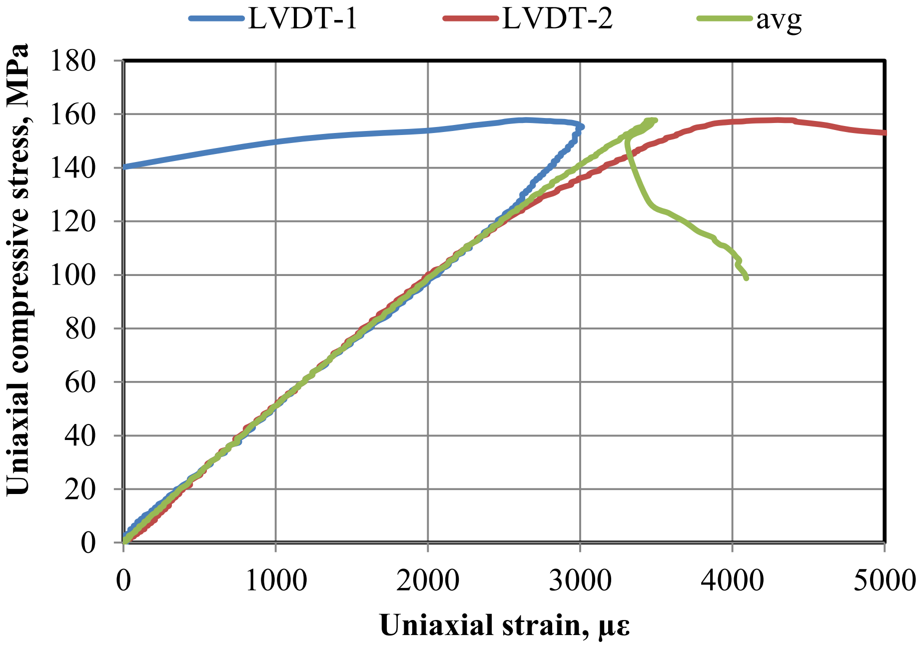

Figure 4.3 **'Type-II' response of UHPC (UML1) cylinder in uniaxial compression.**

The rational basis upon which the safe design of structural elements are made would suggest limiting the utility of compressive resistance energy to that corresponding the peak load and corresponding strain, while the remaining is ignored as safety margin. This suggestion is illustrated in Figure ‎4.4. The reason for this is clear, as the post-peak behavior is not consistently stable: both type-I and type-II responses have been recorded for the same UHPC mixture.

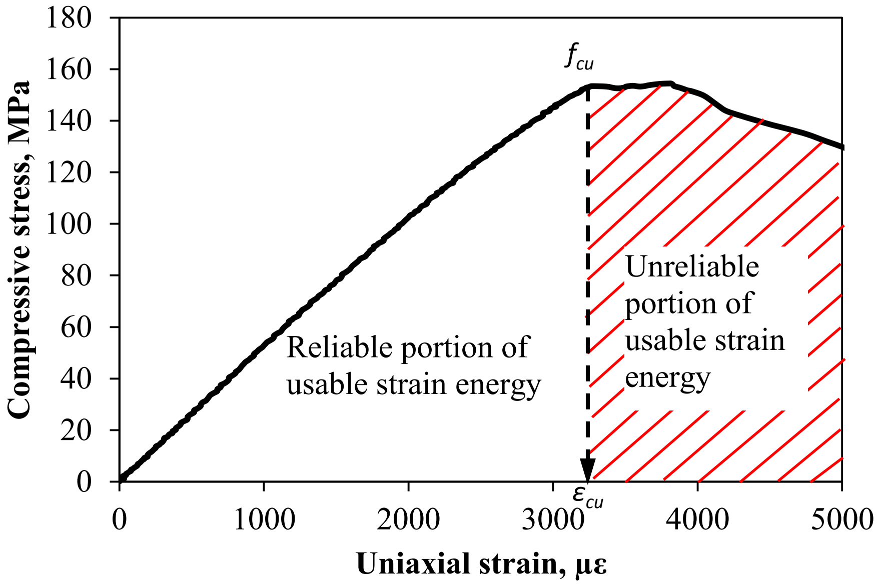

Figure 4.4 General response of UHPC cylinder in uniaxial compression.

The foregoing discussion has given a picture of the stress-strain behavior. The peak stresses (f_{cu}) and the corresponding strains (ε_{cu}) were picked up for each specimen for the UHPC mixtures of Group-I, considered in this study. The detailed analysis of the test results related to overall behavior of UHPC mixtures in compression are discussed in the following sections, leading to their mechanical characterization.

4.2.2 Peak stress and strain

The peak axial stress in compression (or simply compressive strength), f_{cu}, is an essential design parameter for a concrete material. For all cylindrical specimens tested for the Group-I UHPC mixtures, Table 4.5 shows the individual values of f_{cu}. With regard to geometry of specimen used for test in compression, it is a good idea to compare the average peak strengths obtained from 50 mm cube and 76 mm diameter cylinder for a same UHPC mixture. This comparison is shown in Figure 4.5. The cube strengths were found to be about 11 % above corresponding cylinder strengths. The coefficient of variation (COV) was introduced in order to furnish ideas of relative degrees of variation due to large differences in value ranges, as against the standard deviation.

Table 4.5 Peak compressive strengths of Group-I UHPC mixtures.

Mix ID	f'_c, MPa					Avg	SD	COV,%
UMS	162	165	158	157	160	153	8.1	5
	145	143	149	149	144			
UMN	149	148	150	158	147	151	4.0	3
	151	150	158	149	148			
UML	158	157	154	148	152	154	4.9	3
	156	153	163	146	153			

In the current analyses, the peak strain for a particular specimen refers to the strain (ε_{cu}) corresponding to the peak stresses (f_{cu}). As previously highlighted, this definition was adopted in line with what may be employed as the maximum usable strain in design sense, rather than the actual maximum value. Table 4.6 presents the ε_{cu} values corresponding to the f_{cu} values tabulated in Table 4.5. These results show that the usable strains for these UHPC mixtures is a little above 3000 με. A value of ε_{cu} = 3500 με may be safely taken tentatively as recommended design value. Additionally, since the COV values in this case are a little higher than those for f_{cu} values, it can be concluded that ε_{cu} tends to exhibit more scatter than f_{cu}.

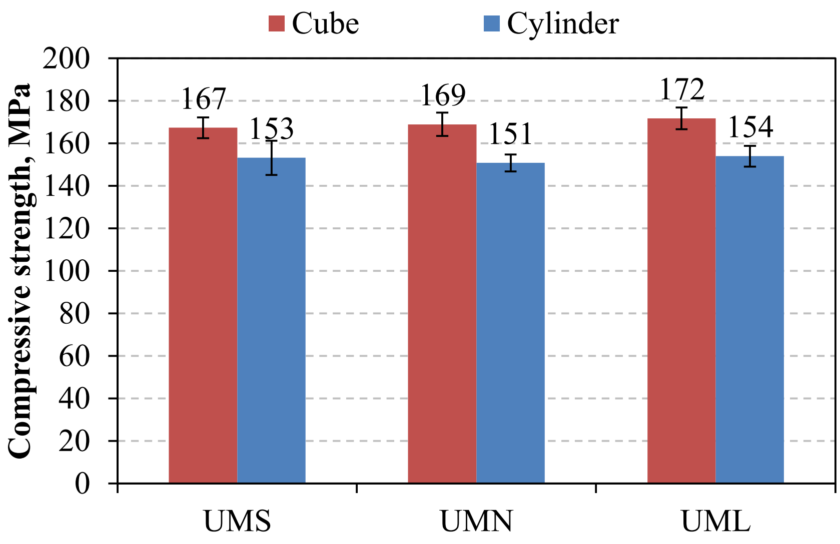

Figure 4.5 Comparison of cube and cylinder strengths in uniaxial compression.

Table 4.6 Peak compressive strains of Group-I UHPC mixtures.

Mix ID	ε_{cu}, mm/mm					Avg	SD	COV
UMS	3391	3816	3667	3713	3276	3379	310	9
	2989	2966	3402	3034	3540			
UMN	3195	3494	3368	3207	3264	3350	116	3
	3414	3310	3287	3517	3448			
UML	3483	3098	3805	3195	3299	3341	241	7
	3287	3195	3678	3276	3092			

4.2.3 Stiffness and non-linearity

For characterizing the UHPC mixtures in terms of elastic stiffness, two types of modulus of elasticity were calculated using stress-strain data. These are the tangential and the secant moduli of elasticity, E_c and E_{cs}, respectively. The tangential modulus was obtained in a similar way to that specified in ASTM C469, in which the lower strain was taken as

50 µε and the corresponding stress ($\sigma_{50\mu\epsilon}$) taken as the lower stress, while the upper stress is taken as $0.4f_{cu}$ with the corresponding strain taken as the upper strain. That is

$$E_c = \frac{0.4f_{cu} - \sigma_{50\mu\epsilon}}{\epsilon_{0.4f_{cu}} - 50\mu\epsilon} \tag{4.1}$$

This is usually referred to as chord modulus of elasticity, which does not necessarily correspond to the slope of the initial linear part of the stress-strain curve for low to medium strength (15 to 45 MPa) concretes.

However, for UHPC class concretes with compressive strengths ranging from about 130 MPa to more than 250 MPa, the chord modulus of elasticity corresponds exactly to the tangential modulus of elasticity or the initial linear part of the stress-strain curve. The secant modulus was taken as the slope of the line joining the point of zero stress (and strain) to the point of peak stress on the stress-strain curve. That is

$$E_{cs} = \frac{f_{cu}}{\epsilon_{cu}} \tag{4.2}$$

The calculations of two moduli of elasticity are illustrated in Figure 4.6. The results of these stiffness parameters are shown in Table 4.7 and Table 4.8, in the same order of specimens as before.

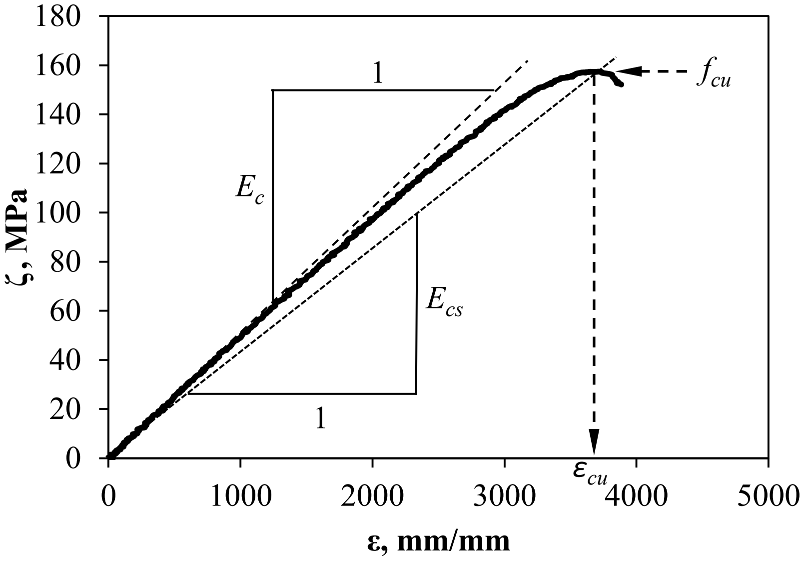

Figure 4.6 **Computation of tangential and secant moduli of elasticity.**

Table 4.7 **Tangential modulus of elasticity for Group-I UHPC mixtures.**

Mix ID	E_c, Mpa					Avg	SD	COV
UMS	48.7	50.3	50.2	48.8	49.2	49.3	1.1	2
	49.0	47.3	51.1	49.9	48.2			
UMN	49.2	48.9	50.0	51.3	48.6	49.4	1.3	3
	49.2	50.9	51.0	47.7	47.6			
UML	50.0	54.9	51.7	51.4	49.9	51.0	2.0	4
	47.8	49.7	53.3	50.2	51.3			

Table 4.8 **Secant modulus of elasticity for Group-I UHPC mixtures.**

Mix ID	E_{cs}, Mpa					Avg	SD	COV
UMS	47.4	43.2	42.9	42.4	48.8	45.5	3.1	7
	48.3	48.4	43.9	48.6	40.7			
UMN	46.3	42.4	44.4	49.2	45.1	45.0	2.3	5
	44.0	45.3	48.1	42.2	43.0			
UML	45.3	50.8	40.6	46.2	46.2	46.3	2.9	6
	47.4	48.0	44.2	44.5	49.6			

It can be noted from the COV values in Table 4.7 and Table 4.8 that E_{cs} has more scatter in values than E_c. This scatter is associated to the large variations in the behaviors of different specimens of the same batch of UHPC mixtures at peak. This observation is expected since the peak behavior is governed by fiber activation process, rather than the composition of matrix, which is may not be expected to be very consistent.

Based on the illustration shown in Figure 4.6, it is expected that the secant stiffness will always be less than the tangential stiffness. The extent to which the former is less than the latter is itself a measure of the degree of curvature of the respective stress-strain curve. This leads to the concept of non-linearity of stress-strain curves. Intuitively, the ratio of secant to tangent modulus, L_c, is a valid linearity descriptor. This can be represented as

$$L_c = \frac{E_{cs}}{E_c} \times 100\ \% \tag{4.3}$$

Ultra-high strength concrete materials are known to exhibit relatively high stiffness, and therefore less „default‟ ductility, which translates to less degrees of non-linearity, in reference to conventional concretes. That is the major reason why fibers are required in such brittle materials in order to help in absorbing the fracture energy dissipated at failure, thus imposing a good degree of composite ductility, even though the stress-strain curve may show high degree of linearity (or low degree of non-linearity). For the Group-I UHPC mixtures, Table 4.9 shows the computed dimensionless linearity parameters.

Table 4.9 Linearity parameters for Group-I UHPC mixtures.

Mix ID	L_c, %					Avg	SD	COV
UMS	97.3	85.9	85.5	86.9	99.2	92.3	7.1	8
	98.6	102.2	85.9	97.5	84.4			
UMN	94.1	86.7	88.7	95.9	92.9	91.0	3.1	3
	89.4	89.0	94.4	88.5	90.4			
UML	90.6	92.5	78.5	89.9	92.6	90.8	6.3	7
	99.1	96.5	83.0	88.6	96.6			

Expectedly, the maximum value of L_c is 100 %, describing a behavior that is linear from the initial loading stage up to failure. However, this expectation may not always be the case, as can be seen in one case in Table 4.9. Linearity value larger than 100 % indicates unusual stiffening of the specimen as loading progressed. Table 4.9 established that the average linearity for these three Grade 150 MPa UHPC mixtures was about 91 %. Obviously, the degree of linearity will approach 100 % for higher UHPC grades.

4.2.4 Compression stress block

As discussed earlier, the average degree of linearity of the three Group-I mixtures were about 91 %. Therefore, the compression block shape at the ultimate limit state (ULS) can be approximated with a triangular shape, as against the usual rectangular shape employed in the conventional low to high strength concretes. In this study, two idealization schemes were proposed for the triangular stress block, as shown in Figure 4.7.

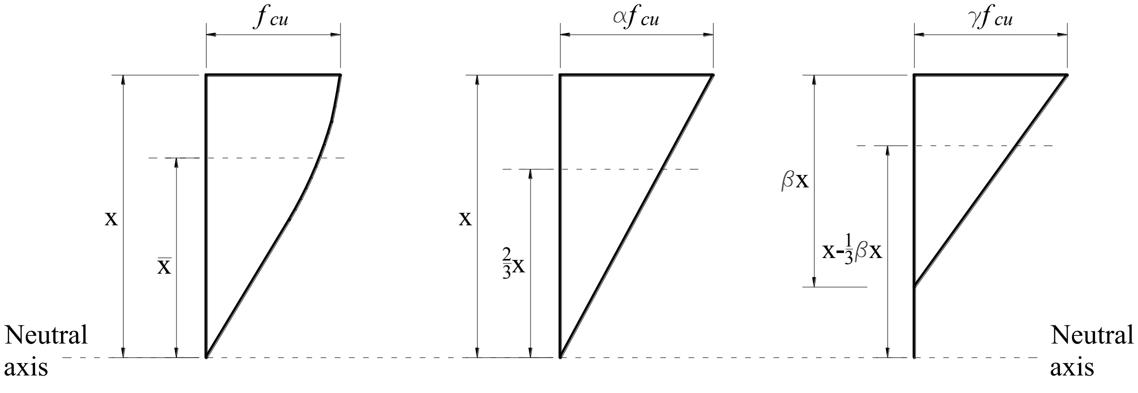

(a) (b) (c)

Figure 4.7 **Schematics of compressive stress blocks at ULS: (a) actual stress-strain curve; (b) Proposed approximation scheme-I; (c) Proposed approximation scheme-II**

Individual stress-strain curves were integrated numerically to obtain both the areas under the respective curve and the corresponding location of centroids from the neutral axes. The parameters of the proposed stress block were then obtained by least square fitting of the approximation block models with the integration data, on the bases of force and moment equivalence. The values of α, β and γ were found to be 1.0725, 1.0, and 1.0725, respectively. Hence the stress-block idealization scheme-I is sufficient. It may be recalled that the area under the post-peak portion of the stress-strain curve had been ignored, as illustrated in Figure 4.4 on the basis of conservative design consideration.

4.2.5 Summary of compressive response parameters

The complete results of the compressive behavior parameters for the three UHPC mixtures under Group-I are summarized in Table 4.10.

Table 4.10 Summary of compressive response parameters for Group-I UHPC mixtures.

UHPC ID	f_{cu}, MPa	ε_{cu}, με	E_c, GPa	E_{cs}, GPa	L_c
UMS	162	3391	48.7	47.4	97.3
	165	3816	50.3	43.2	85.9
	158	3667	50.2	42.9	85.5
	157	3713	48.8	42.4	86.9
	160	3276	49.2	48.8	99.2
	145	2989	49.0	48.3	98.6
	143	2966	47.3	48.4	102.2
	149	3402	51.1	43.9	85.9
	149	3034	49.9	48.6	97.5
	144	3540	48.2	40.7	84.4
UMN	149	3195	49.2	46.3	94.1
	148	3494	48.9	42.4	86.7
	150	3368	50.0	44.4	88.7
	158	3207	51.3	49.2	95.9
	147	3264	48.6	45.1	92.9
	151	3414	49.2	44.0	89.4
	150	3310	50.9	45.3	89.0
	158	3287	51.0	48.1	94.4
	149	3517	47.7	42.2	88.5
	148	3448	47.6	43.0	90.4
UML	158	3483	50.0	45.3	90.6
	157	3098	54.9	50.8	92.5
	154	3805	51.7	40.6	78.5
	148	3195	51.4	46.2	89.9
	152	3299	49.9	46.2	92.6
	156	3287	47.8	47.4	99.1
	153	3195	49.7	48.0	96.5
	163	3678	53.3	44.2	83.0
	146	3276	50.2	44.5	88.6
	153	3092	51.3	49.6	96.6

4.3 Characteristic stress-strain behavior in tension

For the characterization of the UHPC mixtures in tension, flexural and direct tension tests were conducted. Each of the two types of tension tests were carried out on both un-notched and notched specimens. The following sub-sections discuss the results of the tension tests conducted on the UHPC specimens as a part of mechanical characterization.

4.3.1 Flexural tensile behavior

As mentioned earlier, this test was conducted on 70 × 70 × 280 mm un-notched UHPC prisms using a 4-point (three equal spans) loading configuration on an overall flexure span of 210 mm. Full details of this test are presented earlier in Section 3.3.2. Twelve prisms were tested for each of the three UHPC mixtures. Figure 4.8 shows the failure behavior of flexural prism specimens after testing. It should be noted that even though only one wide crack can be clearly seen in these failed specimens, most of them exhibited the so-called multi-cracking that is expected due to strain hardening of UHPC material. However, the initial multiple fine cracks preceding the crack localization are difficult to see at the scale of the images in Figure 4.8 (a). In order to show these multiple cracks, close-up images were taken with the cracks traced by colored markers, as shown in Figure 4.8 (b). Typical stress-deflection behaviors for three specimens of UMS mixture are shown in Figure 4.9.

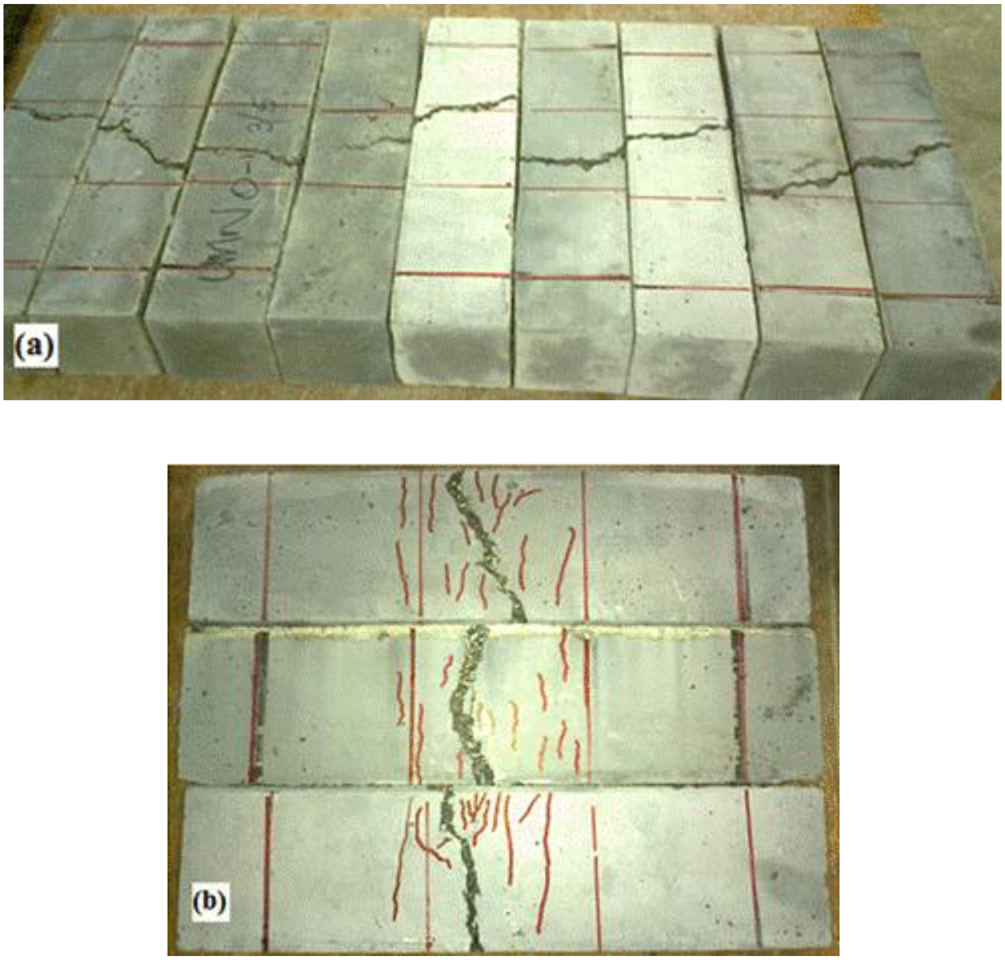

Figure 4.8 Un-notched flexural tensile (4-point) prism specimens after testing: (a) general view; (b) close-up view highlighting multiple cracks in the middle span.

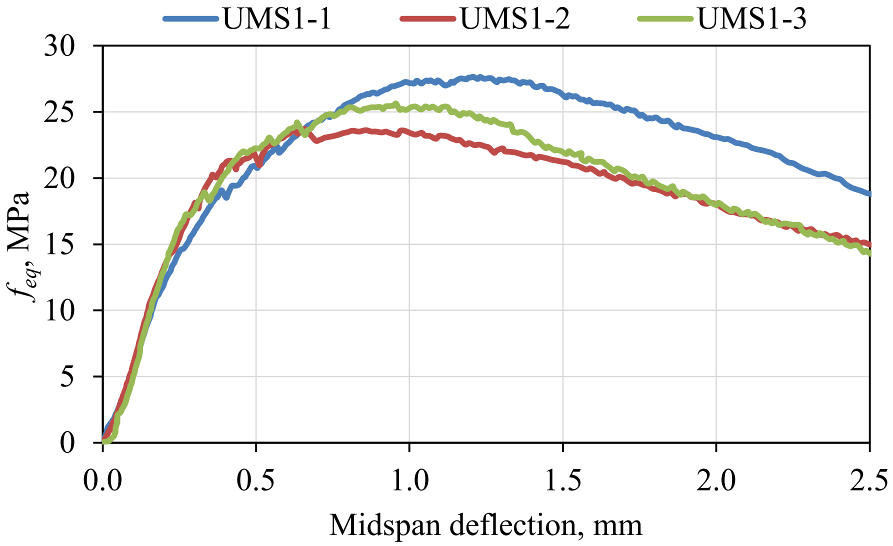

Figure 4.9 Typical documented stress-deflection behavior.

4.3.2 Cracking strengths (un-notched)

Figure 4.10 shows a typical initial portion of stress-deflection behavior, highlighting the calculation of the cracking stress, f_{cr}. The results of the cracking strengths are shown in Figure 4.11, Figure 4.12, Figure 4.13, and Figure 4.14. The error bars in these graphs represent standard deviations. Each data point shown by a bar represents an average of three values. Four bars shown in each figure belong to four different batches of the same UHPC mixture.

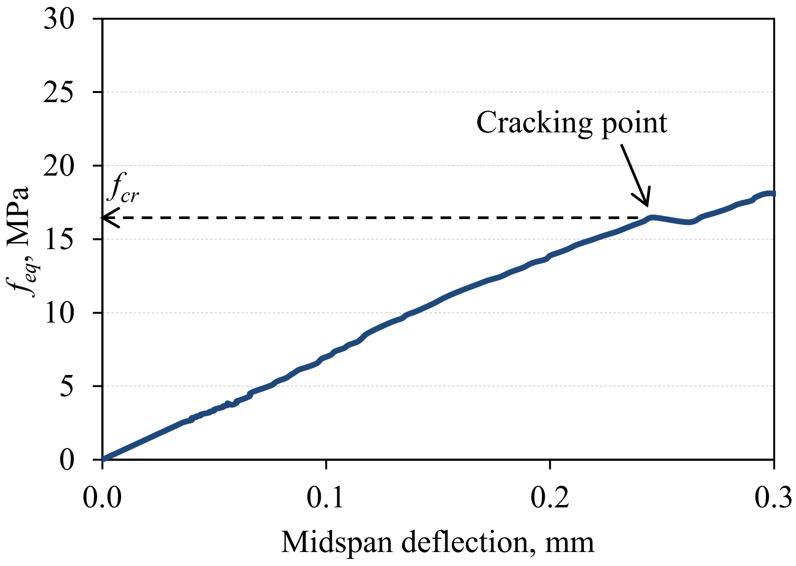

Figure 4.10 **Calculation of cracking stress.**

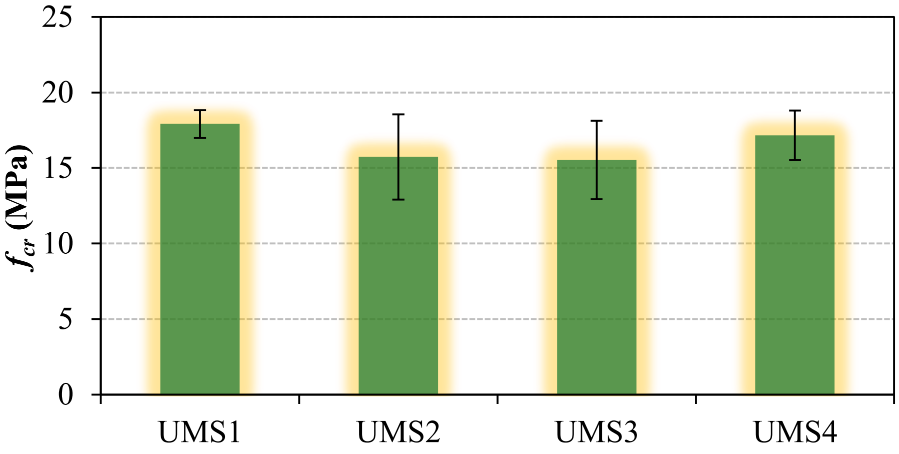

Figure 4.11 **Cracking strength for UMS.**

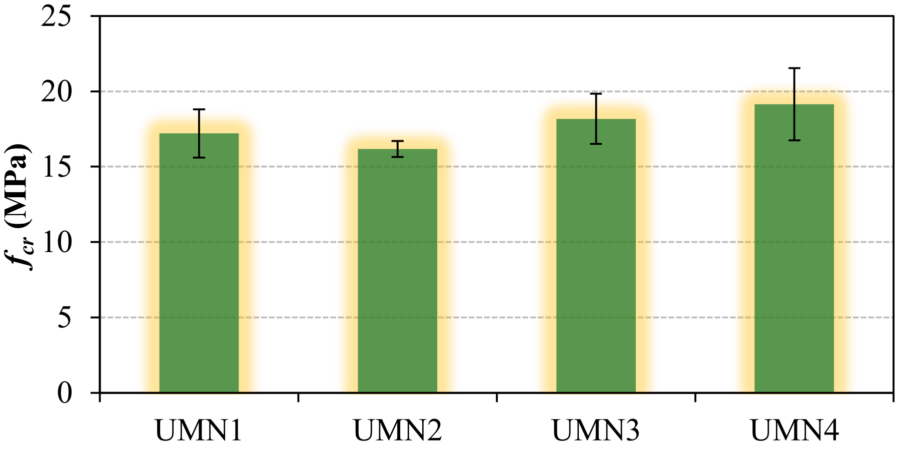

Figure 4.12 **Cracking strength for UMN.**

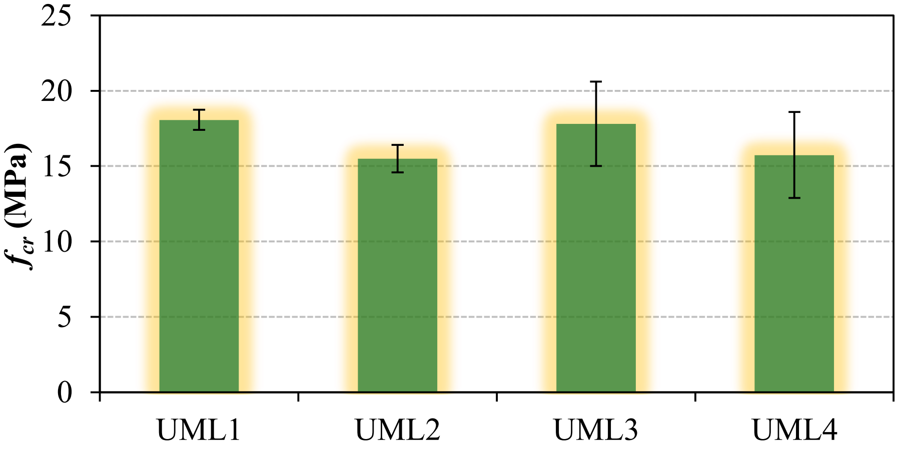

Figure 4.13 **Cracking strength for UML.**

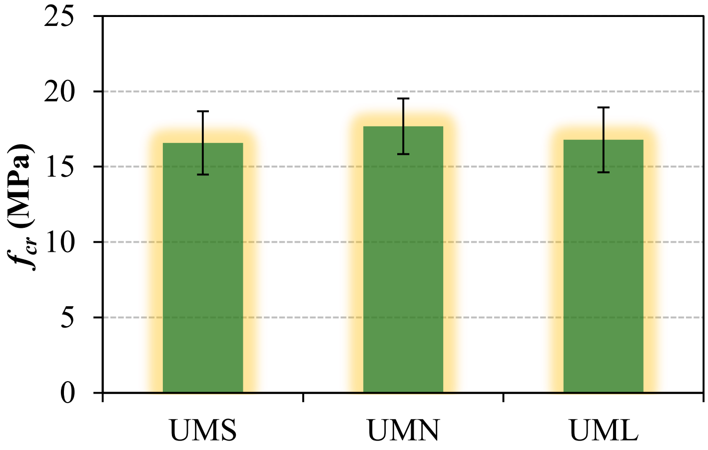

Figure 4.14 Cracking strengths of three UHPC mixtures of Group-I.

4.3.3 Flexural strengths

Figure 4.15 shows a typical full stress-deflection behavior of UHPC prism specimen, highlighting the general outlook of the behavior as well as the calculation of the peak equivalent flexural strength, $f_{eq,max}$. The equivalent flexural stress, f_{eq}, is computed from the basic relationship

$$f_{eq} = \frac{3Pa}{bh^2} \tag{4.4}$$

where

P = applied load,

a = shear span,

b = cross-section width, and

h = cross-section depth

Ideally, for third-point loading (four-point loading configuration with three equal spans), the parameters *a*, *b*, and *h* should all be equal. However, due to issues related to the finishing of the top surface of the specimens, *h* varied slightly. The value of the depth of cross-section used in f_{eq} calculations is the average of three values within the middle span of the specimen. The results of the f_{eq} are shown in Figure 4.16, Figure 4.17, Figure 4.18, and Figure 4.19. Each data point represents an average of three values. The error bars in these graphs represent standard deviations. Four bars shown in each figure belong to four different batches of the same UHPC mixture.

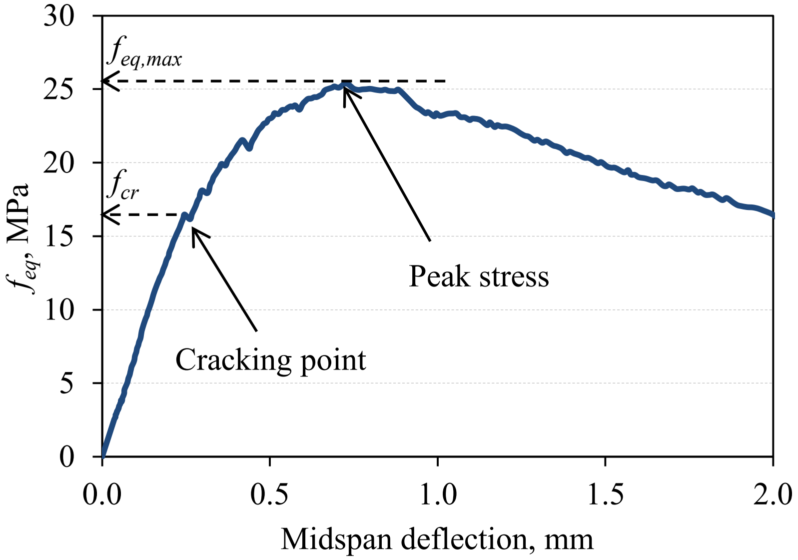

Figure 4.15 **Calculation of peak equivalent stress.**

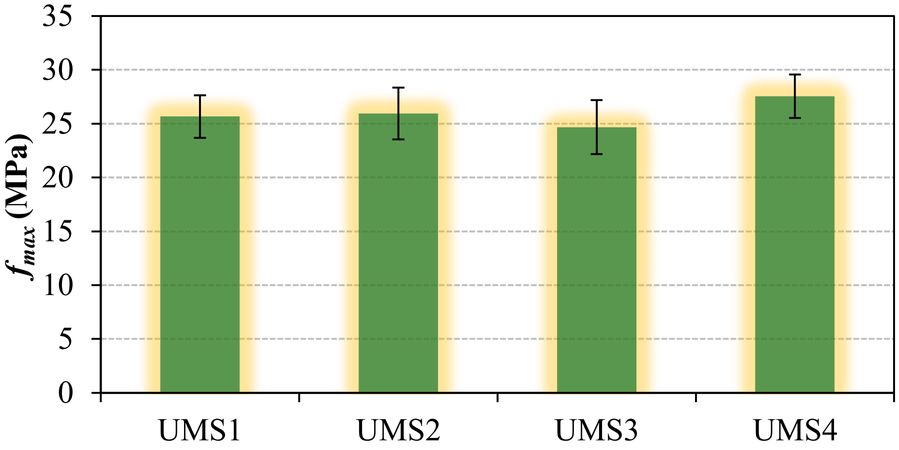

Figure 4.16 **Flexural strength for UMS.**

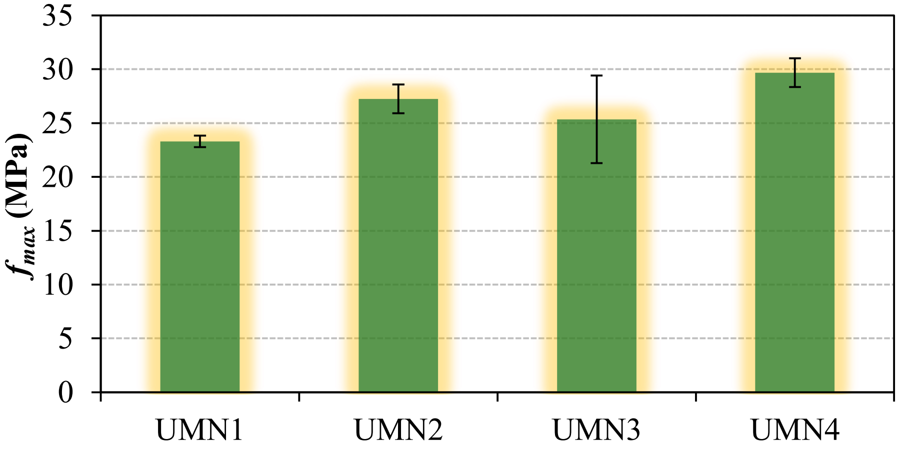

Figure 4.17 **Flexural strength for UMN.**

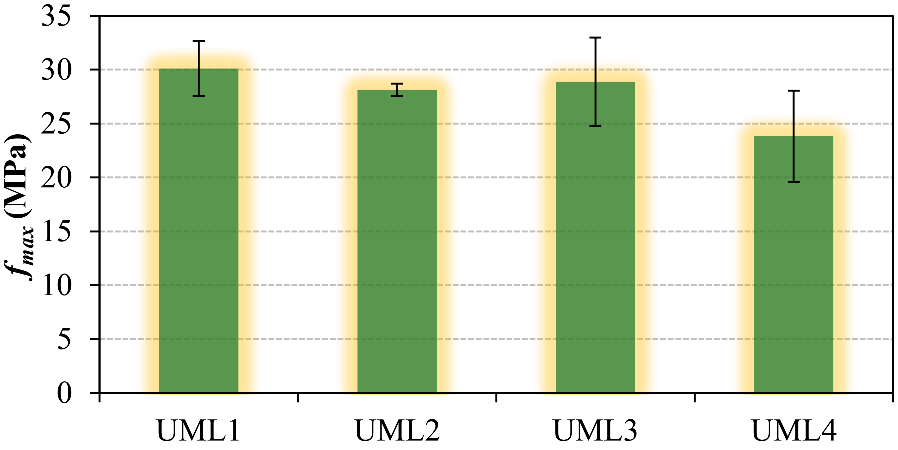

Figure 4.18 Flexural strength for UML.

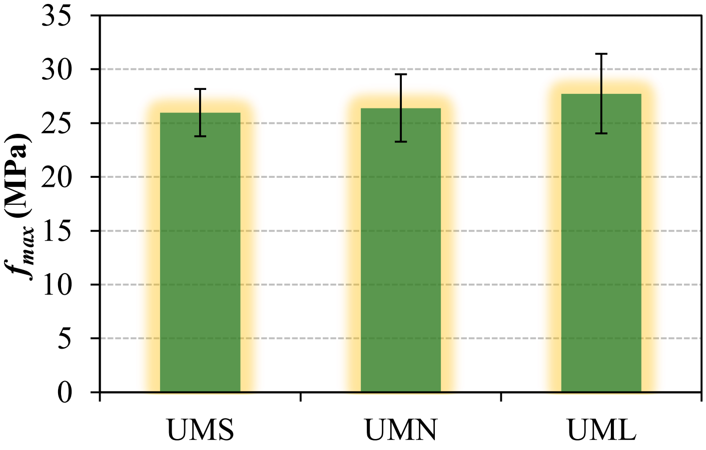

Figure 4.19 Flexural strengths of three UHPC mixtures of Group-I.

Figure 4.20 shows the comparison of cracking strength and flexural strength. Each data point represents an average of three values. The error bars, representing standard deviation indicates low scatter of the individual values that made up the average. In addition, Figure 4.21 depicts the relationship between cracking and flexural strengths for Group-I UHPC mixtures. It appears that there is slight dependency of the peak flexural stress on the matrix cracking strength. Further, Figure 4.21 indicates that the peak strengths varied between 1.3 to 2.0 times the cracking stresses. This variation may be attributed to the unreliable trend in the post-cracking scenario.

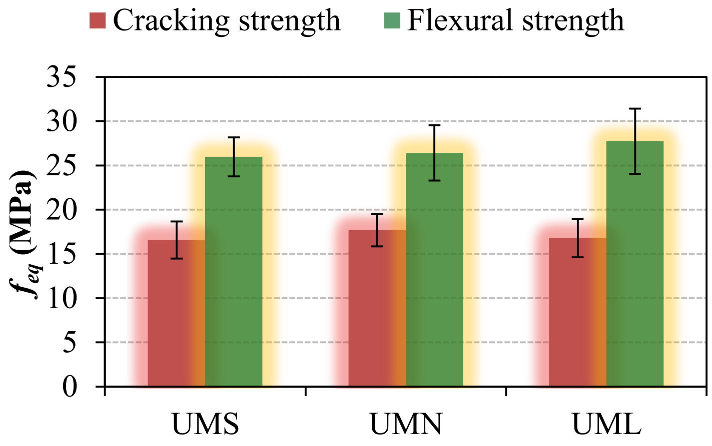

Figure 4.20 Comparison of cracking and flexural strength for all Group-I UHPC mixtures.

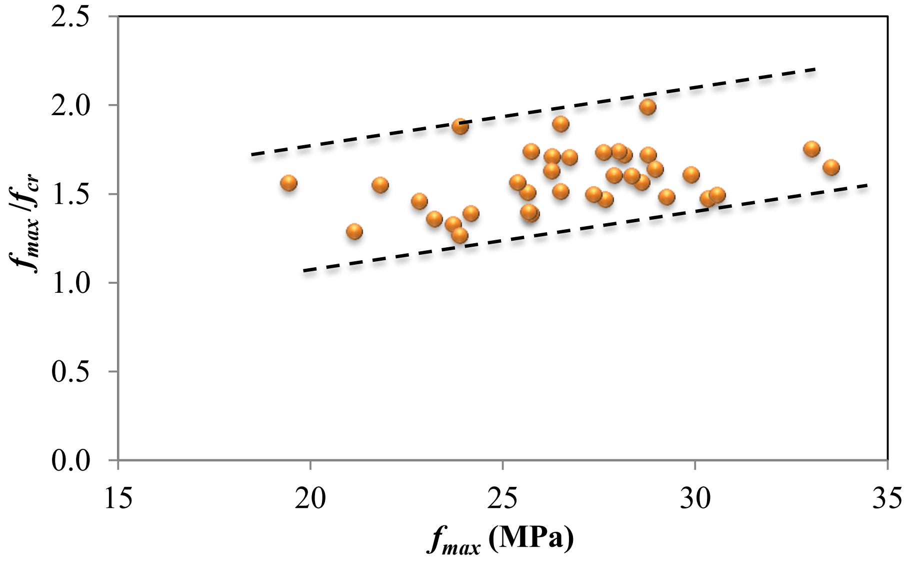

Figure 4.21 Cracking-flexural strength relationship for Group-I UHPC mixtures.

The cracking strength, or limit of proportionality in flexure (f_{cr}), is an overestimation of the actual matrix tensile strength (σ_t). This has been attributed to the so-called „scale effect‟ that results from the presence of the fibers in UHPC [6, 67]. Hence it is customary to correct the cracking strength by the CEB-FIP code formula [6], given as follows:

$$\sigma_t = f_{cr}\left[\frac{\beta\left(\frac{h}{100}\right)^{0.7}}{1+\beta\left(\frac{h}{100}\right)^{0.7}}\right] \tag{4.5}$$

Where, β is the „fiber efficiency‟ factor, while h (in mm) is the depth of the prism specimen. The factor β varies between 1 and 2 and increases with increasing matrix brittleness. In this study, an estimate of β = 1.5 was adopted. Therefore, given h = 70 mm, the correction factor for the tested prisms equals 0.539. Consequently, all the flexural tensile properties of the three UHPCs can be summarized as shown in Table 4.11.

Table 4.11 Summary of flexure tensile parameters for Group-I UHPC mixtures.

Mixture	f_{cr} (MPa)	SD	f_{max} (MPa)	SD	f_t (MPa)	SD
UMS	16.6	2.1	26.0	2.2	8.9	1.1
UMN	17.7	1.8	26.4	0.9	9.5	1.0
UML	16.8	2.1	27.7	1.1	9.0	1.2

4.3.4 Post-cracking constitutive law in 3-point flexure

This test was conducted on 70 mm × 70 mm × 280 mm UHPC prism specimens having 7.0 mm deep notches at the center point of bottom in a 3-point loading configuration on a flexure span of 210 mm. Like the un-notched flexural test, a crosshead displacement-controlled loading was employed. Full details of the test are provided in Section 3.3.2. Twelve prisms were also tested for each Group-I UHPC mixture, as shown in Table 3.4. Figure 4.22 shows the notched flexural prism specimens before testing. Figure 4.23 and Figure 4.24 also show the damaged notched flexural prism specimens after testing.

Figure 4.22 Notched flexural tensile (3-point) prism specimens before testing.

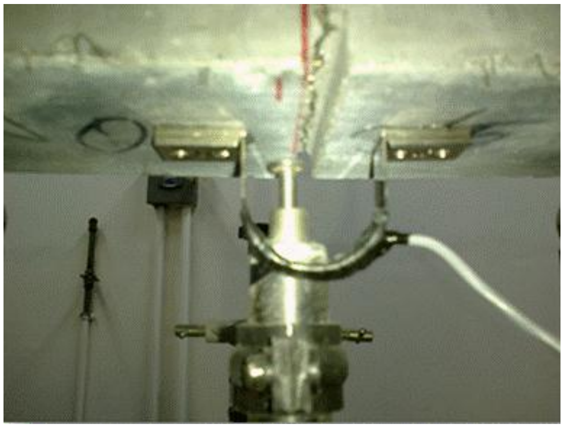

Figure 4.23 Notched flexural tensile (3-point) prism specimens during testing, showing CMOD installed across a notch.

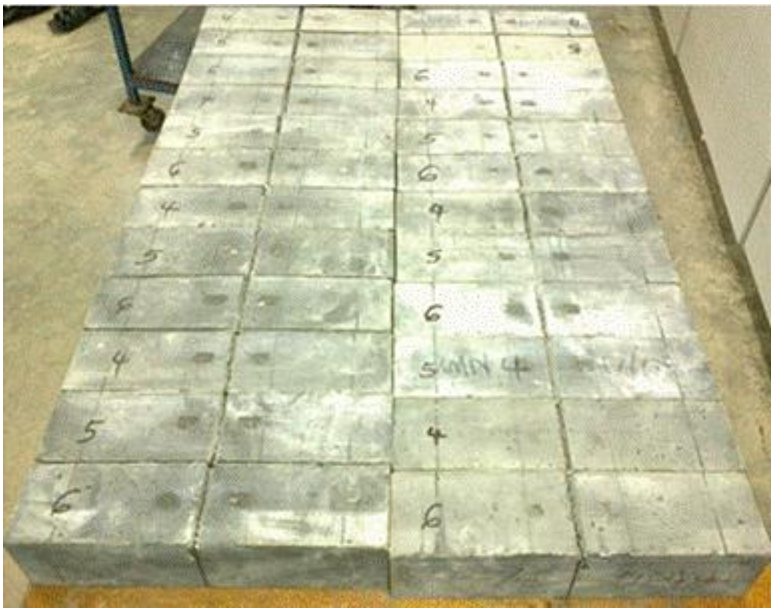

Figure 4.24 **Notched flexural tensile (3-point) prism specimens after testing, showing crack in notches.**

A typical documented post-cracking constitutive law (i.e., stress-crack width law) for a set of three prism specimens is shown in Figure 4.25, while Figure 4.26 shows the documented stress-deflection behavior for the same set of specimens. Efficient fiber activation is evident from the curves in Figure 4.25 and Figure 4.26. The equivalent flexural strength in this case was computed from the following relationship:

$$f_{eq} = \frac{3PL}{2b(h-d')^2} \tag{4.6}$$

Where,

L = flexure span, and

d' = notch depth

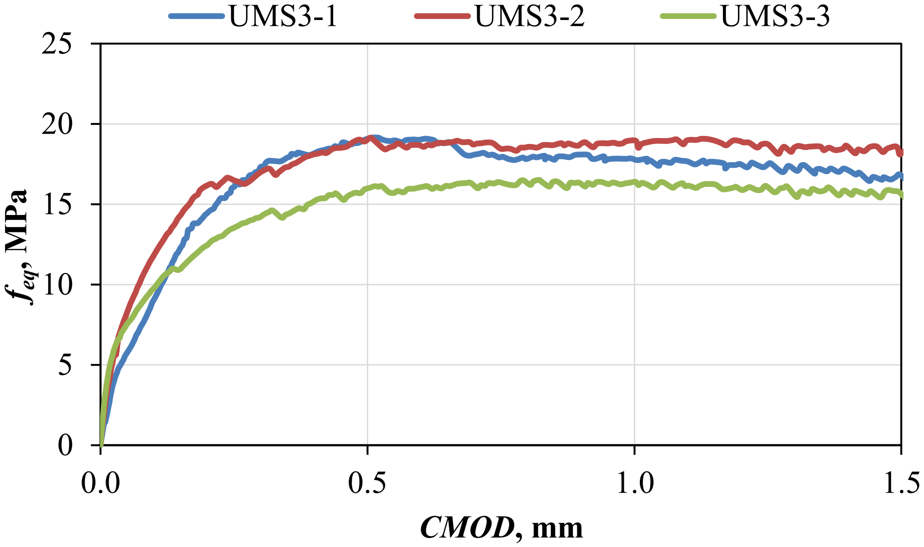

Figure 4.25 Typical documented stress-crack width behavior.

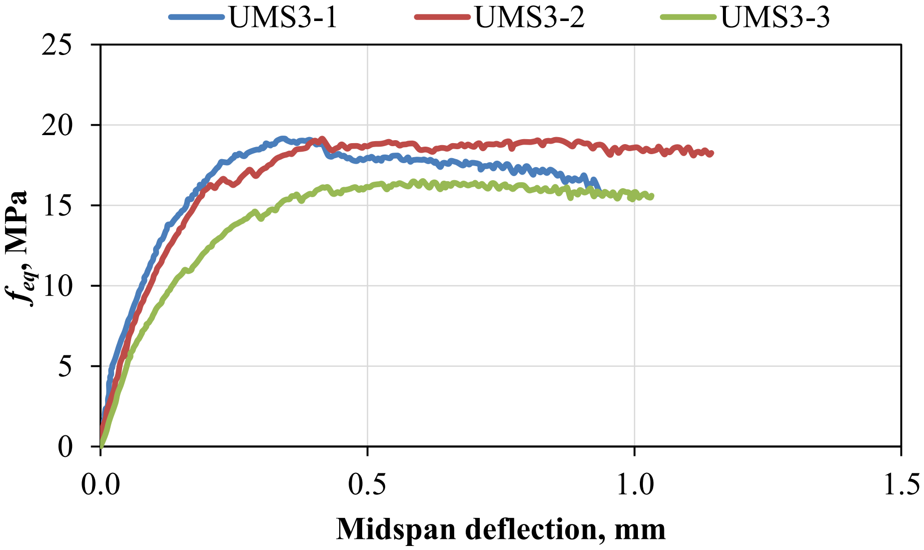

Figure 4.26 Typical documented stress-deflection behavior.

4.3.5 Cracking strengths

Figure 4.27 shows the initial portion of a typical stress-*CMOD* behavior of notched specimens of UHPC under flexure, highlighting the calculation of the cracking stress at the notch. Unlike the case of un-notched prisms, the cracking point is usually not well defined from the curve. Therefore, it is customary to fit the initial straight portion of the curve to a straight line. If the slope of this line is a_0, the intersection of the stress-*CMOD* curve with a line with slope $0.95a_0$ is taken as the cracking point. This is clearly illustrated in Figure 4.27. The stress at this point is the cracking stress, f_{cr}, while the corresponding *CMOD* defines the end of elastic crack mouth opening, at a critical value w_c. Subsequently, the recorded values of *CMOD* are dominated by actual growth of the crack width.

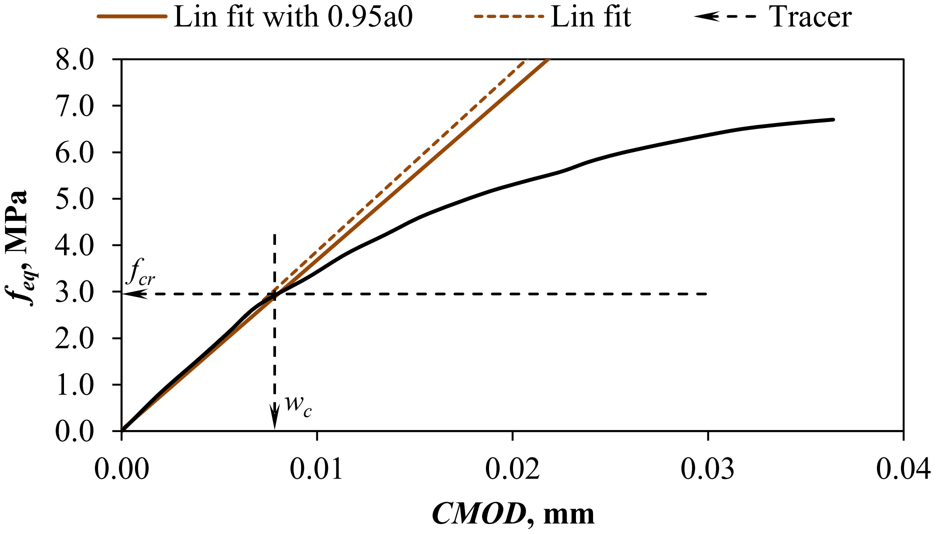

Figure 4.27 **Calculation of cracking stress and width for notched flexural specimens.**

Finally, the actual crack mouth opening, w_{cr}, can be obtained from

$$w_{cr} = CMOD - w_c \tag{4.7}$$

This origin shifting process results in stress–crack width (f_{eq} - w_{cr}) curve. Figure 4.28 shows the initial part of a typical f_{eq} - w_{cr} curve for Group-I UHPC mixtures. For the same specimen whose behavior is under consideration, the full f_{eq} - w_{cr} curve is depicted in Figure 4.29, showing the fiber activation and fiber pullout phases, in addition to fiber activation steps.

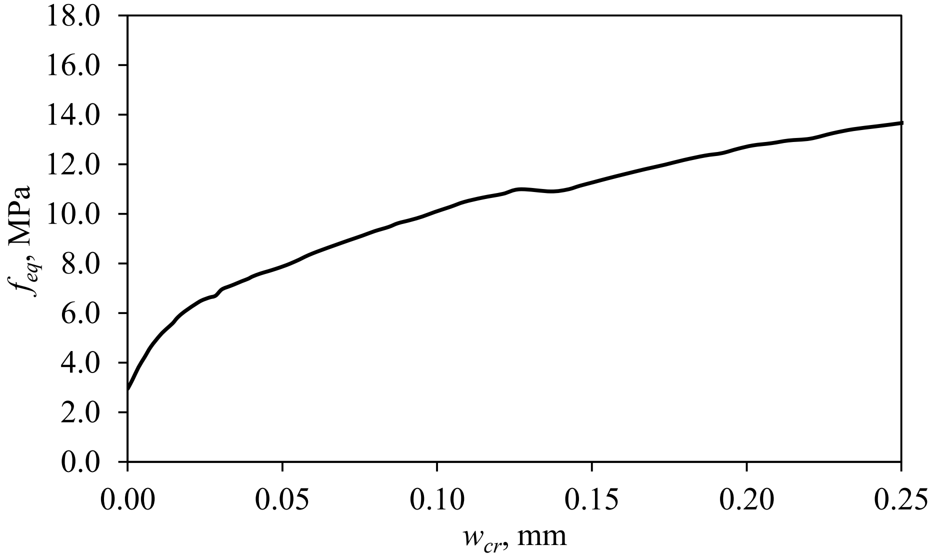

Figure 4.28 **Resultant stress-crack width behavior after 'origin shift'.**

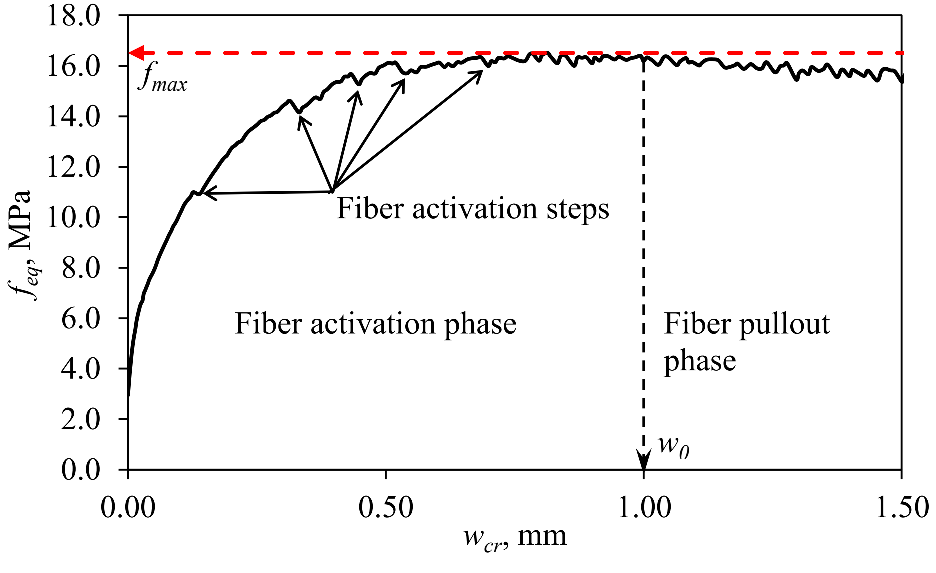

Figure 4.29 Full stress-crack width behavior showing fiber activation-pullout response.

The results of the cracking strengths of notched flexural prisms are shown in Figure 4.30, Figure 4.31, Figure 4.32, and Figure 4.33. Each data point represents an average of three values. The error bar, representing the standard deviation of each data point indicates very large spreads, unlike in the case of un-notched prisms. This may be due to possible variations in the profile of notch tips from one specimen to another. Additionally, the cracking stresses here are much lower as compared to those obtained for un-notched prisms.

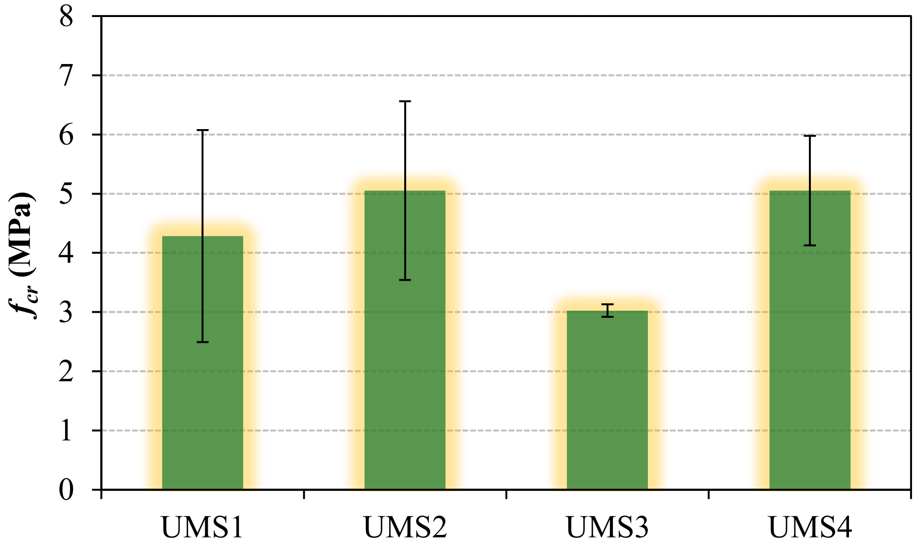

Figure 4.30 **Cracking strength of UMS notched flexural prisms.**

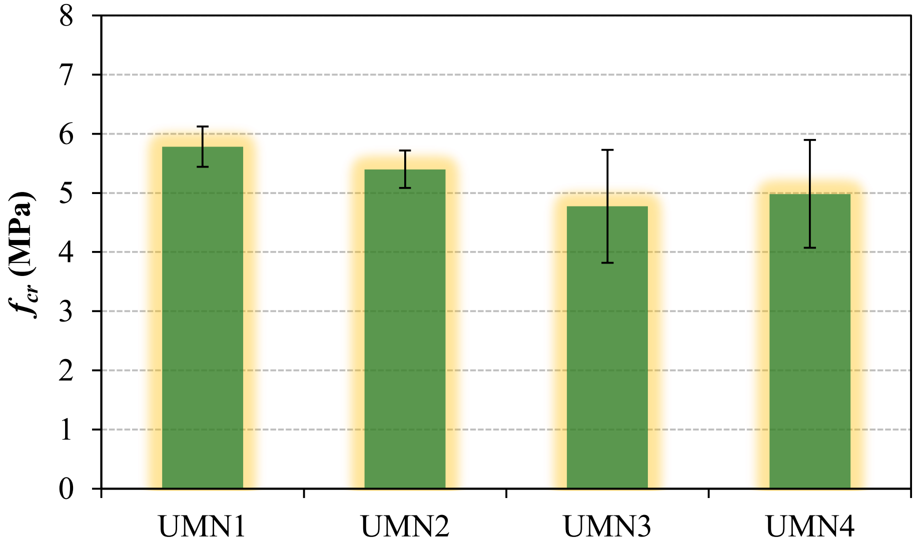

Figure 4.31 **Cracking strength of UMN notched flexural prisms.**

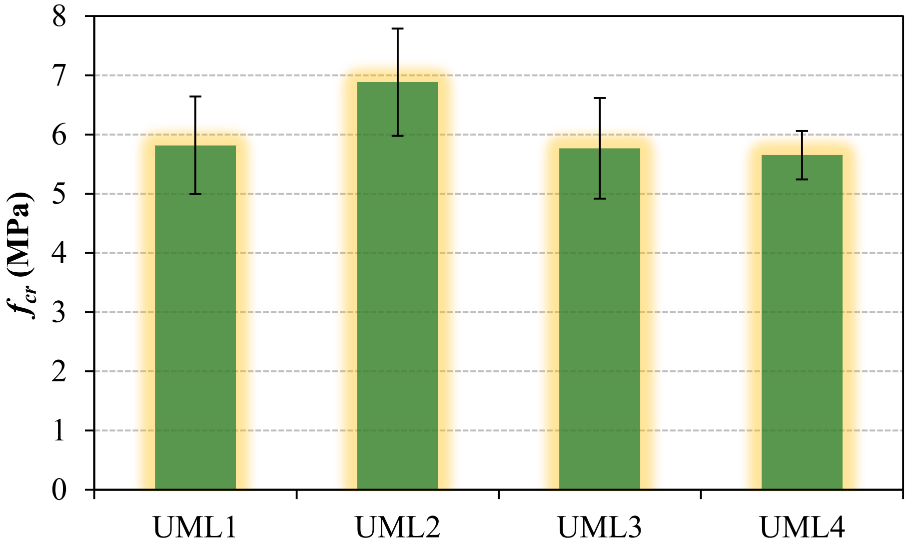

Figure 4.32 **Cracking strength of UML notched flexural prisms.**

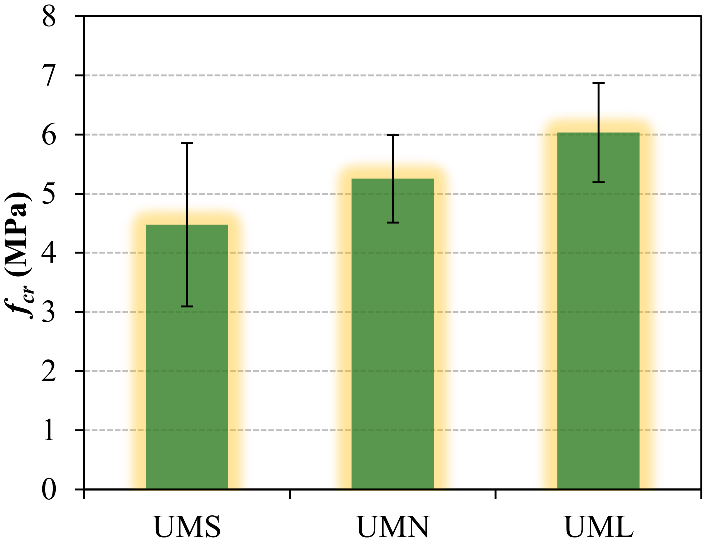

Figure 4.33 **Cracking strength of notched flexural prisms for all Group-I UHPC mixtures.**

4.3.6 Peak Flexural strengths

The results of the equivalent peak flexural strengths of notched prisms are shown in Figure 4.34, Figure 4.35, Figure 4.36, Figure 4.37, and Figure 4.38. Each data point represents an average of three values. Like the case of cracking stress, there are very large variations in the results of peak flexural strengths of the notched specimens. Figure 4.38 compares the cracking and peak flexural strengths of notched prisms for Group-I UHPC mixtures. Additionally, Figure 4.39 depicts the relationship between the peak stress and the cracking stress for notched prisms. Based on the information in Figure 4.39, peak flexural stresses ranged between about 4 to 8 times the cracking strength, while specimens with higher cracking strengths tend to have lower peak strengths.

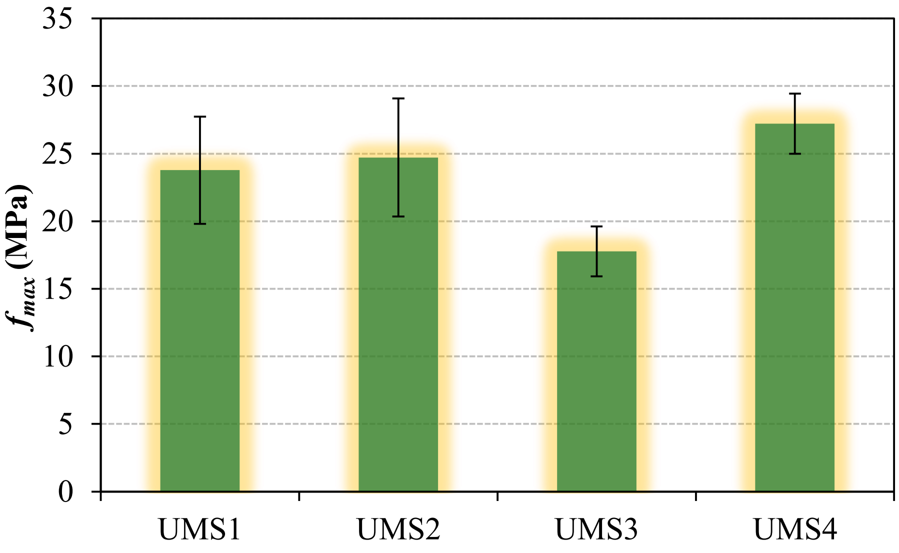

Figure 4.34 **Peak strength of UMS notched flexural prisms.**

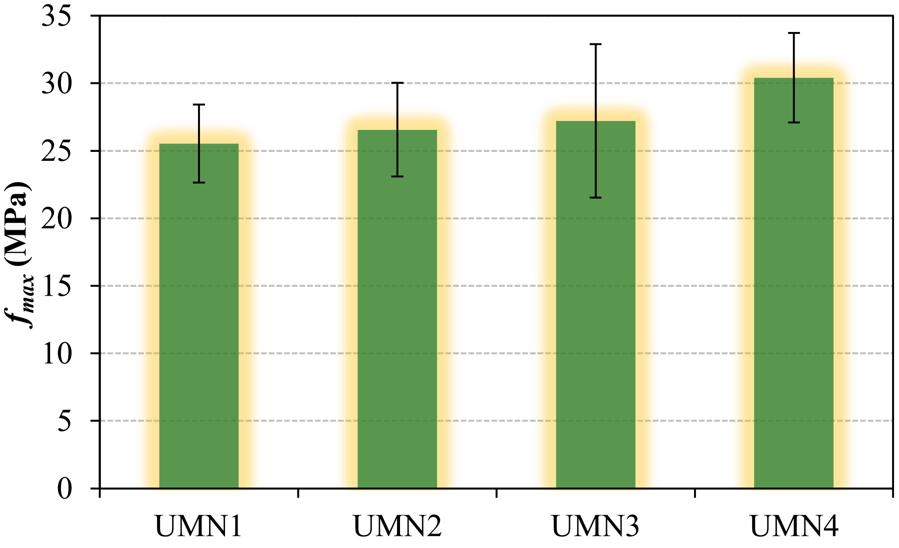

Figure 4.35 Peak strength of UMN notched flexural prisms.

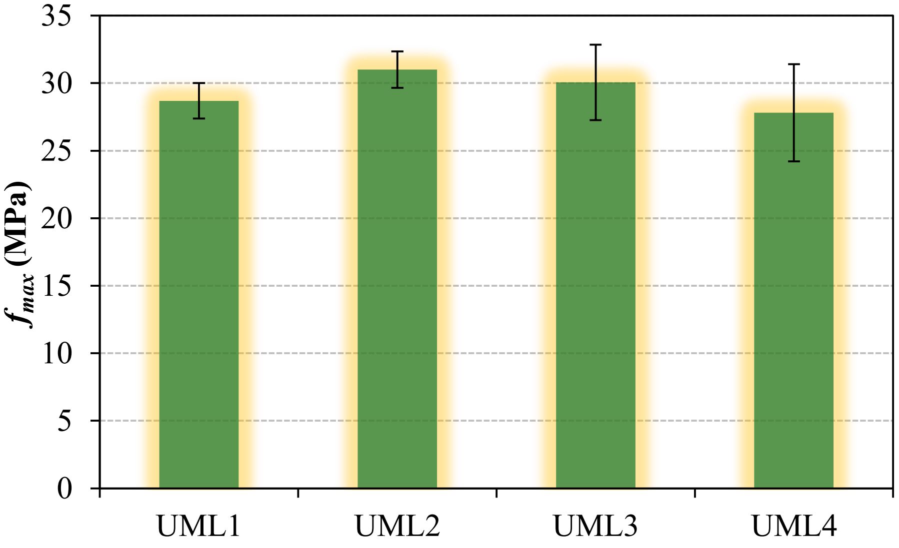

Figure 4.36 Peak strength of UML notched flexural prisms.

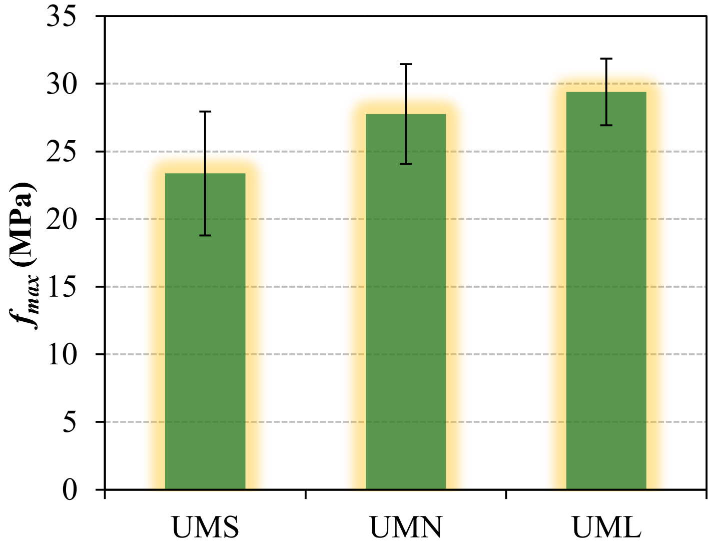

Figure 4.37 Peak strength of notched flexural prisms for all Group-I UHPC mixtures.

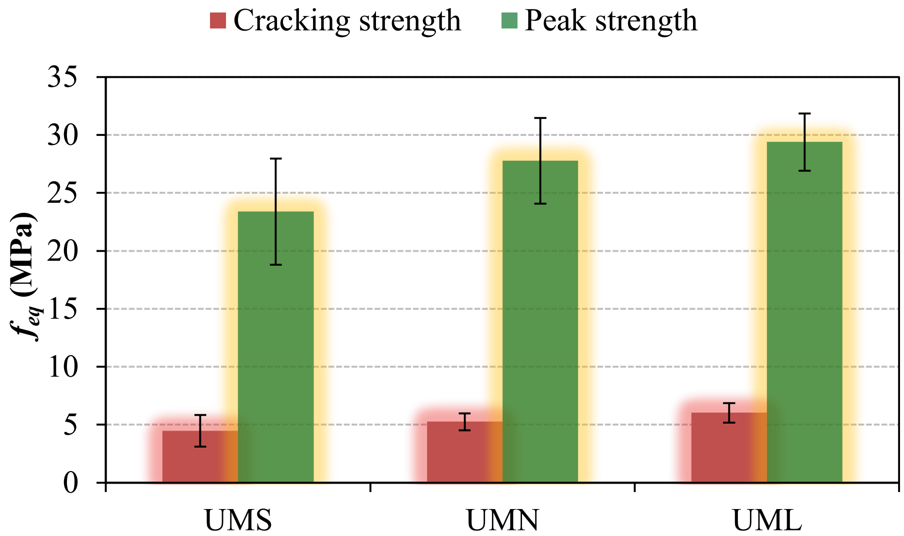

Figure 4.38 Comparison of cracking and peak flexural strength of notched for Group-I UHPC mixtures.

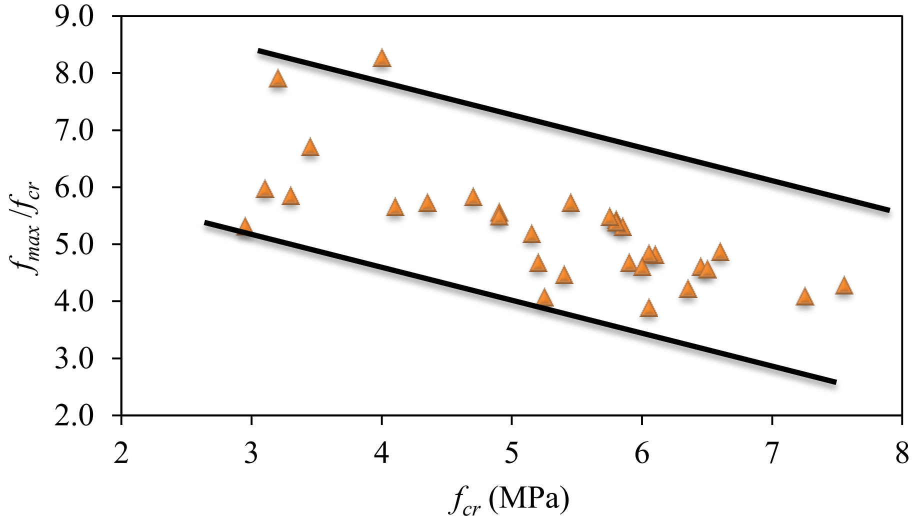

Figure 4.39 **Cracking-peak flexural strength relationship of notched prisms for Group-I UHPC mixtures.**

4.4 Characteristic stress-strain behavior in direct tension

Mechanical characterization tests for stress-strain behavior in direct tension were conducted on dogbones having cross section dimensions 40 × 40 mm using a gauge length of 100 mm. Figure 4.40 shows the instrumentation scheme for stress-strain behavior test in direct tension. Full details of the test are provided in Section 3.3.2. Figure 4.41 shows a typical documented load-displacement behavior. Using the cross-section size and gauge length, the stress-strain behavior was obtained, as shown in Figure 4.42.

It should be noted that the material exhibited a very good ductile behavior, in which about 95 % of the peak stress was sustained up to a strain level of 8,000 με, which is more than the yield strain of the high strength steel bar utilized in the present study to reinforce the UHPC beams. Additionally, it is worth noting that the strain recorded beyond the cracking strain of about 400 με is essentially a composite crack-bridging-based strain, which includes widening of several micro-cracks within the gauge length. The behaviors of most specimens tested in direct tension are quite similar to the typical behavior shown in Figure 4.42. The average value of direct tensile strength was 8.2 MPa.

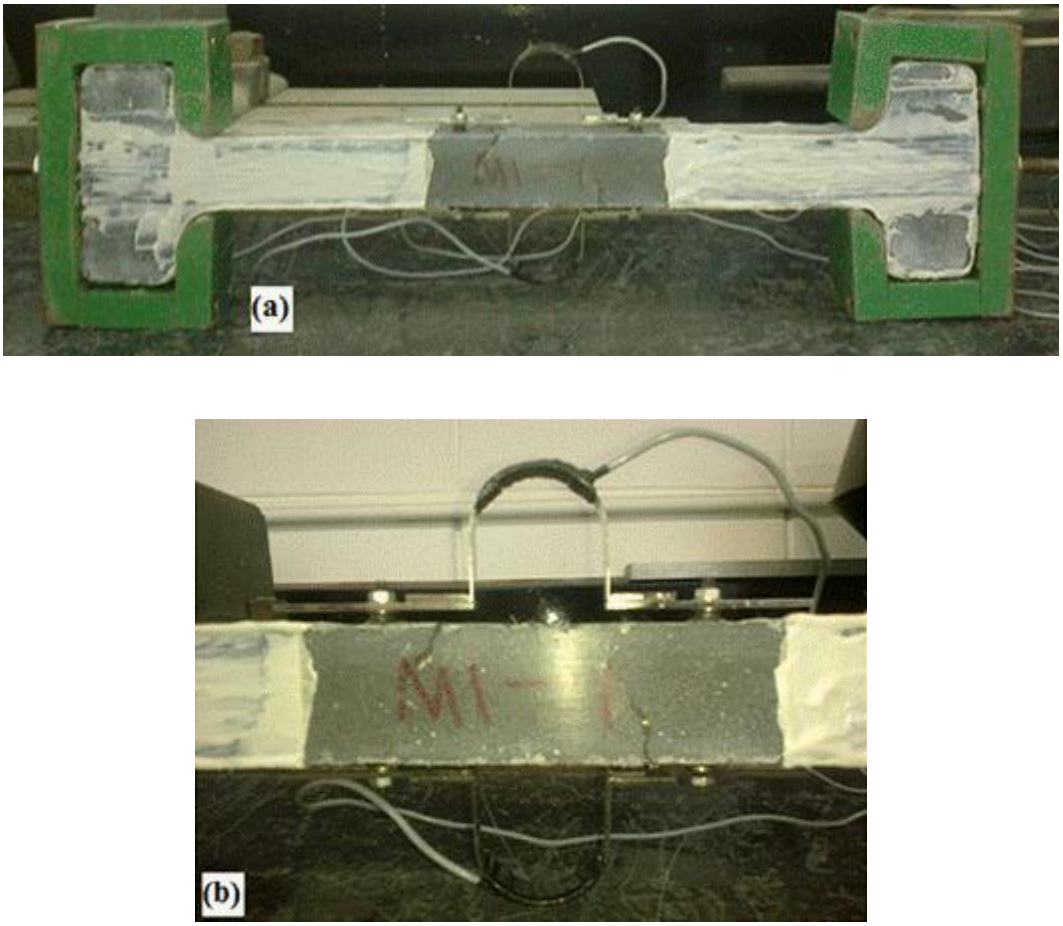

Figure 4.40 Instrumentation configuration for the stress-strain behavior in direct tension (un-notched): (a) dogbone with a pair of gripping adaptor; (b) close-up view of the gauged area.

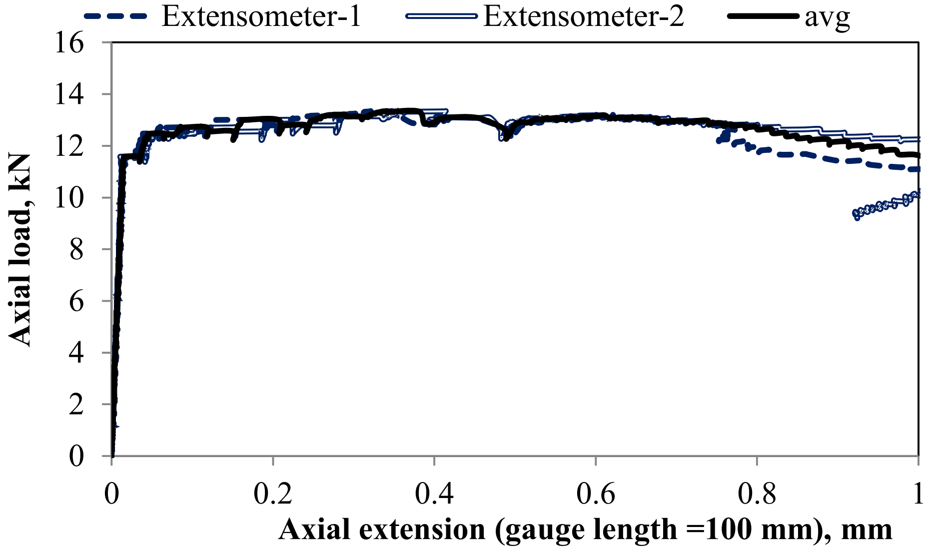

Figure 4.41 **Typical recorded load-deformation response of dogbones.**

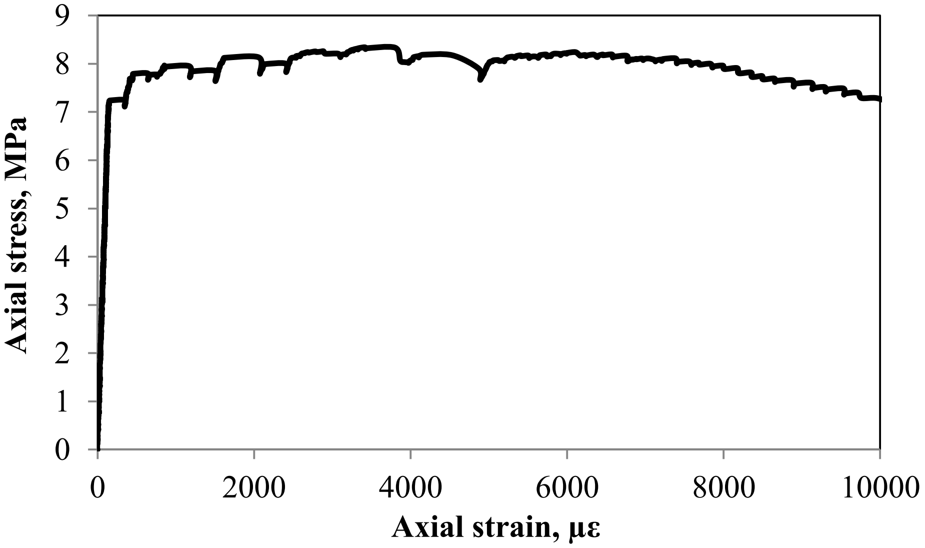

Figure 4.42 **Typical documented stress-strain behavior of UHPC dogbones.**

4.5 Stress-crack width behavior in direct tension

Similar to the mechanical characterization tests for stress-strain behavior in direct tension, the stress-crack width tests were conducted on dogbone specimens having cross sectional dimensions of 40 × 40 mm, but with notches of 4 mm depth at the center of the prismatic portion of the dogbone. In addition, an extensometer with a gauge length of 50 mm was installed across the notches. Figure 4.43 shows typical documented stress–extension (*σ*–*δ*) responses of a set of notched dogbone specimens.

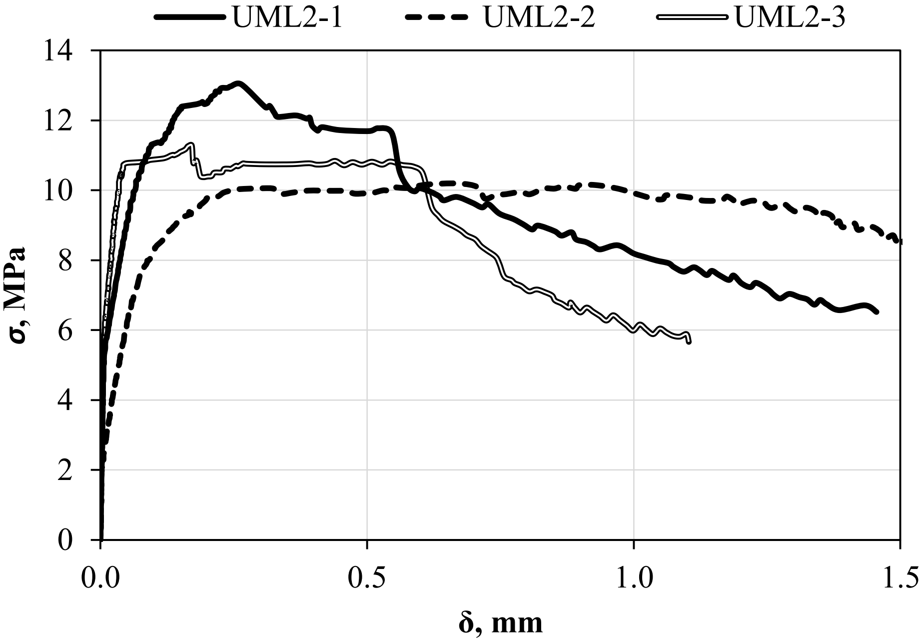

Figure 4.43 **Typical documented load-extension responses of notched dogbone specimens.**

Due to the reduced cross-section area (which in turn leads to reduced stiffness) at the notch section, notch extension dominates the recorded extension, δ, by the *CMOD* transducer installed across the notch. Further, the ultimate objective of this test is to develop stress–crack width (σ-w_{cr}) constitutive relations for the respective UHPC mixture. Therefore, the aim of the test can be achieved in the same way as done for the notched flexural test (Section 4.3.4), which involves an origin shifting process for converting σ-δ curve to σ-w_{cr} curve. Consequently, the calculation procedure for obtaining the cracking stress (σ_{cr}) and corresponding notch opening displacement (w_c) is depicted in Figure 4.44 for notched UHPC specimens in direct tension. The initial part of the σ-δ curve shown in Figure 4.44 indicates a well-defined cracking point, unlike the case of notched flexural test (Figure 4.27).

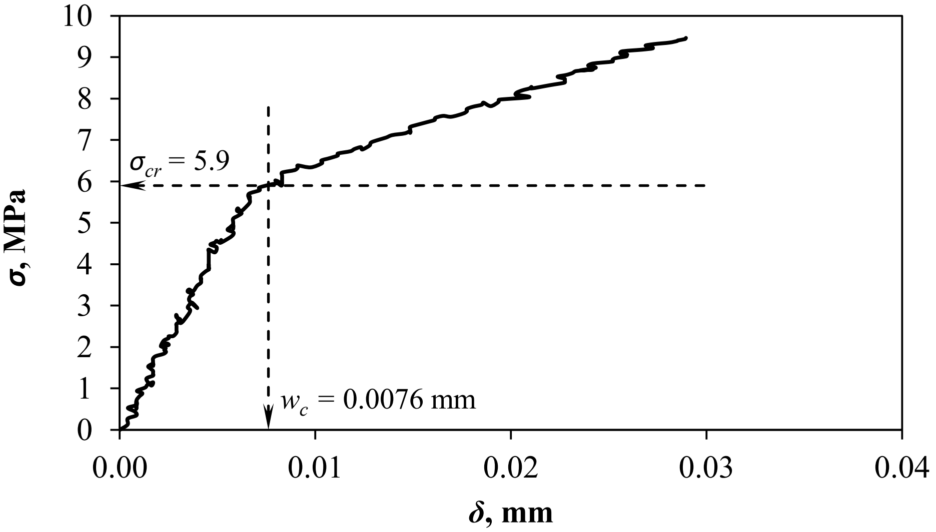

Figure 4.44 **Calculation of cracking stress and corresponding extension for notched dogbones specimens.**

Figure 4.45 shows the initial part of the resulting σ-w_{cr} curve for the specimen under consideration after the origin shift process. It can be seen clearly in Figure 4.45 that the specimen exhibited an excellent post-crack fiber activation behavior, resulting in sufficient hardening and subsequent crack widening while the peak stress was still sustained in the crack grown process. The complete σ-w_{cr} behavior of a set of specimens for one UHPC mixture (UML) is shown in Figure 4.46. The behavior shown in Figure 4.46 indicates that fiber pullout started from a crack width of 0.6 mm, which is way beyond the 0.1 mm maximum crack width permitted by the French code at ULS.

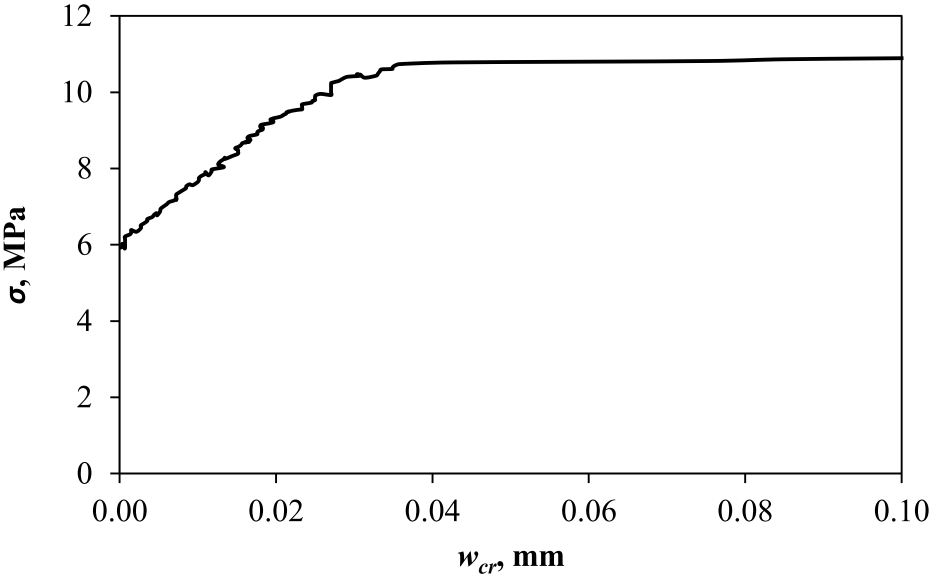

Figure 4.45 **Resultant stress-crack width behavior after 'origin shift'.**

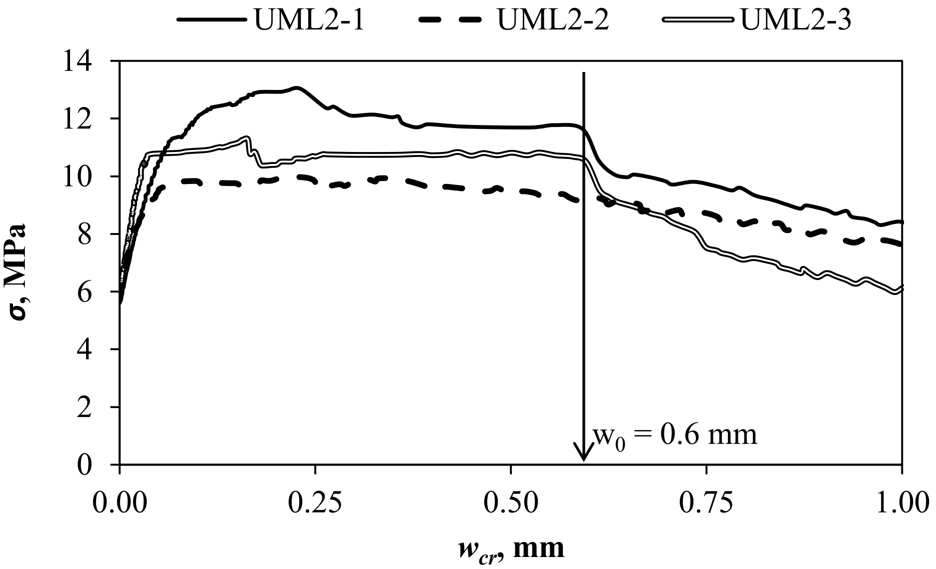

Figure 4.46 Stress-crack width behavior of UML dogbone specimens.

CHAPTER 5

RESULTS AND DISCUSSION-PART II

(FLEXURAL BEHAVIOR OF REINFORCED UHPC BEAMS)

As described earlier in Section 3.4.2, passively reinforced UHPC beam specimens were fabricated using two UHPC mixtures (UMS and UMSN), tested and evaluated for their flexural responses. This chapter presents the results of the experimental work conducted for studying the flexural response of passively reinforced UHPC beams. The test results are discussed within the framework of the technical and practical application of UHPC beams.

5.1 Post-Casting thermal characteristic

Both the reference UHPC (UMS) and the low-cement version (UMSN) mixtures used in the fabrication of UHPC beams were evaluated for evolution of heat of hydration utilizing beam with a depth of 300 mm. The temperature of the hydrating concrete in plywood mold was measured at the mid-length section of the beam at three points: bottom, side and core. Figure 5.1 and Figure 5.2 show the temperature-time curve for UMS and UMSN beams, respectively, measured over the first 48 hours of casting. In both mixtures, bottom of the section had the least temperature at all times, while the highest temperature was recorded at the core of the section monitored. The core temperature is expected to be the highest for obvious reason of the core being the farthest point from the beam faces, which exchange heat at faster rates with the much cooler ambient. However, the observed low temperature of the bottom face indicates that the metallic casting table with which it is in contact enhances cooling more than the side face of the wooden form, which experienced air-cooling. The peak temperature recorded for UMS and UMSN beams were 56.1 and 50.5 °C, while the corresponding temperature difference between the core and the bottom were 4.5 and 3 °C, respectively.

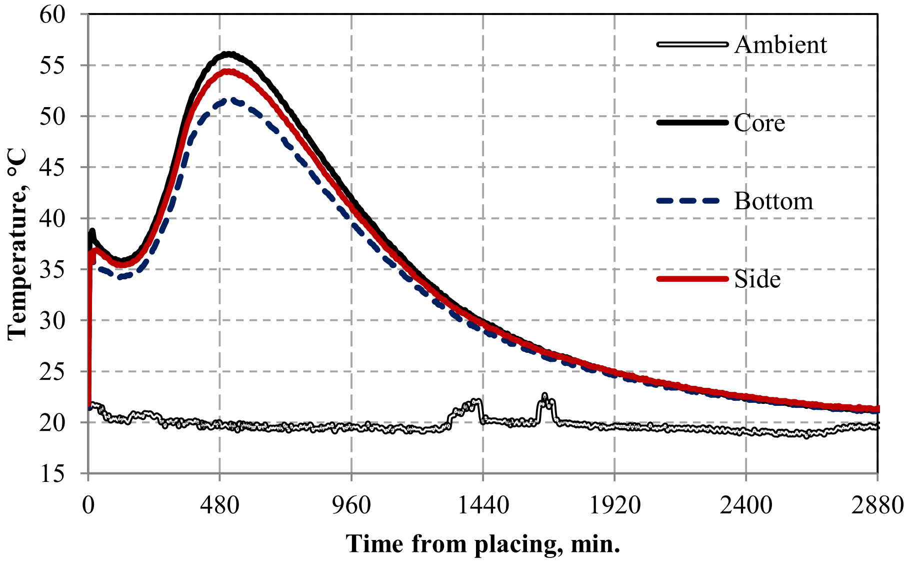

Figure 5.1 **Temperature-time curve of the beam made with control UHPC mixture (UMS).**

(Average Ambient temperature = 20°C)

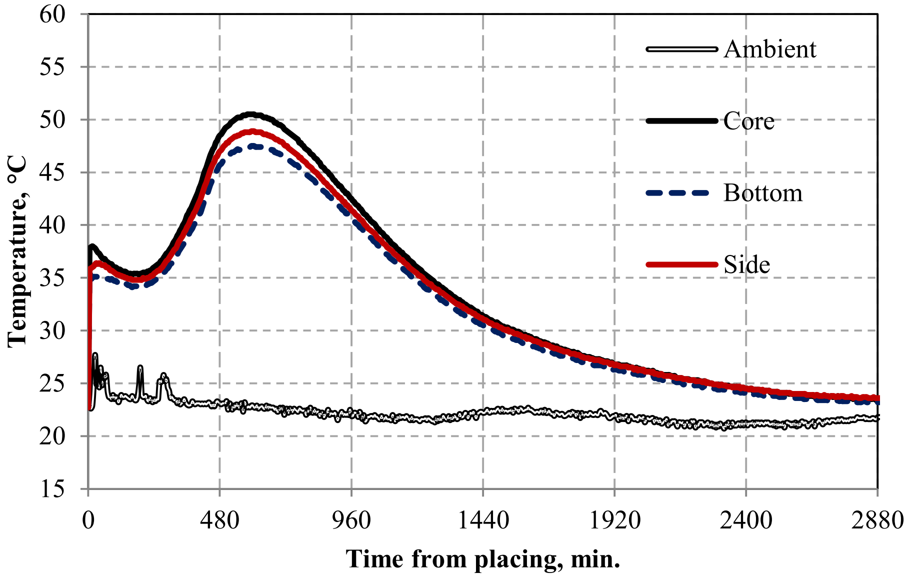

Figure 5.2 **Temperature-time curve of the beam made with low-cement UHPC mixture (UMSN).**

Avg. Ambient temperature = 22°C

The implication of the temperature differences between the beam core and its bottom face is the expected development of tensile stresses on the bottom faces of the beams. The induced tensile stresses by the temperature differential can be quantified if thermal and mechanical properties of the UHPC mixtures are available at the age range when the differences are significant (i.e., from six to ten hours of casting). In the absence of such data, it can still be semi-quantitatively concluded that UMS beam will experience about 50 % higher tensile stresses at the bottom because of the higher temperature difference, as compared to UMSN. Consequently, the cracking tendency (or matrix damage) will be higher in UMS than in UMSN if the value of induced tensile stresses is higher than the instantaneous matrix tensile strength. In cases of occurrence of such damages, regardless of the presence of fibers, load induced cracks will appear at lower loads than expected from undamaged matrix. Further, since the bottom faces of the beams, which will be in tension in the course of loading as simply supported members, are more prone to early tensile damages, it can be recommended to avoid casting the beams on surfaces that may enhance faster cooling of the bottom faces. Additionally, it can be concluded that UHPC beams made of UMSN are likely to possess slightly higher load capacities than ones made of UMS, since flexure and shear capacities depends on UHPC matrix strength.

Figure 5.3 shows the comparison of core temperature profiles for the two mixtures in the first six hours of casting. It can be seen in

Figure 5.3 that the two mixtures had the same initial post-mixing temperature. Following placement in the molds for beam specimens, the mixtures started to cool down under the influence of the much cooler ambient, then the temperature started elevating due to initiation of heat evolution process after about two hours of placing the fresh UHPC in the mold. However, UMS released heat of hydration at higher rate than UMSN, as expected from the higher cement content in the former (900 kg/m^3) than in the latter (630 kg/m^3).

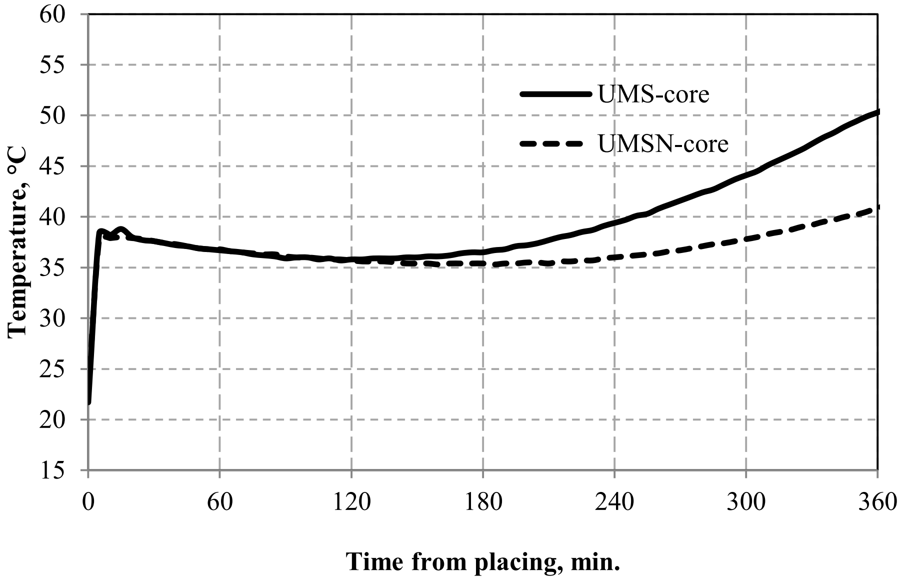

Figure 5.3 **Comparison of core temperature profiles for the first 6 hours for UMS and UMSN.**

The core temperature profiles for the two mixtures up to 48 hours of casting are shown in Figure 5.4. Even though UMS heat evolution was faster initially, the total area under the temperature-time curve, obtained by numerical integration, was found to be approximately the same in both mixtures, even though UMSN had 30 % less cement than UMS. This indicates that at a very high amount of cement (e.g., above 500 kg/m^3) and very low water/cement (e.g., below 0.25), most of the part of the added cement remains un-hydrated.

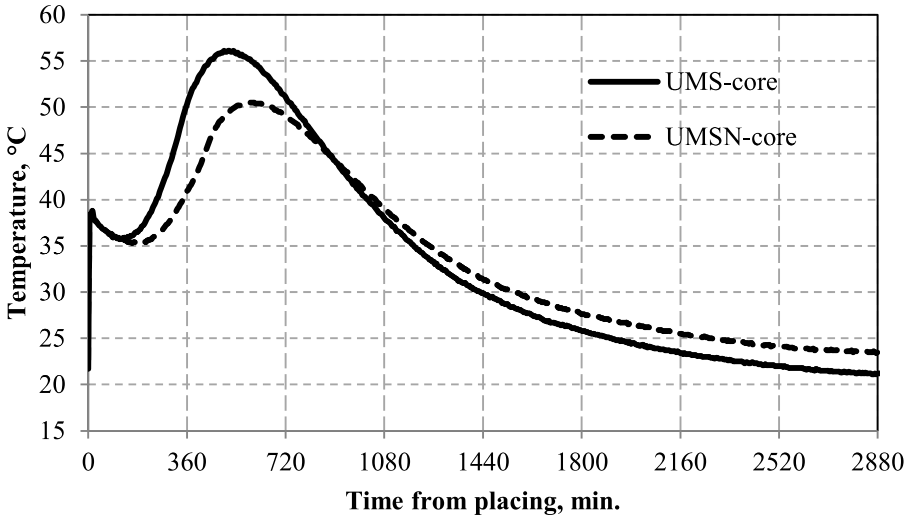

Figure 5.4 **Comparison of core full temperature profiles for UMS and UMSN.**

5.2 Mechanical Properties of UHPC mixtures Used in Beams

As stated earlier, small specimens were cast along with the casting of each beam for mechanical characterization and quality control of the UHPC mixtures used. Table 5.1 presents the description of notations used in the presentation of quality control test results. The results obtained from the quality control specimens are presented in Figure 5.5 through Figure 5.9. Each data point is an average of all specimens tested for each beam series for a particular UHPC mixture. Additionally, the error bars on each data point represent standard deviations.

Table 5.1 **Description of notations used in the presentation of quality control test results.**

Series/mixes	Description
UMS	Average result of mechanical characterization test as reference for UMS results obtained from quality control test
SB-UMS	Average of all UMS specimens cast from same batch as SB-Series beams
DB-UMS	Average of all UMS specimens cast from same batch as DB-Series beams
SB-UMSN	Average of all UMSN specimens cast from same batch as SB-Series beams
DB-UMSN	Average of all UMSN specimens cast from same batch as DB-Series beams

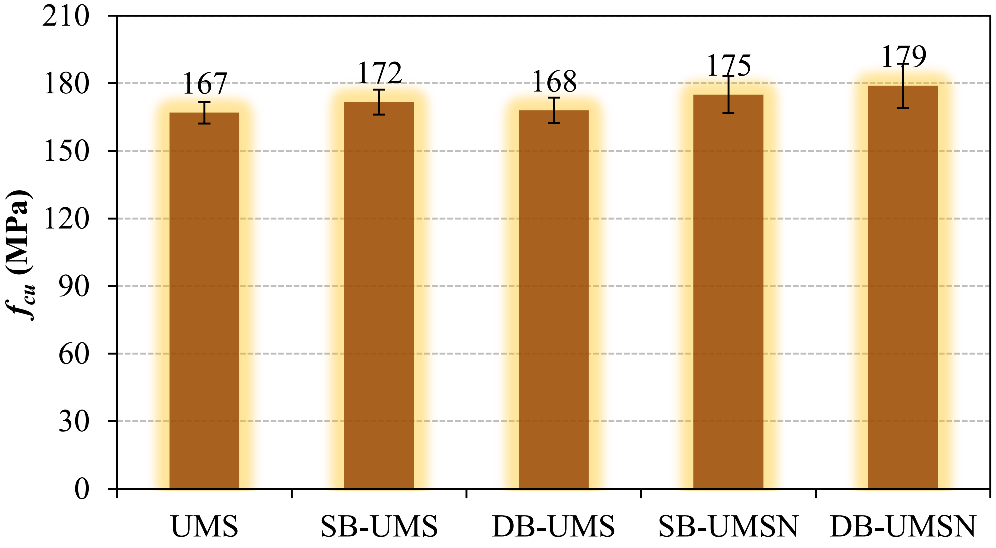

Figure 5.5 **Cube compressive strength.**

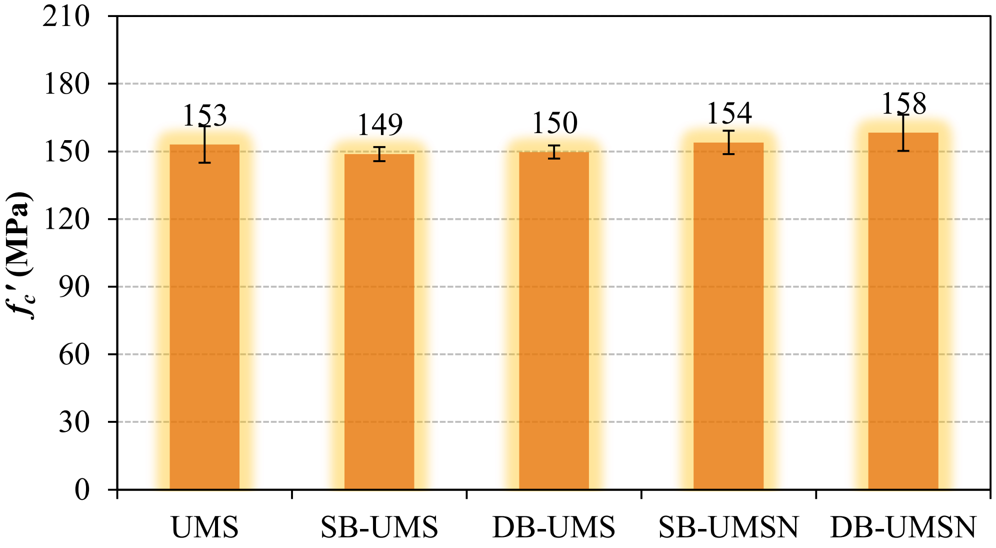

Figure 5.6 **Cylinder compressive strength.**

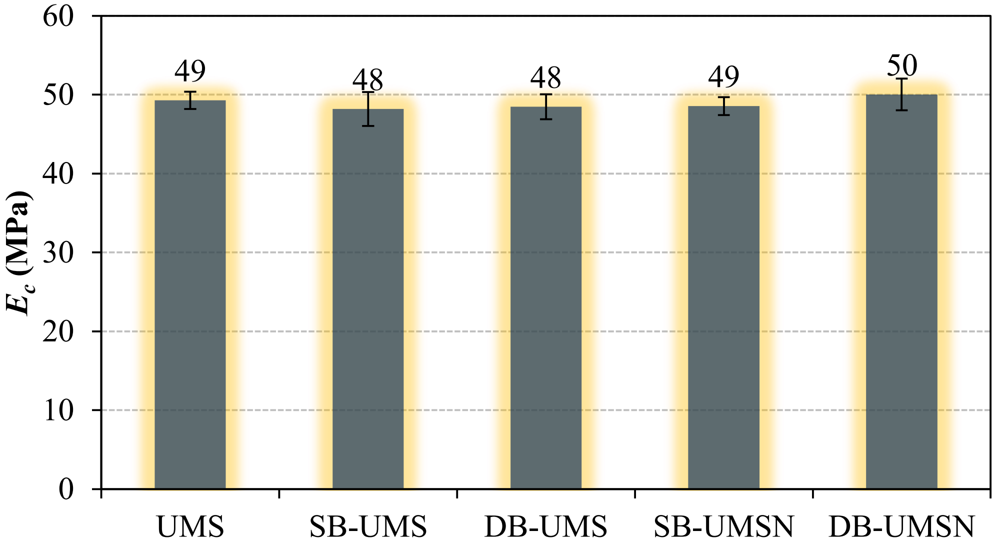

Figure 5.7 **Modulus of elasticity.**

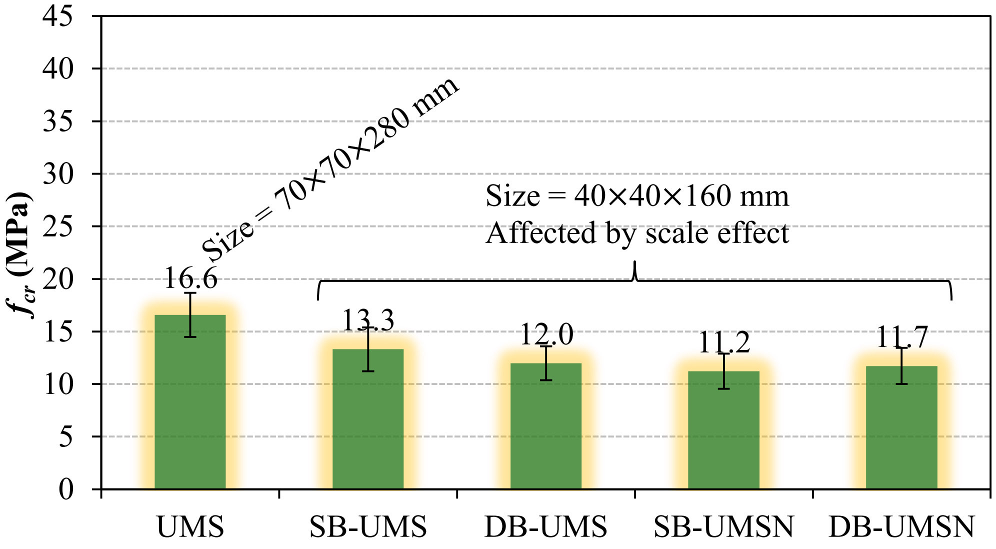

Figure 5.8 Flexural cracking strength.

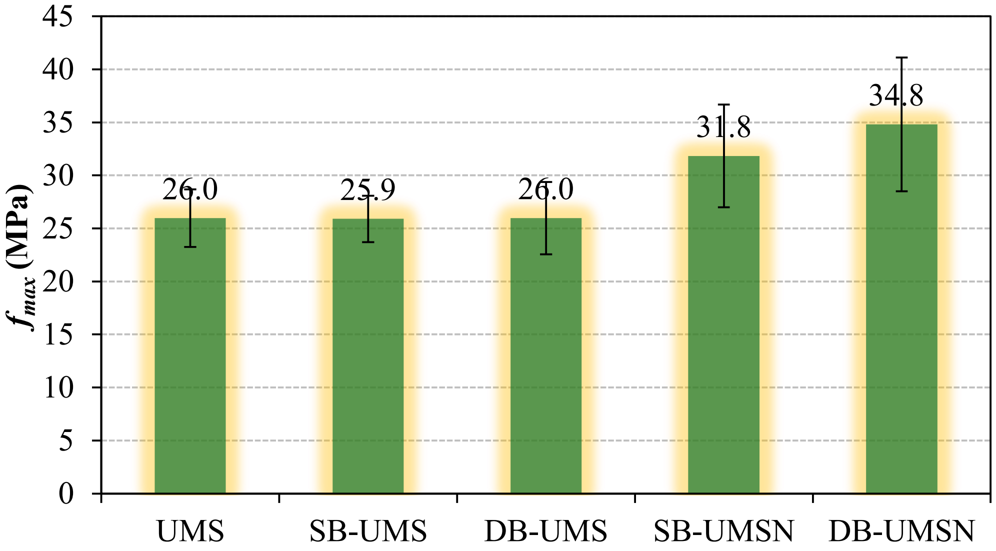

Figure 5.9 Equivalent flexural strength (peak flexural strength).

From the results presented in Figure 5.5 through Figure 5.9, it can be noted that for UMS, the results of quality control tests were similar to those obtained from the mechanical characterization tests. The only exception is the flexural cracking strength, which was underestimated in quality control tests due to size effect, as shown in Figure 5.8. However, there are some levels of discrepancy between the average properties of UMS and UMSN. These differences are presented in Figure 5.10. The values shown on the vertical axis in Figure 5.10 represents the ratio of the amount with which the respective property of UMSN is larger than that of UMS, expressed as percentages. It can be observed in Figure 5.10 that differences in both f_{cu} and f_c' are insignificant in terms of their possible effect on the flexural capacities of reinforced beams made from the two UHPC mixtures. Further, the recorded difference in the value of f_{cr} has no effect on the flexural capacity of the beams, since it may only affect the first cracking load of the beam, which is not well defined, as discussed later in Section 5.3.1. However, it is possible that the large difference between the two mixtures in terms f_{max} may affect the flexural capacities of beams made with these mixtures. The reason is that f_{max} governs the ability of the concrete for stress redistribution in the course of load bearing, which may affect the ultimate failure behavior as well as ultimate load. It may be noted that there is no significant difference between the values of modulus of elasticity of the two mixtures.

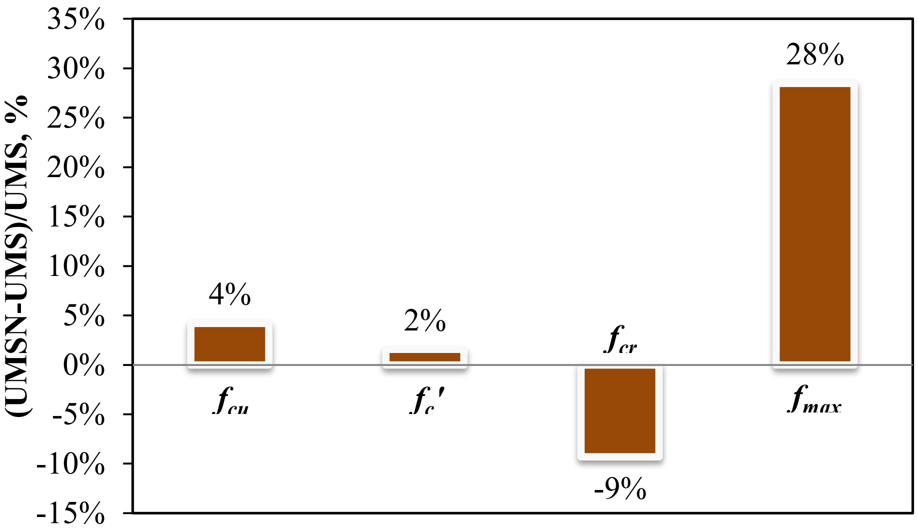

Figure 5.10 **Percent of differences between UMSN and UMS mechanical properties.**

(f_{cu} = cube compressive strength, f_c' = cylinder compressive strength, f_{cr} = flexural cracking strength, and f_{max} = peak equivalent flexural strength)

5.3 Flexural response of the beams

The flexural responses of the beams were evaluated in terms of load-deflection response, failure behavior, and evolution of load-induced damage.

5.3.1 Theoretical ‘first-crack’ load

Based on elementary mechanics of materials, the theoretical first cracking load P_{cr} can be computed using the Equation 5.1 in terms of the matrix cracking stress (σ_{cr}), gross moment of inertia of the cross section about the centroidal axis (I_g), shear span (a), and the centroid of the section measured from the bottom face (y_t):

$$P_{cr} = \frac{2\sigma_{cr} I_g}{a y_t} \tag{5.1}$$

Taking a σ_{cr} of 8 MPa (about the average value obtained from the direct tension tests), and ignoring the contribution of the steel bars to the bending stiffness, the calculated approximate values of the cracking loads are 32.4 kN and 57.6 kN, respectively for SB- and DB-Series beams. However, appreciable differences are noted considering UHPC composite sections in which the contributions of the steel bars are included in the calculation of bending stiffness. Figure 5.11 shows the theoretical P_{cr} for the SB- and DB-series beams. The value on the bar for each beam specimen represents the error of underestimation in the respective case. It can be concluded from Figure 5.11 that the error resulting from ignoring the steel contribution to the bending stiffness ranges from 12 % to 19 %. Hence, the composite values are used as reference in subsequent discussions.

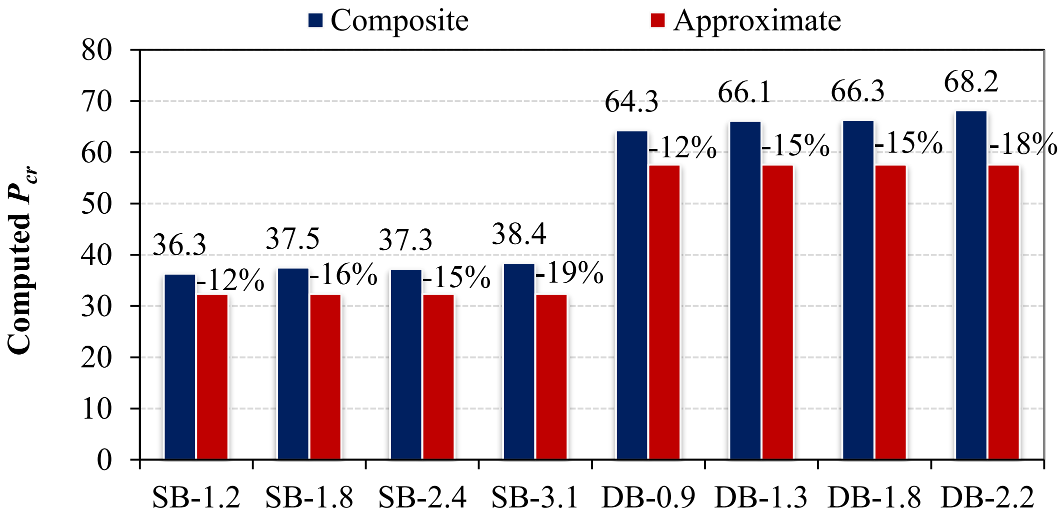

Figure 5.11 **Theoretical first-cracking loads for SB- and DB-Series beams.**

5.3.2 Experimental load-deflection responses

Cracking and stiffness degradation

A virgin beam has a certain initial elastic stiffness before loading. As load increases, the stiffness degrades at some stages of the loading to varying degrees. Figure 5.12 and Figure 5.13 shows the general load-deflection response of a typical passively reinforced UHPC beam. From Figure 5.12 and Figure 5.13, it can be noted that there are four stages of the flexural response of passively reinforced UHPC beam. The Stage-I is the initial linear response, prior to the incidence of the first crack in UHPC. Stage-II is the stiffness transition region. Stage-III is the post-crack hardening of the rebar-UHPC composite. As indicated in Figure 5.12 and Figure 5.13, the composite behavior is linear during most part of Stage-III of the flexural response. The Stage-IV begins with the incidence of rebar yielding, while tension regions of UHPC undergo crack localization and widening.

Typically, at a load of about 45 kN, a gradual change in the flexural stiffness of the beam can be noted from Figure 5.12. However, the apparent crack load noted is about 25 % larger than the theoretical first crack load, as indicated in Figure 5.12. It can thus be inferred that the fiber action was responsible for maintaining a linear response of the beam beyond the actual cracking load. The change point of flexural stiffness then corresponds to the point at which the fiber pullout started. Since the fiber pullout process happens gradually, a sharp transition would not be expected at the change point of flexural stiffness.

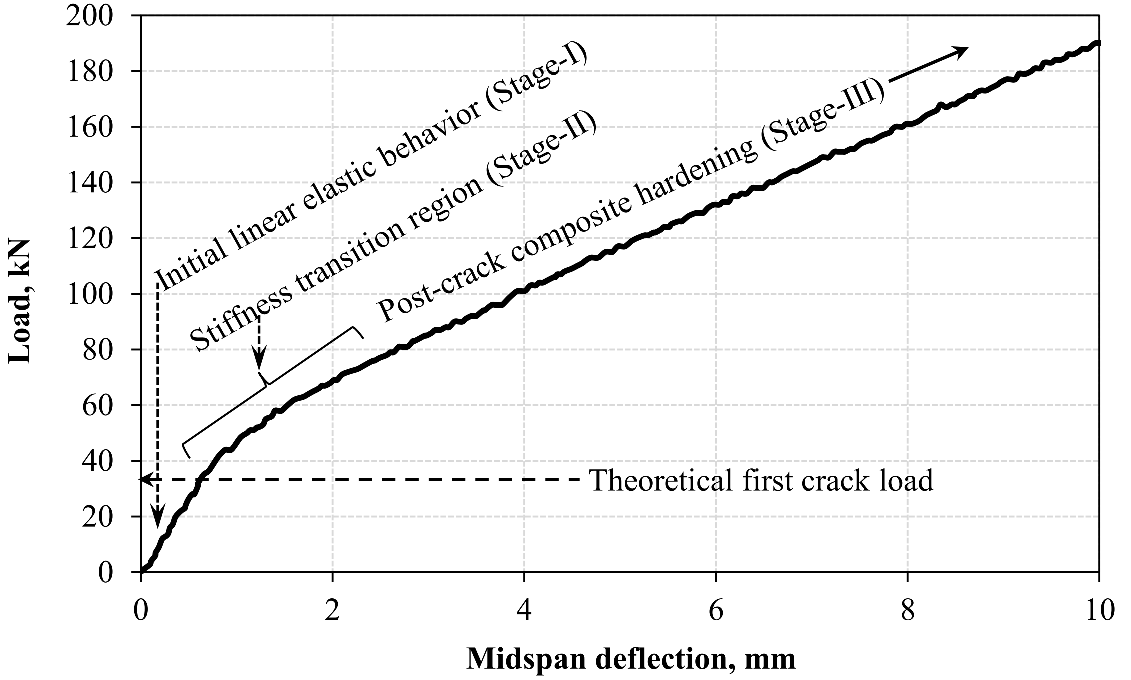

Figure 5.12 Typical initial portion of load-deflection curve (for SB-1.2-UMSN) showing flexural behavior.

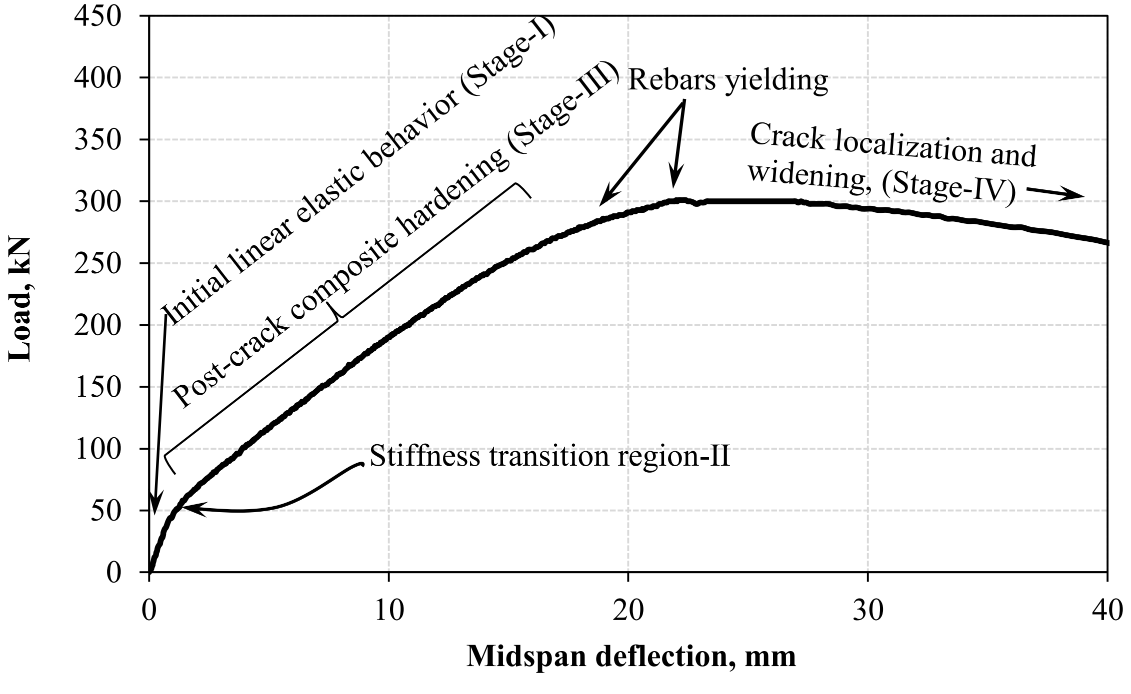

Figure 5.13 Typical overall load-deflection curve (for SB-1.2-UMSN) showing flexural behavior.

The reason behind observed stiffness transition behavior exhibited by the beam (Figure 5.12) can be explicitly explained using the stress-crack width behavior shown in Figure 5.14 (discussed in Section 4.5). As clearly indicated in Figure 5.14, the matrix-fiber system in UHPC exhibits pseudo-strain hardening behavior, which enables it to sustain further stress of about 80 % of the cracking stress before significant loss of tensile stiffness took place. During the pseudo-strain hardening behavior, stress redistribution occurs, leading to multi-cracking (formation of multiple cracks) which aid distribution of stresses within body of the stressed beam.

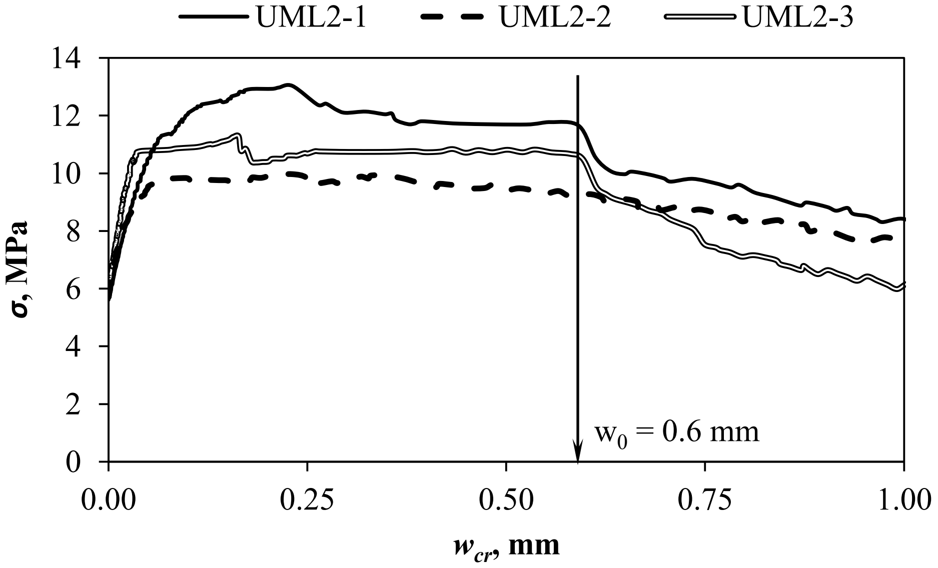

Figure 5.14 Typical stress-crack width behavior (of UML) in uniaxial tension.

Furthermore, it is important to compare the stiffness transition point obtained from the load-deflection curve to that obtained from the concrete and longitudinal steel strains. Figure 5.15 shows the evolution of concrete strains at the top and bottom faces of the

UHPC beam, while Figure 5.16 shows the strains at the longitudinal steel bars, both at the midspan section of the reinforced UHPC beam. It is noteworthy that the strain measurements on the bottom steel bars and the concrete surface strain measurement have indicated the stiffness transition behavior better than in deflection measurements. This observation can be attributed to the fact that the strains were measured over short gauge lengths of 60 mm and 7 mm for concrete and steel strain gauges, respectively. Thus, local deformation effects are registered by the strain gauges, while center-point deflection measurements reflect the average global response of concrete-steel composite system.

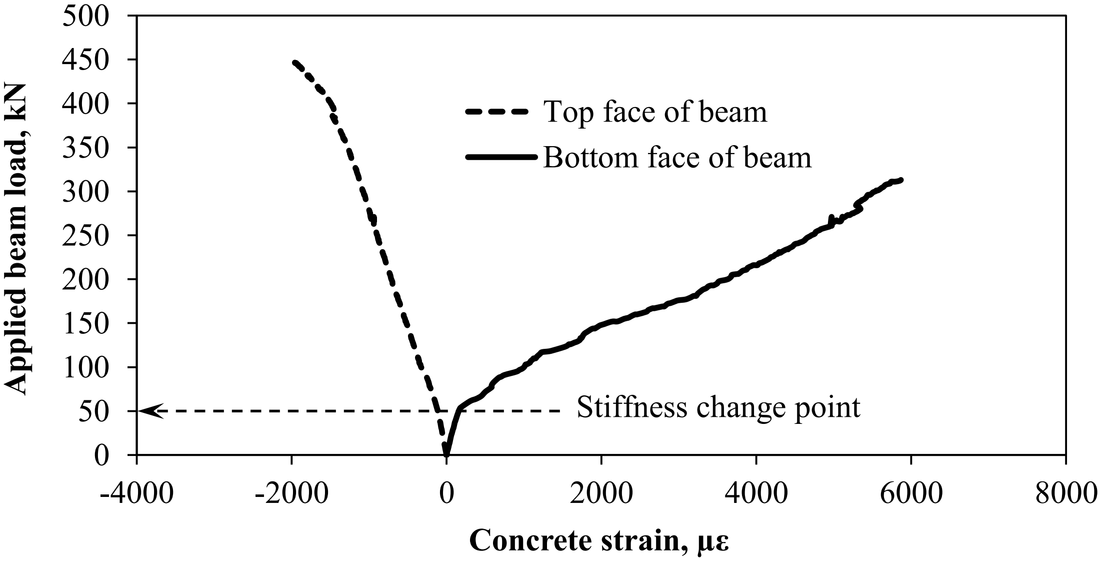

Figure 5.15 **Concrete top and bottom strains at the midspan of SB-1.2-UMSN.**

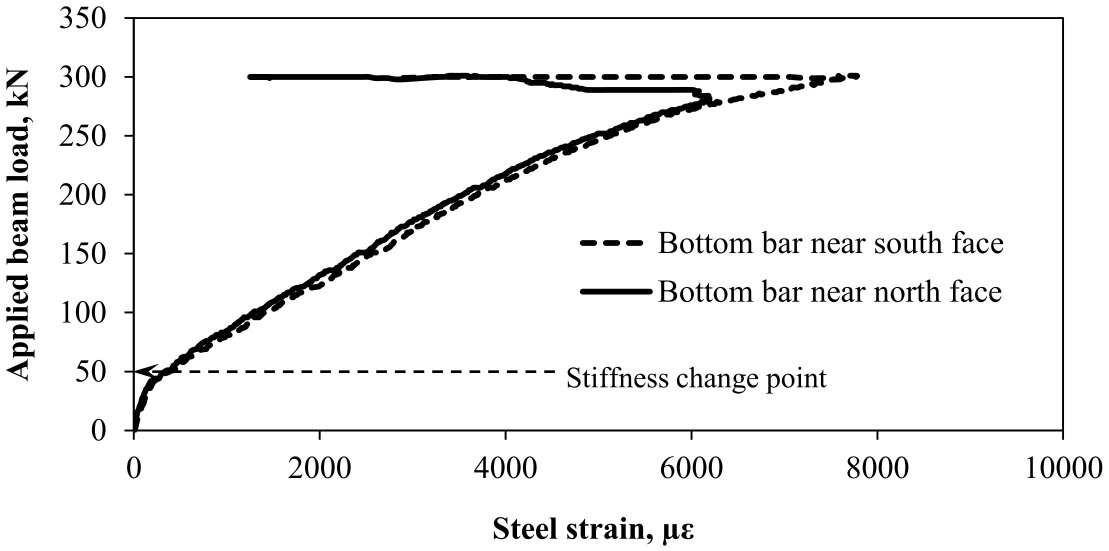

Figure 5.16 Longitudinal steel strains at the midspan of SB-1.2-UMSN.

General load-deflection response of SB-Series beams

Figure 5.17 and Figure 5.18 show the midspan deflection for SB-UMS and SB-UMSN beams, respectively. It can be observed that the flexural stiffness of the beams at the Stage-III (post-crack composite hardening) increases significantly as ρ increases. This means that Stage-III is generally controlled by the tensile actions of embedded rebars. This is expected as this stage of the flexural behavior follows the post-fiber pullout behavior of concrete below the rebars in the tension zone of the beam's cross-section. Since higher values of ρ increases the overall UHPC-rebar composite stiffness, the significant increase of Stage-III stiffness of the beam as ρ increases is justified.

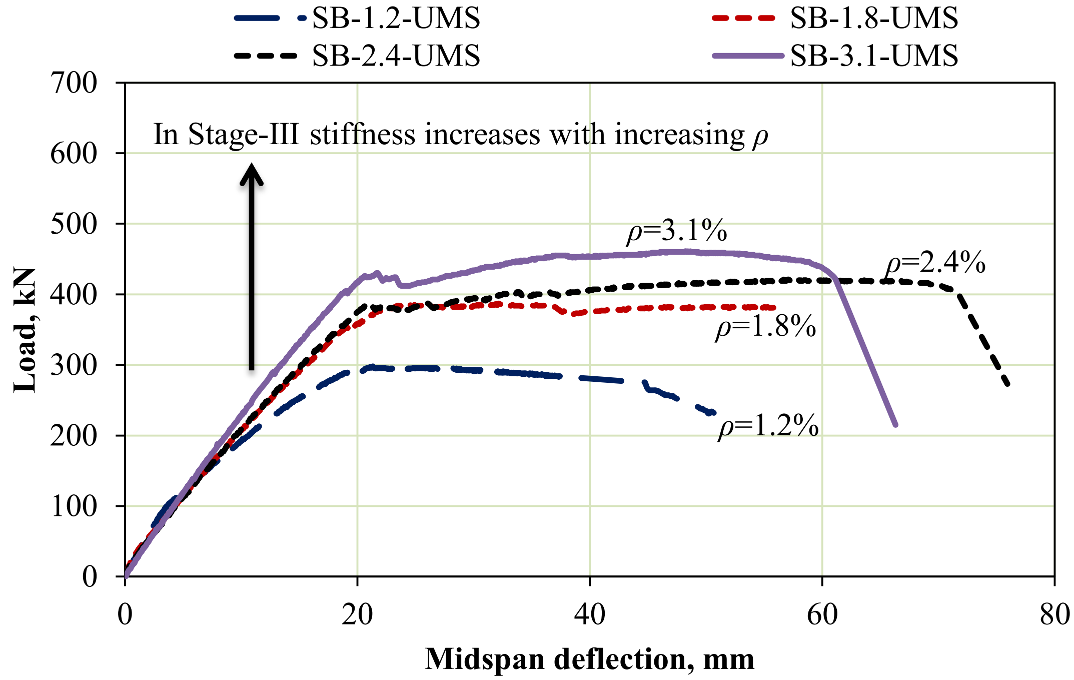

Figure 5.17 Load-deflection response of SB-UMS beams.

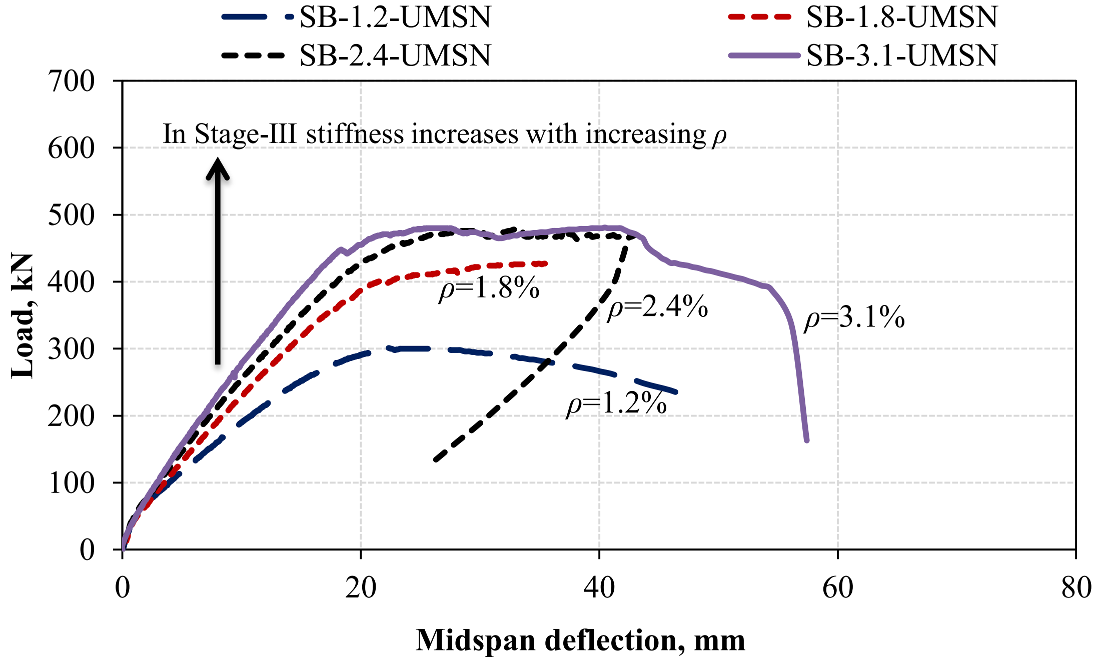

Figure 5.18 Load-deflection response of SB-UMSN beams.

5.3.3 Failure behaviors of SB-Series beams

Considering the general outlook of the deformation behaviors of the SB-Series beams, as shown in Figure 5.17 and Figure 5.18, all the four set of beams have indicated ductile flexure failure modes. Detail discussions of specific failure behavior of these beams are presented in the following subsections.

SB-1.2-UMS and SB-1.2-UMSN (ρ = 1.2 %)

For the beam SB-1.2-UMS, having ρ = 1.2 %, fine flexural cracks appeared as the loading progressed. It was observed that the first set of flexural cracks appeared at about 100 kN, based on visual monitoring of the middle section of the beam. This load level is about one-third of the peak load. However, the theoretical first cracking load as well as that obtained from the load-deflection curve is less than 50 kN. This indicates that the actual crack width of the initial sets of flexural cracks were too small to be observed visually, without the use of sensitive crack-monitoring aids. Therefore, it can be concluded that, instead of continuous widening of the first set of cracks, further loading of the beam resulted into formation of new cracks accompanied by stress redistribution in the tensile zones of the beam.

In the course of further loading, several diagonal hairline cracks appeared at shear dominant regions near support. However, these diagonal cracks did not hinder the growth of flexural cracks. As loading progressed further, new flexural cracks appeared while the width of some of the existing cracks increased. The final failure happened when a major flexural crack became unstable, leading to rupture of the two tensile steel bars. Crushing of the compression block took place before the tensile steel bars ruptured. The failure of behavior of SB-1.2-UMSN was quite similar to that of SB-1.2-UMS. Since both beams have the same cross-sectional configuration, it can thus be concluded that the difference in the UHPC mixtures has no effect on the flexural response of passively reinforced UHPC beam with $\rho = 1.2$ %.

Figure 5.19 and Figure 5.20 show the unloaded post-failure deformed configuration of SB-1.2-UMS and SB-1.2-UMSN, respectively. The total ultimate load recorded for SB-1.2-UMS and SB-1.2-UMSN were 298 kN and 301 kN, respectively. Extensive flexure cracks and flexure-shear cracks can be noted on both beams even after removal of load. Additionally, the ultimate failure behavior was more like "tearing failure", indicating that the neutral axis depth is very low at the ultimate state. From these observations, it may be concluded that the passively reinforced UHPC beam with $\rho = 1.2$ % is grossly under-reinforced where failure is controlled by steel reinforcement.

Figure 5.19 Unloaded post-failure deformed configuration of SB-1.2-UMS ($\rho = 1.2$ %).

Figure 5.20 Unloaded post-failure deformed configuration of SB-1.2-UMSN (ρ = 1.2 %).

Figure 5.21 shows the comparison of the load-deflection responses for the beams SB-1.2-UMS and SB-1.2-UMSN. Figure 5.21 indicated that the two beams exhibited the same flexural response at all stages of loading. This observation agrees with the observed similar failure behavior during testing, as discussed earlier.

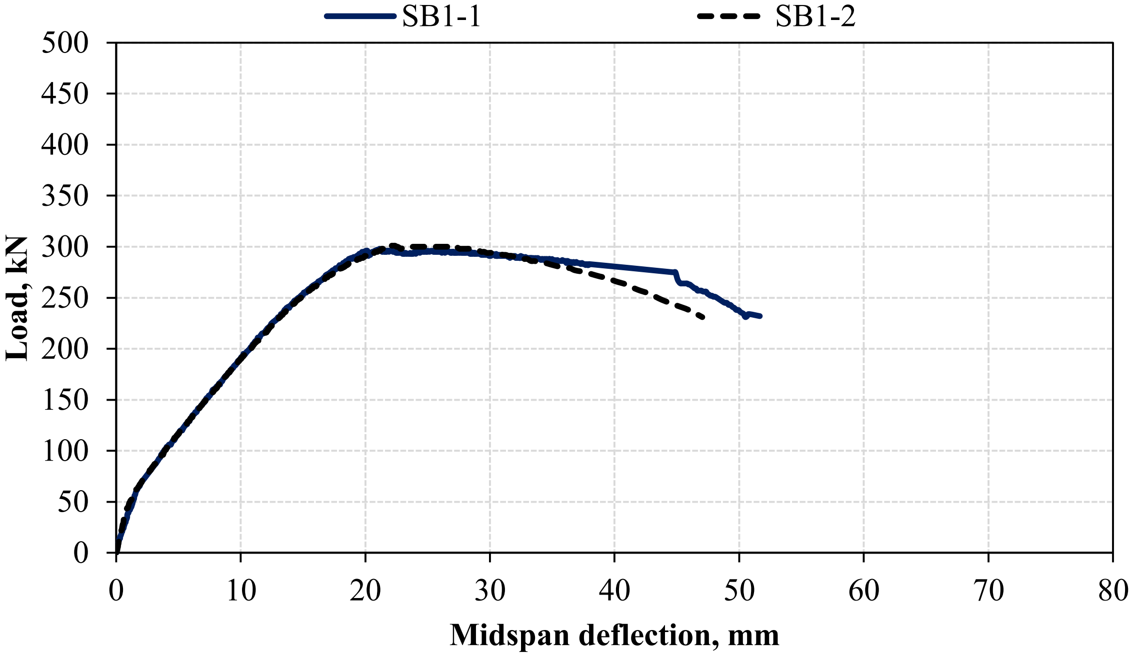

Figure 5.21 Comparison of Load-deflection response of SB-1.2-UMS and SB-1.2-UMSN.

SB-1.8-UMS and SB-1.8-UMSN (ρ = 1.8 %)

For SB-1.8-UMS, fine flexural cracks were observed as the loading progressed. Further loading caused the appearance of some inclined hairline shear cracks. While the number and width of flexural cracks continued to increase, the shear cracks were passive. The final failure happened when two major flexural cracks became unstable, leading to rupture of the three tensile rebars. The rupture of tensile rebars and extensive damage of the compression block took place almost simultaneously. The extent of the compression block damage in SB-1.8-UMS was much more than that in SB-1.2-UMS (same mixture but percentage reinforcement lower than SB-1.8-UMS). The total ultimate load recorded for beam SB-1.8-UMS was 387 kN. Figure 5.22 shows the post-failure deformed configuration of SB-1.8-UMS after unloading, showing heavy damage at both tension and compression zones of the beam at the midspan.

Figure 5.22 **Unloaded post-failure deformed configuration of SB-1.8-UMS, showing heavy flexure damage.**

Additionally, Figure 5.23 shows that shear cracks were minimal, though their widths under peak load were more than what can be seen from the figure. The fact that the width of shear cracks are negligible after unloading indicates that there were very little permanent damages across the cracks, similar to the case of SB-1.2-UMS. This fact clearly indicates that the UHPC materials utilized to fabricate the beams exhibited significant effect on post-crack elastic behavior resulting in little plastic damage, due to the efficient fiber activation in the materials.

Figure 5.23 **Unloaded post-failure deformed configuration of SB-1.8-UMS, showing light damage in shear zone.**

SB-1.8-UMSN had flexural behavior from the onset of loading to before failure, very similar to that of SB-1.8-UMS. However, the behavior of former at failure was a little different from that observed in the latter. Figure 5.24 shows the post-failure deformed configuration of SB-1.8-UMSN. It can be noted in Figure 5.24 that the degree of compression block damage in the SB-1.8-UMSN was less than in the SB-1.8-UMS. This fact is quite obvious by comparing Figure 5.22 and Figure 5.24. Consequently, the ultimate failure load of SB-1.8-UMSN was 429 kN, about 11 % more than that recorded for SB-1.8-UMS. Figure 5.25 shows the comparison of the Load-deflection response of corresponding SB-1.8-UMS and SB-1.8-UMSN. Figure 5.25 indicates that the behavior of the two beams were identical until close to the peak load when the UMSN beam exhibited further load carrying capacity. Since both beams have the same cross-section and reinforcement configuration, the higher capacity in the UMSN beam may be associated with some superior qualities in the UMSN mixture. This is worth exploring.

Figure 5.24 Unloaded post-failure deformed configuration of SB-1.8-UMSN, showing heavy flexure damage.

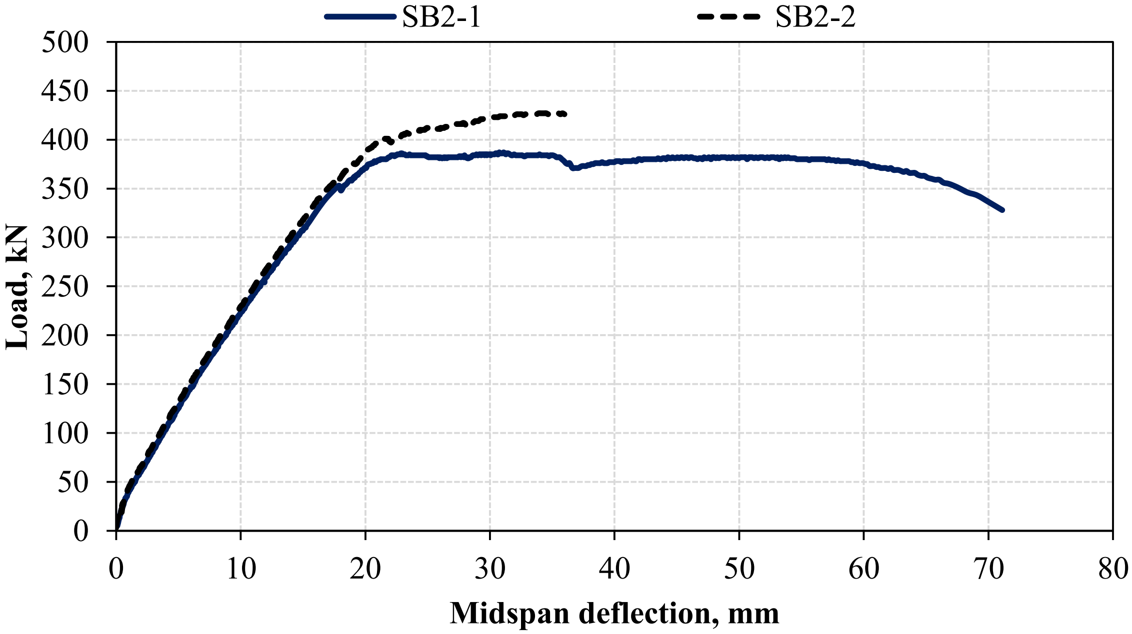

Figure 5.25 Comparison of Load-deflection response of SB-1.8-UMS and SB-1.8-UMSN.

Two factors may be responsible for the superior performance of UMSN beam in the neighborhood of the peak load. The first factor pertains to higher post-fiber activation strength observed in UMSN. It may be recalled that the peak equivalent flexural strength, f_{max}, of UMSN was found to be about 28 % more than that of UMS (Section 5.2, Figure 5.10). As stated earlier, f_{max} governs the ability of the concrete to exhibit stress redistribution behavior in the course of load bearing, which may influence the failure behavior as well as increase the ultimate load.

The second factor that may be responsible for the higher ultimate load capacity observed in SB-1.8-UMSN relates to the hydration thermal characteristics. As discussed in Section 5.1, the pre-loading matrix damage tendency in beams made with UMS is about 50 % higher than in UMSN beams, regardless of the presence of fibers in the mixtures. This is because the load induced tensile cracks in beams are expected to appear at lower loads than expected from undamaged matrix. Due to the two factors mentioned above, it may therefore be concluded that UMSN beams are expected to exhibit higher load bearing capacities as well as different modes of failure.

SB-2.4-UMS and SB-2.4-UMSN ($\rho = 2.4$ %)

SB-2.4-UMS developed flexural cracks in succession as the loading progressed, in the way similar to the previous two cases. The flexural cracks were followed by emergence of diagonal hairline shear cracks, while the flexural cracks got progressively strained. However, unlike in previous two cases, the final failure happened when extensive damage of the compression block occurred, leading to instability of the damaged block. The compression block damage happened after the progressive widening of one major flexural crack, which remained well bridged by the two outermost tensile steel bars up to the final failure stage of compression block failure. Consequently, the two outermost tensile rebars did not rupture, unlike in the two previous cases. The extent of the compression block damage in SB-2.4-UMS was more than that observed in SB-1.8-UMS. Figure 5.26 shows the post-failure deformed configuration of SB-2.4-UMS, exhibiting heavy damage at the compression block, while tension damage was well bridged by the un-ruptured outermost tensile rebars.

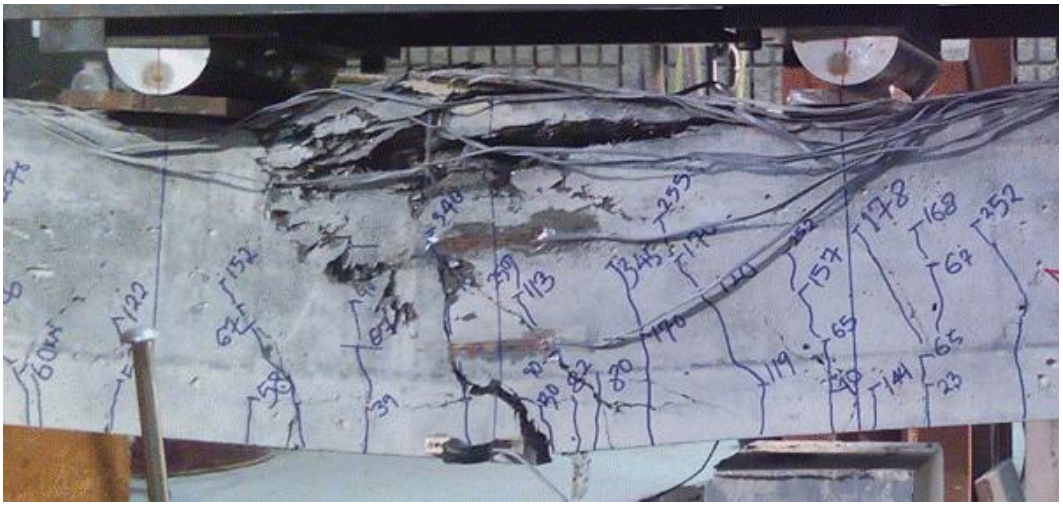

Figure 5.26 **Unloaded post-failure deformed configuration of SB-2.4-UMS, showing heavy damage.**

Further, Figure 5.27 shows that shear cracks in SB-2.4-UMS were minimal, though their widths under peak load were more than what can be seen from Figure 5.27. This means that there were low permanent damages across the cracks, though the residual crack widths were more than those observed in the case of SB-1.2-UMS and SB-1.8-UMS. The total ultimate load recorded for this beam was 421 kN.

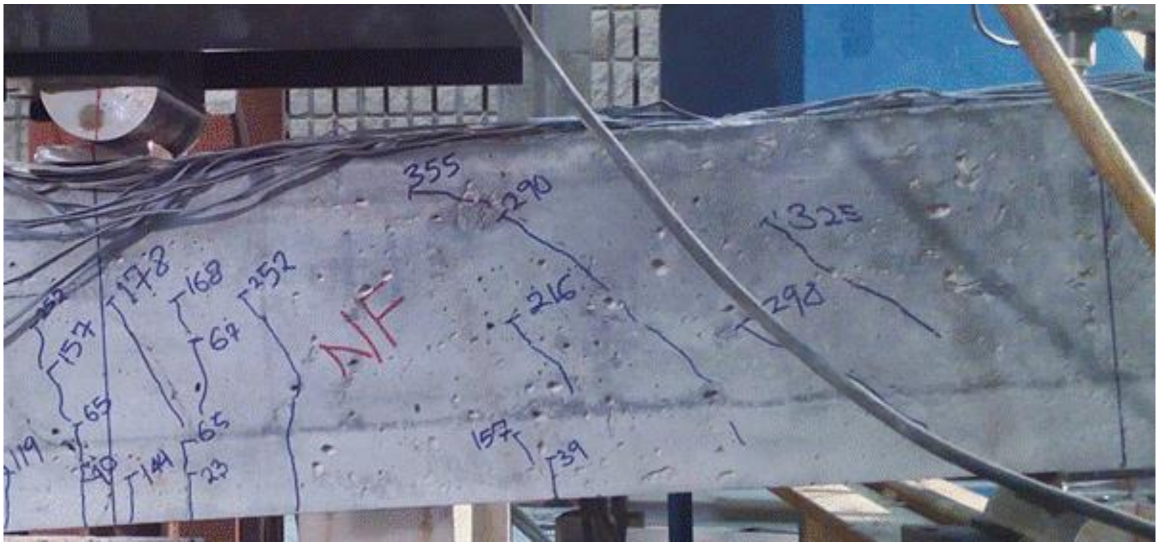

Figure 5.27 Unloaded post-failure deformed configuration of SB-2.4-UMS, showing low damage in shear zone.

Furthermore, the observed failure behavior of SB-2.4-UMS, as shown in Figure 5.26, indicates that the beam may be over-reinforced. However, unlike in the case of traditional reinforced concrete beams, it may be incorrect to conclude that the over-reinforcement is undesirable in case of passively reinforced UHPC beams. This current idea of over-reinforcement is taken from traditional reinforced concrete beam design, in which the failure of the beam is compression-controlled, particularly when the strain in the layer of rebar that is closest to the tension face of the beam is less than the yield strain at the moment the compression concrete crushes. The main problem with an over-reinforced beam is that its failure is compression-controlled, leading to brittle failure that occurs suddenly with little or no warning of impending failure. The sudden failure of compression-controlled section is caused by the brittle nature of the failure of traditional concrete in compression, as opposed to the ductile failure of steel in the tension zone of the cross-section in a tension-controlled section. A compression-controlled section is undesirable in traditional reinforced concrete design. In cases such undesirable sections is inevitable, engineering codes of practice impose low strength reduction factors to such sections. However, due to fiber actions at failure, UHPC usually exhibits ductile compression failure mode. This has been reported in the literature as well as in the present study. Therefore, examination of the level of practical ductility of a passively reinforced UHPC beam exhibiting a compression-controlled failure mode is essential. This is pursued in the following discussion.

Figure 5.28 shows the load-deflection response of SB-2.4-UMS. Although the failure mode shown in Figure 5.27 indicates that the failure of this beam is likely compression-controlled, its load-deflection response shown in Figure 5.27 clearly indicates a very ductile failure, resulting in large deflection of 70 mm before the final failure. This observation may be attributed to the ductile nature of UHPC failure in compression, coupled with its ability to exhibit stress redistribution. Hence, the compression-controlled failure of SB-2.4-UMS may not necessarily be taken as undesirable, as sufficient warning of impending failure can be observed due to the very large deflection exhibited before the final loss of load bearing.

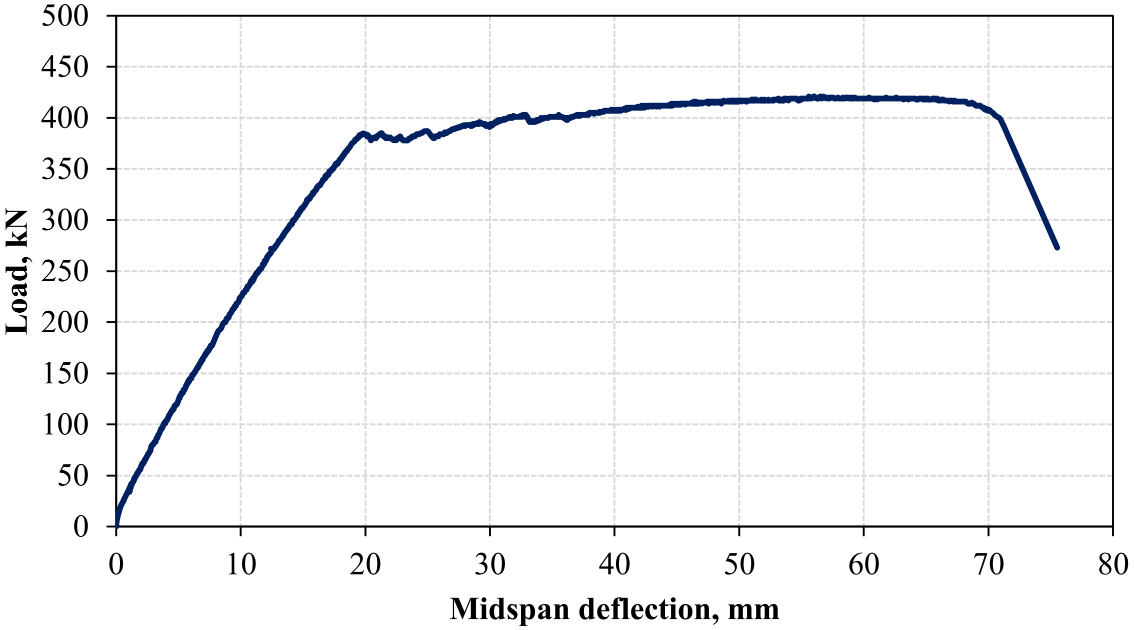

Figure 5.28 Load-deflection response of SB-2.4-UMS.

SB-2.4-UMSN showed initial behavior similar to its UMS counterpart (SB-2.4-UMS), but continued to take more loads beyond the documented peak load of SB-2.4-UMS. Consequently, the previously less active network of diagonal shear cracks were activated and grew wide, almost at the same rate as one major flexure crack within maximum moment region. This indicates that the shear capacity of SB-2.4-UMSN is slightly less than or equal to its flexural capacity. The concurrent shear and flexure failure happened simultaneously with progressive compression block damage. Finally, the stiffness of the beam got degraded with a mixture of shear and flexural damage. However, the stiffness degradation was still sufficient to sustain its peak load over a large eccentric deflection. The beam had to be unloaded to protect the underlining instrumentation, but was reloaded afterwards in order to see the final damage behavior. Figure 5.29 shows the unloaded post-failure deformed configuration of SB-2.4-UMSN, showing appreciable flexural tension, flexure-shear and diagonal shear damages.

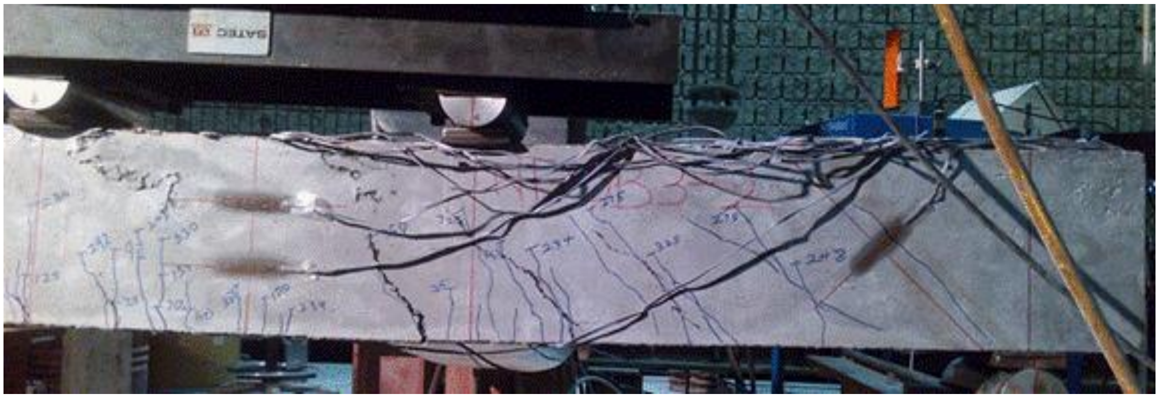

Figure 5.29 Unloaded post-failure deformed configuration of SB-2.4-UMSN, showing extensive damages.

Furthermore, the load-deflection response of SB-2.4-UMSN is shown in Figure 5.30 for a comparison of its load-deflection response with that of its UMS counterpart (SB-2.4-UMSN). In the end, the peak load documented for the UMSN version of SB-2.4 was 480 kN, a 14 % increase over the peak load recorded for the UMS version of SB-2.4.

Since the bottom tension rebars of SB-2.4 beams did not rupture at the ultimate load, it is important to examine the evolution of strain in these rebars. Figure 5.31 and Figure 5.32 show the lateral load-strain curves for longitudinal steel bars in SB-2.4-UMS and SB-2.4-UMSN, respectively.

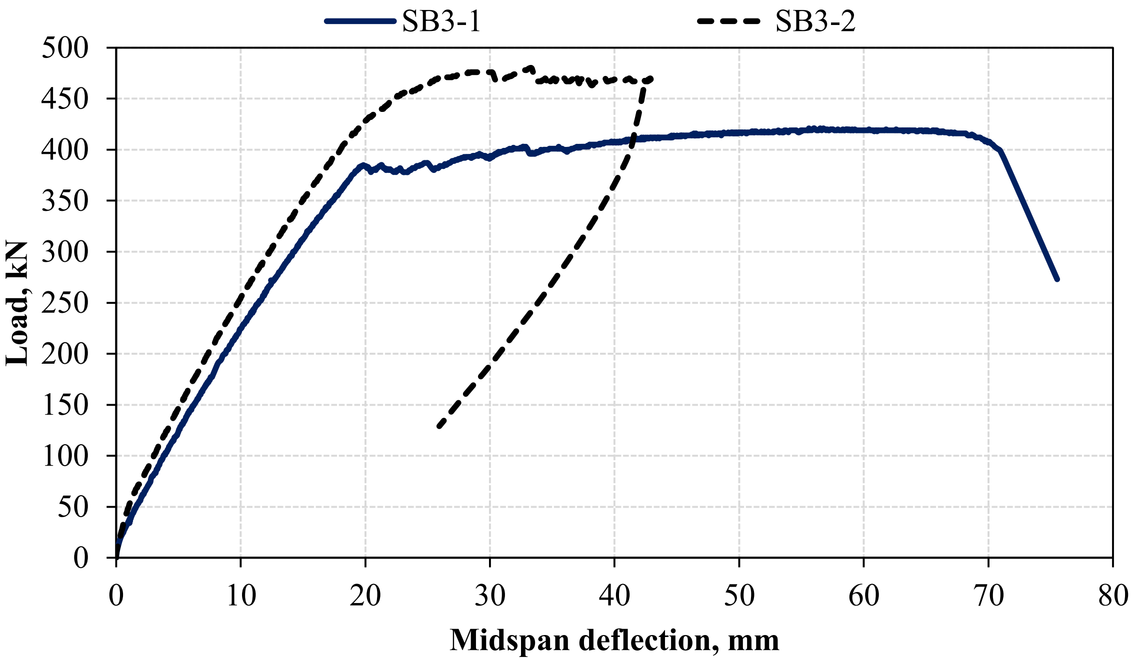

Figure 5.30 Comparison of Load-deflection response of SB-2.4-UMS and SB-2.4-UMSN.

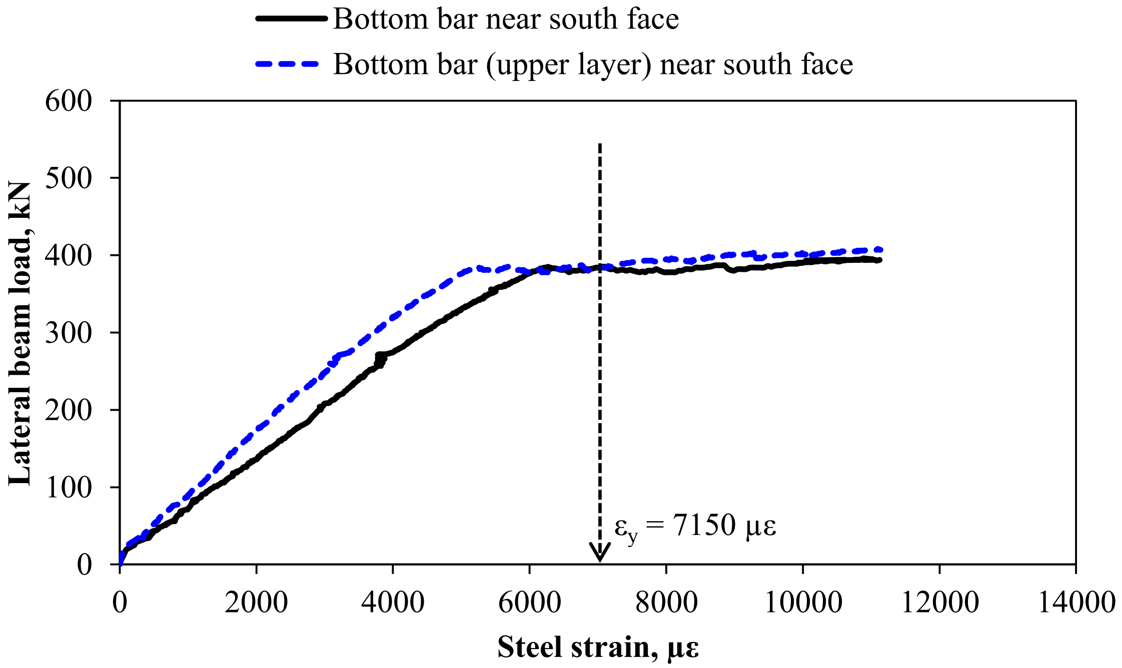

Figure 5.31 Load-strain curves for longitudinal steel bars in SB-2.4-UMS.

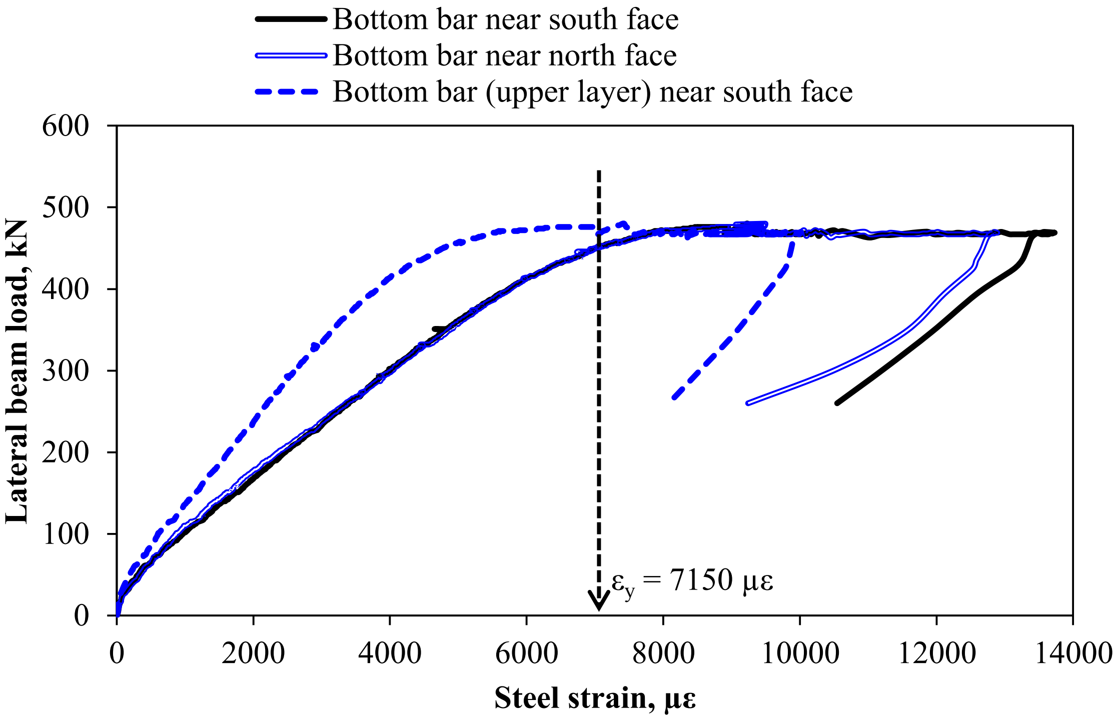

Figure 5.32 **Load-strain curves for longitudinal steel bars in SB-2.4-UMSN.**

It is quite clear from Figure 5.31 and Figure 5.32 that both layers of steel bars have yielded when the beams finally failed in compression. Additionally, the recorded large strains in the tension rebars indicate that the beam deformation was also governed by yielding of rebars alongside the ductile yielding of compression block. Therefore, it can be concluded that the failure of SB-2.4 beams are not fully compression-controlled, but a mode of failure in the transition region.

SB-3.1-UMS and SB-3.1-UMSN (ρ = 3.1 %)

Flexural cracks appeared on **SB-3.1-UMS** as loading progressed and later followed by some fine shear cracks. Initially the flexural cracks continued to widen as new ones emerge, in spite of emerging diagonal shear cracks. However, unlike in the previous three cases, the growth of the flexural cracks paused, while the network of diagonal shear cracks got activated and started growing wide, while new diagonal shear and flexure-shear cracks emerged. As loading progressed on the beam, the shear-dominant area of the beam hardened and cracking activities remained passive due to full activation of fibers. Following the stagnation in the growth of shear cracks, the previously deactivated flexural cracks resumed, while flexure damages increased. In a similar way to the case of SB-2.4-UMS, the final failure happened when extensive damage of the compression block occurred and became unstable, while the major flexural cracks remained well bridged by the fibers and the three outer layer of tensile rebars up to the ultimate failure state.

Figure 5.33 shows the post-failure deformed configuration of SB-3.1-UMS, indicating heavy damage in the compression and shear zones, and a moderate flexural tension damage. The compression block damage was concurrent with large-scale stiffness degradation of the shear-damaged area. Therefore, further deflection of the damaged beam was eccentric towards the more damaged side of the beam, as shown in Figure 5.33. Consequently, the rupture of the three outer layer tensile rebars did not occur, like in the last case of SB-2.4 beams. However, the extent of the compression block damage in SB-3.1-UMS was more than that observed in SB-2.4-UMS. The damage of the compression block in SB-3.1-UMS was so extensive that that the two top bars experienced buckling, as indicated in Figure 5.33. In addition, Figure 5.33 shows that the shear damages were extensive, and there were significant permanent damages across the shear cracks. The total ultimate load recorded for this beam was 461 kN, highest among the SB-Series.

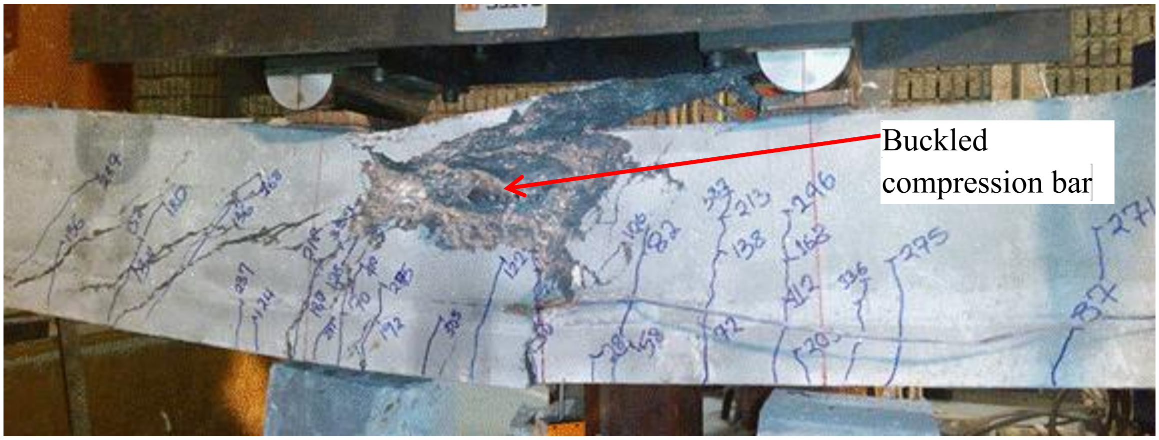

Figure 5.33 **Unloaded post-failure deformed configuration of SB-3.1-UMS, showing heavy compression block damage in addition to severe damage in shear zone.**

The documented behavior of **SB-3.1-UMSN** was very similar to that of its SB-3.1-UMS prior to the attainment of the first peak load. The pre-peak response can better be appreciated in Figure 5.34, which shows the comparison of the Load-deflection response of corresponding SB-3.1-UMS and SB-3.1-UMSN. In the neighborhood of the first peak load, there was a significant bearing damage under the two loading noses, although the magnitude of damage was much higher under one loading nose than the other. This bearing damage can be seen in Figure 5.35. As the first peak load in SB-3.1-UMSN was higher than that of SB-3.1-UMS, it can be said that the bearing stress at that point had exceeded the UHPC material"s bearing strength. This was in spite of the bearing pad measure (Figure 5.35) employed to keep the bearing stress minimal. Therefore, this observation reinforces the previous conclusion reached that UMSN had a better fiber activation behavior which enabled stress redistribution and consequential higher load capacity of reinforced UHPC beams made with UMSN mixture. The implication of the higher load capacity is the increase in shear and bearing stresses. These lead to emergence of shear and bearing damages, thus changing the failure mode from flexure-dominant to shear-, bearing-, or shear-bearing-dominant mode. This explains the observed failure behavior of SB-3.1-UMS.

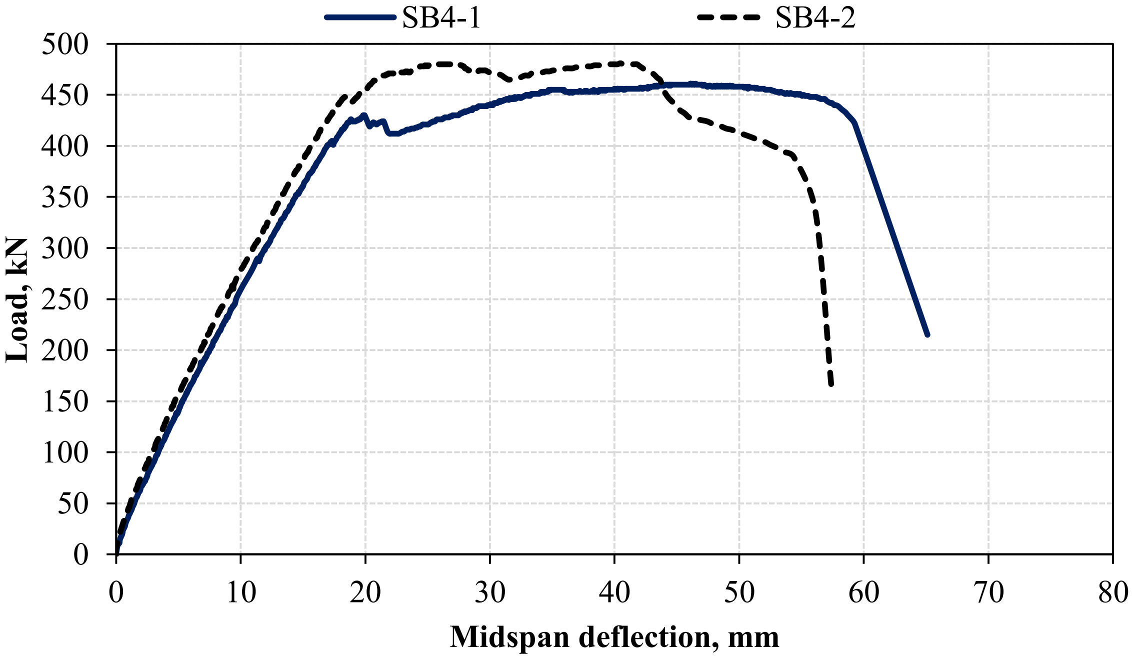

Figure 5.34 **Comparison of Load-deflection response of SB-3.1-UMS and SB-3.1-UMSN.**

Consequently, there was a significant interaction between the heavily-damaged bearing and shear zones, in addition to very high compressive block distress, all of which resulted in a large scale degradation of one side of the beam in the shear-bearing area.

Ultimately, the maximum load sustained by the UMSN beam was 481 kN (which is only 4 % increase over that of its UMS twin) corresponding to the activation of the tension rebars in the upper layer. Like in SB-2.4-UMSN, the SB-3.1-UMSN beam made with UMSN could have developed a much higher ultimate load than SB-3.1-UMS if the shear and bearing failures are successfully prevented.

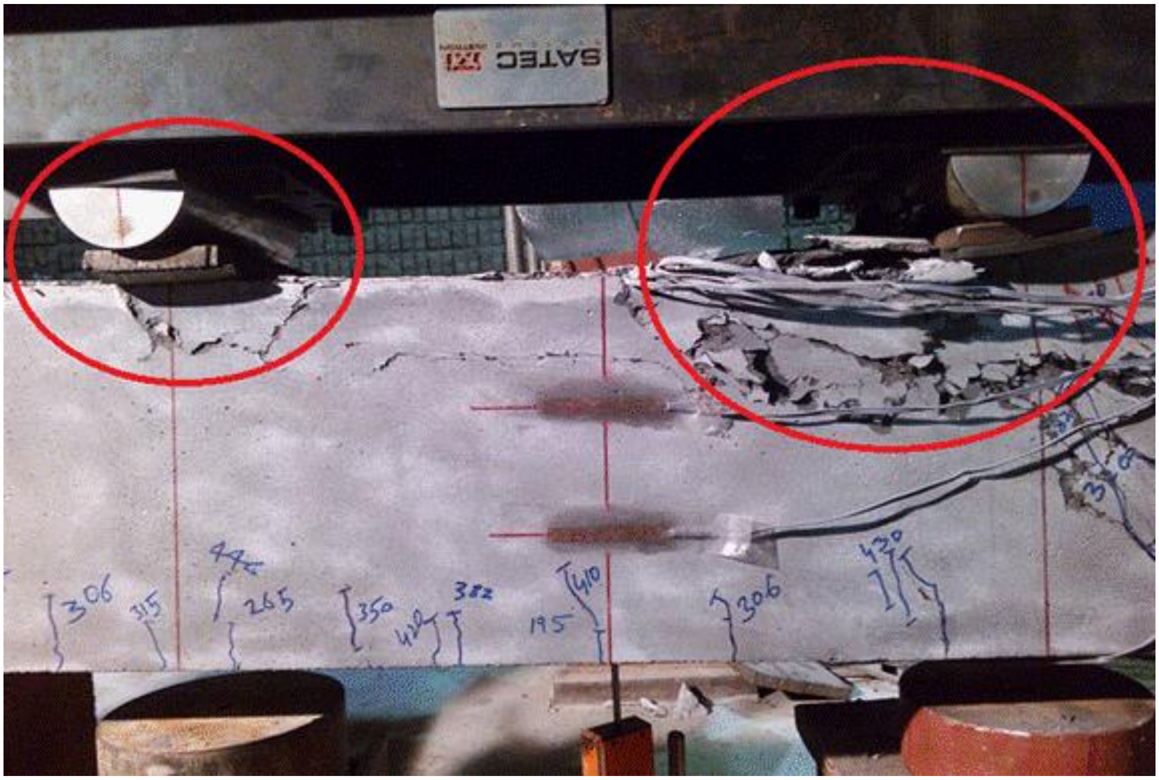

Figure 5.35 **Unloaded post-failure deformed configuration of SB-3.1-UMSN, showing heavy bearing damage.**

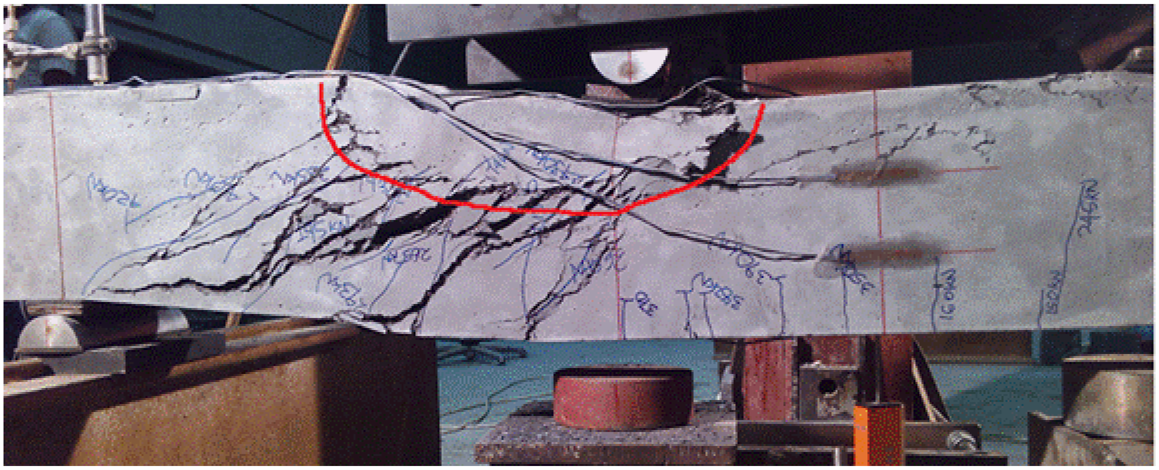

Figure 5.36 **Unloaded post-failure deformed configuration of SB-3.1-UMSN, showing heavy shearing and bearing damages.**

Furthermore, it will be interesting to examine the behaviors of the two bottom longitudinal steel layers in these two beams (SB-3.1-UMS and SB-3.1-UMSN). Figure 5.37 and Figure 5.38 show the load-strain curves for SB-3.1-UMS and SB-3.1-UMSN, respectively. It is indicated that the outer layer bottom steel bars have yielded prior to the peak load in the two beams, while the inner layer did not yield. Therefore, unlike in the case of SB-2.4-UMS and SB-2.4-UMSN, SB-3.1-UMS and SB-3.1-UMSN can be said to have their shear capacities less than flexural capacities. This observation can be attributed to excessive tension steel reinforcement ratio. Further, the over-reinforcement explanation can be backed by the documented ultimate failure behavior of the compression block, as indicated by the buckled compression bar in Figure 5.33. Therefore, it can be concluded that SB-3.1 beams are compression-controlled. However, as discussed previously, they exhibit highly ductile failure behaviors accompanied by sufficient warning of impending failure.

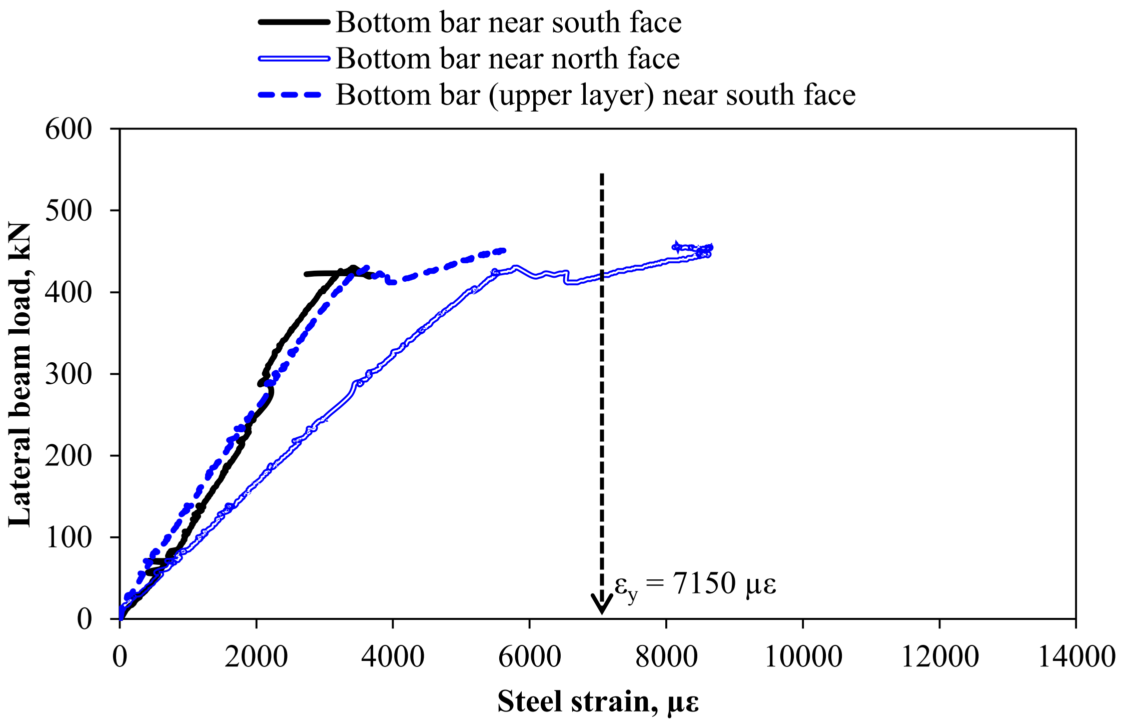

Figure 5.37 Load-strain curves for longitudinal steel bars in SB-3.1-UMS.

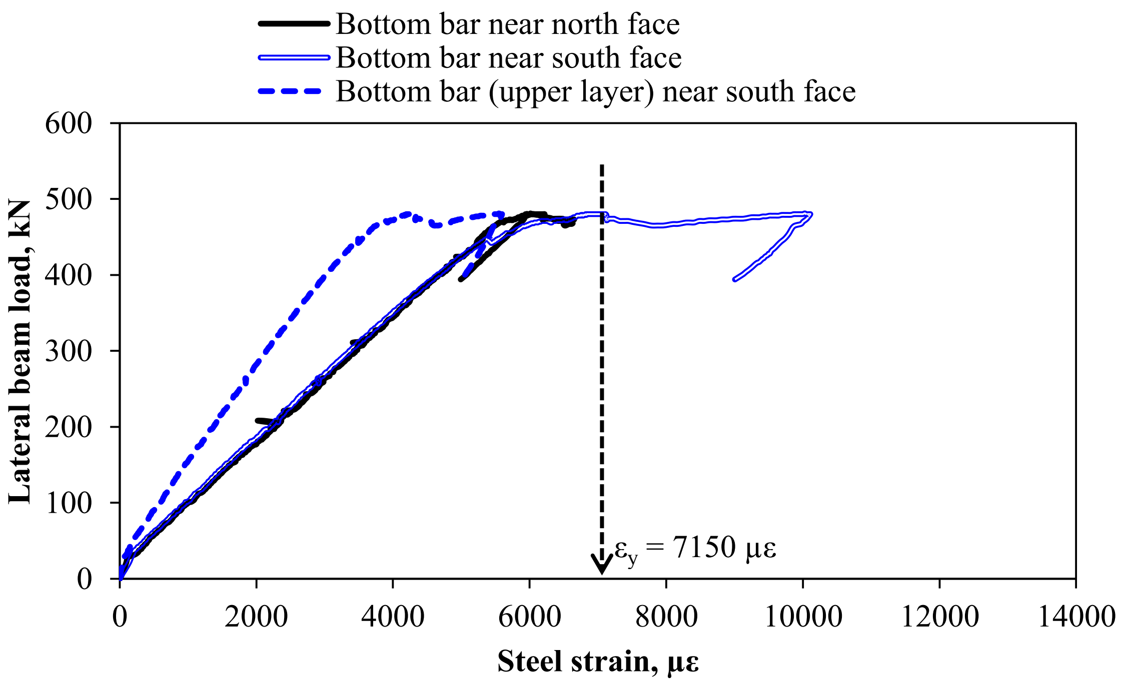

Figure 5.38 Load-strain curves for longitudinal steel bars in SB-3.1-UMSN.

Summary of ultimate behavior of SB-Series beams

Table 5.2 shows the overall Summary of ultimate behavior of SB-Series beam.

Table 5.2 **Summary of documented behavior of SB series beam at ultimate.**

SN	Specimen ID#	Max. load, kN	Flexure damage	Shear damage	Bearing damage
1	SB-1.2-UMS	298	Severe, failed	V. low	-
2	SB-1.8-UMS	387	Severe, failed	V. low	-
3	SB-2.4-UMS	421	Severe, failed	Low	-
4	SB-3.1-UMS	461	Severe, failed	High	Severe
5	SB-1.2-UMSN	301	Severe, failed	Very low	-
6	SB-1.8-UMSN	429	Severe, failed	Low	-
7	SB-2.4-UMSN	480	Very high, failed	Very high, failed	-
8	SB-3.1-UMSN	481	Severe, failed	severe, failed	Severe

5.3.4 Failure behaviors of DB-Series beams

DB-0.9-UMS (ρ = 0.9 %)

In case of **DB-0.9-UMS**, hairline flexural cracks appeared within the midspan region as the loading progressed. Further loading after the appearance of the hairline flexural cracks induced several diagonal hairline cracks in the shear-dominant regions near supports. The network of shear cracks actively grew as load increased, but at a rate lower than that of the more active flexural cracks. Further loading caused the diagonal shear cracks to grow wider and longer, but the shear damage progress was later halted by fiber activations while flexural damage continued to progress rapidly. The final failure happened when a major flexural crack became unstable, leading to the rupture of both the tensile steel bars. Minor crushing of the compression block occurred before the rupture of the tensile rebars. The ultimate load recorded for DB-0.9-UMS was 465 kN. Figure 5.39 shows the post-failure deformed configuration of DB-0.9-UMS after unloading, indicating very light damage at the compression zone and very wide tensile crack. Additionally, Figure 5.39 indicates that the shear cracks were extensive, and there were significant permanent shear damages.

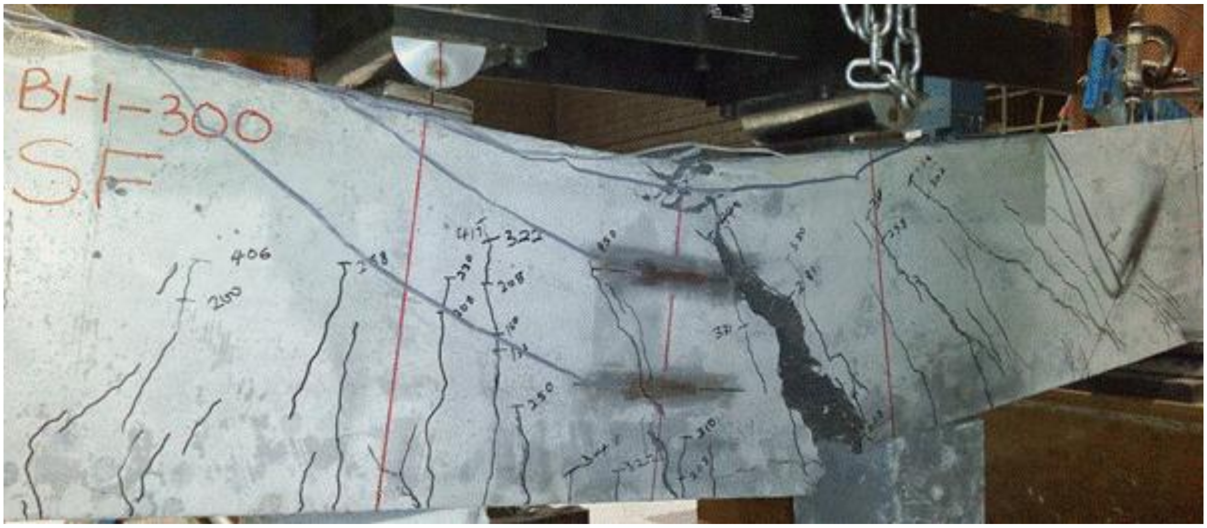

Figure 5.39 **Unloaded post-failure deformed configuration of DB-0.9-UMS, showing heavy compression block damage in addition to serious damage in shear zone.**

Figure 5.40 shows the load-deflection response of DB-0.9-UMS. The response shown in Figure 5.40 indicates a softening post-peak failure behavior of DB-0.9-UMS. Additionally, like the case of SB-Series beams, Figure 5.40 indicates that the transition of bending stiffness of DB-0.9-UMS was not well defined, occurring at the load levels of about 70 to 80 kN. This is higher than the computed theoretical first-crack load shown earlier (Figure 5.11). In addition, Figure 5.41 and Figure 5.42 show the concrete strain recorded on both side faces of DB-0.9-UMS, measured at third-depth from bottom and top of the beam, respectively. Unlike in the case of load deflection response (Figure 5.40), the indicated load level at which the bending stiffness of DB-0.9-UMS changed in Figure 5.41 and Figure 5.42 are very close to the computed theoretical composite first-crack load of 64.3 kN (Figure 5.11).

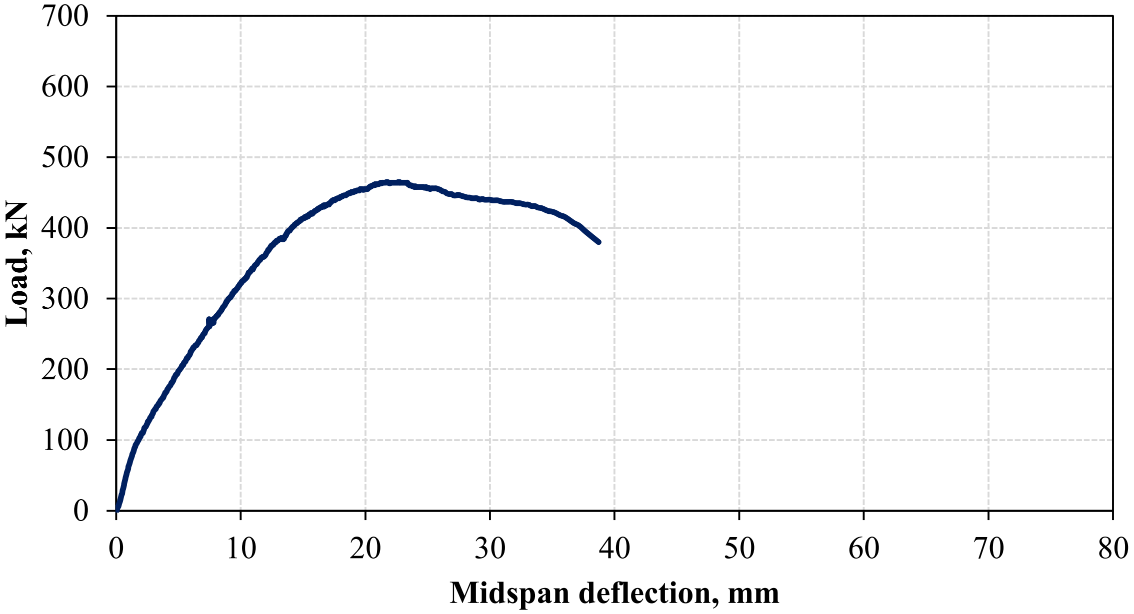

Figure 5.40 **Load-deflection response of DB-0.9-UMS.**

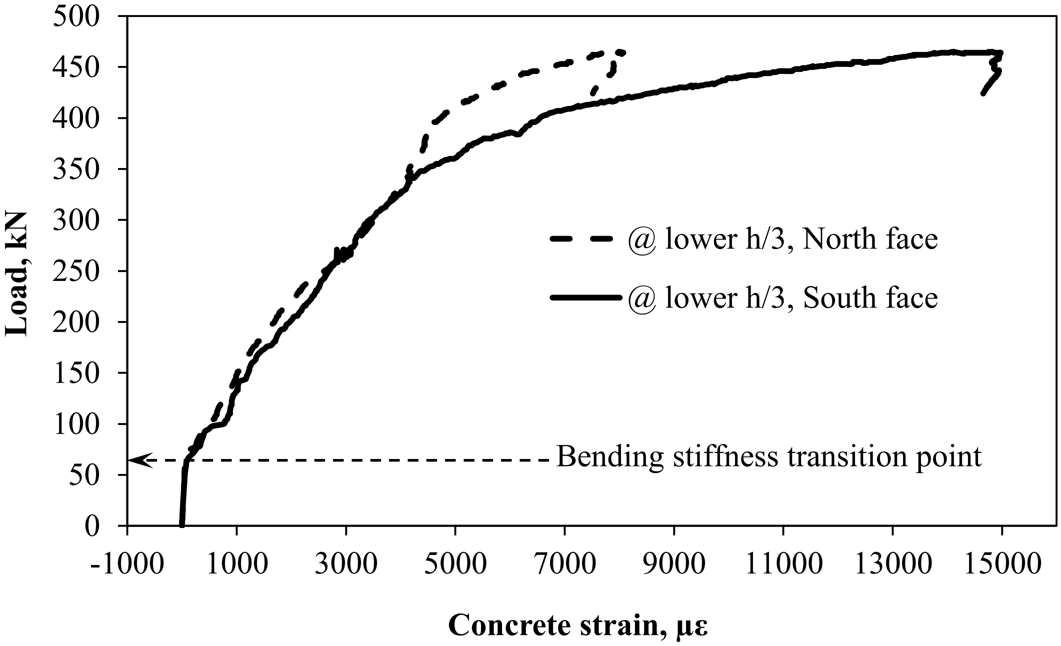

Figure 5.41 Concrete strain on the faces of DB-0.9-UMS at h/3 measured from bottom.

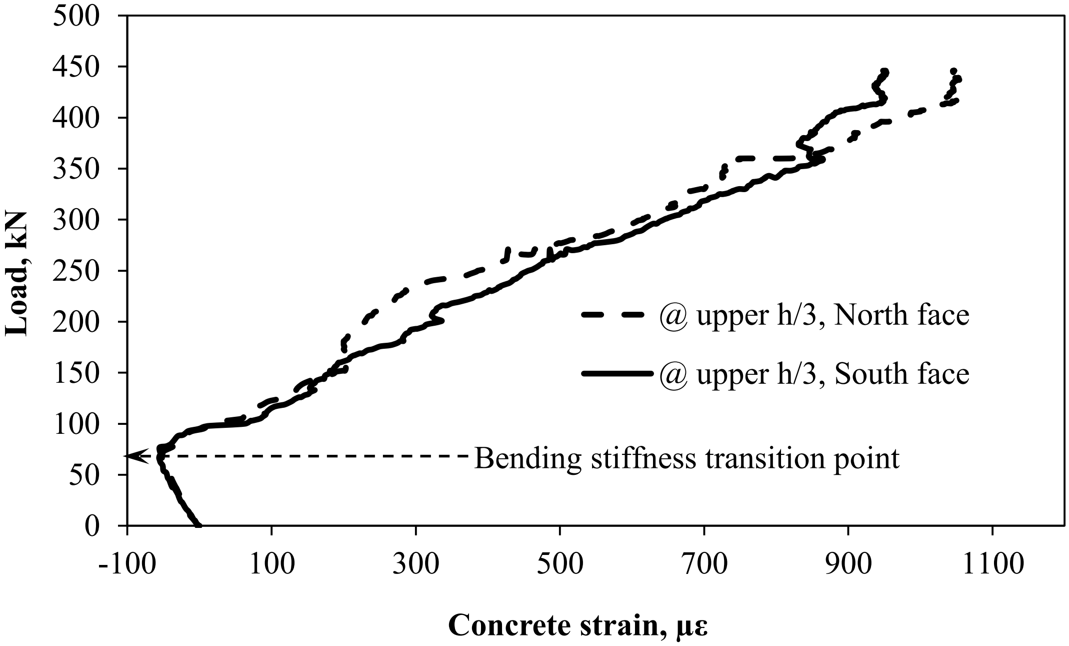

Figure 5.42 Concrete strain on the faces of DB-0.9-UMS at h/3 measured from top.

It should be noted that the flexure damage behavior of DB-0.9-UMS described above is similar to that of SB-1.2-UMS (which also had two tension rebars) in general. However, there are two major differences in the specific failure behavior of the two beams.

Firstly, DB-0.9-UMS exhibited a rapid loss of flexural resistance, as compared to SB-1.2-UMS. The rapid loss of flexural resistance in DB-0.9-UMS can be explained by the lower ρ in DB-0.9-UMS as compared to SB-1.2-UMS. In order to explore this aspect of the behavioral differences of the two beams, it is very important to compare their load-deflection responses. Figure 5.43 shows the comparison of the load-deflection responses of DB-0.9-UMS and SB-1.2-UMS.

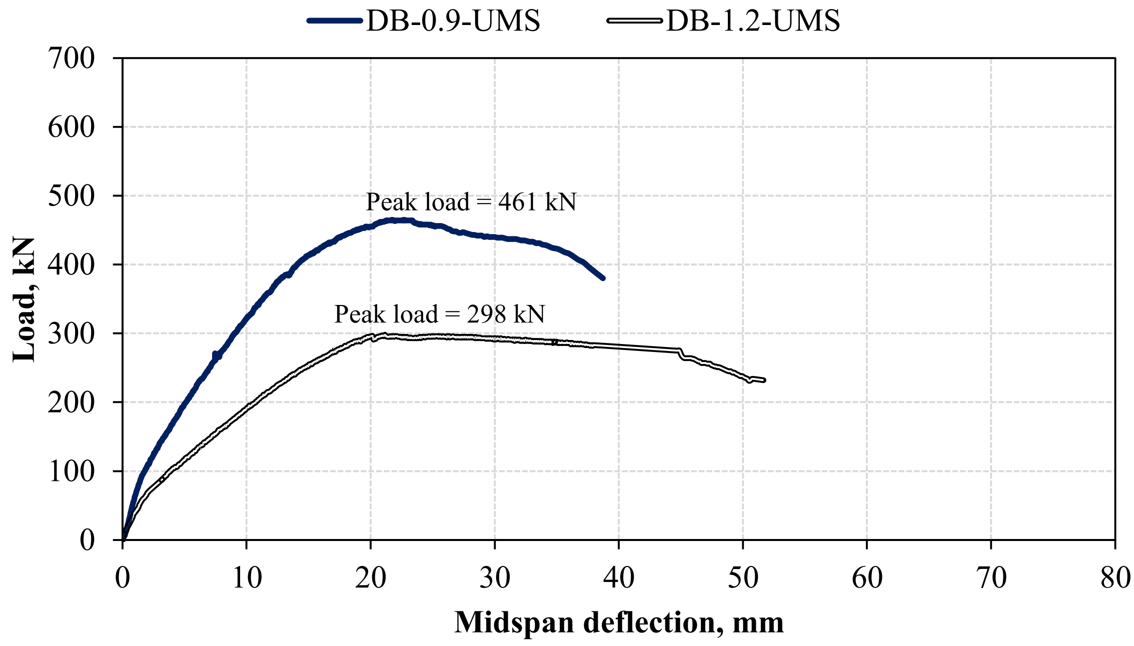

Figure 5.43 **Comparison of load-deflection response of SB-1.2-UMS and DB-0.9-UMS.**

As clearly indicated in Figure 5.43, the rapid loss of flexural resistance in DB-0.9-UMS, as highlighted earlier, is evident from the steeper and shorter softening branch of its post-peak response, as compared to that of SB-1.2-UMS. Additionally, DB-0.9-UMS exhibited a higher State-III bending stiffness than SB-1.2-UMS, in spite of lower ρ in the former than in the latter. This is due to the larger depth in DB-0.9-UMS, as the percentage of undamaged part of the tension block is higher in DB-0.9-UMS than in SB-1.2-UMS.

The second major difference in the specific failure behavior of DB-0.9-UMS and SB-1.2-UMS pertains to the magnitude of shear damage prior to the final failure in flexure. Based on the data shown in Figure 5.43, the peak load recorded in SB-1.2-UMS is only 65 % of that recorded in DB-0.9-UMS. Since SB-1.2-UMS also exhibited some levels of shear damage, the evolution of shear damage in DB-0.9-UMS is expected to progress significantly far before the peak load. The fact that the final failure was controlled by flexure damage indicates that the shear capacity of DB-0.9-UMS is higher than its flexural capacity.

DB-1.3-UMS (ρ = 1.3 %)

As loading of **DB-1.3-UMS** progressed, hairline flexural cracks appeared, like in the case of all other beams. Upon further loading, a large number of hairline diagonal shear cracks emerged. Like the case of the previously discussed beam (DB-0.9-UMS), further loading after the emergence of diagonal shear cracks caused increase in length and width of the shear cracks, followed by hardening by fiber activations. Subsequently, the flexural cracks growth progressed at slow rates. However, unlike the case of the beam with a lower ρ (DB-0.9-UMS), further loading beyond this point activated the network of shear cracks and started to grow rapidly, while flexural cracks stopped further activity. The final failure occurred when a major diagonal shear crack rapidly became unstable, leading to complete failure of the beam in shear. An insignificant crushing of the compression block took place before the final shear failure, while the flexural cracks were still well bridged by tensile steel bars. The total ultimate load recorded for this beam was 590 kN. This is 27 % higher than the peak load recorded load for DB-0.9-UMS.

Figure 5.44 shows the post-failure deformed configuration of DB-1.3-UMS after unloading. A minor damage in the tensile zone and very wide diagonal shear damage can be noted from Figure 5.44. Thus, it can be concluded that increasing ρ from 0.9 to 1.3 % changed the failure behavior of the beam from flexure to shear. Since DB-1.3-UMS was not reinforced against shear failure, it can be concluded that the recorded peak load of 590 kN at ρ = 1.3 % is the shear capacity of DB-1.3-UMS.

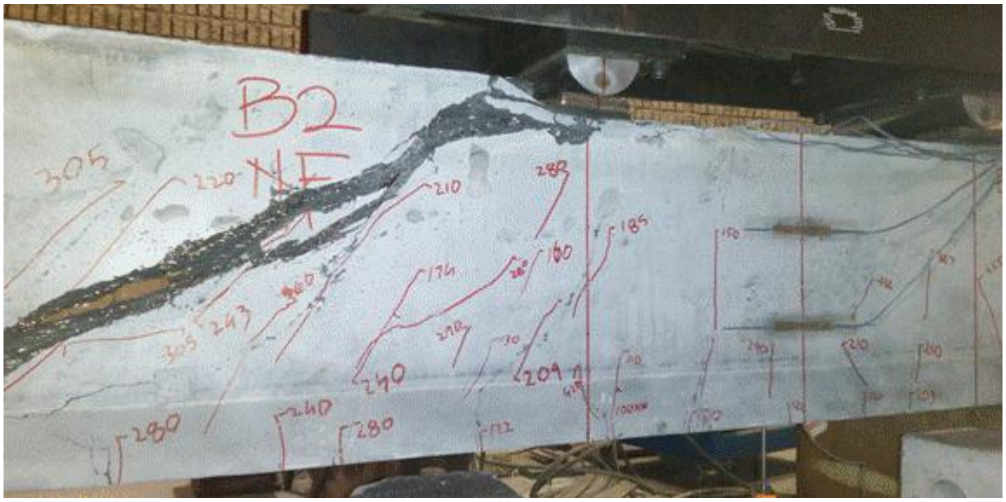

Figure 5.44 Unloaded post-failure deformed configuration of DB-1.3-UMS, showing heavy shear damage.

Figure 5.45 shows load-deflection response of DB-1.3-UMS. The response indicated in Figure 5.45 is typical of shear failure, as the midspan deflection does not indicate any form of softening behavior. The maximum midspan deflection recorded was about 24 mm at peak load corresponding to the shear capacity of the beam.

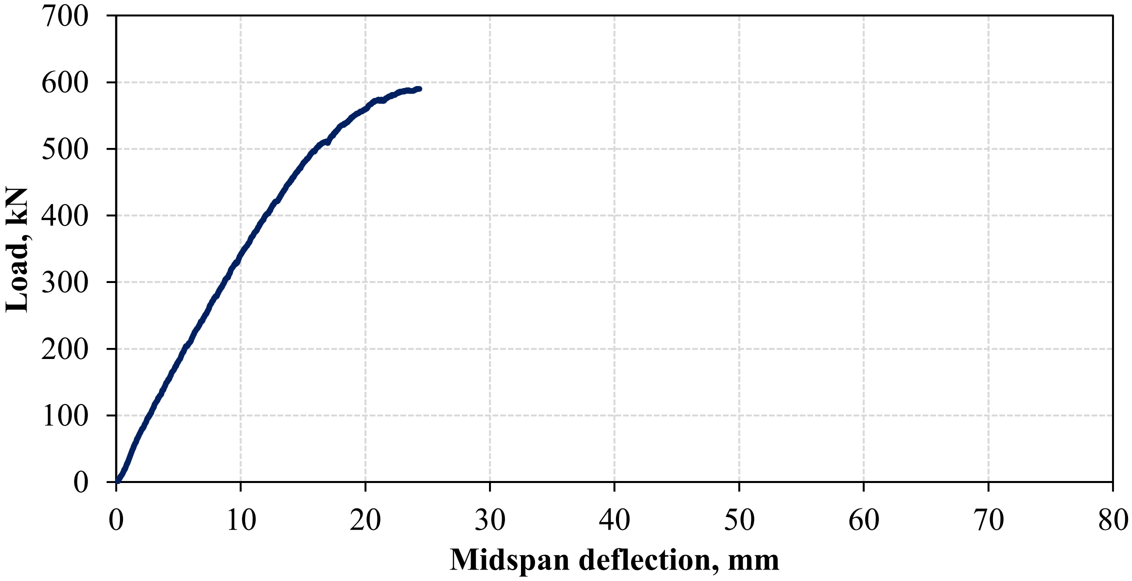

Figure 5.45 Load-deflection response of DB-1.3-UMS.

Furthermore, since DB-1.3-UMS has exhibited a shear failure mode, it will be of interest to investigate the evolution strain in the tensile rebars as the beam load increases up to the peak load. Figure 5.46 shows evolution of tensile strain in the tension rebars at midspan as the load applied on DB-1.3-UMS increases. It is interesting to note in Figure 5.46 that the tension rebars at the bottom of DB-1.3-UMS has yielded prior to the failure of the beam in shear. On the basis of the reported low flexure damage of the beam at midspan, the tension rebars are not expected to yield. The observed yielding of these rebars, as shown in Figure 5.46, can be attributed to the tensile stresses exerted on the rebars while acting as ties in the arch action that results after the formation of compression struts in diagonally cracked short beams [84-86].

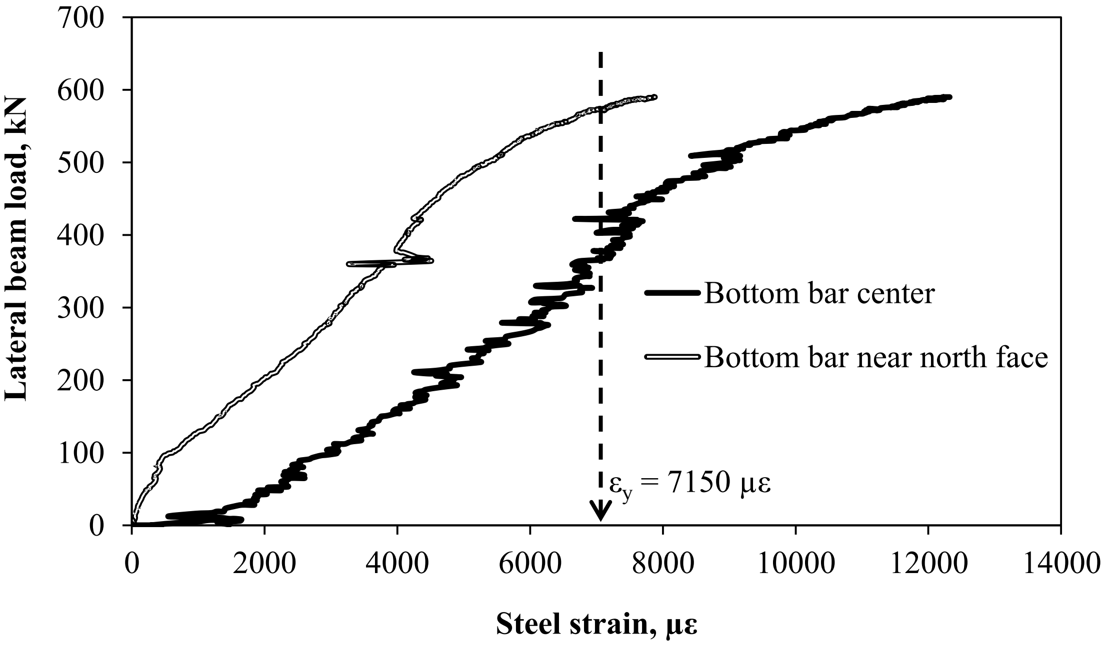

Figure 5.46 Load-strain curve of tension rebars at midspan of DB-1.3-UMS.

DB-1.8-UMS (ρ = 1.8 %)

The structural behavior of **DB-1.8-UMS** was found similar to that of DB-1.3-UMS. Like the latter, the former also experienced light flexural damage at midspan and severe shear damage near the supports. However, no crushing of the compression block was observed in DB-1.8-UMS. Figure 5.47 shows load-deflection response of DB-1.3-UMS. Shear failure mode is evident in Figure 5.47, like the case of DB-1.3-UMS. The ultimate load recorded for DB-1.8-UMS (with ρ = 1.8) was 592 kN, same as the recorded peak load of 590 kN for DB-1.3-UMS (with ρ = 1.3), in spite of differences in their ρ levels. Based on this observation, it may be thought that the peak load of 590 kN is the shear capacity of the beam, and that the inclusion of one extra steel bar (although in two layers) in DB-1.8-UMS does not add to the shear capacity of the beam. However, it appears that the beam suffered premature shear failure. This issue will be addressed shortly.

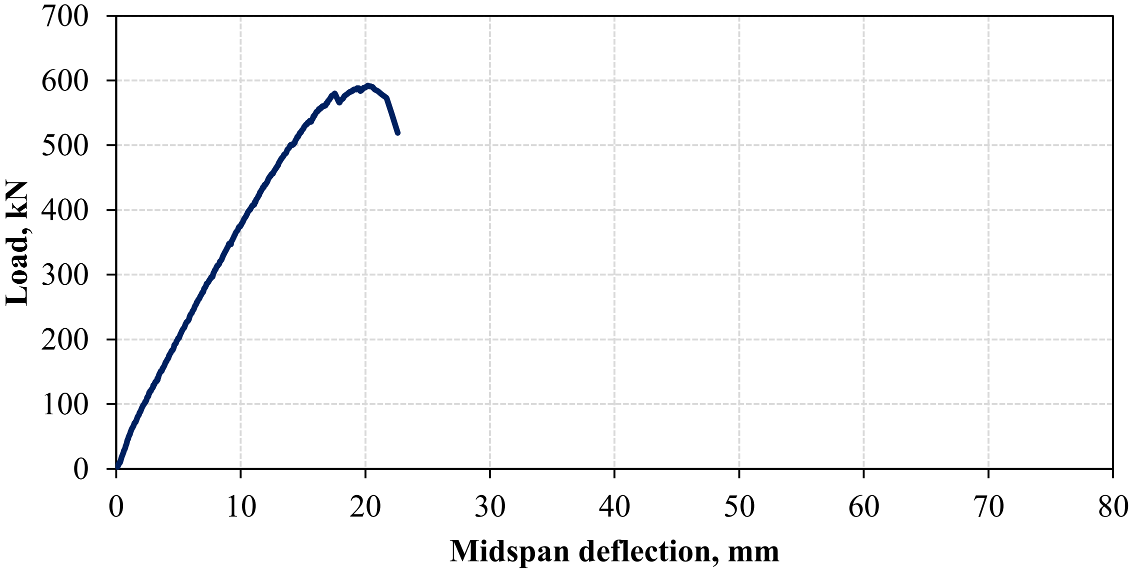

Figure 5.47 **Load-deflection response of DB-1.8-UMS.**

Figure 5.48 shows the post-failure deformed configuration of DB-1.8-UMS after unloading, showing light damage at the tensile zone and very heavy shear damage. The depicted post-failure configuration in Figure 5.48 is quite similar to that of DB-1.3-UMS. In order to understand the nature of failure of DB-1.8-UMS, as shown in Figure 5.48, it is important to present the image of the shear-damaged area taken prior to the damage. Figure 5.49 shows the shear-damaged region of DB-1.8-UMS prior to the final damaged state of the beam (as shown in Figure 5.48). Figure 5.49 indicates that DB-1.8-UMS had bulb holes as well as cold joints developed due to faulty placement in the course of casting the beam.

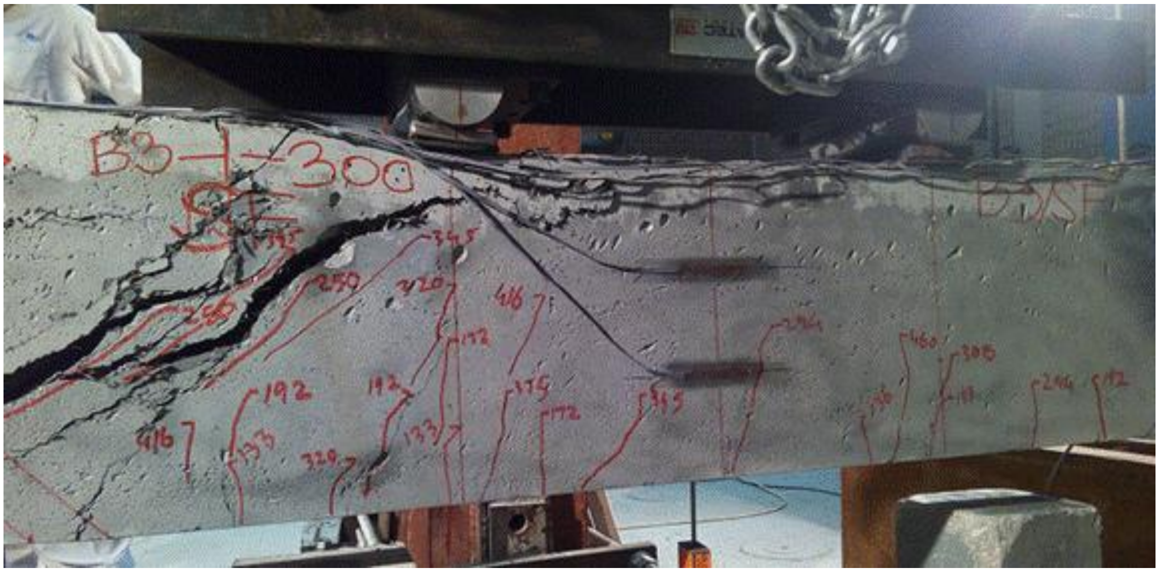

Figure 5.48 **Unloaded post-failure deformed configuration of DB-1.8-UMS, showing heavy shear damage.**

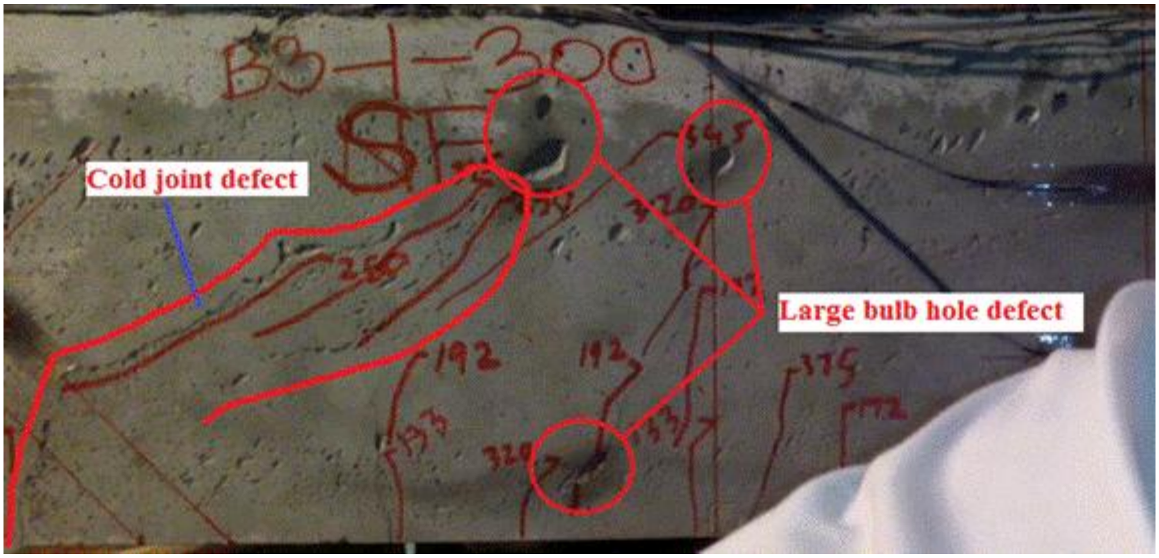

Figure 5.49 **Unloaded post-failure deformed configuration of DB-1.8-UMS, showing heavy shear damage.**

It is an interesting and educating coincidence that all the stated pre-loading defects are present in the region where high shear-induced tension stresses are expected. Therefore, the failure of DB-1.8-UMS may be taken as premature failure due to low shear strength of the defective region. Therefore, the equality of peak load in both DB-1.3-UMS and DB-1.8-UMS may not necessary lead to a conclusion that the shear strength of the beam is not influenced by differences in ρ, as stated earlier.

Additionally, since DB-1.8-UMS also exhibited a shear failure mode, it will be of interest to investigate the evolution of strain in the tensile rebars as the beam load increases up to the peak load, as done earlier in the case of DB-1.3-UMS. Figure 5.50 shows evolution of tensile strain in the two layers of tension rebars at midspan as the load applied on DB-1.8-UMS increased. Unlike the case of DB-1.3-UMS (Figure 5.46), it can be noted from Figure 5.50 that tension rebars in both layers in DB-1.8-UMS have not yielded before the final failure of the beam in shear. The explanation for this observation may be sought in the pre-loading defects on DB-1.8-UMS in the shear-critical region of the beam. It was stated earlier that the tension rebars acts as tie in a post-shear crack arch action. However, the compression strut comprises of the chunk of concrete between inclined shear cracks Figure 5.48 indicates that the compression strut on the western side of DB-1.8-UMS is weak. Therefore, the force exerted on the tension rebars acting as tie may not be enough to cause the tie to yield prior to the strut failure.

Overall, the inclusion of DB-1.8-UMS in this discussion despite its pre-loading defects serves a very good purpose of exposing the demerits of casting UHPC beams from two sides of the mold, rather than from one side, as stated earlier. Casting from two sides will increase the chance of the formation of cold joints, as noted in the case of DB-1.8-UMS.

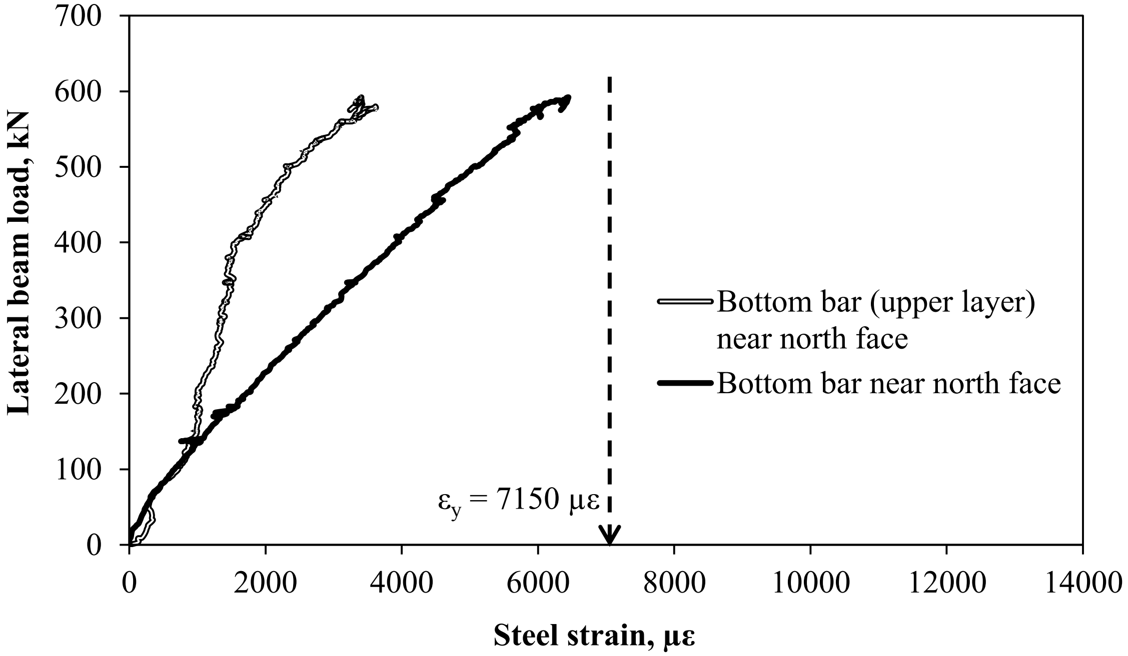

Figure 5.50 **Load-strain curve of tension rebars at midspan of DB-1.8-UMS.**

DB-2.2-UMS (ρ = 2.2 %)

The structural behavior of **DB-2.2-UMS** was found essentially to be the same with that of DB-1.8-UMS, from the inception of loading up to the final failure. However, the ultimate load recorded for DB-2.2-UMS was 664 kN, which is a 12 % increase above that of DB-1.8-UMS. Since the failure of this beam is primarily shear-controlled, it indicates that the extra shear capacity is due to the addition of an extra steel bar to the bottom layer. Hence, it can be concluded that *ρ* has an effect on the shear capacity of the beam, albeit insignificant. Figure 5.51 shows the post-failure deformed configuration of DB-2.2-UMS after unloading. Like the cases of DB-1.3 and DB-1.8, Figure 5.51 indicates light damage in the tensile zone and heavy shear damage in the shear-critical zone of DB-2.2-UMS.

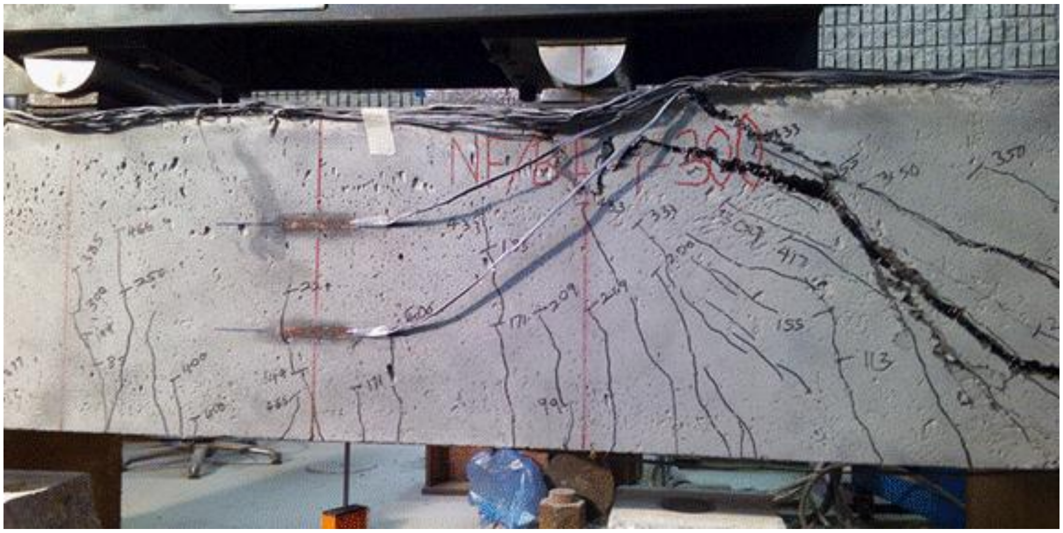

Figure 5.51 Unloaded post-failure deformed configuration of DB-2.2-UMS, showing heavy shear damage.

Figure 5.52 shows the load-deflection response of DB-2.2-UMS, clearly indicating shear failure mode due to the absence of flexural ductility in the load-deflection response, as in the cases of DB-1.3 and DB-1.8. An interesting fact revealed in Figure 5.52 is that the load-deflection response of DB-2.2-UMS does not indicate any apparent degradation of the initial bending stiffness of the beam until a load level of about 420 kN, which is about two third of the peak load. This observation confirms the previous claim that the bending stiffness of the reinforced UHPC beams increases with ρ. For all other beam configurations considered in this study, the noted influence of ρ on bending stiffness manifested at Stage-III (post-first-crack response). However, in the case of DB-2.2-UMS, influence of ρ on bending stiffness manifested in terms of enforcing the initial linear bending response up to load levels near failure of the beam. Since the beam has failed in shear, the deviation from the stiffness noted at about load level of 420 kN can be attributed mainly to accelerated deflection due to shear damages that initiated the final failure of the beam.

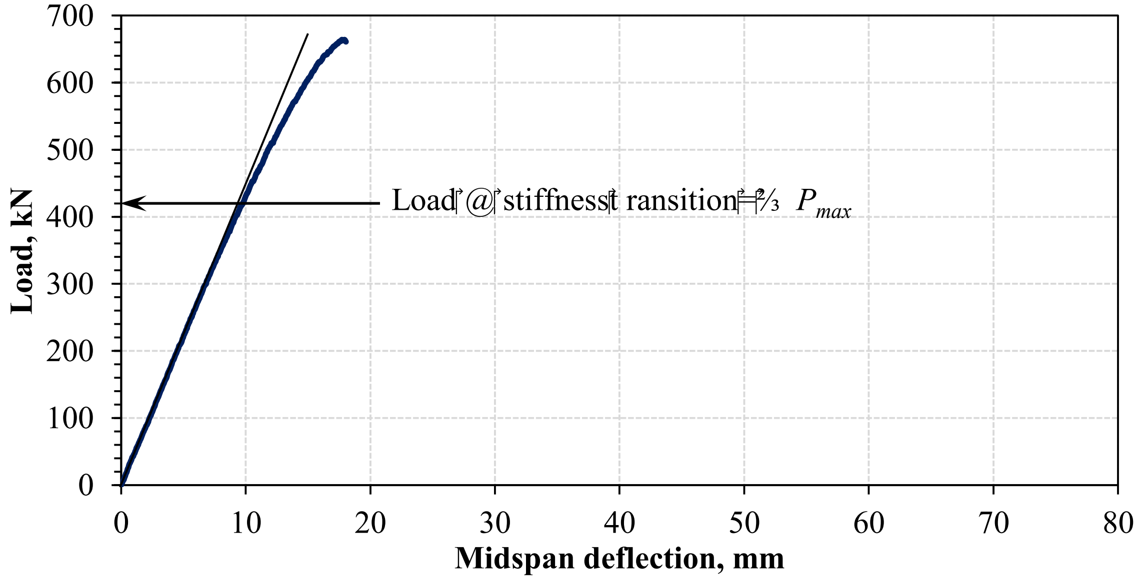

Figure 5.52 **Load-deflection response of DB-2.2-UMS.**

Like the cases of DB-1.3 and DB-1.8, it is important to investigate the evolution strain in the tensile rebars in DB-2.2-UMS. Figure 5.53 shows evolution of tensile strain in the two layers of tension rebars at midspan as the load applied on DB-2.2-UMS increased. Although the upper layer of tensile rebar may not have yielded at the peak load of the beam, it can be noted from Figure 5.53 that the lower layer tension rebars of DB-2.2-UMS have yielded before final failure of the beam in shear. This observation reinforced the validity of the tie action explanation for the yielding of the tension bars. Additionally, the observed yielding of lower layer tension rebars of DB-2.2-UMS also validates the claim that DB-1.8-UMS has failed prematurely due to the failure of compression strut that resulted from the defective shear-critical region of the DB-1.8-UMS.

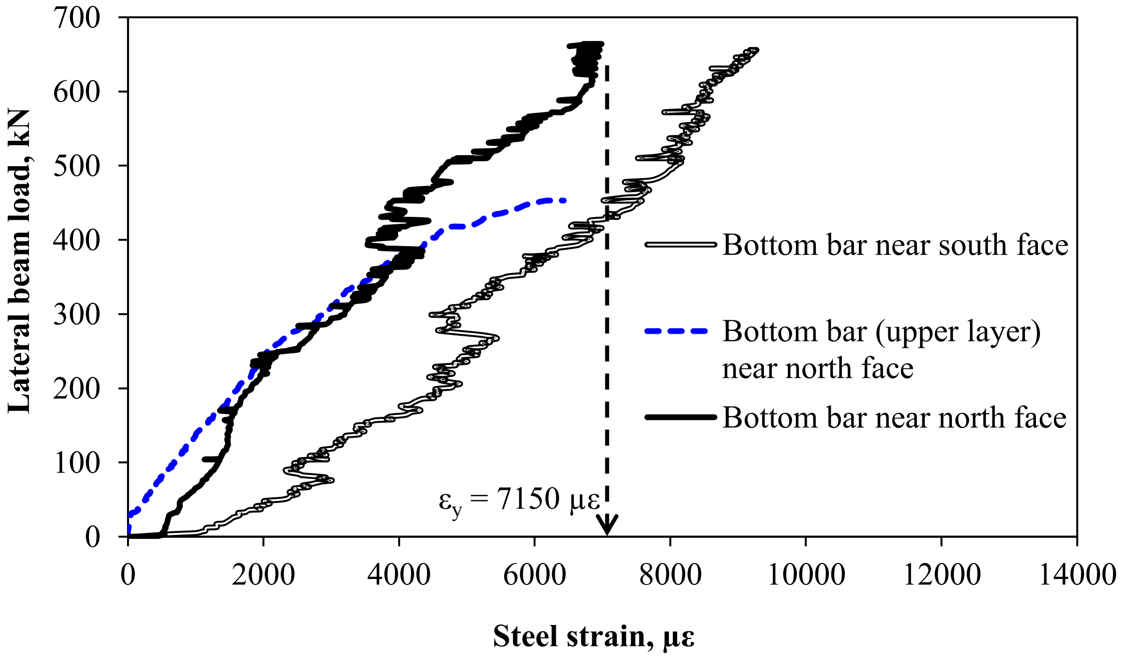

Figure 5.53 Load steel strain curve at midspan for DB-2.2-UMS.

Ultimate behavior of DB Beams

Table 5.3 shows a summary of the failure behavior of all the four tested DB-Series beams. Additionally, Figure 5.54 shows the general load-midspan deflection response of DB-Series beams. Like the SB-Series beams, Figure 5.54 indicates that the Stage-III bending stiffness of DB-Series beams also increases with increasing *ρ*.

Table 5.3 **Summary of documented behavior of DB series beam at ultimate.**

SN	Specimen ID#	Max. load, kN	Flexure damage	Shear damage
1	DB-0.9-UMS	465	Severe, failed	Moderate
2	DB-1.3-UMS	590	Moderate	Severe, failed
3	DB-1.8-UMS	592	Very low	Severe, failed
4	DB-2.2-UMS	664	Very low	Severe, failed

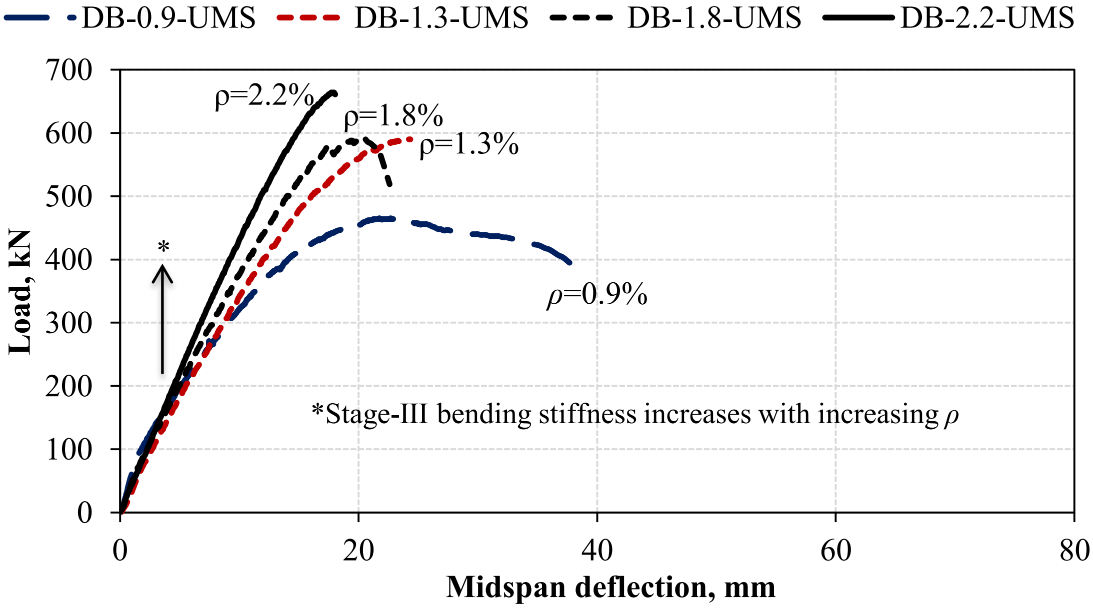

Figure 5.54 **Load-deflection response of DB-Series beams.**

5.3.5 Summary of structural behavior of reinforced UHPC beams

The experimental work reported in this chapter as well as the results and developed discussions are summarized in the following subsections.

UHPC Mixtures utilized

UMS having cement content of 900 kg/m^3, and UMSN having 30 % of cement in UMS replaced by NZ, resulting in cement content of 630 kg/m^3.

Post-Casting hydration thermal characteristics

The peak temperature recorded at the core of a 300 mm deep beam for UMS (cement content = 900 kg/m^3), while same was 56.1 °C for UMSN (cement content = 630 kg/m^3). The temperature difference between the core and the bottom face of the beam were 4.5 and 3 °C for UMS and UMSN, respectively. The higher temperature differential in UMS increases the matrix damage tendency by about 50 %, as compared to UMSN.

Reinforced UHPC beam sizes, configurations and mixtures

Two sizes of beams (beam series) were tested and evaluated for their structural performance. The eight SB-Series beams had a cross-section size of 150 × 225 mm, and were passively reinforced with ρ levels of 1.2, 1.8, 2.4, and 3.1 %. Four of the SB-Series beams were fabricated using UMS mixture, while the other four were fabricated with UMSN mixture. The four DB-Series beams had cross-section size of 150 × 300 mm, and were passively reinforced with ρ levels of 0.9, 1.3, 1.8, and 2.2 %. The DB-Series beams were fabricated using UMS mixture.

Mechanical characterization

UMS and UMSN were found to have similar mechanical characteristics in terms of compressive strength, modulus of elasticity and flexural cracking strength. However, UMSN possessed a better fiber activation and utility potential than UMS, as indicated by 28 % higher equivalent flexural strength of UMSN than that of UMS.

Peak loads

The effect of ρ and type of UHPC on the peak loads is shown in Figure 5.55.The increase in the peak load with increase in ρ can be seen from Figure 5.54. It should be noted that the result of the defective DB-1.8-UMS is omitted from the graph presented shown in Figure 5.54

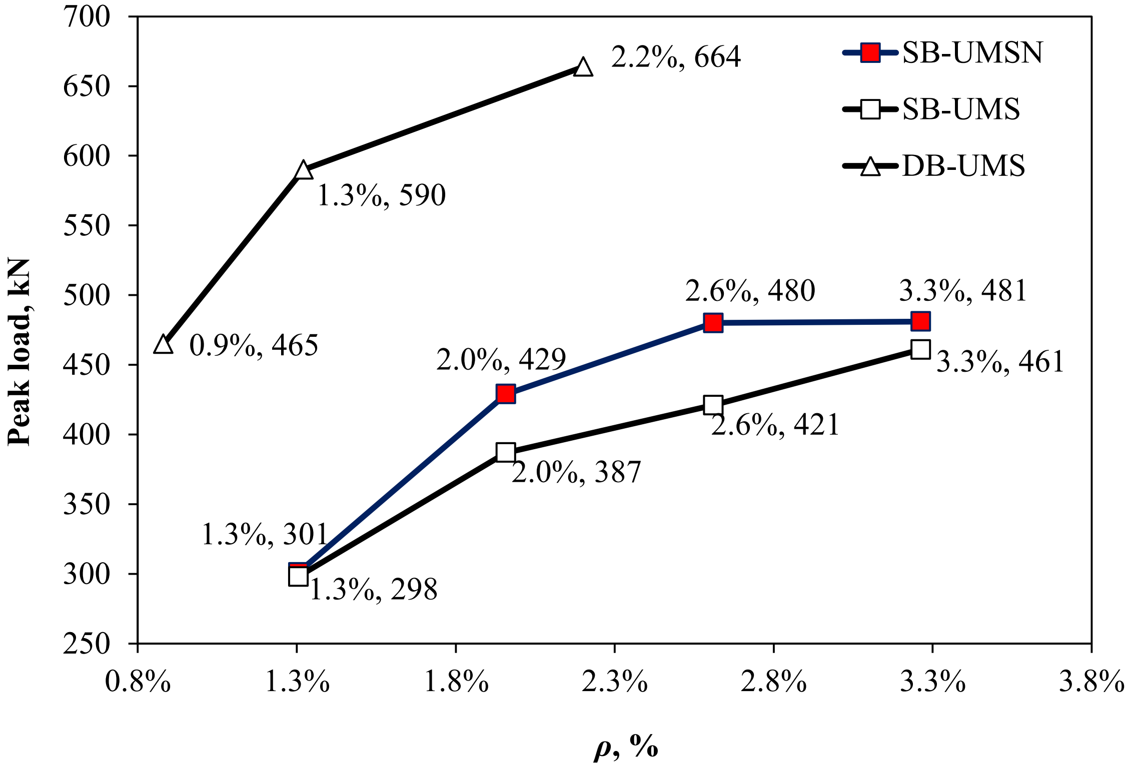

Figure 5.55 Variation of peak load with ρ for all beams.

Structural behavior of UHPC beams

The behaviors of all the passively reinforced UHPC beams tested and evaluated in this study are summarized in this sub-section.

General behavior: The apparent first-crack load obtained from load-deflection curves occur at loads above the theoretical values obtained based on basic strength of materials. Transition of bending stiffness from the initial linear elastic response to the post-first-crack was smooth. Thereafter the post-first-crack flexural response was linear. For beams that failed in flexure, the linear post-first-crack flexural response was followed by yielding of the passive reinforcements in tension, and subsequent ductile softening. However, beams that failed in shear lacked the post-rebar yielding ductile softening behavior. The post first-crack bending stiffness was found to increase significantly with increasing ρ levels. Figure 5.56 shows the general load-midspan deflection curves for all the reinforced UHPC beams considered in this study.

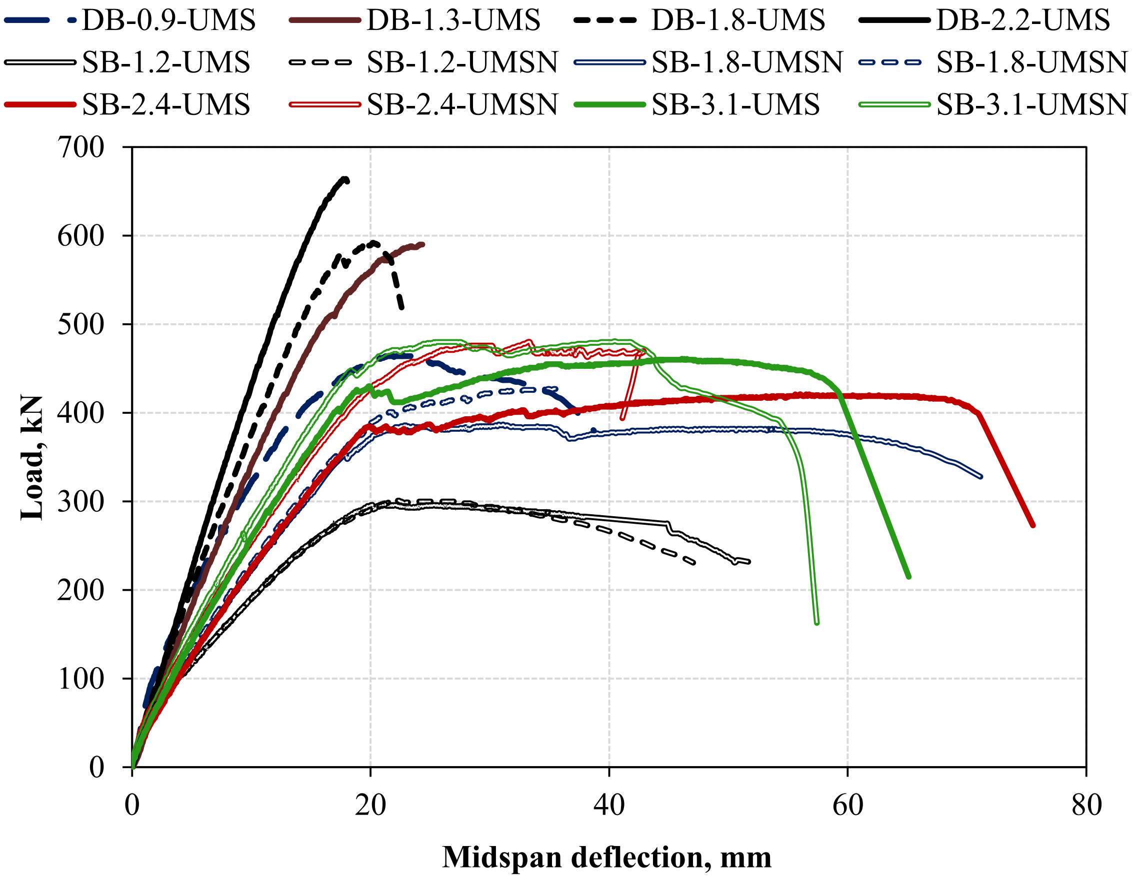

Figure 5.56 **Load-midspan deflection curves for all studied reinforced UHPC beams.**

Effect of UHPC mixture on the behavior of reinforced UHPC beams: Consistently, UMSN beams exhibited higher load capacities than their UMS equivalents. This observation was attributed to by the higher tendency of matrix damage induced by higher thermal gradient recorded in UMS beams, as stated earlier. Coupled with the thermal damage factor was the better fiber activation and utility potential observed in UMSN, as highlighted earlier. Due to the higher load capacities of UMSN beams, their failure behaviors were found to be different than those of equivalent UMS beams, as regards the evolution of shear and bearing damages in addition to flexure damages.

Effect of passive reinforcement ratio, ρ, on the behavior of UHPC beams: Generally, the ultimate load capacity of UHPC beams increased with increasing ρ. For SB-Series UHPC beams having shear span to depth ratio, $a/d = 3.25$ and depth of 225 mm, failure of the beams changed from tension-controlled to compression-controlled as ρ increased. Specifically, SB-Series-UMS beams with ρ of 1.2 and 1.8 % exhibited tension-controlled flexural failure mode, typical of under-reinforced beams, leading to rupture of tension rebars after significant relatively large deflection in excess of 50 mm over the flexure span of 1.75 m. However, SB-Series-UMS beams with ρ of 2.4 % appeared to fail in a transition region between tension- and compression-controlled flexural failures. SB-Series-UMS beams with ρ of 3.1 % exhibited compression-controlled flexural failure mode. The failure of SB-Series-UMS beams with ρ of 2.4 and 3.1 % were accompanied by some degrees of damages in shear-critical regions, as well as extensive damages of compression block, while tension rebars remained unruptured at failure, in a typical behavioral response of over-reinforced beams.

Interestingly, it was found that both tension- and compression-controlled SB beams failed in ductile manners, with the latter exhibiting larger ultimate midspan deflections than the former over the same flexure span. In reference to the mixture effect highlighted earlier, SB-Series-UMSN beams experienced higher shear and bearing damages than equivalent UMS beams, even though they also failed in flexure like corresponding UMS beams.

For DB-Series UHPC beams having shear span to depth ratio, $a/d = 2.43$ and depth of 300 mm, failure of the beam with ρ of 0.9 % exhibited tension-controlled flexural failure mode, typical of under-reinforced beams, leading to rupture of tension rebars after significant large deflection in excess of 40 mm over the flexure span of 1.75 m. However, other DB-Series-UMS beams with $\rho > 0.9$ % exhibited diagonal shear failure mode, accompanied yielding of the tension rebars caused by strut-tie action of the rebars.

CHAPTER 6

FLEXURAL CAPACITY OF PASSIVELY REINFORCED UHPC BEAM SECTIONS

The flexural response of a reinforced UHPC beam is controlled by the compression block action, tension reinforcement deformation characteristics, as well as the post-crack response of UHPC in the tension zone of the cross-section. This chapter highlights the relevant analysis of a typical cross-section of reinforced UHPC beam based on its peculiarities as compared conventional concrete response in flexure.

6.1 Analysis of Passively Reinforced UHPC Beam Sections

6.1.1 Assumptions

The uniaxial compressive stress-strain responses of the UHPC mixtures studied have been discussed extensively in Section 4.2. The general uniaxial compression response was nearly linear up to the peak load, accompanied with significant post-peak compressive strain energy reserve. Thus, triangular compression block parameters were developed from the experimental data for the class of UHPC studied in the present research (Section 4.2.4). Further, Section 4.2.2 has detailed appropriate useable compressive strain at ULS, while Section 4.2.3 has featured typical modulus of elasticity for the studied UHPC mixtures. All these information provide the platform upon which the analysis assumptions are made.

The following assumptions were made in order to obtain relevant relationships for a typical reinforced UHPC cross-section:

1. The section capacity shall be based on satisfying the applicable conditions of equilibrium and compatibility of strains.
2. The strain at any point in the section shall be assumed directly proportional to the distance from the neutral axis.
3. The maximum useable strain ε_{cu} at the extreme compression fiber of UHPC shall be taken as 0.0035.
4. Based on the analysis presented in Section 4.2.4, the concrete compression behavior at ultimate capacity can be approximated by a triangular stress block.

6.1.2 Notations

E_c	Chord modulus of elasticity of UHPC
E_s	Secant modulus of elasticity of UHPC
ϵ_s	Strain in steel bar
ϵ_{su}	Ultimate strain of steel bar
ϵ_c	Strain in concrete

ϵ_{cu}	Ultimate strain of UHPC in compression
ϵ_{ys}	Yield strain of steel bar
ϵ_{ys}	Yield strain of UHPC in tension
f'_t	Yield strain of UHPC in tension
f'_c	Compressive strength of UHPC
f_y	Yield strength of steel bar
A_s	Total area of a group of reinforcement bars
ρ	Reinforcement ratio
ρ_b	Reinforcement ratio at balanced strain condition
ρ_{min}	Minimum reinforcement ratio
ρ_{max}	Maximum reinforcement ratio
α_{1E}	Equivalent compression stress block parameter
α_{2E}	Equivalent tension stress block parameter
c	Depth of neutral axis
x_b	Depth of neutral axis at the at balanced strain condition
x_u	Depth of neutral axis at the ultimate moment capacity
M_n	Nominal moment capacity of a passively reinforced beam section

6.1.3 Formulations

Conditions of reinforced UHPC section at nominal strength

A UHPC section reinforced with passive steel bars is depicted in Figure 6.1. The strain condition is same as for traditional reinforced concrete, in accordance with the analysis Assumption 2. The stress condition consists of triangular compression block and rectangular tension block.

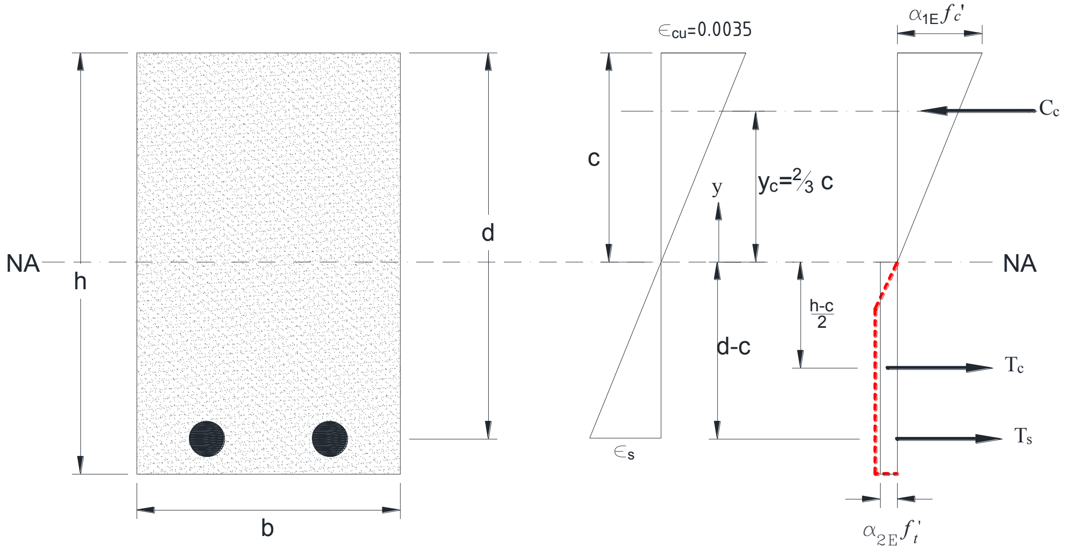

(a) Singly Reinforced UHPC section (b) Strain condition at nominal strength (c) Stress condition at nominal strength

Figure 6.1 **Conditions of passively reinforced rectangular UHPC section at nominal strength.**

Equivalent compression stress block parameter

Figure 6.2 shows a typical stress-strain curve of UHPC in compression. Based on previous discussions presented in Section 4.2.2, a value of $\epsilon_{cu} = 3500$ με (0.0035) was recommended as design value for UHPC. In addition, the compression block parameter, α_{1E}, may also be taken as 1.0, based on previous discussions offered in Section 4.2.4 4.2.2. This value is conservatively justified because the actual value obtained by least-square fitting of the experimental data was α_{1E} = 1.0725. This is in addition to the fact that significant compression strain energy available in the post-peak region of the stress-strain curve has been ignored by the methodology through which the compression block parameter was obtained, as detailed in Section 4.2.4.

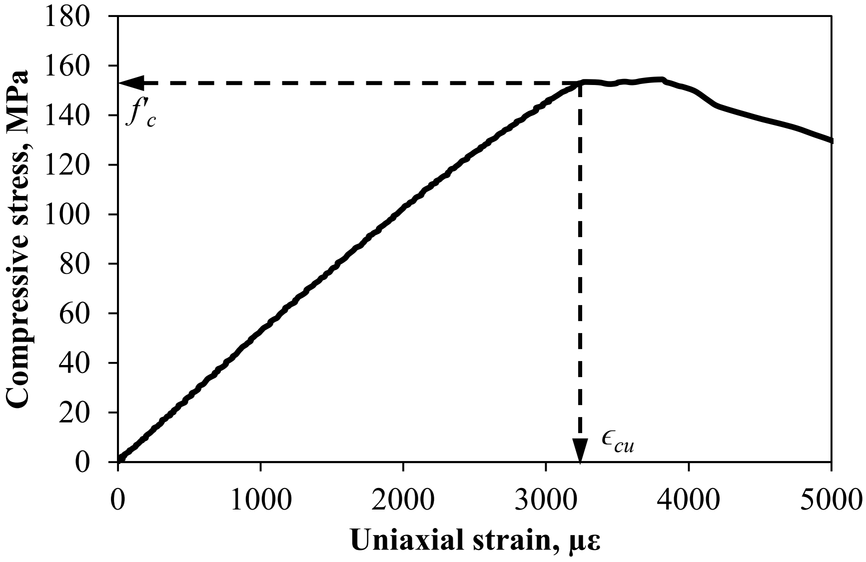

Figure 6.2 **Typical response of UHPC in uniaxial compression.**

Equivalent tension stress block parameter

Figure 6.3 shows a typical stress-strain curve of UHPC in direct tension. As discussed earlier in Section 4.4, strain values recorded beyond the cracking strain of about 400 με

(0.0004) are composite crack-bridging-based strains, which include widening of several micro-cracks within the gauge length. Based on the illustration shown in Figure 6.3, the following values can be conservatively taken:

$f'_t = 8$ MPa, $\alpha_{2E} = 0.75,$ $\epsilon_{yc} = 5000$ με $= 0.0005\ mm/mm$

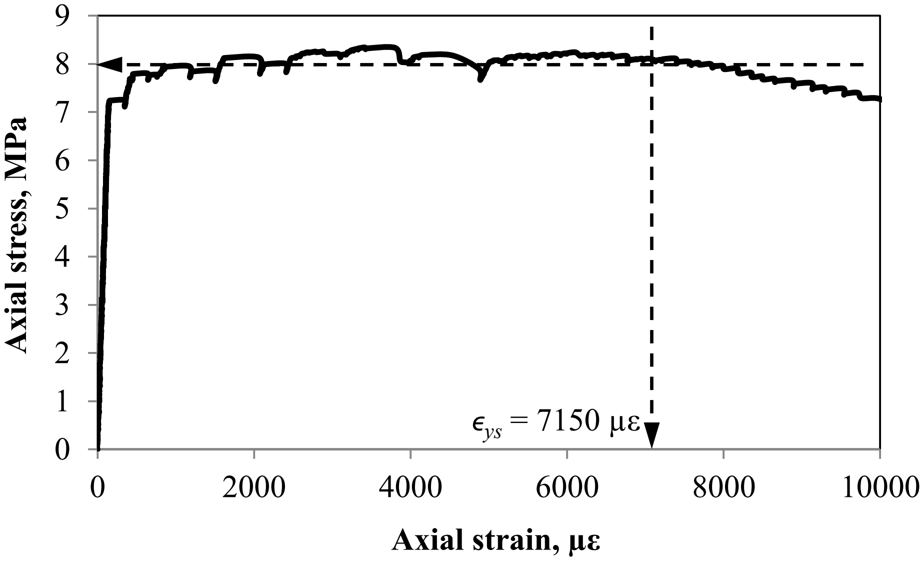

Figure 6.3 **Typical response of UHPC in uniaxial direct tension.**

Passive reinforcement ratio at a balanced strain condition, ρ_b

The balanced strain condition is a state at which the maximum strain at the extreme compression fiber of the UHPC just reaches the crushing strain, ϵ_{cu}, when the maximum tensile strain in the passive steel reaches the yield value, ϵ_{ys}. Figure 6.4 depicts the conditions of a passively reinforced rectangular UHPC section at balanced strain condition

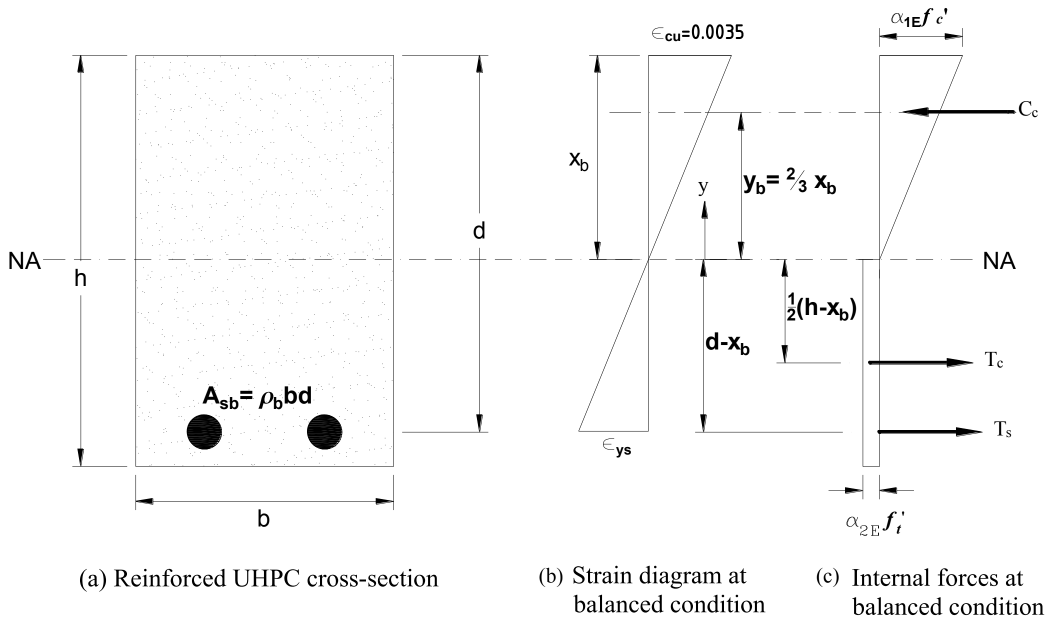

Figure 6.4 **Conditions of passively reinforced rectangular UHPC section at balanced condition.**

For the case of balanced strain condition, the following relationships are presented:

Compressive force in concrete,

$$C_c = \frac{1}{2} \alpha_{1E} \, f_c{}' \, b \, x_b \tag{6.1}$$

Let the reinforcement ratio at balance strain condition, ρ_b, be defined as

$$\rho_b = \frac{A_{sb}}{bd} \tag{6.2}$$

Tensile force in steel,

$$T_s = f_y \, \rho_b bd \tag{6.3}$$

Tensile force in UHPC,

$$T_u = \alpha_{2E}\, f_t{}' b(d - x_b) \tag{6.4}$$

Considering equilibrium of forces ($T_u + T_s = C_c$),

$$\rho_b = \frac{0.5\alpha_{1E}\, f_c{}' x_b - \alpha_{2E}\, f_t{}'(d - x_b)}{f_y\, d} \tag{6.5}$$

or

$$\rho_b = \frac{(0.5\alpha_{1E}\, f_c{}' + \alpha_{2E}\, f_t{}')}{f_y}\frac{x_b}{d} - \frac{\alpha_{2E} f_t{}'}{f_y} \tag{6.6}$$

The strain compatibility condition needs to be invoked to replace $\frac{x_b}{d}$ in Equation 6.6 by terms of material strains at balance strain condition. From the geometry of Figure 6.4,

$$\frac{x_b}{d} = \frac{\epsilon_{cu}}{\epsilon_{cu} + \epsilon_{ys}} \tag{6.7}$$

Therefore,

$$\rho_b = \frac{(0.5\alpha_{1E}\, f_c{}' + \alpha_{2E}\, f_t{}')}{f_y}\, \frac{\epsilon_{cu}}{\epsilon_{cu} + \epsilon_{ys}} - \frac{\alpha_{2E} f_t{}'}{f_y} \tag{6.8}$$

Where, ϵ_{cu}can be taken as $\epsilon_{cu} = 0.0035$, as in analyses assumption 4.

From the data above, for an ASTM grade 60 steel with $f_y = 420\ MPa$,

$$\rho_b = \frac{(0.5 \times 1.0 \times 150 + 0.75 \times 8)}{420}\, \frac{0.0035}{0.0035 + 0.0021} - \frac{0.75 \times 8}{420} = 0.1063$$

It should be noted that ρ_b increases with $f_c{}'$and $f_t{}'$, and inversely proportional to f_y. As such, the value of ρ_b obtained as 10.6 % in this example is about three times that of a normal strength traditional concrete with the same rebar grade.

Various values of ρ_b can be tabulated for various steel yield strengths, as shown in Table 6.1.

Table 6.1 **Values of ρ_b for UHPC at various steel yield strengths.**

Rebar Designation	f_y (MPa)	ρ_b
ASTM A615 / A615M	420	0.1063
GS06/ISO B500BR	500	0.0825
ASTM A722/A722 M (PSB1080)	1080	0.0239
	1400	0.0150

From the values presented in Table 6.1, it can be noted that the ρ_b for conventional high yield steel bars in UHPC beam is too high to be practical. In order to establish this claim, it is important to visualize the practical arrangement of rebars making 10.6 % of a typical UHPC beam cross-section. For SB-Series beam with b = 150 mm and h = 225 mm, 18 numbers of 16 mm diameter bars are required. The practical arrangement of these rebars in the beam is shown in Figure 6.5. The arrangement shown in Figure 6.5 implies that the bottom 71 % of the cross-section is occupied by reinforcement. This scenario is impractical. However, for the case PSB1080 with $f_y \approx$ 1400 MPa, Table 6.1 indicates that ρ_b = 1.5 %, which will result into a more practical steel arrangement in the beam. Therefore, for passively reinforced UHPC, steel bars with high yield strength ($f_y \geq$ 1000

MPa) should be used to keep the values of ρ_b in the practical ranges. This was the reason PSB1080 rebars were utilized as passive reinforcements in the present study.

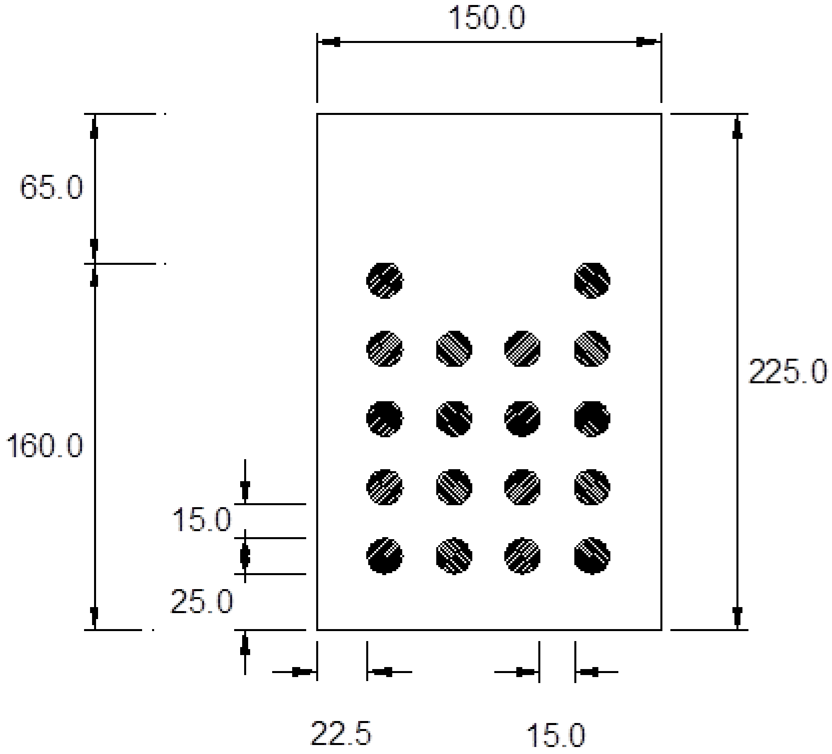

Figure 6.5 **Practical arrangement of rebars corresponding to ρ_b = 10.6 % in a UHPC beam cross-section.**

Furthermore, it is important to note that the maximum allowable reinforcement ratio in a beam cross-section, ρ_{max}, is always a fraction of ρ_b, as will be shown shortly. However, SB-1.8 beams have shown exceptional ductility, leading to rupture of the tension rebars, even though they had ρ = 1.8 %, which is larger than the value of ρ_b = 1.5 %. Therefore, the value of ρ_b according to Table 6.1 for the rebar grade used in this research (PSB1080 with $f_y \approx 1400$ MPa), cannot be taken in the same sense as in traditional reinforced concrete design. Further examination of practical ρ limits is pursued in the next section.

Maximum reinforcement ratio, ρ_{max}

For non-prestressed flexural members at nominal moment capacity, ACI 318-08 Clause 10.3.5 prescribes a minimum net tensile strain of $\epsilon_t \leq 0.004$ in tension rebars, at the instance the extreme compression fiber of concrete reaches ϵ_{cu}. This is approximately twice the yield strain for grade 60 steel ($\epsilon_y \approx 0.0021$). The main idea behind this prescription is to ensure that the steel has yielded completely, when the concrete starts to crush at the compression zone. Similar to Equation 6.7, the strain compatibility condition for this case yields

$$\frac{x_{\epsilon_{t,min}}}{d} = \frac{\epsilon_{cu}}{\epsilon_{cu} + \epsilon_{t,min}} \tag{6.9}$$

Like in Equation 6.8,

$$\rho_{max} = \frac{(0.5\alpha_{1E}\, f_c{}' + \alpha_{2E}\, f_t{}')}{f_y}\left(\frac{x_{\epsilon_{t,min}}}{d}\right) - \frac{\alpha_{2E} f_t{}'}{f_y} \tag{6.10}$$

$$\Rightarrow \rho_{max} = \frac{(0.5\alpha_{1E}\, f_c{}' + \alpha_{2E}\, f_t{}')}{f_y}\frac{\epsilon_{cu}}{\epsilon_{cu} + \epsilon_{t,min}} - \frac{\alpha_{2E} f_t{}'}{f_y} \tag{6.11}$$

Again, for an ASTM grade 60 bar, and assuming

$\alpha_{1E} = 1.0;\ \alpha_{2E} = 0.75;\ \ f_t{}' = 8\ MPa;\ \epsilon_{t,min} = 0.004$

$$\rho_{max} = \frac{(0.5 \times 1.0 \times 150 + 0.75 \times 8)}{420}\frac{0.0035}{0.0035 + 0.004} - \frac{0.75 \times 8}{420} = 0.0757 \approx 0.7\rho_b$$

For a general case, it may be reasonable to set $\epsilon_{t,min} = 2\epsilon_y$. Thus, various values of ρ_{max} can be tabulated for various steel yield strengths, as shown in Table 6.2.

Table 6.2 Values of ρ_{max} for various steel yield strengths.

Rebar Designation	f_y (MPa)	ρ_b	ρ_{max}	ρ_{max}/ρ_b
ASTM A615 / A615M	420	0.1063	0.0734	0.6906
GS06/ISO B500BR	500	0.0825	0.0547	0.6631
ASTM A722/A722 M (PSB1080)	1080	0.0239	0.0112	0.4686
	1400	0.0150	0.0069	0.4628

These values are different, as expected, from the ACI traditional limit of $\rho_{max} \approx {}^{3}/_{4}\,\rho_b$ for Grade 40 to 60 rebars. Similar to the case of ρ_b discussed in the last section, it can be seen from Table 6.2 that the value of ρ_{max} of 0.69 % cannot be accepted. This is based on the fact that SB-1.2 beams exhibited failure behaviors indicating that they were grossly under-reinforced, resulting into rupture of tension rebars, even though they had ρ = 1.2 %, which is larger than the value of supposed ρ_{max} = 0.69 %. Therefore, future studies need to look into establishing the correct reinforcement ratio limits for UHPC beams reinforced with high strength rebars.

Minimum reinforcement ratio, ρ_{min}

Referring again to Figure 6.1, the nominal moment capacity is given by

$$M_n = T_s\left(d - \frac{c}{3}\right) + T_c\left(\frac{2c}{3} + \frac{h-c}{2}\right) \tag{6.12}$$

Substituting for the force terms,

$$M_n = A_s f_y \left(d - \frac{c}{3}\right) + \alpha_{2E}\, f_t{}' b(h - c)\left(\frac{2c}{3} + \frac{h-c}{2}\right) \tag{6.13}$$

Equation 6.13 is based on the assumption that the section is cracked. For low factored moments, the reinforcement requirement will be so low that the computed nominal strength obtained from Equation 6.13 will be lower than the cracking strength of plain uncracked section. In order to enforce the desirable ductile failure mode on the section, the minimum reinforcement ratio is that which satisfies the following criteria

$$\varphi M_n = \varphi \left[A_s f_y \left(d - \frac{c}{3}\right) + T_c \left(\frac{2c}{3} + \frac{h-c}{2}\right)\right] \geq \left(M_{cr} = \frac{f_{cr} I_g}{y_t}\right) \tag{6.14}$$

where φ is a strength reduction factor,

M_{cr} is the cracking moment,

f_{cr} is the cracking strength,

I_g is the gross moment of inertia of the cross-section about the centroidal axis, and y_t is the distance of the centroid of the cross-section to the tension face of the beam.

For the rectangular section, setting $A_s = A_{min}$ in Equation 6.14, we can obtain

$$A_{min} = \frac{1}{2\varphi f_y (3d - c)} \left[f_{cr} b h^2 - \varphi \alpha_{2E} f_t{}' b (d - c)(c + 3h)\right] \tag{6.15}$$

where, $A_{min} = \rho_{min} bd$

Assuming a ductile section with $\varphi = 0.9$, then

$$\rho_{min} = \frac{1}{2\varphi f_y d(3d-c)}\left(f_{cr}h^2 - \varphi\alpha_{2E}f_t{}'(d-c)(c+3h)\right) \tag{6.16}$$

At the ultimate state, neutral axis depth, *c*, has to be obtained from equilibrium of forces, as

$$C_c = T_s + T_c, \qquad or$$

$$\frac{1}{2}\alpha_{1E}\, f_c{}'\, b\, c = \rho b d f_y + \alpha_{2E}\, f_t{}' b(d - \, c)$$

$$\Rightarrow c = \frac{2\rho_{min} d f_y + 2\alpha_{2E} f_t{}' d}{\alpha_{1E}\, f_c{}' + 2\alpha_{2E} f_t{}'} \tag{6.17}$$

For the present case, using the following parameters:

$f_{cr} = 7$ MPa, $f_y = 1400$ MPa, $d = h - 32.5$ mm $(A_s\ in\ one\ layer)$, $\alpha_{1E} = 1.0$,

$\alpha_{2E} = 0.75$, $f_c{}' = 150$ MPa, $f_t{}' = 8.0$ MPa

Using Equation 6.17 in 6.16 and solving the resulting non-linear equation for ρ_{min} yields

$$\rho_{min} = -0.00116 \tag{6.18}$$

The small value obtained for this example indicates that, mathematically, there is no minimum value for ρ. However, like in previous cases, lower practical limit needs to be established for ρ in passively reinforced UHPC beams in future studies.

6.2 Mechanistic Modeling of Peak Loads

6.2.1 Depth of neutral axis at nominal moment capacity

Equation 6.13 has been derived, based on considerations of equilibrium of the internal force and moment as well as strain compatibility conditions, as reproduced below as Equation 6.19, in which c has been replaced by the depth of neutral axis (NA) at the nominal strength, x_u

$$M_n = A_s f_y \left(d - \frac{x_u}{3}\right) + \alpha_{2E}\, f_t{}' b(h - x_u)\left(\frac{2x_u}{3} + \frac{h - x_u}{2}\right) \tag{6.19}$$

Equation 6.19 gives the nominal moment strength of a rectangular passively reinforced UHPC beam, assuming a flexure failure mode. Since the actual modes of failure of the reinforced beams tested in the present research are not controlled by flexure in most cases, Equation 6.19 is not expected to predict the experimental moment strength of the beams correctly. Therefore, empirical adjustments are required using the actual experimental results. This will be addressed shortly.

As a starting point, it is important to calculate the experimental values of the depths of neutral axis (NA), x_u, in Equation 6.19 for all the studied beams. Figure 6.6 shows the strain profiles in the cross-section of a reinforced UHPC beam at nominal strength. The details of strain gauge (SG) labels as well as strain notations used in Figure 6.6 are shown in Table 6.3. It is clear from Figure 6.6 that the value of x_u at nominal moment strength can be obtained from simple geometry if the strain readings in the SGs are known. Since any two points are sufficient to define the straight line AB in Figure 6.6, x_u can be obtained geometrically in three independent ways with each of the three pairs of SGs, i.e., CT-CB, CH-CL, and ST-SB. The fourth way of obtaining x_u is the usual geometry method, presented in Equation 6.20:

$$x_u = \frac{\epsilon_{cu} d}{\epsilon_{ys} + \epsilon_{cu}} \tag{6.20}$$

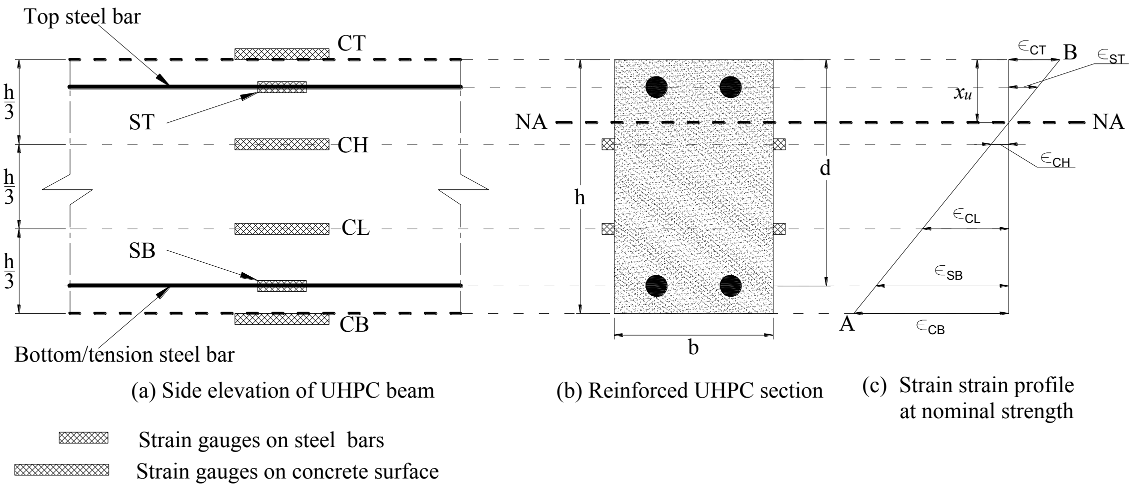

(a) Side elevation of UHPC beam

(b) Reinforced UHPC section

(c) Strain strain profile at nominal strength

Figure 6.6 Strain profiles at nominal strength from strain gauges on steel bars and concrete.

Table 6.3 Details of strain gauge labels used in Figure 6.5.

Strain gauge (SG) label	Description	Strain notation	Description
CT	Concrete SG at top of beam	ϵ_{CT}	Strain recorded in CT
CH	Concrete SG at h/3 from top of beam	ϵ_{CH}	Strain recorded in CH
CL	Concrete SG at h/3 from bottom of beam	ϵ_{CL}	Strain recorded in CL
CB	Concrete SG at bottom of beam	ϵ_{CB}	Strain recorded in CB
ST	Steel SG on top rebar	ϵ_{ST}	Strain recorded in ST
SB	Steel SG on tension rebar	ϵ_{SB}	Strain recorded in SB

Figure 6.7 shows the values of x_u obtained in the four different ways, as stated earlier. As can be noted from Figure 6.7, there are large variations in the values of x_u obtained by the four methods. This is expected, as the SGs are prone to damage before the peak final failure. Therefore, it is important to select the method(s) that are expected to produce reliable estimates. The most reliable of all the SGs, for capturing strain at ultimate load, are those on the steel bars. This is because all SGs mounted on concrete surfaces are prone to damage from cracking of the substrate (concrete) that occur before the ultimate state. On the other hand, the steel SGs can be assumed to be preserved inside concrete. Additionally, the strain profile method (using Equation 6.20) may also be taken as alternative. Hence, x_u values from ST-SB and the strain profile methods were used to estimate the peak load.

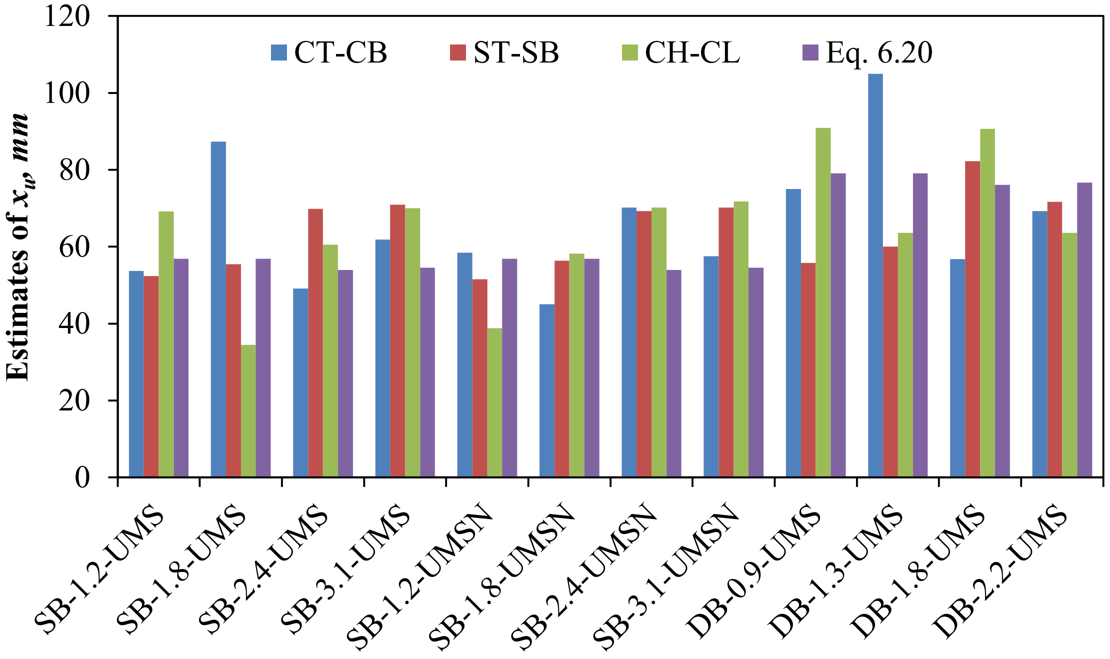

Figure 6.7 **Estimates of the NA depth at nominal moment strength, x_u.**

6.2.2 Peak load at nominal moment capacity

In order to obtain the peak load, P_{max}, corresponding to M_n, it should be noted that

$$\begin{aligned} M_n &= \frac{P_{max}}{2} a \\ \Rightarrow P_{max} &= \frac{2M_n}{a} \end{aligned} \tag{6.21}$$

Where a is the shear span used in the flexural testing, which was fixed at 625 mm, as stated in Section 3.4.6. Using Equations 6.19 and 6.20 in 6.21, two sets of P_{max} can be obtained by taking sets of x_u values from ST-SB and the strain profile methods. These two sets of P_{max} are compared with the experimental values in Figure 6.8. It can be noted in Figure 6.8 that the mechanistic model results are very close. However, these calculated values of P_{max} overestimated the experimental values. The percentage values on the data points represent this error of overestimation.

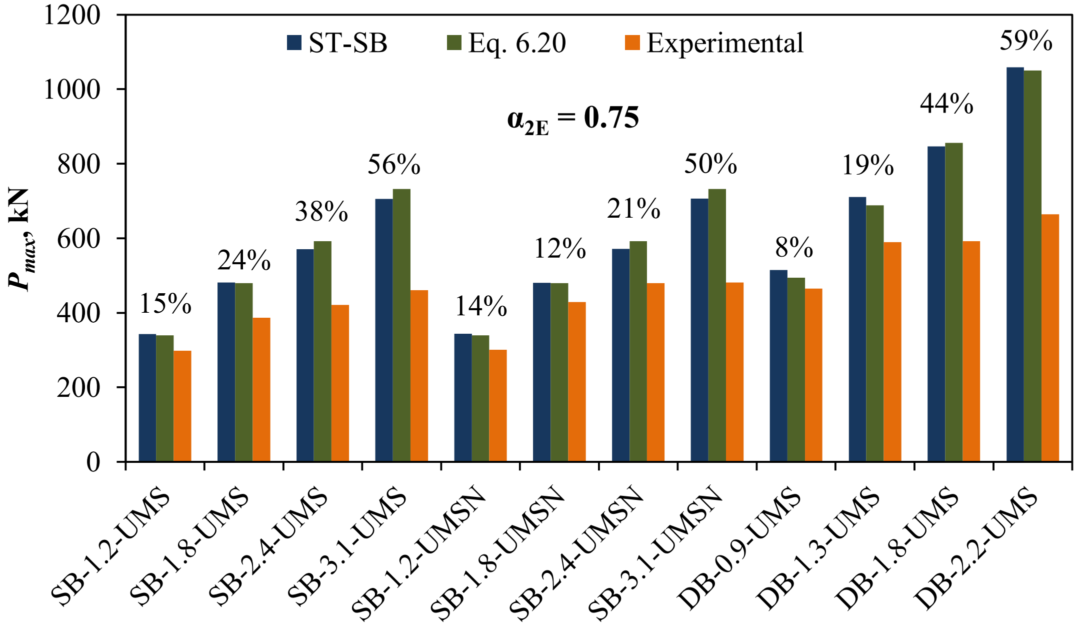

Figure 6.8 **Comparison of mechanistic model estimates of P_{max} (α_{2E} = 0.75), with experimental values.**

It is interesting to note that the error due to overestimation of the experimental results by the mechanistic model is slightly reduced by using $\alpha_{2E} = 0.50$, as depicted in Figure 6.9. Additionally, the mechanistic model has nearly accurately captured the experimental values for beams with low values of ρ. A fact worth noting is that the error due to overestimation increases with ρ, as can be clearly seen in Figure 6.8 and Figure 6.9. This observation is attributable to the fact that shear damage, in addition to bearing damage in some cases, evolved in the failure behavior as ρ increased. The evolution of higher magnitudes of non-flexural damage will obviously reduce the flexural strength of the beam. This has been discussed in detail in previously.

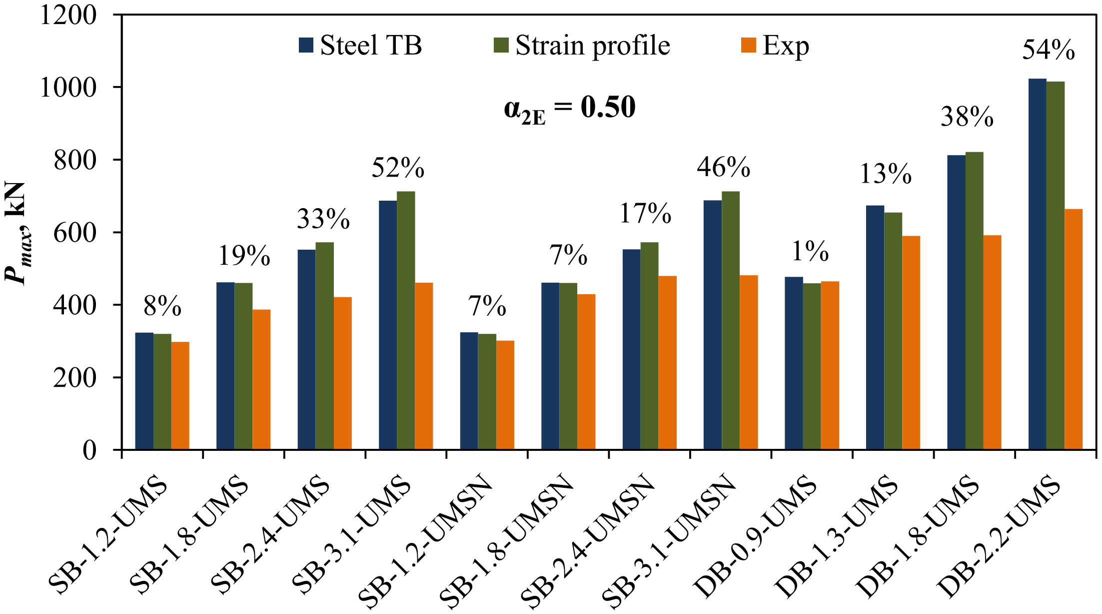

Figure 6.9 **Comparison of mechanistic model estimates of P_{max} ($\alpha_{2E} = 0.50$), with experimental values.**

In order to account for the ρ level in the beams, a semi-mechanistic model was attempted, by introducing shear and ρ parameters of the beams and then carrying out least square fitting of the model with the experimental values (adjusted R^2 = 0.99). This new model is presented in Equation 6.22, as a replacement for the flexure-only Equation 6.19.

$$M_n = \left[A_s\, f_y \left(d - \frac{x_u}{3}\right) + \alpha_2 f_{tmax}\, f_t' b(h - x_u)\left(\frac{2x_u}{3} + \frac{h - x_u}{2}\right)\right] \rho^{\gamma} + \beta \left(\frac{a}{d}\right)^{\kappa} \tag{6.22}$$

$$\alpha_2 = 0.03;\ \gamma = 0.3374;\ \beta = 2.7176 \times 10^7; \kappa = -73952.8;\ x_u = \frac{\epsilon_{cu} d}{\epsilon_y + \epsilon_{cu}}$$

Figure 6.10 shows the comparison of the estimates of P_{max} obtained from the semi-mechanistic model, Equation 6.22, with experimental values. There is a significant improvement in the overall outlook of the error of estimation. However, more experimental data are needed from future studies to model the failure loads properly.

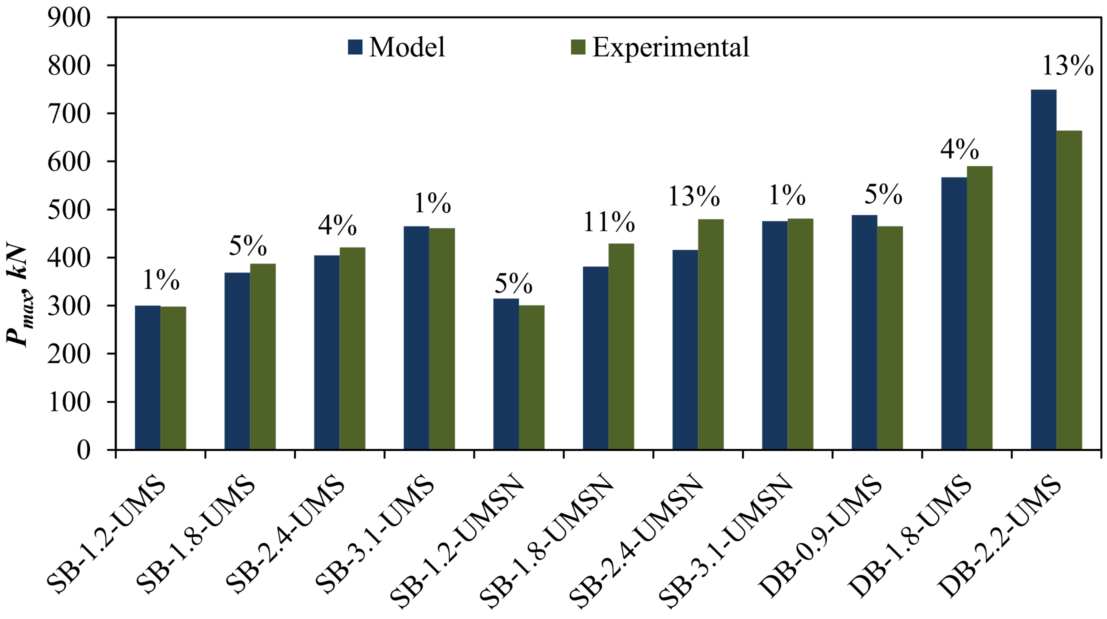

Figure 6.10 **Comparison of semi-mechanistic model estimates of P_{max} with experimental values.**

CHAPTER 7

CONCLUSIONS

The experimental data obtained in the present work was rigorously analyzed using several analytical tools, culminating in the generation of significant amount of secondary information. In addition, the generated information led to a number of useful facts regarding the behavior and practical utilization of ultra-high performance concrete (UHPC) in passively reinforced structural beams.

The outcomes of the present research work can be summarized as follows.

1. It was noted that the partial replacement of microsilica (MS), an imported material available in the Kingdom, by natural volcanic zeolite (NZ) and limestone powder (LSP) does not affect the performance of resulting UHPC. Instead, it was found that the partial replacement of MS with LSP imparted a little improvement in the mechanical characteristics of the reference UHPC.
2. The three UHPC mixtures utilized for mechanical characterization possess similar mechanical characteristics, both in tension and compression.
3. The average cube strength of the UHPCs ranged from 167 MPa to 172 MPa, while the cylinder compressive strengths were in the range of 151 MPa to 154 MPa. The resultant geometric effect was obtained with the cylinder compressive strength being about 11 % higher than that of the cube specimens.
4. The modulus of elasticity of the UHPC mixtures in compression was about 49 GPa, while the stress-strain responses in uniaxial compression were about 91 % linear.

Consequently, a single-parameter triangular compression stress block was found adequate for use in ultimate limit state design of passively reinforced UHPC beams.

5. The design strain at peak stress can be taken as $\epsilon_{cu} = 3500\ \mu\varepsilon$ (0.0035), even though a good proportion of the tested specimens showed some post-peak ductility, resulting in much higher strains in the vicinity of the peak stress.
6. It was convincingly proved that the inter-batch mechanical characteristics of the studied UHPC mixtures were invariants, pointing to a high degree of repeatability of the UHPC mechanical properties from batch to batch, and consequently a high degree of reliability of the mechanical properties for use in the design of structural members.
7. The observed invariance of compressive strength across the UHPC mixtures was also replicated in tension test results. All the UHPC mixtures exhibited similar behaviors in tension. The average matrix strength in direct tension obtained from un-notched prismatic UHPC specimens was about 8.2 MPa, while the corresponding value from 4-point flexure, after correcting for the so-called scale effect, was about 9 MPa.
8. The peak temperature recorded at the core of a 300 mm deep beam for UMS mixture while same was 56.1 °C for UMSN mixture. The temperature difference between the core and the bottom face of the beam were 4.5 and 3 °C for UMS and UMSN, respectively. The higher temperature differential in UMS increased its matrix damage tendency by about 50 %.
9. UMS and UMSN mixtures were found to have similar mechanical characteristics in terms of compressive strength, modulus of elasticity and flexural cracking strength.

However, UMSN mixture possessed a better fiber activation and utility potential than UMS, as indicated by 28 % higher equivalent flexural strength of UMSN than that of UMS.

10. The post-first-crack bending stiffness, the evolution of shear and bearing damages, and the ultimate load capacity of passively reinforced UHPC beams were found to increase significantly with increasing ρ levels.
11. Beams fabricated using UMSN mixture consistently exhibited higher load capacities than their UMS mixture equivalents due to the higher tendency of matrix damage induced by higher thermal gradient in UMS beams as well as the better fiber activation and utility potential observed for UMSN mixture. Due to the higher load capacities of beams prepared using UMSN mixture, their ultimate failure behaviors were found to be different than those of equivalent beams made with UMS mixture.
12. SB-Series-UMS beams with ρ of 1.2 and 1.8 % exhibited tension-controlled flexural failure mode, which was accompanied by rupture of tension rebars, while those with ρ of 2.4 % failed in a transition mode. SB-Series-UMS beams with ρ of 3.1 % exhibited compression-controlled flexural failure mode. All SB-Series beams exhibited high ductility.
13. DB-Series UHPC beams with ρ of 0.9 % exhibited ductile tension-controlled flexural failure mode, which led to the rupture of tension rebars. DB-Series-UMS beams with $\rho > 0.9$ % exhibited diagonal shear failure modes, which were preceded by extensive diagonal cracks indicating exceptional stress redistribution ability of the UHPC mixtures which was aided by their excellent fiber activation capabilities.

14. For structural beams, high strength steel bars with $f_y \geq 1000$ MPa are required to obtain acceptable structural behavior of reinforced UHPC beams.

15. Finally, it was found that the flexural beams with „moderately high‟ reinforcement ratio of about 3.1 % pose no safety challenges in the behavior of passively reinforced UHPC beams, as those beams exhibited exceptional ductility that offer sufficient warnings for impending failures.

16. A semi-mechanistic model is proposed to predict the flexural capacity of passively reinforced UHPC beams, with a fair degree of accuracy.

RECOMMENDATION FOR FUTURE STUDIES

1. Due to the constraint in the available mixing capacity of the planetary concrete mixer utilized in the present study, the length of the beams tested was limited to only 2 m, leading to the use of a relatively low a/d. Consequently, as the levels of ρ increased, flexural failures were mixed with evolved shear and bearing damages. Hence, it is essential for future studies to include longer span beams to ensure „flexure-dominant‟ behaviors. In addition, studies of passively reinforced deep and short UHPC beams are required to ensure „shear-dominant‟ behaviors. These will help in further understanding of the structural behaviors of passively reinforced UHPC beams.
2. Templates for limits of passive reinforcement ratios in flexural UHPC beams have been established in the present study. However, the limitation of data did not allow an adequate treatment of the subject. Therefore, future studies need to build on the current template and come up with adequate levels of limits of passive reinforcement ratios, i.e., ρ_{min}, ρ_b, and ρ_{max}.

REFERENCES

[1] Fehling, E., et al., *Entwicklung, Dauerhaftigkeit und Berechnung Ultra-Hochfester Betone (UHPC) [development, durability and design of UHPC] in DFG research report FE 497/1-1.* Structural Materials & Engineering Series No. 1, 2005.

[2] ajna, A., E. Denarié, and V. Bras, *Assessment of a UHPFRC based bridge rehabilitation in Slovenia, two years after application, in Ultra High Performance Concrete and Nanotechnology in Construction, 3rd Intl. Symp. on Ultra High Performance Concrete and Nanotechnology for High Performance Construction Materials.* Structural Materials & Engineering Series No. 19, 2012: p. 937–944.

[3] Piotrowski, S. and M. Schmidt, *Life-cycle cost analysis of a UHPC-Bridge on example of two Bridge Refurbishment Designs, in Ultra High Performance Concrete and Nanotechnology in Construction, 3rd Intl. Symp. on Ultra High Performance Concrete and Nanotechnology for High Performance Construction Materials.* Structural Materials & Engineering Series No. 19, 2012: p. 957–964.

[4] Schmidt, C., *Whitetopping of asphalt and concrete pavements with thin layers of ultra high performance concrete – construction and economic efficiency (Dissertation, University of Kassel, in German).* Structural Materials & Engineering Series, No. 20, 2012.

[5] Russell, H.G. and B.A. Graybeal, *Ultra-High Performance Concrete: A State-Of-The-Art Report for The Bridge Community*, 2013, The Federal Highway Administration (FHWA): 1200 New Jersey Avenue, Washington DC 20590, 202-366-4000, USA. p. 171.

[6] fédération internationale du béton *CEB-FIP Model Code 2010 Final draft*, in *Bulletins 65 & 66*2012, fédération internationale du béton (fib): Lausanne.

[7] Schmidt, M. and D. Jerebic, *Basis for Sustainable Structures – the Gaertner- platz Bridge in Kassel in 2nd Intl. Symp. on Ultra High Performance Concrete.* Structural Materials & Engineering Series No. 10, 2008: p. 619–625.

[8] Fehling, E., et al., *Introduction*, in *Ultra-High Performance Concrete UHPC*2014, Wilhelm Ernst & Sohn, Verlag für Architektur und technische Wissenschaften GmbH & Co. KG. p. 1-4.

[9] SETRA-AFGC, *Bétons Fibrés à Ultra-Hautes Performances, Recommandations Provisoires, (Ultra High Performance Fibre-Reinforced Concrete, Interim Recommendations)*, 2002, SETRA-AFGC,Groupe de travail BFUP: Paris, France.

[10] Davila, R.S., *Recommendations for the design of ultra-high performance concrete structures*, in *Dept. of Civil and Environmental Engineering*2007, Massachusetts Institute of Technology: Massachusetts Institute of Technology, USA.

[11] Park, H., *Model-based optimization of ultra high performance concrete highway bridge girders*, in *Dept. of Civil and Environmental Engineering*2003, Massachusetts Institute of Technology: Massachusetts Institute of Technology, USA. p. 139.

[12] JSCE Concrete Committee, *Recommendations for design and construction of high performance fiber reinforced cement composites with multiple fine cracks (HPFRCC)* in *Concrete engineering series no. 82,* 2008, Japan Society of Civil Engineers (JSCE), Japan: Japan.

[13] JSCE Concrete Committee, *Recommendation for design and construction of ultra high strength fiber reinforced concrete structures (Draft)*, in *JSCE Guidelines for Concrete, No. 9.,*2006, Japan Society of Civil Engineers (JSCE), Japan.

[14] Bache, H.H. *Densified Cement Ultra/Fine Particle-Based Materials*. in *2nd Intl. Conf. on Superplasticizers in Concrete*. 1981. Ottawa, Ontario, Canada.

[15] Scheffler, B. and M. Schmidt, *Application of ultra-high performance concrete for multifunctional road pavements, in Ultra High Performance Concrete and Nanotechnology in Construction, 3rd Intl. Symp. on Ultra High Performance Concrete and Nanotechnology for High Performance Construction Materials.* Structural Materials & Engineering Series No. 19, 2012: p. 913–920.

[16] Schmidt, M., et al., *Brückenfamilie aus ultrahochfestem Beton in Niestetal und Kassel [series of UHPC bridges in Niestetal Valley and Kassel]*. Beton-und Stahlbetonbau, 2006. **101**(3): p. 198-204.

[17] Collepardi, S., et al., *Mechanical properties of modified reactive powder concrete.* ACI Special Publication, 1997. **173**.

[18] Fehling, E., et al., *Principles for the production of UHPC*, in *Ultra-High Performance Concrete UHPC*2014, Wilhelm Ernst & Sohn, Verlag für Architektur und technische Wissenschaften GmbH & Co. KG. p. 5-22.

[19] Fehling, E., et al., *Design principles*, in *Ultra-High Performance Concrete UHPC*2014, Wilhelm Ernst & Sohn, Verlag für Architektur und technische Wissenschaften GmbH & Co. KG. p. 65-104.

[20] Graybeal, B., *Material Property Characterization of Ultra-High Performance Concrete*, 2006, FHWA, U.S. Department of Transportation: McLean, VA.

[21] Perry, V. and D. Zakariasen, *First use of ultra-high performance concrete for an innovative train station canopy.* Concrete Tecnology Today-Portland Cement Association, 2004. **25**.

[22] Heinz, D. and H. Ludwig. *Heat Treatment and the Risk of DEF Delayed Ettringite Formation in UHPC*. in *International Symposium on Ultra High Performance Concrete*. 2004.

[23] Graybeal, B.A., *Characterization of the Behavior of Ultra-High Performance Concrete*, in *Civil Engineering*2005, University of Maryland (College Park, Md.): Digital Repository at the University of Maryland.

[24] Soutsos, M.N., S.G. Millard, and K. Karaiskos, *Mix design, mechanical properties and impact resistance of reactive powder concrete (RPC).* Proceedings of international workshop on high performance fiber reinforced cementitious composites in structural applications, 2005.

[25] Richard, P. *Reactive Powder Concrete: A New-Ultra High Strength Cementitious Material*. in *Proceedings of the Fourth International Symposium on the Utilization of High-Strength/High-Performance Concrete*. 1996. Paris, France.

[26] Hassan, A.M.T., S.W. Jones, and G.H. Mahmud, *Experimental test methods to determine the uniaxial tensile and compressive behaviour of Ultra High Performance Fibre Reinforced Concrete(UHPFRC).* Construction and Building Materials, 2012. **37**: p. 874-882.

[27] Graybeal, B.A. and F. Baby, *Development of direct tension test method for ultra-high-performance fiber-reinforced concrete.* ACI Materials Journal, 2013. **110**(2): p. 177-186.

[28] Hakeem, I.Y.A., *Structural Behavior of Unreinforced Hybrid Slab Elements Cast with Ultra-High Performance Concrete (UHPC)*, in *Civil Engineering*2014, King Fahd University of Petroleum and Minerals (Saudi Arabia): Ann Arbor. p. 183.

[29] Fehling, E., et al., *Mechanical properties of the hardened concrete*, in *Ultra-High Performance Concrete UHPC*2014, Wilhelm Ernst & Sohn, Verlag für Architektur und technische Wissenschaften GmbH & Co. KG. p. 23-58.

[30] Leutbecher, T., *Rissbildung und Zugtragverhalten von mit Stabstahl und Fasern bewehrtem Ultrahochfesten Beton (UHPC) [crack formation and tensile loadbearing behaviour of UHPC reinforced with steel bars and fibres](Dissertation, University of Kassel).* Structural Materials & Engineering Series No. 9, 2008: p. 913–920.

[31] Pfyl, T., *Tragverhalten von Stahlfaserbeton [structural behaviour of steel fibrereinforced concrete] (Dissertation, ETH No. 15005)*, 2003, ETH Zurich.

[32] Behloul, M., *Analyse et modélisation du comportement d'un matériau à matrice cimentaire fibrée à ultra hautes performances : bétons de poudres réactives, du matériau à la structure*, 1996. p. 1 vol. (182 p.).

[33] Jungwirth, J., *Zum Zugtragverhalten von zugbeanspruchten Bauteilen aus Ultra-Hochleistungs-Faserbeton [on the tensile loadbearing behaviour of fibre-reinforced UHPC components in tension]. Dissertation thesis No. 3429*, 2006, Faculty of Architecture, Civil & Environmental Engineering (ENAC), Ècole Polytechnique Fédérale de Lausanne (EPFL).

[34] Li, V.C. and C.K.Y. Leung, *Steady-state and multiple cracking of short random fiber composites.* Journal of Engineering Mechanics, 1992. **188**(11): p. 2246–2264.

[35] Baby, F., et al., *Proposed flexural test method and associated inverse analysis for ultra-high-performance fiber-reinforced concrete.* ACI Materials Journal, 2012. **109**(5): p. 545-555.

[36] Baby, F., et al., *UHPFRC tensile behavior characterization: Inverse analysis of four-point bending test results.* Materials and Structures/Materiaux et Constructions, 2013. **46**(8): p. 1337-1354.

[37] ASTM C1018, *Standard Test Method for Flexural Toughness and First-Crack Strength of Fiber-Reinforced Concrete (Using Beam With Third Point Loading) (Withdrawn 2006)*, 1997, ASTM International: West Conshohocken, PA.

[38] Richard, P. and M. Cheyrezy, *Composition of reactive powder concretes.* Cement and Concrete Research, 1995. **25**(7): p. 1501-1511.

[39] Tanaka, Y., et al. *Design and construction of Sakata-Mirai footbridge using reactive powder concrete*. in *Proceedings of the 1st fib Congress*. 2002.

[40] Graybeal, B.A. and J.L. Hartmann, *Strength and durability of ultra-high performance concrete.* Proceedings of the 2003 PCI National Bridge Conference, 2003.

[41] Tue, N., F. Dehn, and et al., *Composite elements made of steel tubes and ultrahigh strength concrete as motor of innovation in final report to Bilfinger Berger AG (unpublished)*, 2004, Leipzig University.

[42] Hartmann, J. and B. Graybeal, *ABANDON THE USUAL : ULTRA-HIGH-PERFORMANCE CONCRETE PROVES STRONGER - AND STRANGER - THAN THE CONVENTIONAL.* Roads & Bridges, 2005. **43**(6): p. 5p.

[43] Behloul, M. and et al., *Fatigue Flexural Behavior of Pre-Cracked Specimens of Special UHPFRC, in Seventh International Symposium on the Utilization of High-Strength/High-Performance Concrete.* American Concrete Institute, Farmington Hills, MI, 2005. **II**(SP-228): p. 1,253–1,268.

[44] Lappa, E.S., C.R. Braam, and J.C. Walraven, *Static and Fatigue Bending Tests of UHPC, in Proceedings of the International Symposium on Ultra High Performance Concrete.* Kassel University Press, Kassel, Germany, 2004: p. 449–458.

[45] Schmidt, M., et al.,. *Durability of Ultra High Performance Concrete*. in *Proceedings of the 6th International Symposium on High Strength/High Performance Concrete*. 2002. Leipzig, Germany.

[46] Lohaus, L. and K. Elsmeier, *Fatigue Behaviour of Plain and Fibre Reinforced Ultra-High Performance Concrete, in Proceedings of Hipermat 2012 3rd International Symposium on UHPC and Nanotechnology for High Performance*

Construction Materials. Kassel University Press, Kassel, Germany, 2012: p. 631–637.

[47] Grünberg, J., et al., *Multi-Axial and Fatigue Behaviour of Ultra-High-Performance Concrete, in Proceedings of the Second International Symposium on Ultra High Performance Concrete.* Kassel University Press, Kassel, Germany, 2008: p. 485–492.

[48] Fehling, E., K. Bunje, and T. Leutbecher, *Design Relevant Properties of Hardened Ultra High Performance Concrete, in Proceedings of the International Symposium on Ultra High Performance Concrete.* Kassel University Press, Kassel, Germany, 2004: p. 327–338.

[49] Francisco, P., et al. *Ultra High Performance Concrete for Prestressed Elements—Interest of Creep Prediction (Paper 5.2.1).* in *Proceedings of the International Workshop on Ultra High Performance Fibre Reinforced Concrete—Designing and Building with UHPFRC: State of the Art Development*. 2009. Marseille, France: AFGC/fib.

[50] Francisco, P., et al., *Creep and Shrinkage Prediction for a Heat-Treated Ultra High Performance Fibre-Reinforced Concrete, in Proceedings of Hipermat 2012 3rd International Symposium on UHPC and Nanotechnology for High Performance Construction Materials.* Kassel University Press, Kassel, Germany, 2012: p. 325–331.

[51] Ichinomiya, T., et al., *Experimental study on mechanical properties of ultra-high-strength concrete with low-autogenous-shrinkage.* ACI Special Publication, 2005. **228**: p. 1,341–1,352.

[52] ASTM C157, *Standard Test Method for Length Change of Hardened Hydraulic-Cement Mortar and Concrete*, 2008, ASTM International: West Conshohocken, PA.

[53] Acker, P. and M. Behloul, *Ductal® Technology: A Large Spectrum of Properties, A Wide Range of Applications, in Proceedings of the International Symposium on Ultra High Performance Concrete.* Kassel University Press, Kassel, Germany, 2004: p. 11–23.

[54] Burkart, I. and H.S. Müller, *Creep and Shrinkage Characteristics of Ultra High Strength Concrete (UHPC), in Proceedings of the Second International*

Symposium on Ultra High Performance Concrete. Kassel University Press, Kassel, Germany, 2008: p. 469–476.

[55] Eppers, S. and C. Müller, *Autogenous Shrinkage Strain of Ultra-High-Performance Concrete (UHPC), in Proceedings of the Second International Symposium on Ultra High Performance Concrete.* Kassel University Press, Kassel, Germany, 2008: p. 433–441.

[56] Ma, J., et al., *Comparative Investigations on Ultra-High Performance Concrete With and Without Coarse Aggregates, in Proceedings of the International Symposium on Ultra High Performance Concrete.* Kassel University Press, 2004: p. 205–212.

[57] Ocel, J. and B. Graybeal, *Fatigue Behavior of an Ultra-High Performance Concrete IGirder*, in *Proceedings of the PCI National Bridge Conference (Compact Disc, Paper 82)*2007: Phoenix, AZ.

[58] Staquet, S. and B. Espion, *Early-Age Autogenous Shrinkage of UHPC Incorporating Very Fine Fly Ash or Metakaolin in Replacement of Silica Fume, in Proceedings of the International Symposium on Ultra High Performance Concrete.* Kassel University Press, Kassel, Germany, 2004: p. 587–599.

[59] Suzuki, M., I. Maruyama, and R. Sato, *Properties of Expansive-Ultra High-Strength Concrete, in Seventh International Symposium on the Utilization of High-Strength/High-Performance Concrete.* American Concrete Institute, Farmington Hills, MI, 2005. **II**(SP-228): p. 1,159–1,173.

[60] Kim, S., et al., *Shrinkage Behavior of Ultra High Performance Concrete at the Manufacturing Stage, in Proceedings of Hipermat 2012 3rd International Symposium on UHPC and Nanotechnology for High Performance Construction MaterialsInternational Symposium on Ultra High Performance Concrete.* Kassel University Press, Kassel, Germany, 2012: p. 317–324.

[61] Stürwald, S. and E. Fehling, *Design of Reinforced UHPFRC in Flexure, in Proceedings of Hipermat 2012 3rd International Symposium on UHPC and Nanotechnology for High Performance Construction MaterialsInternational Symposium on Ultra High Performance Concrete.* Kassel University Press, Kassel, Germany, 2012: p. 443–450.

[62] Graybeal, B.A., *Structural Behavior of Ultra-High Performance Concrete Prestressed I-Girders*, 2006, FHWA, U.S. Department of Transportation, Report No. FHWA-HRT-06-115.

[63] Graybeal, B., V. Perry, and M. Royce, *UHPC Ultra-High Performance Concrete*, in *NHI Innovations Webinar*2010.

[64] Meade, T.M. and B.A. Graybeal. *Flexural Response of Lightly Reinforced Ultra-High Performance Concrete Beams*. in *Proceedings of the Third International fib Congress and Exhibition Incorporating the PCI Annual Convention and National Bridge Conference(Compact Disc, Paper 101)*. 2010. Washington, DC.

[65] Chuang, E., *Ductility enhancement of high performance cementitious composites and structures*, in *Dept. of Civil and Environmental Engineering*2002, Massachusetts Institute of Technology: Massachusetts Institute of Technology, USA. p. 319.

[66] fédération internationale du béton -Task Group 8.6, *Draft of Bulletin on Ultra High Performance Fiber Reinforced Concrete (unpublished)*, 2011, fédération internationale du b ton (fib), Ta sk Group 8.6.

[67] SETRA-AFGC, *Fiber concrete ultra-high performance - Recommendations - Revised Edition*, 2013, SETRA-AFGC,Groupe de travail BFUP: Paris, France.

[68] Meyer, C., *The greening of the concrete industry.* Cement and Concrete Composites, 2009. **31**(8): p. 601-605.

[69] Rashad, M.M., et al., *Transformation of silica fume into chemical mechanical polishing (CMP) nano-slurries for advanced semiconductor manufacturing.* Powder Technology, 2011. **205**(1–3): p. 149-154.

[70] Najamuddin, S.K., *Production of medium to low strength concrete utilizing indigenous waste products*, 2011, King Fahd University of Petroleum and Minerals (Saudi Arabia): Ann Arbor. p. 194.

[71] Adekunle, S., et al., *Properties of SCC prepared using natural pozzolana and industrial wastes as mineral fillers.* Cement and Concrete Composites, 2015. **62**: p. 125-133.

[72] Ahmad, S., I. Hakeem, and M. Maslehuddin, *Development of UHPC mixtures utilizing natural and industrial waste materials as partial replacements of silica fume and sand.* Scientific World Journal, 2014. **2014**.

[73] Graybeal, B.A., *Ultra-High Performance Concrete*, in *Technical Notes*2011, Federal Highway Administration, McLean, VA. p. 8p.

[74] Mazanec, O., D. Lowke, and P. Schiel, *Mixing of high performance concrete: Effect of concrete composition and mixing intensity on mixing time.* Materials and Structures/Materiaux et Constructions, 2010. **43**(3): p. 357-365.

[75] Graybeal, B.A., *Material Property Characterization of Ultra-High Performance Concrete*, 2006. p. 186p.

[76] SETRA-AFGC, *Bétons Fibrés à Ultra-Hautes Performances, Recommandations Provisoires - Annexes, (Ultra High Performance Fibre-Reinforced Concrete, Interim Recommendations - Appendices)*, 2002, SETRA-AFGC,Groupe de travail BFUP: Paris, France.

[77] RILEM TC 162-TDF, *Rilem TC 162-TDF: Test and design methods for steel fibre reinforced concrete - Bending test.* Materials and Structures/Materiaux et Constructions, 2002. **35**(253): p. 579-582.

[78] Wang, C.K., C.G. Salmon, and J.A. Pincheira, *Reinforced Concrete Design*. 7th ed. 2006: Wiley.

[79] Hallal, A., et al., *Combined effect of mineral admixtures with superplasticizers on the fluidity of the blended cement paste.* Construction and Building Materials, 2010. **24**(8): p. 1418-1423.

[80] Bonavetti, V., et al., *Limestone filler cement in low w/c concrete: A rational use of energy.* Cement and Concrete Research, 2003. **33**(6): p. 865-871.

[81] Bosiljkov, V.B., *SCC mixes with poorly graded aggregate and high volume of limestone filler.* Cement and Concrete Research, 2003. **33**(9): p. 1279-1286.

[82] Ahmad, S., et al., *Properties of self-consolidating concrete made utilizing alternative mineral fillers.* Construction and Building Materials, 2014. **68**: p. 268-276.

[83] Liu, S. and P. Yan, *Effect of limestone powder on microstructure of concrete.* Journal Wuhan University of Technology, Materials Science Edition, 2010. **25**(2): p. 328-331.

[84] Dang, V.H., R. François, and D. Coronelli, *Shear behaviour and load capacity of short reinforced concrete beams exposed to chloride environment.* European Journal of Environmental and Civil Engineering, 2016. **20**(4): p. 379-395.

[85] Daejoong Kim, W.K. and N.W. Richard, *Arch Action in Reinforced Concrete Beams—A Rational Prediction of Shear Strength.* Structural Journal. **96**(4).

[86] Shuraim, A.B., *A novel approach for evaluating the concrete shear strength in reinforced concrete beams.* Latin American Journal of Solids and Structures, 2014. **11**: p. 93-112.

Vitae

Name :Saheed Kolawole Adekunle

Nationality :Nigerian

Date of Birth :6/3/1979

Email :saeedadekunle@gmail.com

Address :GBK 45, Gbedemuke zone, Atolu Lay-out, Oremeji-
Agugu, Ibadan, Oyo State, Nigeria

Academic Background

MS Civil Engineering (June, 2012), King Fahd University of Petroleum and Minerals, Dhahran 31261, Saudi Arabia.

Research area: Concrete material science and engineering

Thesis: *A study on developing self-consolidating concrete (SCC) utilizing indigenous natural and industrial waste materials*

BEng Civil Engineering (March, 2003), University of Ilorin, Ilorin, Nigeria.

Senior project: *Finite Element Analysis of Bridge Deck Using Visual Basic*

Publications (See Web URLs below)

ORCID	http://orcid.org/0000-0003-2160-1502
Scopus	https://www.scopus.com/authid/detail.uri?authorId=56294076700
ResearchGate	https://www.researchgate.net/profile/Saheed_Adekunle
Google Scholar	https://scholar.google.com/citations?user=4VTq7S0AAAAJ&hl=en